Automatização de sistemas para aquisição de dados fotométricos em aeroluminescência

Primavera Botelho de Souza, Delano Gobbi , Cristiano Max Wrasse e Hisao Takahashi
Instituto Nacional de Pesquisas Espaciais (INPE) – Brasil

Resumo

Este trabalho apresenta o projeto de desenvolvimento de software para dois instrumentos ópticos: o sistema de fotometria convencional, de um filtro inclinável, e o sistema de imageamento usando uma câmera CCD com seis filtros de interferência fixos. Os equipamentos operam de forma automatizada na obtenção de medidas fotométricas de radiância e temperatura das emissões de aeroluminescência da alta atmosfera. A automatização do software consiste no gerenciamento temporal dos períodos de observação adequados para aquisição de dados de aeroluminescência.

1. Introdução

Atualmente, a pesquisa em Luminescência Atmosférica tem como objetivo o estudo das variações de comportamento ondulatório das camadas de aeroluminescência nas regiões equatorial, média e baixa latitude. O grupo de Luminescência Atmosférica do INPE possui instrumentos ópticos operando nos diversos observatórios distribuídos ao longo do território nacional que por características da própria pesquisa, são locais distantes dos grandes centros e de difícil acesso. Portanto a automatização de equipamento surgiu como solução para atender plenamente as necessidades inerentes ao tipo de estudo.

A ênfase deste trabalho está nos exemplos de solução computacional para sistema de tempo real, interfaces de comunicação, recursos para tratamento de imagens e gerenciamento temporal. Sendo dois sistemas distintos, as soluções de software para a interface com cada equipamento diferem, porém ambos os projetos obedecem às restrições impostas para validação dos dados em aeroluminescência.

As Seções 2 e 3 contêm uma descrição do projeto do software de operação para os dois instrumentos ópticos. Em seguida, é discutida na Seção 4 a automatização onde é apresentado um conjunto de tarefas para obtenção dos períodos de observação válidos, cuja implementação compõe uma biblioteca de subrotinas e funções que pode ser integrada a qualquer sistema de aquisição de dados de aeroluminescência.

2. Descrição do projeto do software de fotometria em aeroluminescência

O software de operação do sistema de fotometria de aeroluminescência foi desenvolvido em Visual Basic 6.0 e baseia-se na interface visual com o operador que envia comandos de operação para o fotômetro. A interpretação destes comandos obedece ao protocolo de comunicação PC/fotômetro estabelecido para o projeto. Os *frames* de comunicação contêm as mensagens transmitidas através da interface serial RS232, que implementa o conceito **mestre-escravo** ver, por exemplo, Tanenbaum, 1990). ao comandar e receber resposta sob demanda do usuário (Figura 1).

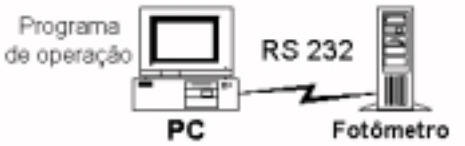

Fig 1 – Interface serial entre o PC e o fotômetro

As respostas enviadas pelo fotômetro, são armazenadas em um vetor cujos elementos são bytes. A quantidade, o formato e a seqüência de bytes armazenados por *frame* varia de acordo com o comando solicitado, definido no protocolo de comunicação. A figura 2 mostra a organização dos bytes dentro de cada *frame.*

SINC	TIPO	TAM	**DADOS...**	CKS

Fig 2 – Organização dos dados do fotômetro por *frame*

O formato do *frame* de transmissão ou recepção apresentado na Figura 2, mostra os campos de dados que a serem processados. A descrição de cada campo consiste em:

- SINCRONISMO - Palavra de sincronismo: “EB90”;
- TIPO DE OPERAÇÃO – Byte contendo o código do comando ou resposta da função a ser executada;
- TAMANHO – Contém a quantidade de bytes que serão transmitidos no restante do *frame;*
- DADOS – Campo opcional de tamanho variável, ou seja, pode conter amostras do céu ou de calibração adquiridas, valor de inclinação dos filtros, bem como dados de *status* de funcionamento do fotômetro;
- CKS – O valor do byte representa a integridade da mensagem.

A Tabela 1, a seguir, apresenta os comandos, respostas e tamanho das mensagens definidos para o protocolo de comunicação.

Tabela 1: Comando, resposta e tamanho e das mensagens

Comandos	bytes	Resposta	bytes
Reset Photometer	5	Received Message	5
Photometer ON	5	Received Message	5
Photometer Off	5	Received Message	5
Stop Optical Calibration	5	Received Message	5
End Type Operation	5	Received Message	5
Sky Observation	5	Sky Observation	14
Sensitivity Calibration	5	Sensitivity Calib. Data	14
Internal Calibration	5	Internal Calib. Data	14
Optical Calibration	6	Optical Calib. Data	8
Send Status	5	Status Data	17

Os comandos *reset, on/off* e *status* relacionam-se com o funcionamento do fotômetro, enquanto os comandos *internal*, *sensitivity* e *optical calibration* são, respectivamente, as calibrações interna, externa e óptica do fotômetro. A função *Sky Observation* executa a observação da emissão OH(8-3) na atmosfera (região da mesosfera). Em seguida, estes dados são armazenados e processados, transformando-se em dados de intensidade da emissão do OH(8-3) e temperatura da região da mesosfera (80 a 100 km) (ver, por exemplo, Meriwether, 1989; Greet, 1998 e Takahashi, 1999). São gerados arquivos de dados de observação, calibração, dados processados e de registro de erros a cada dia de observação. As Figuras 3 e 4 mostram, respectivamente, o arquivos de dados originais e dados processados.

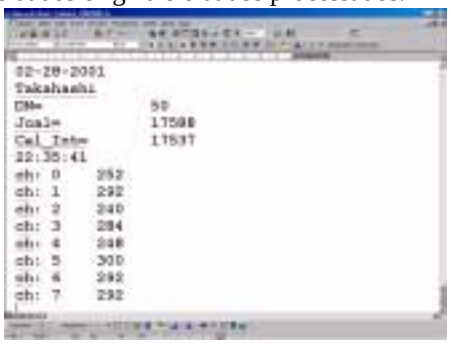

Fig 3 – Arquivo de dados fotométricos originais

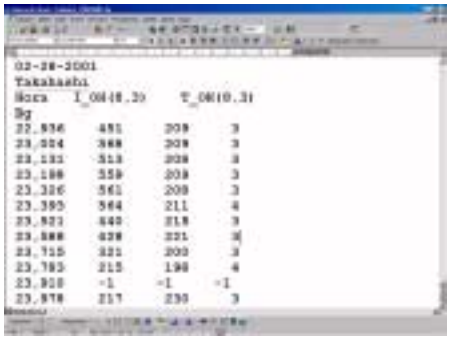

Fig 4 – Arquivo de dados fotométricos processados

A aquisição de dados é realizada somente nos períodos noturnos, durante a fase da lua nova e minguante quando os efeitos de contaminação espectral são minimizados. Para os períodos válidos, o modo de operação do fotômetro pode ser manual ou automático.

- Manual – Realiza a função de observação do céu para um período definido pelo operador;
- Automático – Realiza a função de observação do céu sob o gerenciamento de rotinas que consultam arquivos contendo parâmetros de astrometria definidos pelo Departamento de Aplicações Astronômicas do U.S. Naval Observatory (detalhes descritos na Seção 4).

O modo de operação do fotômetro é indicado na tela de visualização e monitoração dos dados de observação da radiância e temperatura da emissão de OH(8-3). A Figura 5 mostra a tela de visualização dos dados do fotômetro FotAntar1 em operação na Estação de Comandante Ferraz, Antártida.

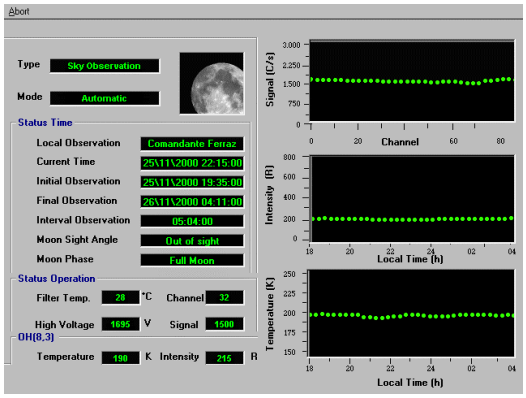

Fig 5 – Tela de visualização dos dados do fotômetro FotAntar 1.

3. Descrição do projeto do software de imageamento em aeroluminescência

O software de operação do sistema de imageamento aeroluminescência é o resultado da interação de rotinas desenvolvidas em: *Visual Basic* 6.0, V++ 4.0 (Digital Optics), e *Interactive Data Language* (IDL 5.3), com o objetivo de executar cooperativamente (Selic et al, 1994) as funções de aquisição, gerenciamento e visualização de imagens de aeroluminescência.

O sistema de imageamento, integrado pela *KEO Consultants* para o INPE, inclui os seguintes componentes:

- Sistema óptico: Composto pelo conjunto de lentes e filtros, que seleciona o espectro da emissão a ser adquirido;
- Câmera CCD: Produzida pela *Photometrics*, consiste, basicamente, em um conjunto de células sensíveis à luz;

- Sistema de Controle: Composto pelo sistema de roda de filtro e de controle do *shutter* da camera. Utiliza a interface de comunicação serial (RS232) entre o PC e a camera CCD.

O programa principal consiste em uma rotina escrita em Visual Basic que realiza a interface com o operador, estabelecendo os critérios de operação, tais como: seqüência de posicionamento dos filtros, características das imagens, o modo de operação (automático/manual) relacionado aos períodos de observação válidos para aeroluminescência. O programa principal também dispara o programa macro que inclui o conjunto de rotinas V++ escritas para o controle da roda de filtro, sistema de *shutter* e rotinas incorporadas que recebem e processam os parâmetros contendo as características do filtro e da imagem (como, por exemplo, tempo de exposição, ganho, emissão). Em seguida, é feita a aquisição e armazenamento da imagem.

A comunicação entre o programa principal e o programa V++ é feita através de sinalizadores (*flags)* escritos na área de *clipboard* do windows compartilhada pelos dois aplicativos. A sinalização entre os programas indica o término ou um novo evento de aquisição de imagem. Além disto, indicam a mudança de estado entre as operações de aguardar ou assumir o controle da execução entre os dois aplicativos, que consiste em vários processos concorrentes (tarefas) que necessitam comunicar e sincronizar as operações entre eles (Gomaa, 1986).

Quando, a cada término de aquisição, o controle volta ao programa principal, é feita a exibição das imagens, como mostra a Figura 6 com a tela de operação do imageador (CCD-LUME2), que no momento encontra-se em operação no observatório de São João de Cariri (PB).

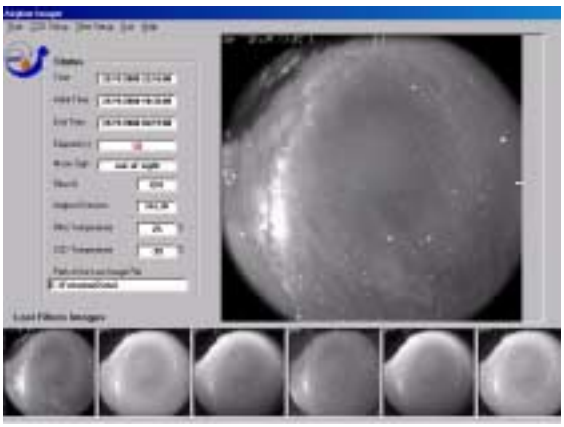

Fig 6 – Imagens de emissão de aeroluminescência na região da alta atmosfera (acima de 80km)

Em decorrência das limitações de formatos dos arquivos de imagem aceitos pela linguagem, foi estabelecida uma interface com a linguagem IDL sob a forma de funções incorporadas a biblioteca de funções/objetos do Visual Basic (OCX). Por ser o IDL uma linguagem dirigida ao tratamento de imagens, esta interação permitiu implementar uma série de recursos de visualização nas imagens de aeroluminescência.

4. Automatização

O objetivo do modo de operação automático de aquisição de dados de aeroluminescência é determinar a logística temporal para efetuar observações de aeroluminescência atmosférica noturna adequadas, minimizando a contaminação do espectro lunar e solar. A determinação deste período é calculada pelo algoritmo de interpretação dos parâmetros astrométricos do US Naval Observatory, nomeado ***LUME-NOVAS***, que determina o período de observação de aeroluminescência. O Departamento de Aplicações Astronômicas do U.S. Naval Observatory fornecem posições e movimento de estrelas e objetos do sistema solar em cooperação com outras agências americanas, organizações de outros países e com a união astronômica internacional.

Os parâmetros de entrada para o conjunto de rotinas ***LUME-NOVAS*** consiste em três arquivos em formato ASCII, obtidos no site do Departamento de Aplicações Astronômicas, quando são fornecidos os seguintes parâmetros:

- Ano;
- Tipo de tabela (*sun, moon, twilight*);
- Longitude;
- Latitude;
- Fuso horário.

Sendo geradas as seguintes tabelas:

- Tabela dos horários de *SunRise/SunSet* [$R_{\odot}$, $S_{\odot}$];
- Tabela dos horários de *MoonRise/MoonSet* [$R_{☾}$, $S_{☾}$];
- Tabela dos horários de *Nautical Twilight,* Inicial e Final [T_B, T_E].

A partir da leitura dos dados contidos nas três tabelas, são executadas tarefas que foram projetadas como módulos seqüencialmente coesos, cujos dados de saída de um servem de entrada para o próximo (Meilir Page-Jones, 1988). A seqüência dos módulos a serem implementados seria:

- Introduzir as coordenadas do local de observação equivalente à última escolha realizada pelo operador. A definição do local de observação está relacionada com o prefixo do nome do conjunto dos três arquivos;
- Identificar a data e a hora local, baseadas no relógio do microcomputador que gerencia o instrumento, com o objetivo de localizar no conjunto de 3 arquivos os dados referentes às quantidades $R_{\odot}$, $S_{\odot}$; $R_{☾}$, $S_{☾}$; T_B, T_E;

- Definir o vetor ($R_{✱}$, $S_{✱}$; $R_{☽}$, $S_{☽}$; T_B, T_E) para a data do dia (*Same Day – sd*) e para data do dia seguinte (*Next Day* – nd), baseando-se na data e horário local atual;
- Definir um conjunto de datas propícias para aquisição de dados de aeroluminescência, denominado *período de observação*. Este conjunto é determinado através de uma varredura sobre a tabela anual para ($R_{☽}$, $S_{☽}$), detectando as datas dos extremos vizinhos da fase de lua nova. O comprimento do grupo geralmente está em torno de 17 – 20 dias, dependendo da latitude local e da época do ano;
- Determinar o horário de máxima elevação da Lua (90^o em relação ao horizonte), de acordo com uma geometria simplificada do trânsito lunar previsto para os valores no intervalo de ($R_{☽}$, $S_{☽}$);
- Calcular, a cada instante, a elevação da Lua em relação ao horizonte. O valor obtido indica, ao operador, as condições de observação mais adequadas para iniciar uma operação manual de aquisição de dados de aeroluminescência.

Como resultado da execução das tarefas já descritas, obtém-se o período de observação para o qual a data do dia deverá pertencer ou não aquele conjunto de datas propícias. A validação da data atual em relação ao período de observação consiste na idéia central da automatização, cuja a seqüência lógica está representada no seguinte pseudocódigo:

IF *data atual* $\in$ *Período de Observação* **THEN**

Determinar hora local de início e término das observações de aeroluminescência, utilizando o seguinte princípio de decisão:

IF T_B (sd) > $\delta \times S_{☽}$(sd) **THEN** (1)

Inicio = T_B (sd)

ELSE

Inicio = $\delta \times S_{☽}$(sd)

END IF

IF T_E (nd) > $\delta \times R_{☽}$(nd) **THEN**

Fim = T_E (nd)

ELSE

Fim = $\delta \times R_{☽}$(nd)

END IF

ELSE

Imprimir "Não existem valores para Inicio, Fim"

END IF

O modo automático consiste, portanto na verificação periódica de duas condições:

1. Se a *data atual pertence ao período de observação;*
2. Se a condição 1 for verdadeira, comparar o intervalo entre a hora atual e a hora de inicial (Inicio) para que o computador possa aguardar o instante inicial;
3. Durante a aquisição de dados, comparar o intervalo entre a hora atual e a hora final para que o computador possa finalizar a operação.

[1] δ é um fator de tolerância à presença da Lua nas observações rotineiras de aeroluminescência.
(1-δ) = 10% (fotomultiplicadoras) ou 3% (CCD – imageadores)

Resultados e conclusão

O sistema de fotometria – FotAntar1, encontra-se operando em modo automático desde de fevereiro de 2001 na estação Comandante Ferraz no continente antártico. O sistema de imageamento – CCD-LUME2 também encontra-se operando em modo automático desde outubro de 2000 na cidade de São João de Cariri a 80km de Campina Grande (PB). Conforme citação anterior, em ambos os experimentos, as localidades são de difícil acesso inviabilizando a presença de técnicos especializados para operarem os equipamentos diariamente. Entretanto, a automatização dos sistemas, permitiu que sejam feitas apenas visitas periódicas para coleta de dados armazenados e manutenção do equipamento. Uma análise dos dados adquiridos, embora recentes, revela um conteúdo significativo na busca de fenômenos geofísicos particulares, ou seja a qualidade dos dados alcançou um nível satisfatório para o estudo em aeroluminescência.

Por fim, a automatização de sistemas de aquisição reflete uma tendência da pesquisa científica em aeroluminescência: o gerenciamento remoto de instrumentos ópticos, que deve ser o resultado de um trabalho em conjunto com o especialista na área de computação, que possibilite a geração de produtos de software mais confiáveis e eficientes para produção científica.

Referências

1. Digital Optics Limited. **V++ Precision Digital Imaging System**. http://www.digitaloptics.co.nz, Maio 2000.
2. Gomma. H., **Software Development of real-time system**. ACM 29,7. 657-668, 1986.
3. Greet, P. A.; French, W. J. R.; Burns, G. B.; Williams, P. F. B.; Lowe, R. P.; Finlayson, K. OH(6,2) spectra and rotational temperature measurements at Davis, Antarctica. **Ann. Geophysices,** v.16, n.1, p.77-89, 1998.
4. Keo Consultants, **Telecentric Imaging System for INPE**. Reference Manual, 1999.
5. Meriwether, J. W. A Review of the photochemistry of selected Nightglow emissions from the mesopause. **J. Geophys. Res.**, v.94, n.D12, p.14629-14646, 1989.
6. Photometrics, **Software Guide for Windows System**. Reference Manual, 1998.
7. Page-Jones, M. **Projeto Estruturado de Sistemas**, McGraw-Hill, p. 131, 1988.
8. Takahashi, H.; Batista, P .P.; Buriti, R. A.; Gobbi, D.; Nakamura T.; Tsuda, T.; Fukao, S., Response of the airglow OH emission, temperature and mesopause wind to the atmospheric wave propagation over Singaraki, Japan. **Earth Planets and Space**, v.51, n.7 e 8, p.863-875, 1999.
9. Tanenbaum, A. S., **Structured Computer Organization**. Ed. Prentice Hall. 3ª Edição, 1990.
10. U.S.Naval Observatory, Astronomical Applications Departmento **NOVAS**.http://aa.usno.navy.mil/data/docs/RS_OneYear.html, Set. 2000.

Computer Simulations of Rayleigh-Taylor Instability in Ionospheric Plasmas

Abraham C.-L. Chian, Erico L. Rempel, Elbert E. Macau, Eurico R. de Paula, Fabiano S. Rodrigues, Reinaldo R. Rosa, Instituto Nacional de Pesquisas Espaciais-INPE, São José dos Campos-SP, Brazil; Adriano H. Cerqueira and M. Jaqueline Vasconcelos, DCET, Universidade Estadual de Santa Cruz, Ilhéus-BA, Brazil

Introduction

The generalized Rayleigh-Taylor instability due to the combined destabilizing effects of the gravity, ambient electric and magnetic fields and neutral wind is the physical mechanism that drives the growth of equatorial and low-latitude spread-F, which leads to the formation of plasma bubbles – depleted density irregularities in the ionosphere [1]. Radio waves from satellites during their propagation through these ionospheric irregularities are scattered causing scintillation of the radio signals received on the ground. The amplitude and phase scintillations of the GPS (Global Positioning System) signals are a useful tool for remote sensing of the ionospheric irregularities. Hence, the theoretical and experimental studies of the Rayleigh-Taylor instability and its implications on equatorial and low-latitude spread-F are important for modern satellite-based telecommunications systems. The initial conditions which lead to an event of spread-F depend in a complex way on the dynamical state of the ionosphere and the neutral atmosphere and on the dynamical patterns of gravity waves in the upper atmosphere.

Methodology

Considerable effort has been put in the development of nonlinear theories of spread-F based on computer simulations of the Rayleigh-Taylor instability [2-5]. Of particular interest is how a plasma instability can evolve into chaos and turbulence [1, 6, 7]. It was shown by numerical solutions of a nonlinear MHD wave equation that intermittent plasma turbulence with power-law power spectrum [6] and onset of plasma turbulence via global bifurcations such as interior and boundary crises [6, 7] can be produced due to the intrinsic nonlinearity of plasma processes. We report some results of computer simulations of the nonlinear evolution of the Rayleigh-Taylor instability by numerically solving the Kuramoto-Sivashinsky equation which can describe the spatio-temporal dynamics of a hydrodynamic instability [8]. By seeking periodic solutions, we expand the solutions in a discrete spatial Fourier series and solve the Kuramoto-Sivasinhsky equation using a spectral method. A bifurcation diagram is constructed from the numerical solutions by varying the control parameter representing the 'viscosity' damping of the fluid plasma. A rich variety of nonlinear periodic (regular) and chaotic (turbulent) states are identified. The relation between the chaotic state and turbulence is established. We apply the results of our computer simulations to the observation of turbulent power spectrum in association with the F-region ionospheric irregularities measured by the GPS receivers. One example of a GPS signal power spectrum is shown in Figure 1. In addition, we carry out a comparative study of the Rayleigh-Taylor instability in ionospheric plasmas and astrophysical plasmas [9, 10]. Using a SPH (Smooth Particle Hydrodynamics) numerical code, we simulate three-dimensional plasma jets in the presence of magnetic fields.

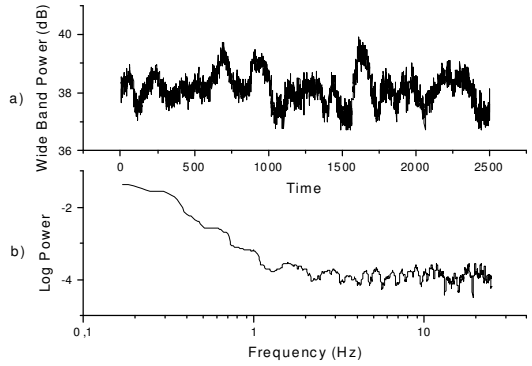

Figure 1– Example of GPS amplitude signal for about 50 seconds (a) and respective power spectrum (b).

Discussion

We analyzed the role played by the MHD instabilities in the internal dynamical structures of jets, in particular, the emergence of internal shocks. Finally, we point out the fundamental importance of performing three-dimensional simulations by showing how some structures that appear in two-dimensional simulations are absent in the three-dimensional simulations.

Acknowledgments This work is supported by CNPq and FAPESP.

References

[1] Kelley, M.C., 1989, The Earth's Ionosphere – Plasma Physics and Electrodynamics, Academic Press, San Diego.

[2] Herang, C.S., Sofko, G.I., and Kelly, M.C., 1998, Numerical simulations of mid-latitude ionospheric perturbations produced by gravity waves, J. Geophys. Res. 103, 6977.

[3] Kuo, F.S., Chou, S.Y., and Shan, S.J., 1998, Comparision of topside and bottomside irregularities in equatorial F region ionosphere, J. Geophys. Res. 103, 2193.

[4] Sekar, R., and Kelly, M.C., 1998, On the combined effects of vertical shear and zonal electric field patterns on nonlinear equatorial spread F evolution, J. Geophys. Res. 103, 20735.

[5] Basu, B., 1999, Nonlinear saturation of Rayleigh-Taylor instability in the presence of time-dependent equilibrium, J. Geophys. Res. 104, 6859.

[6] Chian, A.C.-L., Borotto, F.A., and Gonzalez, W.D., 1998, Alfvén intermittent turbulence driven by remporal chaos, Astrophys. J. 505, 993.

[7] Chian, A.C.-L., Borotto, F.A., and Rempel, E.L., 2001, Alfvén Boundary Crisis, International J. Bifurcation and Chaos, in press.

[8] Babchin, A.J., Frenkel, A.L., Levich. B.G., and Sivashinsky, G.I., 1983, Nonlinear saturation of Rayleigh-Taylor instability in thin films. Phys. Fluids 26, 3159.

[9] Cerqueira, A.H., and Dal Pino, E.M.D., 1999, Magnetic field effects on the structure and evolution of overdense radiatively cooling jets. Astrophyys. J. 510, 828.

[10] Cerqueira, A.H., and Dal Pino, E.M.D., 2001, On the influence of magnetic fields on the structure of photostellar jets, Astrophys. J. 550, L91.

Determinação da temperatura da mesosfera superior através das observações de emissões de aeroluminescência das bandas da OH(6-2) e OH(8-3).

Wrasse, Cristiano Max; Takahashi, Hisao; Gobbi, Delano.
Instituto Nacional de Pesquisas Espaciais –INPE
Av. dos Astronautas, 1758 – Jardim da Granja, CP: 515, Cep: 12201-970, São José dos Campos (SP), Brasil.
cmw@laser.inpe.br

Abstract
The OH(6-2) band has been monitorated during 1998 and 1999 at the Space Center of Cachoeira Paulista, (22,7°S, 45°W) using a tilting photometer. The rotational tempeature was obtained using ratio of $P_1(4)/P_1(2)$ lines, and the Eisntein coeficients of Mies (1974) [=Mies], Langhoff et al. 1986 [=LWR] and Turbull and Lowe, 1989 [=T&L]. The temperature obtained using T&L coeficients are 14 K greater than LWR coeficients and 8 K greater than Mies coeficients. The temperature of the OH(6-2) was also comparated with the temperature of the OH(8-3).

1. Introdução

A temperatura da mesosfera superior, região em torno de 85 a 95 km, pode ser obtida através da temperatura rotacional da molécula OH (e.g. Meriwether, 1974; Takahashi et al., 1989). Perfis de emissões atmosféricas, obtidos por foguetes, mostraram que a camada emissora de OH está localizada entre 80 e 100 km de altitude, com um pico entre 85 e 90 km na região da mesopausa. A espessura desta camada está em torno de 7 a 10 km (Meriwether, 1989). Ao comparar-se a intensidade entre duas ou mais linhas de emissão de um ramo dentro de uma banda, pode-se determinar a temperatura rotacional da OH (Greet et al., 1998). Esta temperatura é função da razão entre a intensidade de duas linhas de emissão. Isto deve-se ao fato de que a freqüência de colisão da molécula OH, calculada pela teoria cinética dos gases, é da ordem de 10^4 s^{-1} em altitudes próximas a 85 km (Sivjee e Hamwey, 1987). Este valor representa um tempo de colisão cerca de 100 vezes o tempo de vida da molécula de OH^* garantindo, assim, o equilíbrio térmico das populações em níveis de energia rotacional com o ambiente. A temperatura na região de emissão varia entre 150 e 250 K, dependendo da localização geográfica, da estação do ano e dos fenômenos relacionados às perturbações atmosféricas (Waltersheid et al., 1987). De acordo com Williams (1996), a temperatura para os ramos P da molécula OH(6,2) pode ser expressa pela relação:

$$T_{n,m} = \frac{E_{v'}(J'_m) - E_{v'}(J'_n)}{\mathrm{k}\ln\left[\frac{I_n}{I_m}\,\frac{A(J'_m,6\rightarrow J''_{m+1},2)}{A(J'_n,6\rightarrow J''_{n+1},2)}\,\frac{2J'_m+1}{2J'_n+1}\right]} \quad (1)$$

onde, $T_{n,m}$ é a temperatura rotacional estimada das intensidades relativas, I, de duas transições dos níveis rotacionais J'_n, J'_m, (nível vibracional superior v'), para J'_{n+1}, J'_{m+1}, (nível vibracional inferior v''). $E_v(J)$ é a energia do nível J,v e $A(J',v'\rightarrow J'',v'')$ é o coeficiente de Einstein de J',v' para J'',v''.
Acredita-se que dentre os coeficientes de Einstein utilizados em trabalhos desta natureza, àqueles obtidos por Nelson et al. (1990) representam com maior precisão as transições energéticas de níveis vibracionais inferiores da molécula de OH. Em níveis vibracionais superiores, os coeficientes de Einstein publicados na literatura apresentam grandes divergências. Em geral, os valores de intensidade relativa calculados por Turnbull e Lowe (1989) são os mais elevados; e os calculados por Langhoff et al. (1986) apresentam os menores valores. Por exemplo, para Δv=5, caso da molécula OH(8-3), tal diferença é de um fator de 4 entre as intensidades (Golden, 1997). Os valores dos coeficientes de Einstein dependem da precisão da função do momento de dipolo elétrico e das funções de onda a serem empregadas. Nenhuma destas quantidades parece ser conhecida com suficiente precisão para os valores de v e J usados. Estes são os fatores que fazem com que os coeficientes de Einstein existentes na literatura apresentem diferenças entre os seus valores, ocasionando grandes variações na determinação da intensidade de emissão e, consequentemente, da temperatura rotacional da molécula OH.
Dentre os vários coeficientes de Einstein mencionados acima, somente os obtidos por Mies (1974), Langhoff et al. (1986) [LWR] e Turnbull e Lowe (1989) [T&L] foram utilizados neste trabalho. Durante os anos de 1998 e 1999 foram realizadas medidas ininterruptas da temperatura rotacional e da intensidade de emissão da molécula OH(6-2) no Observatório de Luminescência de Cachoeira Paulista, (SP), totalizando 107 noites de observações. Em suma, a temperatura da molécula OH(6-2) foi determinada utilizando os coeficientes de Einstein de

*Significa que a molécula hidroxila está em um estado excitado.

Mies, LWR e T&L. A instrumentação, metodologia e os resultados são discutidos a seguir.

2. Instrumentação e Obtenção dos Dados

O fotômetro utilizado para medir a temperatura rotacional possui um sistema de inclinação do filtro. Esta técnica permite efetuar uma varredura espectral em torno do comprimento de onda central do filtro de interferência. Este fotômetro também mede as emissões do O_2, OI (557,7 nm e 630 nm) e Na.

As linhas de emissão $P_1(2)$, $P_1(3)$ e $P_1(4)$, da banda da OH(6-2), são obtidas através de uma varredura espectral entre 838 nm e 848 nm. A intensidade destas linhas rotacionais estão relacionadas com a temperatura rotacional T_{ROT} pela seguinte expressão:

$$I_{J',J''} = A(\upsilon = 6, J' - \upsilon = 2, J'').\frac{2.(2J''+1)}{Q(\upsilon)}. \qquad (2)$$
$$\exp\left(\frac{-F(J',J'')}{kT_{ROT}}\right)$$

$I_{J',J''}$ na expressão acima representa a intensidade da linha rotacional oriunda da transição vibro-rotacional ma molécula OH^* entre os níveis *J'* e *J''*; *A* é a probabilidade da transição ou coeficiente de Einstein; *F(J',J'')* é o termo da energia rotacional, *k* é constante de Boltzmann e T_{ROT} é a temperatura rotacional.

A determinação da temperatura rotacional da molécula OH(6-2) é feita utilizando a razão de linhas $P_1(4)/P_1(2)$, sendo que esta possui uma acentuada dependência com a temperatura em comparação com outra combinações, como por exemplo a razão de linhas $P_1(3)/P_1(2)$. A linha $P_1(3)$ não foi utilizada neste trabalho, pois próxima a ela, precisamente em 843 nm, há outras duas linhas de emissão, $P_1(12)$ e $P_2(12)$ referentes à banda OH(5-1), contaminando as observações do espectro desejado. A calibração da sensibilidade absoluta do fotômetro, entre os comprimentos de onda de 839 e 847 nm, foi realizada em laboratório utilizando dois difusores de óxido de magnésio, MgO, e uma fonte de luz calibrada. Uma outra fonte de luz calibrada foi utilizada para avaliar a variação da sensibilidade diária. A estimativa do erro instrumental, devido à função de transmissão do filtro e às incertezas da sensibilidade absoluta, determinam um erro no cálculo da intensidade e da temperatura rotacional da ordem de ±10% e ±5 K, respectivamente. A resolução temporal do fotômetro é limitada pelo tempo de observação dos cinco filtros mais um obturador, que é utilizado para medir o ruído de escuro da fotomultiplicadora. A taxa de amostragem resultante é de 3,3 minutos, o suficiente para medir oscilações na camada de emissão devido à passagem de ondas de gravidade.

As observações da intensidade e da temperatura da OH(6-2) foram realizadas no Observatório de Luminescência de Cachoeira Paulista (SP), (22,5 °S, 45° W), durante os anos de 1998 e 1999, obtendo um total de 107 noites de observação, todas elas com pelo menos 3 horas de observação. Estas medidas fotométricas foram realizadas a cada duas semanas por mês, durante o período de lua nova, iniciando no final do crepúsculo astronômico e terminando no início do crepúsculo náutico. As noites de observação selecionadas para esta análise apresentavam céu claro, sem cobertura de nuvens, cuidado este devido a sua contaminação espectral nas medidas.

3. Comparação da temperatura rotacional entre os coeficientes de Einstein

As temperaturas rotacionais da molécula OH(6-2), medidas pelo fotômetro MULTI2, foram determinadas utilizando os coeficientes de LWR, Mies e T&L.

A Figura 1 apresenta a média mensal para os anos de 1998 e 1999. Observa-se que as temperaturas da molécula OH(6-2) obtidas utilizando os coeficientes de Einstein de T&L apresentam os maiores valores, sendo 14 K maior do que as temperaturas obtidas por LWR e 8 K maiores do que as temperaturas calculadas por Mies. Os menores valores de temperaturas são devidos aos ao conjunto de coeficientes empregados por LWR.

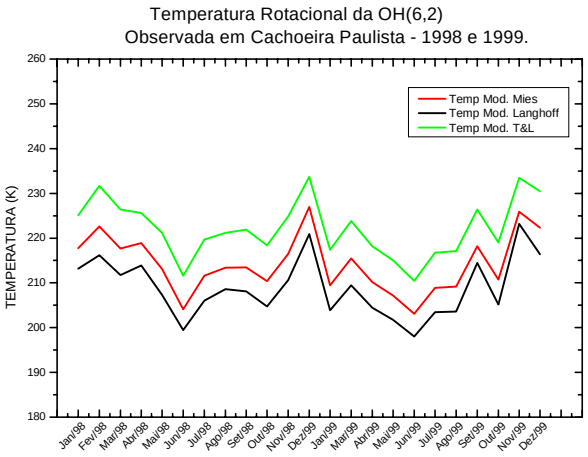

Figura 1 – Média mensal da temperatura da molécula OH(6-2) determinada utilizando o conjunto de coeficientes de Einstein devido a T&L, LWR e Mies.

A temperatura rotacional da molécula OH(8-3) foi determinada utilizando uma série de dados oriundas de outro fotômetro instalado no mesmo observatório,

durante os meses de Agosto a Novembro de 1999, totalizando 19 noites de observações.

Comparando as temperaturas rotacionais da molécula OH(8-3) e da molécula OH(6-2), observaram-se que o conjunto de coeficientes que apresentaram as temperaturas mais semelhantes são àqueles devidos a Mies para a molécula OH(6-2) e devido a LWR para a molécula OH(8-3).

4. Conclusão

A temperatura rotacional determinada através de distintos conjuntos de coeficientes de Einstein mostrou que a temperatura da molécula OH(6-2) via T&L apresentou os maiores valores. Os menores valores de temperatura foram apresentados por LWR.

Ao comparar-se a temperatura rotacional entre as moléculas OH(6-2) e OH(8-3), utilizando-se de distintos conjuntos de coeficientes de Einstein, observou-se que os resultados mais próximos ocorreram com o uso dos coeficientes por Mies para a molécula OH(6-2) e com o emprego dos coeficientes por LWR para a molécula OH(8-3).

É importante salientar que entre os coeficientes de Einstein existentes na literatura aqueles que apresentam as maiores diferenças entre os seus valores são àqueles devido às transições $\Delta v=4$ e $\Delta v=5$, como é o caso das moléculas OH(6-2) e OH(8-3); porém, o mesmo não ocorre para as transições inferiores, $\Delta v=1$ e $\Delta v=2$ (Golden,1997). Outro fator que pode contribuir na diferença da temperatura entre as moléculas OH(6-2) e OH(8-3) diz respeito às linhas de emissão adotadas em cada uma das bandas para determinar a temperatura, sendo que cada linha de emissão apresenta um comportamento diferente em função da variação da temperatura.

5. Referências Bibliográficas

Golden, S. A. Kinetic parameters for OH nightglow consistent with recent laboratory measurements. **J. Geophys. Res.**, v.102 n.A9, p.19969-19976, 1997.

Greet, P. A.; French, W. J. R.; Burns, G. B.; Williams, P. F. B.; Lowe, R. P.; Finlayson, K. OH(6,2) spectra and rotational temperature measurements at Davis, Antarctica. **Ann. Geophysices,** v.16 p.77-89, 1998.

Langhoff, S. R.; Werner H. J.; Rosmus, P. Theorical transitions probabilities for the OH Meinel system. **J. Mol. Spectros**., v.188, p.507-529, 1986.

Meriwether, J. W. A Review of the photochemistry of selected Nightglow emissions from the mesopause. **J. Geophys. Res.**, v.94, n.D12, p.14629-14646, 1989.

Meriwether, J. W. High-latitude airglow observations of correlated short-term fluctuations in the hydroxyl Meinel 8-3 band intensity rotational temperature. **Planet. Space. Sci.**, v.23, p.1211-1221, 1974.

Mies, F. H. Calculated vibrational transitions probabilities of OH($X^2\Pi$). **J. Mol. Spectros**., v.53, p.150-188, 1974.

Nelson, Jr. D. D.; Schiffman A.; Nesbit, D. J.; Orlando, J. J.; Burkholder, J. B. $H + O_3$ Fourier-transform infrared emission and laser absorption studies of OH ($X^2\Pi$) radical: An experimental dipole moment function and state-to-state Einstein A coefficients. **J. Chem. Phys.**, v.93, n.10, p.7003-7019, 1990.

Takahashi, H.; Sahai, Y.; Clemecha B. R.; Simonich, D. M.; Teixeira, N. R.; Eras, A.; Lobo, M. R. Equatorial mesospheric and F region airglow emission observed from latitude 4^o south. **Planet Space Sci.,** v.37, p.649-655, 1989.

Turnbull, D. N.; Lowe, R. P. New hydroxyl transitions probabilities and this importance in airglow studies. **Planet. Space Sci**, v.37, n.6, p.723-738,1989.

Walterscheid, R. L.; Schubert, G.; Straus, J. M. A dynamical-chemical model of the wave-driven fluctuations in the OH nightglow. **J. Geophys. Res.**, v.92, n.A2, p.1241-1254, 1987.

Williams, P. F. B. OH rotational temperatures at Davis, Antarctica, via scanning spectrometer. **Planet. Space Sci.,** v. 44, n.2, p.163-170, 1996.

.

Direcionalidade de Ondas de Gravidade sobre Cachoeira Paulista

Amauri Fragoso de Medeiros[1,2], Hisao Takahashi[1], Paulo Prado Batista[1], Delano Gobbi[1], Mike J. Taylor[3]
1.Instituto Nacional de Pesquisas Espaciais (INPE) – Brasil
2. Universidade Federal da Paraíba
3. Space Dynamics Laboratory and Physics Dept., Utah State University, Logan, Utah, USA

Abstract
Um sistema de imageamento da aeroluminescência atmosférica instalado em Cachoeira Paulista (22.7^0 S, 45.0^0) usando uma câmera CCD com quatro filtros de interferência realiza medidas rotineiramente durante 15 dias de cada mês. São imageados o OI 557,7 nm, o O_2(0,1), as bandas de Meinel na região do infravermelho próximo (<930 nm) e o background contínuo em 578 nm. Foram observadas estruturas de ondas na emissão do OH , O_2 e OI557,7 nm. Após a análise de um ano de observações, os resultados sugerem uma direção preferencial das ondas no verão e inverno e a não existência de direção preferencial nas outra estações.

1. Introdução

Já é bem conhecido que as ondas de gravidade desempenham um importante papel no transporte de energia e momento da baixa atmosfera para região da mesosfera e baixa termosfera (MLT), afetando a estrutura de temperatura e a circulação geral desta região. Existem várias técnicas capazes de observar ondas de gravidade, tais como radar, lidar, e medidas de satélite. Todavia, cada instrumento tem sua própria limitação na observação dos parâmetros da ondas de gravidade.

Entre as técnicas acima mencionadas, as observações por radar contribuíram bastante com o estudo de onda de gravidade na região da MLT. Nestas observações, os componentes da onda são analisados através de séries temporais das velocidades radial ou horizontal do vento, oferecendo os parâmetros verticais das ondas através dos perfis das velocidade do vento e sendo mais eficaz para determinar parâmetros horizontais com comprimentos de onda longos.

Por outro lado, o imageamento da aeroluminescência em torno da região da mesopausa é capaz de investigar as estruturas de ondas de gravidade mais diretamente, sendo mais adequado para observar ondas de gravidade com características de períodos curtos (< 1 hora) e pequenos comprimentos de onda horizontal (6~100 km). Em geral, salientam-se dois tipos distintos (ou grupos) de ondas, de acordo com as propriedades espaciais e temporais reveladas nestas medidas. O grupo que mais se sobressai, chamado de *bandas*, usualmente aparecem como uma série extensiva de ondas quasi-monocromáticas que exibem comprimentos de onda horizontal de dezenas a centenas de quilômetros, e persistem por períodos de até 8 horas. O segundo grupo de ondas, por vezes denominado de *ripples*, estendem-se sobre áreas geográficas muito menores (tipicamente menor do que 5000 km^2) e, comumente, apresentam períodos menores do que 45 min (transientes). Estes dois eventos observados possuem origens distintas (Taylor, *et al.,* 1997). Enquanto que o padrão de *bandas* tem sido associado, a orografia (montanhas) e fontes troposféricas; as fontes dos *ripples* são correlacionadas aos processos de instabilidade convectiva e dinâmica (instabilidade de Kelvin-

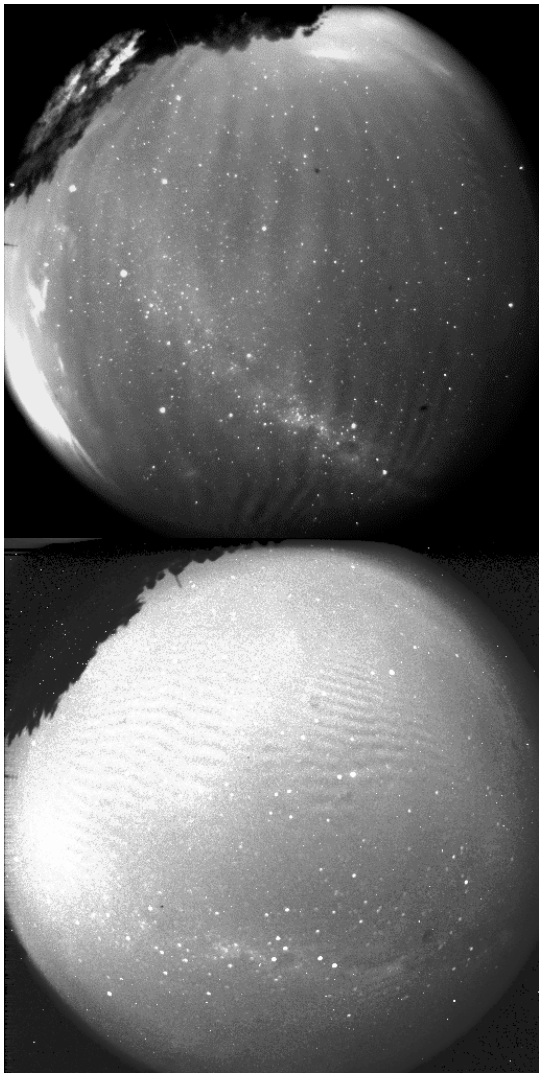

Fig 1 - Imagem do OI557,7 nm mostrando ripples (embaixo) e imagem do OH mostrando bandas (em cima).

Helmholtz). A Figura 1 mostra estes dois tipos de onda detectados em Cachoeira Paulista.

Neste trabalho apresentaremos os resultados iniciais refentes a direção de propagação de 283 eventos de ondas detectados no período de um ano de observação.

.

2. O Equipamento

Observações da aeroluminescência foram realizadas em Cachoeira Paulista (23° S, 45 ° W) usando um imageador all-sky. Este imageador faz parte de um programa de colaboração internacional entre o INPE e o Space Dynamics laboratoty, Utah State University. A CCD do imageador consiste de uma área coletora de 6.45 cm^2, com um array de 1024x1024 com píxeis de 14 bits. Apresenta uma alta eficiência quântica (80 % no visível), baixa corrente escura (0.5 eletrons/pixel/s), baixo ruído de leitura (15 eletrons rms) e alta linearidade (0.05 %). A camera usa uma lente telecêntrica (f/4), all-sky, que é capaz de obter uma alta relação sinal-ruído (20:1) das imagens de estruturas de ondas. Os tempos de integração utilizados foram 15 s para o OH, , 90 s para o OI(5577 nm) e O_2. A imagem foi agrupada para 512x512 pixeis para melhorar a relação sinal-ruído

A tabela 1 mostra as características dos filtros utilizados na observação

Tabela 1 – Características dos Filtros e Alturas Médias das Camadas do Airglow

Filtro	Comprimento de Onda (nm)	Largura de banda (nm)	Altura Média da Camada (km)
OI	557,7	2,65	~96
O_2(0,1)	865,5	12	~94
BG	578,0	10	-
OH	715-930[1]	215	~87

3. Os Resultados

De um total de 69 noites de observações, foram detectados 283 eventos de onda nas imagens do OH, O_2 e OI(557,7 nm). A Figura 2 mostra o número de eventos por hora de observação para cada mês.

Nota-se claramente que a maior atividade de ondas ocorre nos meses de janeiro e de julho. O total de horas de observação foi maior no inverno. A taxa média de eventos foi de 0,7 eventos/hora, com uma taxa maior nos meses de verão e inverno e menos frequente nos meses de equinócio. Isto é provalvelmente atribuído a maior atividade de ondas de gravidade na região da MLT nas estações do solstícios (Tsuda et al., 1994).

A Figura 3 mostra o número de eventos (bandas e ripples) em função do azimute para as quatro estações. A variação sazonal encontrada na direção de

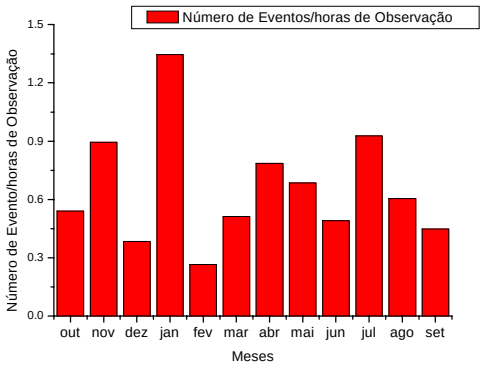

Fig 2 – Distribuição mensal do número de evento por hora de observação

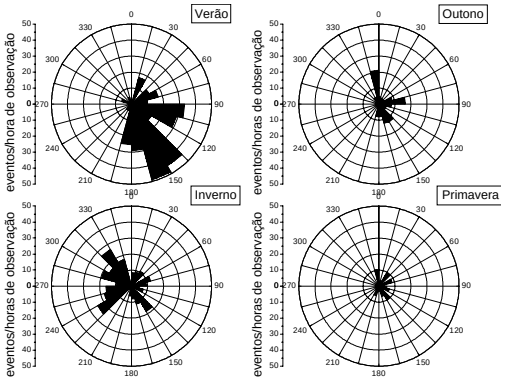

Fig 3 - Distribuição azimutal para as quatro estações do ano do número de eventos por hora de

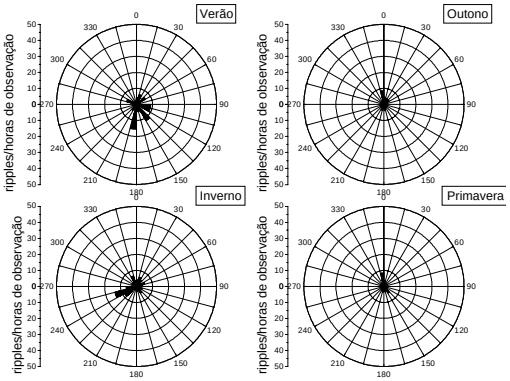

Fig 4 - Distribuição azimutal para as quatro estações do ano do número de ripples por hora de observação

[1] Com um *notch* em 865,5 nm para suprimir o O_2

propagação (direção da velocidade de fase horizontal observada) foi mais evidente no verão e inverno. No verão, a maioria das ondas propagam-se para sudeste. No inverno, a propagação noroeste é a preferencial. Enquanto na primavera e no outono apresentam uma tendência para leste, com um pouco de similaridade com o verão, mas com um número bem menor de eventos. Esta variação sazonal encontrada para direção de propagação corresponde provalvelmente a variação sazonal do ventos na média atmosfera e pode refeletir a filtragem de ondas de gravidade nesta região. Este detalhe será alvo de da discussão adiante.

Considerando em separado os dois tipos de ondas detectados, os ripples não apresentaram uma clara variação sazonal. A Figura 4 mostra a distribuição azimutal para os ripples para cada estação do ano. Nota-se uma pequena tendência para sudeste no inverno e sul no verão, porém o número de ripples é muito pequeno nestes dois períodos e quase inexistente nos meses de equinócio. Não podemos afirmar que exite uma variação sazonal para os ripples.

As bandas por outro lado apresentaram uma clara variação sazonal para direção de propagação. A Figura 5 mostra a distribuição azimutal para bandas em função do número de evento por hora de observação.

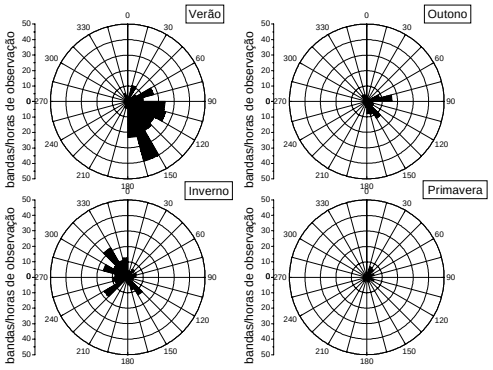

Fig 5 - Distribuição azimutal para as quatro estações do ano do número das bandas por hora de observação

Note a semelhança entre as Figuras 5 e 3, principalmente para inverno, verão e outono. As bandas apresentam uma direção preferencial para sudeste no verão e noroeste no inverno, e com outono mantendo a tendência para leste. Isto sugere que as caracteristicas de direção de propagação horizontal foram mais sensíveis para bandas do que para os ripples.

Como forma de ver mais claramente a variação da direção de propagação foram plotados também gráficos para distribuição mensal. A Figura 5 mostra

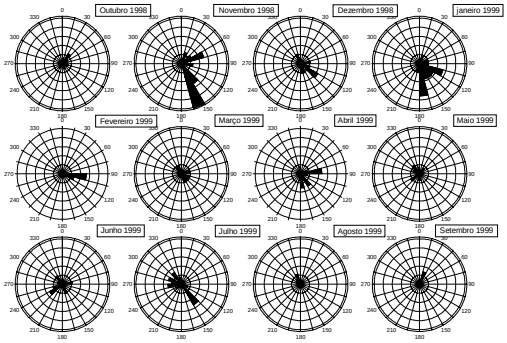

Fig 5 - Distribuição azimutal mensal número de ripples por hora de observação

a distribuição mensal para as bandas.

.Nota-se que a tansição entre o inverno e o verão começa em março e termina em setembro, ou seja, a mudança de direção em março e setembro.

4. Discussão

As bandas são mais comumente observadas e registradas pelos imageadores da luminescência atmosférica, todavia, os ripples não são bem registrados devido à sua caracteristica transiente (Taylor et al. ,1997). Em recentes trabalhos (Taylor et al., 1995, Taylor et al., 1997) investigaram as estruturas dos ripples e bandas, como também a diferença da origem dos mesmos.

A direção de propagação das bandas encontradas neste estudo mostraram uma clara variação sazonal, com uma preferência para sudeste no verão e noroeste no inverno, com a transição começando em março e setembro. Por outro lado, os ripples observados não mostraram uma variação sazonal significativa para direção de propagação. Se considerarmos que as bandas foram geradas na baixa atmosfera, esta variação sazonal pode estar relacionada com a filtragem de ventos em regiões inferiores a mesosfera devido a variação sazonal dos mesmos, o que é consistente com a teoria de filtragem de ondas de gravidade na média atmosfera (Lindzen, 1981). Taylor et al. (1993) sugeriram de observações no verão do Colorado (40° N, 105.6° W) que a direção preferencial de ondas de gravidade vistas em imagens do OH foram atribuídas a filtragem por ventos na média atmosfera sem fazer a distinção entre ripples e bandas. Ao contrário, no nosso estudo esta evidência parece estar mais clara, pois provêm de período de observação maior. Os ripples do nosso estudo parecem não sofrer o efeito da filtragem pelos ventos na média atmosfera, desde que eles não mostraram uma clara variação sazonal. É provável que estes

ripples tenham sido gerados acima do fluxo de vento. Isto é consistente com trabalhos anteriores, que afirmam que os ripples são gerados localmente na região da mesopausa por instabilidades dinâmicas (Taylor and Hapgood, 1990) ou instabilidade convectiva (Fritts et al., 1993).

Sumário

Através de observações do imageamento do airglow realizadas em Cachoeira Paulista (23° S, 45° W) de outubro de 1998 a setembro de 1999 foi estudada a direção de propagação de ondas de gravidade. A direção de propagação horizontal das bandas (direção da velocidade de fase) mostrou uma clara variação sazonal. No verão a direção preferencia foi para sudeste e no inverno para noroeste, com transição nos meses de março e setembro, o que corresponde bem com a filtragem de ondas por meio de vento na média atmosfera. No entanto, os ripples não mostraram uma clara mudança de ordem sazonal na direção de propagação. As bandas são consideradas serem geradas na troposfera e se propagam através da média atmosfera. Para os ripples, ainda não está bem estabelecida à sua origem, porém duas possibilidades são possíveis: a geração local, como também no futuro, pode-se considerar a propagação da baixa atmosfera através de um estudo específico para determinar este tipo de onda.

Referências

1. Fritts D. C., Isler J. R., Thomas G. and Andreassen O., Wave breaking signatures in noctilucent clouds, **Geophys. Res, Lett.**, 20, 2039-2042,1993.
2. Lindzen, R. S., Turbulence and stress owing to gravity wave and tidal breakdown, J. Geophys. Res., 86, 9707-9714,1981.
3. M. J. Taylor and M. A. Hapgood, On the origin of ripple-type wave structure in the OH nightglow emission, **Planet. Space Sci.**, 38, 1421-1430,1990.
4. Taylor M. J., Pendleton W. R., Clark S., Tahahashi H., Gobi D. and Goldberg R. A., Image measumentes of short-period gravity waves at equatorial latitudes, **J. Geophys. Res.**, 102, 26283-26299,1997.
5. Taylor, M. J. and Garcia F. J., A two-dimensional spectral analysis of short period gravity waves imaged in the OI(557.7 nm) and near infra red OH nightglow emissions over Arecibo, Puerto Rico, **Geophys. Res. Lett.**, 22, 2473-2276,1995.
6. Taylor, M. J., E. H. Ryan, T. F. Tuan and R. Edwards, Evidence of preferential directions for gravity wave propagation due to wind filtering in the middle atmosphere, **J. Geophys. Res**., 98(A4), 6047-6057, 1993.
7. Tsuda, T., Y. Murayama, T. Nakamura, R. A. Vicent, A. H. Manson, C. E. Meek, and R. L. Wilson, Variations of the gravity waves characteristics with height, season and latitude revealed by comparative observations, **J. Atmos. Terr. Phys**. 56, 555-568, 1994.

Dynamics from Mesospheric Airglows

Gary Swenson and Alan Liu (University of Illinois, Electrical and Computer Engineering)

l

Abstract

Mesospheric airglows (OH, Na, O_2, and O), resulting from oxygen recombination processes, are layered between 80 and 105 km altitude. Vertical winds resulting from dynamic processes are primarily responsible for intensity variations in the layers. As dynamical scales propagate through the layers, phase information from intensity and temperature measurements provide information on vertical wavelength, and magnitudes of perturbation are related to wave amplitudes. All the characteristics of waves including growth and breaking characteristics are studied using these remote signatures. Recently, Na lidar has made major contributions to calibrations of the remote signatures.

Structure in airglow layers is primarily a result of dynamic motions associated with planetary waves, and in particular at low latitudes, tides and gravity waves. Figure 1 shows a processed image of OH airglow waves taken at Albuquerque, NM. In this case, waves were propagating from the SE to NW, and just prior to sunrise, a wave stream propagated from nearly directly south nearly reaching the zenith by the time this image was taken. On the average, the waves have observed horizontal velocities of 30 m/s, and studies at Albuquerque have shown an average intrinsic phase speed of in excess of 60 m/s. . The dispersion relationship suggests the vertical wavelength of these waves is 25-30 km, with a standard deviation of ~10 km.

Time motion analysis of wave patterns have been studied using movie sequences as well as keograms. An example keogram is shown in Figure 2. On a typical nights observation, images of 1 minute exposure time are acquired every two minutes, yielding 30 images per hour or 250-300 images over a typical night. Keograms are shown with
N-S projections (Figure 2, right) for example. Note that on this example, Waves first appear N of the station and later disappear over the S. This is typical of winter, when waves are predominantly propagating equatorward. In the summer they propagate poleward. Indications from other stations are this is a general trend. On the planetary scale then, the waves are propagating toward the summer pole, the opposite direction of meridional wind which is directed from the summer to the winter pole. Is this a global trend? It is of particular interest to understand if this trend is observed at equatorial as well as mid and high latitude stations.

Winds are measured with Na lidar or meteor radar and are used to infer the intrinsic phase speed. Since the horizontal wavelength is measured from the angular knowledge between phase fronts and the altitude of the structure in the layer, the dispersion relationship can be used to imply the vertical wavelength. The vertical wavelength of these waves is 25-30 km, with a standard deviation of ~10 km.

Wave amplitudes and the degree of airglow brightness perturbations have been studied with chemical models. Figure 3 is a plot of the relationship of wave amplitude to brightness for OH and O2 Atmospheric band intensities as well as rotational temperatures. Note the intensities have a gain of 2-5 in brightness, depending on the vertical wavelength. The relationship is vertical wavelength dependent since shorter vertical wavelengths tend to cancel in the airglow layers whose typical thickness is 8 km.

Vertically propagating waves will have phase change with altitude and as such, layers at different altitudes will reflect the phase (and vertical wavelength).

Since OH and O_2 Atmospheric band emission heights lie ~6 km apart, thephase difference between the observed wave in the respective layers will change with vertical wavelength which is described in the polar plot, Figure 4. An alternative then to measuring the wave phase speed and wind through which the waves are propagating is to measure the vertical wavelength through the phase relationships between respective emission layers or band rotational temperatures. The signal to noise of intensities is high, and straight forward to measure in a short integration time with optical instruments.

In summary, the intrinsic properties of wave can be characterized by the observation of chemical mixing performed by the waves as described here. Horizontal scales are measured by imagers, vertical wavelengths are inferred from mearurements of intrinsic phase speed and calculated with the dispersion relationship, or the vertical wavelengths are measured through phase relationships in the layers and the intrinsic phase speeds calculated with the dispersion relationship. Their amplitudes are inferred through modeled chemical reactions coupled with wave transport models.

Mesospheric Airglows

Combined measurements of airglow and Na lidar have now been used in correlative studes to 'calibrate' and quantify the above model descriptions to put high confidence in interpreations. These relationships extend the ability for ground and satellite measurments of airglow to measured dynamic response in the mesosphere including the wave momentum and energy fluxes of small scale Atmospheric Gravity Waves. These new measurments will be presented:

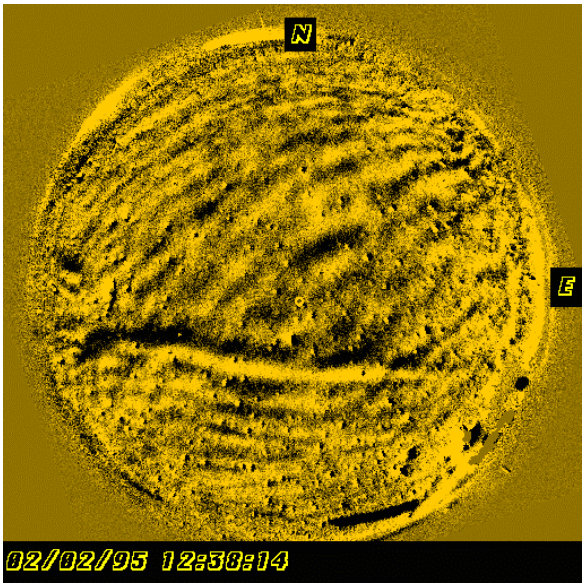

Figure 1 - An allsky image of OH airglow structure from a Time Difference (TD) image sequence separated by 3 minutes in time.

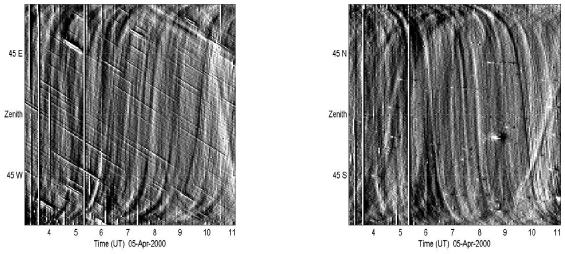

Figure 2 - Keograms for E-W (left) and N-S (right) of wave movement for a night's data at Albuquerueqe, NM. An S shape characterizes the horizon from which the wave appears and then propagates overhead, and off the far horizon, for meridional and zonal components.

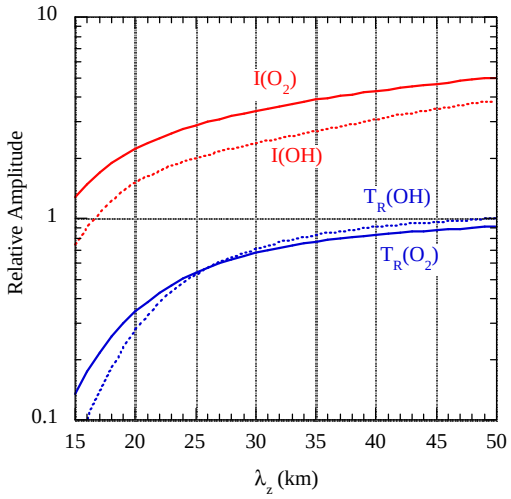

Figure 3 - Amplitudes of I' and T_R' for O_2 and OH normalized by $\rho'(z_0)$.

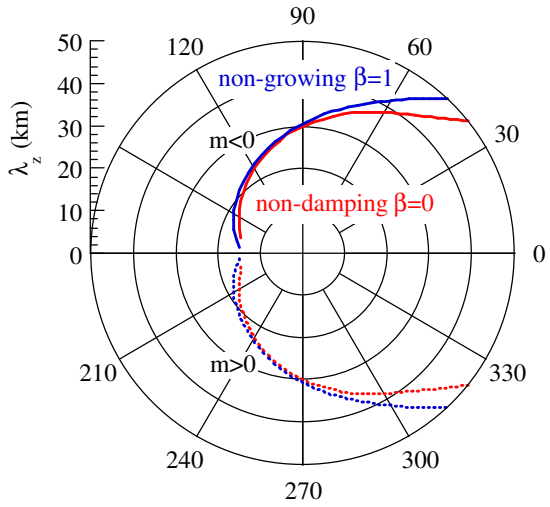

Figure 4 - Phase difference between I' of O_2 and OH. The difference is defined as phase of I'_{OH} subtracted by the phase of I'_{O_2}. Positive phase (0˚-180˚) is I'_{O_2} leading I'_{OH}. Solid (dotted) lines are for upward (downward) propagating waves .

Equatorial Upper Atmosphere Research Satellite: EQUARS

H. Takahashi, M. A. Abdu, B. R. Clemesha, I. S. Batista, W.D. Gonzalez, H. Carvalho.
Instituto Nacional de Pesquisas Espaciais, INPE, CP-515, 12201 Sao Jose dos Campos, SP, Brasil. E-mail: hisao@laser.inpe.br

Abstract

The Brazilian National Institute for Space Research - INPE is planning a satellite mission to study the equatorial middle and upper atmosphere-ionosphere. Launch of the 100 Kg (micro) satellite is expected to take place around 2005-2006. Scientific objective is to understand dynamical and chemical processes, and energy balance of the equatorial middle and upper atmosphere-ionosphere. The experiments to be included in this satellite are still in the definition stage. GPS receiver for occultation measurement, plasma sensors, airglow imager and others are in consideration as possible payloads.

Introduction

From our recent knowledge of dynamical processes in the Earth's middle and upper atmosphere, it is well known that the equatorial atmosphere plays an important role with respect to energy sources, transport, and global circulation. With the generation of atmospheric gravity waves in the troposphere and tidal forcing in the stratosphere, the equatorial atmosphere plays an significant part in the propagation of these wave energies to the upper atmosphere and ionosphere. Furthermore, deposition of momentum and energy in the upper atmosphere generates large scale travelling waves (Planetary waves) and ionospheric disturbances (Plasma bubbles). These waves in turn propagate to middle and high latitudes. It is only in recent years that an integrated picture of the energy balance of the upper atmosphere is beginning to emerge. There can be no doubt that we need better global data if we are to understand the forces at work. Satellite observations can provide the data needed.

The Brazilian National Institute for Space Research, INPE, has been working in the area of space science and technology since 1962. One of our special interests is to understand the dynamical and chemical characteristics of the equatorial atmosphere. Brazil has a large geographical extent in the equatorial regions. Plasma bubbles in the ionosphere directly affect satellite telecommunications. Changes in the global scale circulation of the lower atmosphere, such as those associated with El Niño e La Niña, greatly affect the climate of the Southwest and Northeast regions of Brazil. Ground-based observations carried out up until now are not sufficient to understand such large scale phenomena. Further observations on a global scale are needed. For this reason a satellite-based observation scheme for monitoring the equatorial upper atmosphere on a global scale has been proposed by the Brazilian scientific community. Recent global scale measurements of the upper atmosphere organized by PSMOS/SCOSTEP have also shown the necessity for global scale observation. In a recently initiated SCOSTEP program, EPIC, attention is being focussed on coupling mechanisms in the equatorial middle and upper atmosphere. We hope that the EQUARS satellite will make an important contribution to this program.

The satellite is expected to be launched around 2005-2006. Mission, scientific objectives, satellite technical characteristics and proposed payloads are listed below. It is hoped to launch the satellite from the Alcântara Launch Base on a Brazilian VLS rocket but, depending on vehicle availability, a piggy-back launch together with a larger satellite may be utilized. The experiments to be included in this satellite are still in the definition stage and we are seeking cooperation in this respect.

Scientific mission

Global scale monitoring of the Earth's equatorial middle and upper atmosphere-ionosphere.

Objectives

The study of dynamical, photochemical and ionospheric processes in the equatorial middle and upper atmosphere, with special emphasis on energy transport in the middle and upper atmosphere and the development of plasma bubbles in the ionosphere.

Satellite Characteristics (Preliminary)

- Total Mass: 100 kg
- Payload Mass: 30 kg
- Dimensions: 60 x 70 x 80 cm (l x w x h)
- Available volume for Payload: 60 x 70 x 30 cm
- Attitude Control: 3 axis
- Attitude Sensors: 2 star trackers, Sun sensor, Magnetometer
- Attitude Controllers: Torque rods, Reaction wheels
- Spin Axis: no spin
- Orientation of Satellite:1.0 degree accuracy
- Power Available to the Payload : 30 W
- Total Power Consume: 180 W
- Energy Storage Available (in Wh) 10A.h x 28V = 280 W.h

EQUARS

- Uplink and Downlink Telecommunications Bands: S-band
- Types of Antennas and Orientations: omni-directional
- Available Downlink Rate vs. Distance (kb/s at km): 400 kbps @ 750 km
- On-board Data Storage Capability (MBytes): 800 Mbits
- Temperature Control System: passive thermal control with paint and MLI
- Design Life (years): 2 years

Launch and Orbit:

- Brazilian VLS Launcher or piggy-back
- Nominal orbit: Equatorial (low inclination), 750 km circular

Time Frame:

- 2001: Announcement of opportunity
- 2002: Technical design project fixed and starting construction
- 2005-6: Launch

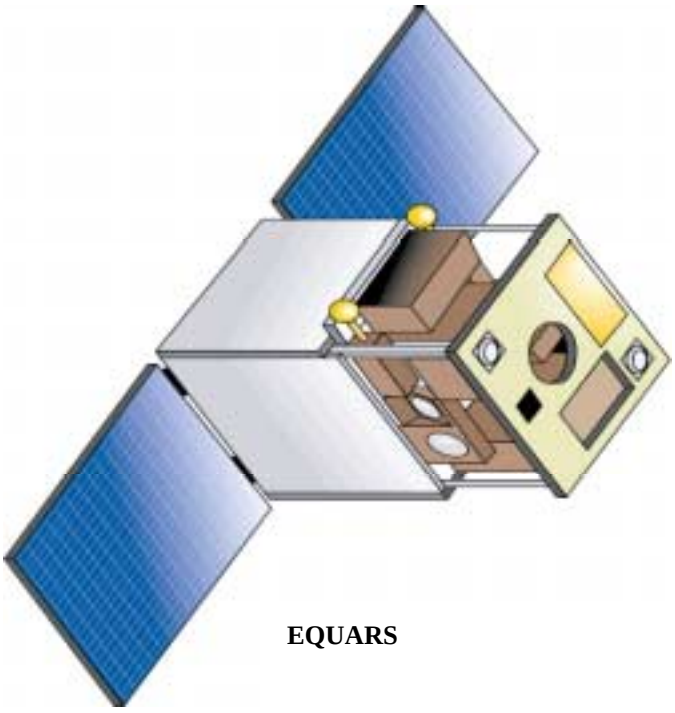

EQUARS

Estimating Daytime, Vertical ExB Drift Velocities in the Equatorial F-region Using Ground-based Magnetometer Observations

David Anderson and Adela Anghel (CIRES, Univ. of Colorado, NOAA/SEC, 325 Broadway, Boulder, CO 80303 email: david.anderson@noaa.gov); Kiyohumi Yumoto (Dept. of Earth and Planetary Sciences, Kyushu Univ. 33, 6-10-1 Hakozaki, Fukuoka 812-8581, Japan); M. Ishitsuka (Observatorio de Ancon/Direccion de IGP, Lima, 27, Peru) Erhan Kudeki (Dept. of Electrical and Computer Eng., Everitt Lab, University of Illinois, 1406 W. Green St., Urbana, IL 61801)

Abstract

The daytime equatorial electrojet is a narrow band of enhanced eastward current flowing in the 100 to 120 km altitude region within +/- 2 degrees latitude of the dip equator. The strength of the electrojet varies considerably from day-to-day and has its origin in the Solar quiet (Sq) current dynamo mechanism and the penetration of electric fields from high latitudes. A unique way of determining the daytime strength of the electrojet is to observe the difference in the magnitudes of the Horizontal (H) component between a magnetometer placed directly on the magnetic equator and one displaced 6 to 9 degrees away. The difference between these measured H values provides a direct measure of the daytime electrojet current, and in turn, the magnitude of the vertical ExB drift velocity in the F region ionosphere. This paper discusses a recent study that has established the relationship between the vertical ExB drift velocity in the ionospheric F region and the daytime strength of the equatorial electrojet in the South American (west coast) longitude sector. Magnetometer H component observations from Canete (0.8 N. dip lat.) and Piura (6.8 N. dip lat.) in Peru and daytime, vertical ExB drift velocities measured by the Jicamarca Incoherent Scatter Radar (ISR) Facility have been used to establish this relationship. The magnetometer observations and the ISR drift measurements were obtained for the period between July, 1998 and June, 1999.

Low Latitude Electrodynamics

It is well known that the effect of neutral winds together with diurnal and semi-diurnal tidal components in the atmosphere cause currents to flow in the 100 to 130 km altitude region. This is the so-called Sq (Solar quiet) wind dynamo current system in the E region. Resulting from this current system is an electrostatic field, $E_{\perp}$, directed eastward from dawn to dusk at low latitudes. The strength of this electric field is about 0.5 mV/m and is responsible for the upward ExB drift velocities of ~ 20 m/sec measured by the Jicamarca ISR. As a result of this electric field, within +/- 2 degrees of the magnetic equator, an enhanced eastward current flows (between 100 and 110 km altitude) known as the equatorial electrojet (see Richmond, 1989; and Reddy, 1989 for in-depth reviews of the neutral wind dynamo and the equatorial electrojet, respectively).

Figure 1 depicts the electric fields and the current systems that are associated with the electrojet. The view is to the North at the magnetic equator viewing the dayside region. If an eastward electric field exists and is perpendicular to B, then a Hall current is generated in the downward direction. Because of the particular geometry at the magnetic equator where magnetic field lines are horizontal, the Hall current, carried by upward moving electrons, quickly polarizes the ionospheric E layer so that an upward directed polarization electric field is produced. This electric field (red arrow) is about 5 to 10 times stronger than the eastward electric field (yellow arrow) that produced it. It is this vertical electric field that is responsible for the eastward equatorial electrojet current (carried primarily by electrons drifting westward with an ExB/B^2 velocity). This current produces the strong enhancement in the H component observed by magnetometers within +/- 2 degrees of the magnetic equator.

Calculating the Relationship between ΔH and ExB Drift

In order to develop the relationship between the strength of the equatorial electrojet and the daytime, vertical ExB drift in the F region, data sets from two magnetometer sites in Peru were obtained. In addition, the observed vertical drift velocities were obtained from the Jicamarca Incoherent Scatter Radar (ISR) facility between June 1998 and July 1999. The 1-minute averaged Horizontal (H) component

Vertical ExB Drift Velocities

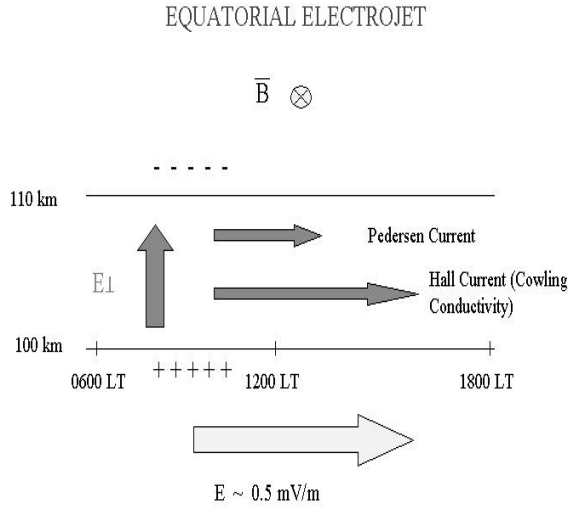

Figure 1 - Schematic diagram of equatorial electrojet electric fields and current systems

observations from Canete, Peru (0.8° N. dip lat.) and Piura, Peru (6.8 ° N. dip lat.) were obtained from the Circum-Pan Pacific Magnetometer Network (Prof. K. Yumoto – Director) and the Jicamarca ISR observed ExB drifts, from Dr. Erhan Kudeki, University of Illinois. Table 1 lists the days in 1998 and 1999 when ExB drifts were measured by the ISR. For each of the magnetometer data sets at Canete and Piura, the nighttime baseline in H was first obtained for each day and then subtracted to give the daytime values. This produced daytime H component values at each of the two stations for the days listed in Table 1. Table 1 also lists the observed, noontime ΔH values (difference between Canete and Piura H values) and the noontime Jicamarca measured ExB drift values on 6 of these days. Figure 2 presents these six points as a ΔH vs ExB drift plot. A linear, least squares fit to these six points yields a straight line with a slope of 2.524 nT/m/sec and a Y intercept of 8.9 nT**.**

Table 1

Date	ΔH (nT)	ExB Drift (m/sec)
July 15, 1998	82	30
Oct. 20, 1998	75	25
Oct. 21, 1998	50	15
Jan. 12, 1999	25	6
Feb. 10, 1999	52	17
Feb. 12, 1999	30	10
July 16, 1998		
Oct. 19, 1998		
Jan. 13, 1999		
Feb. 9, 1999		
Feb. 11, 1999		

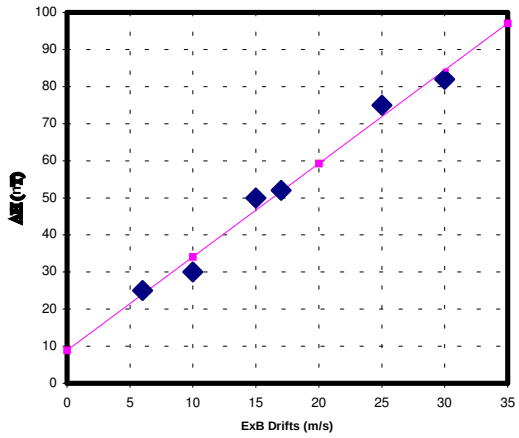

Figure 2 - The linear, least squares line that fits the six noontime points in Table 1

In order to verify that the relationship derived from Figure 2 is realistic and can be applied at other local times, Figures 3 and 4 plot the ΔH-inferred ExB drifts for two days when the Jicamarca ISR measured ExB drifts throughout the day. Figure 3 displays the comparison on July 15, 1998 (day 197) during the daytime hours. The agreement is excellent. Not only does the ΔH-inferred drifts agree with the measured ExB drift values over the longer, hourly time scales but also over the tens-of-minutes time scales. To emphasize this point, Figure 4 compares the drifts on Oct. 21, 1998 (day 294) when rapid changes in ExB drifts occur, due primarily to the penetration of high latitude electric fields to the equatorial region.

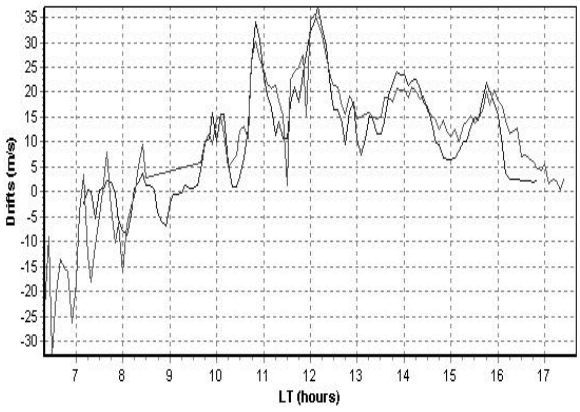

Fig. 3. Comparison of the ΔH-inferred ExB drift velocities (blue line) with the Jicamarca ISR measured ExB drift velocities (red line) on July 15, 1998 (day 197)

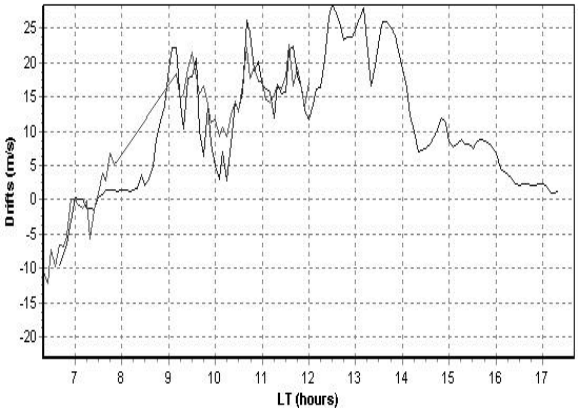

Fig. 4. Same as Figure 3 except on Oct. 21, 1998 (day 294)

Summary

This paper discusses a recent study that has established the relationship between the vertical ExB drift velocity in the ionospheric F region and the daytime strength of the equatorial electrojet in the South American (west coast) longitude sector. Magnetometer H component observations from Canete (0.8 N. dip lat.) and Piura (6.8 N. dip lat.) in Peru and daytime, vertical ExB drift velocities measured by the Jicamarca Incoherent Scatter Radar (ISR) Facility have been used to establish this relationship. The magnetometer observations and the ISR drift measurements were obtained for the period between July, 1998 and June, 1999. It is found that when ΔH and ExB drift are both positive the relationship is given by **ΔH = 2.2789 * ExB drift + 14.0 nT** and when ΔH and ExB drift area both negative then the relationship is **ΔH = 6.13 * ExB drift – 11.0 nT**. Excellent agreement is achieved when the magnetometer-inferred vertical, daytime ExB drift values are compared with the Jicamarca ISR observations of ExB drifts. As a result, a number of important Space Weather science investigations can now be carried out relating to the day-to-day variability of the low latitude ionosphere.

References

Reddy, C. A., " The Equatorial Electrojet, Pageoph, *131*, 485-508, 1989.

Richmond, A. D., "Modeling the Ionospheric Wind Dynamo: A Review", Pageoph, *131*, 413-435, 1989.

Eventos de quebra de onda de gravidade observados em imagens de aeroluminescência de Cachoeira Paulista

D. Gobbi[1], H. Takahashi[1], A. F. de Medeiros[1], M. J. Taylor[2]

[1] Instituto Nacional de Pesquisas Espaciais, São José dos Campos, Brazil
[2] Space Dynamics Laboratory, Utah State University, USA.

Resumo

As emissões de aeroluminescência mesosférica, OI 557.7 nm, OH IR e O_2 (0-1), medidas por um imageador de alta resolução em Cachoeira Paulista (23^o S, 45^o W), com medidas complementares do campo de vento via radar meteórico, na mesma localização, foram usadas, no presente trabalho, para investigação e análise de eventos característicos de quebra de onda de gravidade. As assinaturas das ondas de gravidade exibidas nas imagens de aeroluminescência foram caracterizadas como comprimentos de onda de pequena escala (10 ~ 30 km) e períodos próximos ao período de Brünt-Väisäla (5 ~ 8 min). Durante o curso de desenvolvimento da fase de instabilidade, as estruturas de turbulência expandiram-se em área, quase em alinhamento à direção de propagação da onda. Eventos não lineares desta natureza são, geralmente, de difícil acesso, devido a significativa extensão vertical da camada de emissão, que tende a produzir padrões de cancelamento no movimento de ondas de gravidade de pequena escala.

Future Satellite Based Sensors for Radio Remote Sensing of Low-Latitude Irregularities.

P A Bernhardt and J D Huba (Beam Physics Branch, Plasma Physics Division, Naval Research Laboratory, Washington, DC 20375; Ph. 202-767-0196; Fax 202-767-0631; e-mail: bern@ppdu.nrl.navy.mil); C A Selcher (Transmission Technology Branch, Information Technology Division, Naval Research Laboratory, Washington, DC 20375; Ph. 202-767-2179; e-mail selcher@itd.nrl.navy.mil

Abstract

The equatorial and high-latitude ionosphere has long been known to be the primary source of amplitude and phase fluctuations for VHF, UHF, and L-Band radio waves. A new approach for monitoring ionospheric irregularities that affect radio propagation is being implemented using radio beacons and receivers on satellites in low-earth-orbit (LEO). These system called Coherent Electromagnetic Radio Tomography (CERTO) uses three frequency radio beacons operating at VHF (150.012 MHz), UHF (400.032), and L-Band (1066.752 MHz). Receivers located on the ground and on other satellites record the phase differences between a pair of frequencies. This differential phase data is used to determine the integrated electron density along oblique and vertical paths using satellite to ground geometry and along both vertical and horizontal paths using satellite-to-satellite observations. The space-based radio beacons and receivers are scanning the ionosphere at roughly 8 km/s in LEO. This scan yields high-resolution reconstruction of electron densities using computerized ionospheric tomography (CIT). CIT reconstructions will show many localized features including (1) travelling ionospheric disturbances (TID's) from acoustic gravity waves; (2) ionospheric disturbances from solar eclipses; and (3) low-latitude, plasma plumes.

As radio waves propagate from satellites though regions of ionospheric disturbances, the phase front of the waves becomes distorted. The ionosphere thus acts as a phase screen for a wide range of transmissions from GPS satellites, UHF communications satellites, etc. The irregular phase front becomes highly diffracted as the signal propagates the hundreds of kilometers from the base of the ionosphere to the ground. During times of strong irregularities in both the high-latitude and equatorial ionosphere, the ground signals can show scintillations in both amplitude and phase that make navigation and communications systems inoperable. Once a large-scale irregularity has been formed in the ionosphere, it will persist for hours in the nighttime ionosphere. One basis for scintillation forecast is to monitor the drift of irregularities as they pass between satellite to ground communication links. The Air Force Research Laboratory (AFRL) to produce three-dimensional maps irregularity structures has used a global network of ground receivers in a system called the Scintillation Network Decision Aid (SCINDA). Using CERTO beacons in conjunction with space based receivers, the SCINDA technique will be extended to cover regions, such as the ocean, where ground receivers cannot be deployed. NRL's first satellite receiver to record CERTO signals will be called SCITRIS (Scintillations and Tomography Receiver in Space). SCITRIS will be launched on the US Air Force STPSat1 Satellite. This receiver will record TEC and scintillations along satellite to satellite links CERTO beacons. The first CERTO beacons were placed in polar orbits on the ARGOS and DMSP/S15 satellites that were launched in February and December 1999. Other CERTO radio beacons are scheduled for launch over the next four years on the PICOsat and C/NOFS satellites as well as the six satellites of the COSMIC constellation. A program of measurements and simulations are being employed to optimize the planning for the CERTO/SCITRIS system.

Geomagnetic Field Variations During Periods of Low and High Magnetic Activity at Ferraz Antarctic Station

José M. da Costa, University of Taubaté, São Paulo, Brazil; Severino L. G. Dutra and Nalin B. Trivedi, National Space Research Institute, São José dos Campos, São Paulo, Brazil; Rodrigo P. Sampaio, UNITAU/INPE/CNPq-PIBIC, Brazil; Fabiane Guimarães and Itana A. E. dos Santos, UNITAU/INPE/CNP-PROANTAR, Brazil

Abstract

The measurement of geomagnetic variations is very important for understanding the behavior of the earth's magnetic field and its relation with sun's activity. The present study shows some results on the daily variation and also on detection of geomagnetic pulsations at Ferraz, (62°S, 58°W), in the Antarctic region, during periods of low and high magnetic activity. The station is situated near the border of the South Atlantic Magnetic Anomaly region. The geomagnetic field variations were measured using a high sensitivity ring core three-axis (H,D,Z) fluxgate magnetometer and a pair of magnetic coils. The data analysis included the identification of the dominant frequencies using Fast Fourier Transform (FFT). The main results are discussed taking account the interaction between the solar wind and the earth's magnetic cavity.

Introduction

The measurement of temporal variations of the geomagnetic field is very important for understanding the behavior of sun-earth's relations (e.g. Jacobs, 1970; Trivedi et al., 1997; Pilipenko et al. 2001). The present study shows some results on the diurnal variation and also on the detection of geomagnetic pulsations at Ferraz, (62°S, 58°W), in the Antarctic region, during periods of low and high activity. It is shown some results from the analysis of the data measured from 18 to 20 October, 1999 ($\Sigma Kp < 13$) and 13 to 15 October, 1999 ($\Sigma Kp > 29$). The occurrence of Pc5 and Pc6 pulsations presented substantial increase during the interval of time with higher magnetic activity. Also it is shown the frequency spectra for the north-south Pc5 (150–600 s) geomagnetic pulsations recorded on 3 September, 1998 (ΣKp =14-).

Instrumentation

A high sensitivity, better than 0.1nT, ring core three-axis (H,D,Z) fluxgate magnetometer measured geomagnetic variations in the DC to 4mHz range, at each 2-min, 1-min or 30-sec interval. A pair (X,Y) of magnetic coils measured variations in the 10mHz to 2.5Hz range at each 0.2s. Diesel generators provided the electric power for the fluxgate magnetometer from a distance of about 200 meters. The magnetic coils were operated at a most remote site, about 4 km from the center of Ferraz station, which counted with solar panels and a wind power generator for provision of electric power.

Data Analysis and Results

The data analysis included the study of the daily variation and the identification of the dominant frequencies using Fast Fourier Transform (FFT) for the periods of 3 September, 1998, October 18–20, 1999 and October 13–15, 1999.

Figure 1 shows filtered data for Pc5 frequency range measured with the magnetic coil on the north-south direction. The plots of the daily variations of the geomagnetic field recorded during periods of low (October 20, 1999) and high (October 14, 1999) magnetic activity measured with the fluxgate magnetometer are shown in Figure 2 and Figure 3, respectively. The dynamic spectra of Pc5 (150–600 s) and Pc6 (600–1000 s) pulsations for October 18-20, 1999 and October 13-15, 1999 are shown in Figure 4 and Figure 5, respectively.

Discussion and Conclusions

The analysis of Ferraz data for the periods of 3 September, 1998, October 13-15, 1999 and October 18-20, 1999 revealed the recording of important geomagnetic phenomena. The variations recorded on the period of October 13-15, 1999 are associated with the magnetic storm whose sudden commencement (SSC) occurred at 08:58 UT on October 14, 1999. The Pc5 and Pc6 are associated to space plasma magnetospheric phenomena driven by the interaction of the solar wind with the earth's magnetosphere. The enhancement on Pc5 and Pc6 geomagnetic pulsation activities observed on October 13, 1999 data may reveal large transference of energy from the solar wind to the interior of the magnetosphere.

References

Jacobs, J. A., Geomagnetic Micropulsations, New York: Springer-Verlag, 1970.

Trivedi, N. B., B. R. Arora, A. L. Padilha, J. M. Da Costa, S. L. G. Dutra, F. H. Chamalaun, and A. Rigoti, Global Pc5 geomagnetic pulsation of March 24, 1991, as observed along the American sector, Geophysical Research Letters, 24 (13):1683-1686, 1997.

Pilipenko V., N. Kleimenova, O. Kozyreva, M. Engebretson and O Rasmussen, Long-Period Magnetic Activity During the May 15, 1997 Storm.

Acknowledgments

The authors thank the support of University of Taubaté – UNITAU, National Space Research Institute – INPE and National Research Council/CNPq-PIBIC/PROANTAR

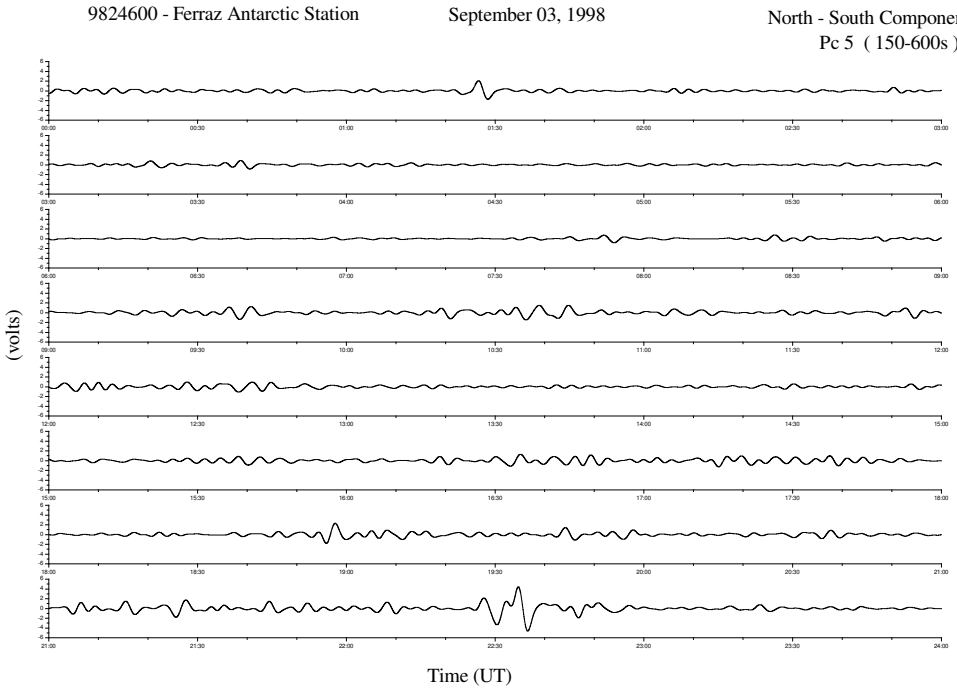

Figure 1 – Pc5 pulsations measured with north-south coil at Ferraz.

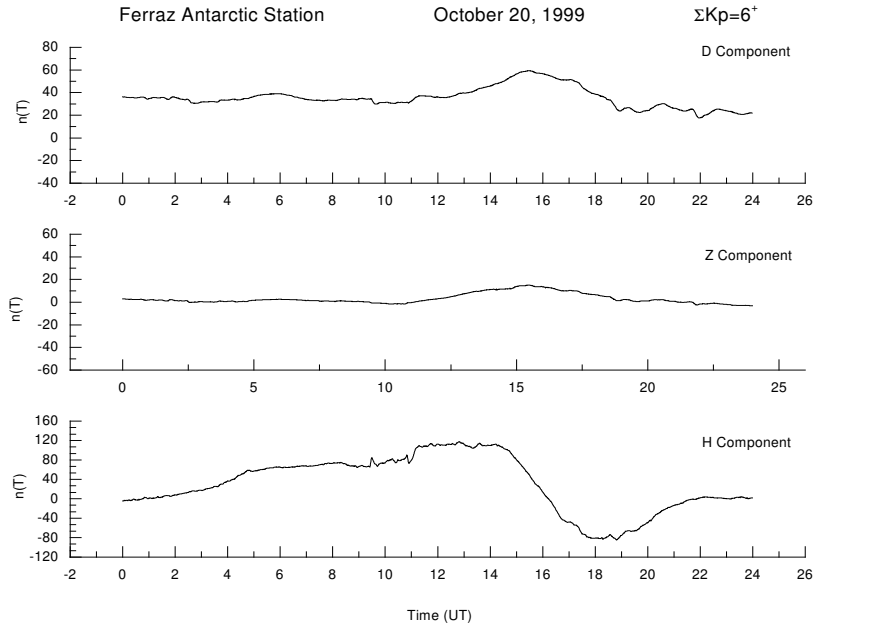

Figure 2 – Geomagnetic field daily variation for October 20, 1999 at Ferraz.

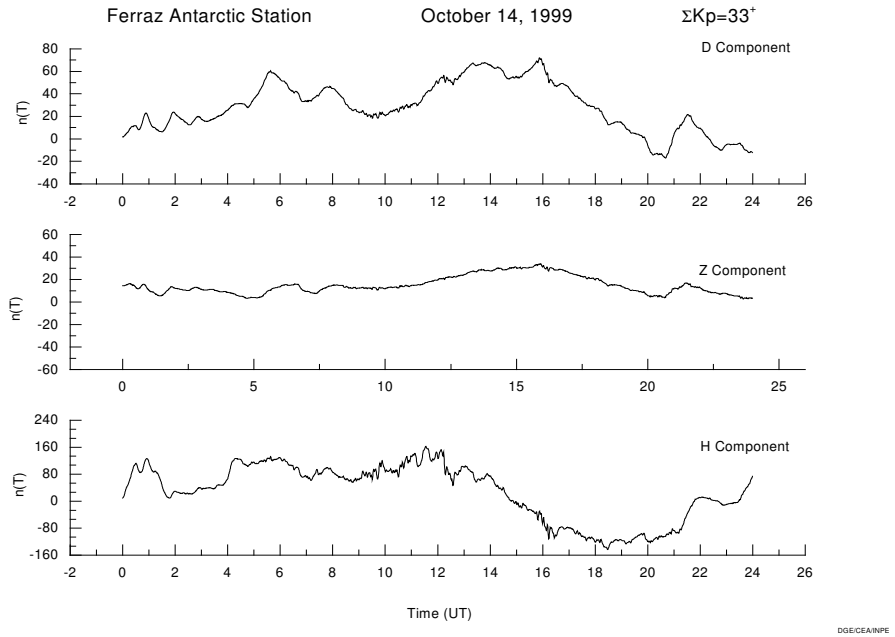

Figure 3 – Geomagnetic field daily variation for October 14, 1999 at Ferraz.

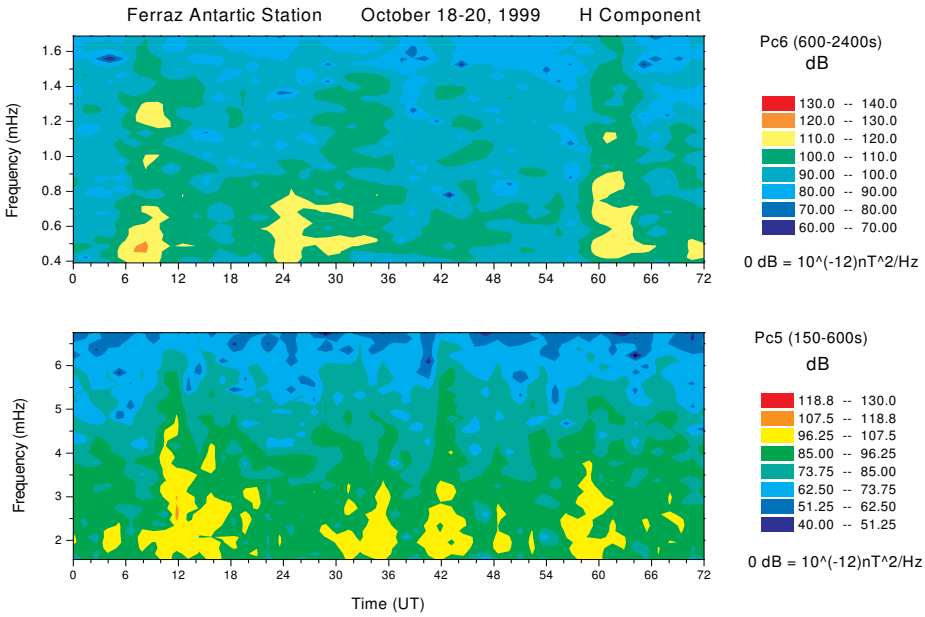

Figure 4 – Pc5-6 dynamic spectra for October 18 – 20, 1999 at Ferraz.

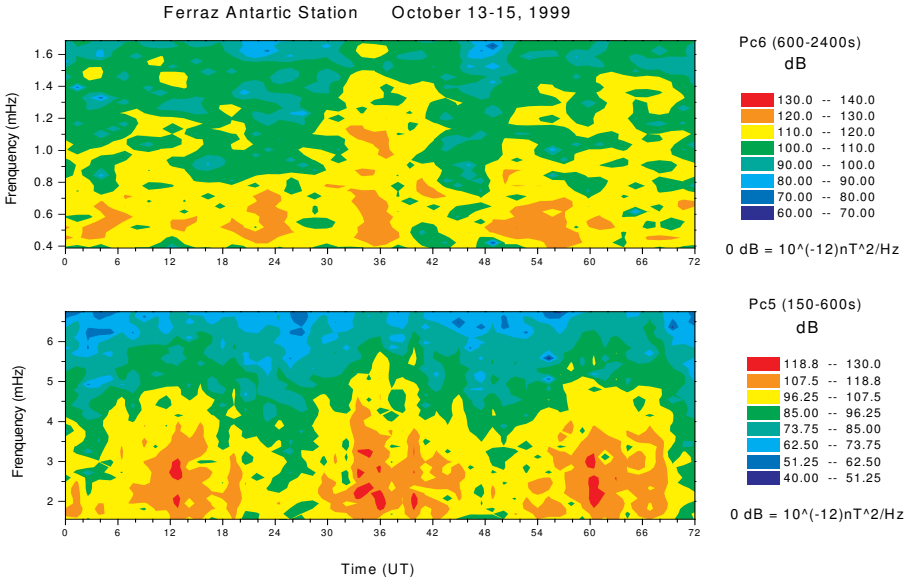

Figure 5 – Pc5-6 dynamic spectra for October 13 – 15, 1999 at Ferraz.

Global Measurement of Low Latitude Plasma Parameters on board the French-Brazilian Microsatellite

P. Muralikrishna, M. A. Abdu, S. Domingos, Instituto Nacional de Pesquisas Espaciais, INPE/MCT, C. P. 515, 12 201-970, São José dos Campos - SP, Brazil., and K. I. Oyama, Institute of Space and Astronautical Science, Sagamihara, Japan (e-mail: murali@dae.inpe.br*)*

Abstract

The French-Brazilian microsatellite (FBM) is scheduled to be launched by the end of the year 2002. It will be placed in a low inclination (about 6 degrees) equatorial circular orbit at a height of 700km. Among the various French and Brazilian experiments, it will carry a Plasma Diagnostics Package (PDP) consisting of three experiments. A High Frequency Capacitance probe (HFC) to measure the absolute electron density along the satellite trajectory, a Langmuir Probe (LP) to measure the relative variation and the spectral distribution of the electron density and an Electron Temperature probe (ETP) to measure the variations in the electron temperature and the space potential. The main objective of the PDP experiments is to make global observations of the characteristic features of the low latitude plasma bubbles, and thereby to study the dynamic and electrodynamic processes that control the generation, development and decay of the plasma bubbles. These satellite observations will be complemented by observation from a network of ionospheric sounding equipments like Ionosondes, Digisondes, Polarimeters, VHF radars operated simultaneously from selected ground stations in Brazil as well as in other collaborating countries. Data from the PDP and the other Brazilian experiments are pre-processed in the Brazilian Payload Computer (BPC) before being sent to the main computer on board. Data on the plasma irregularities collected by the LP experiment can also be pre-processed on board using an FFT algorithm to reduce the data volume without losing information on the spectral distribution of the plasma irregularities.

Introduction

The French-Brazilian microsatellite (FBM) is scheduled to be launched by the end of the year 2002. It will be placed in a low inclination (about 6 degrees) equatorial circular orbit at a height of 700km. Among the various French and Brazilian experiments, it will carry a Plasma Diagnostics Package (PDP) consisting of three experiments. A High Frequency Capacitance probe (HFC) to measure the absolute electron density along the satellite trajectory, a Langmuir Probe (LP) to measure the relative variation and the spectral distribution of the electron density and an Electron Temperature probe (ETP) to measure the variations in the electron temperature and the space potential. The PDP has the principal objective of investigating the electrodynamics and nonlinear processes of the equatorial ionosphere-thermosphere system (EITS) by making global observations of the characteristic features of the low latitude plasma bubbles, and thereby studying the dynamic and electrodynamic processes that control their generation, development and decay. Plasma bubbles are geomagnetic field-aligned depleted flux tubes (with plasma density less by 2-3 orders of magnitude compared to the ambient density) stretching in a few thousands of kilometers between conjugate points north and south of the magnetic equator. Over the equator they are distributed from ~300km where their seeding occurs reaching to ~1500 km or more in their vertical growth processes. The night time Brazilian low latitude ionosphere is strongly controlled by plasma bubble phenomenon. They present significant longitudinal and seasonal dependence in their occurrences, the Brazilian (Atlantic) longitude being a region of globally highest occurrences observed so far.

The observations by the satellite will be supported by ground-based ionospheric and thermospheric measurements in Brazil and at selected locations in other countries using a network of diagnostic instruments that include radars, digisondes/ ionosondes, optical imagers and interferometers and the available GPS satellites.

In the low latitude region where the topology of the geomagnetic field lines is primarily horizontal, plasma instabilities are driven by gravitational forces and by the electric fields and current systems. The observed phenomena include the equatorial spread-F/ plasma bubbles and the electrojet current instabilities. These are associated with another major phenomena of the EITS: the equatorial ionization anomaly. These are highly interdependent phenomena being controlled by common driving forces: the thermospheric wind system and the tidal and magnetospheric dynamo electric fields. It is now rather well established that the equatorial ionospheric plasma is highly unstable to nonlinear plasma instability processes, one of the most important among them being the Rayleigh-Taylor mechanism, that are responsible for the generation of plasma bubbles.

Plasma Measurements on board FBM

The plasma irregularities produce significant modifications to the phase and amplitude of radio waves in different bands used in wide ranging space application areas (telecommunications, geodesy, remote sensing by space shuttle based radars, etc.,). Therefore their investigation is considered to be a priority topic in space research activities by international scientific bodies.

Diverse aspects of this phenomenon, mainly the ambient ionospheric conditions and the electrodynamics that are responsible for its large variability in the occurrence frequency as well as the intensity of occurrence remain unknown till today. On the other hand, a better understanding of these aspects is fundamental in attaining our objectives of improving the predictability of the occurrence of these phenomena. A low-inclination, low-altitude satellite carrying a plasma diagnostics package will substantially improve the observational foundation for investigation of these phenomena. The in situ measurement of the critical parameters proposed here, to be realized on board the Franco-Brazilian scientific satellite, promises to offer important data fundamental for the detailed study of the electrodynamic processes.

It is intended to make high resolution measurements of the plasma density, plasma temperature, spectral distribution of the irregularities using the following experiments.

- High Frequency Capacitance Probe (HFC) for measuring the plasma density.
- A Langmuir Probe (LP) for measuring the electron density and temperature variations and the spectral distribution of plasma irregularities.
- Electron Temperature Probe for measuring the kinetic temperature of the ionospheric electrons.

In the Langmuir Probe experiment the current collected (in the range of 1na to 20μa) by a spherical metallic sensor is measured and later converted into electron number density in the range of 10^3 to $5x10^6$ electrons per cubic centimeter. 3 digital data words of 8 bits each sampled at 16 per second represent the LP current variations (monitored through three different channels) and 1 digital data word of 8 bits sampled at a minimum rate of 2048 per second represents the ac fluctuations in the LP current. The ac fluctuations in the current collected by the sensor in the frequency range of about 10hz to 1000Hz (upper limit imposed by the maximum sampling rate possible) is thus measured. The accuracy of measurement of the LP experiment varies almost logarithmically in the measurement range. At low electron densities the accuracy of measurement is about 10% (corresponding to about 100 electrons per cc while at higher electron densities one can obtain an accuracy of about 2% comparing the dc measurements with the corresponding ac measurements.

In the HFC experiment, changes (about 10% from the mean value) in the frequency of oscillation (about 8MHz.) of an oscillator is measured and later converted into the ambient electron number density within the measurable range of 10^3 to $5x10^6$ electrons per cubic centimeter. 4 digital data words of 8bits each sampled at 16 per second represent the HFC oscillator frequency variation and the experiment mode of operation. The measurement accuracy of the experiment is about 17hz in the frequency of an oscillator of mean frequency of oscillation of about 8MHz. This gives an estimated accuracy of about 100electrons per cc in the electron number density.

In the Electron Temperature Probe experiment the kinetic temperature of the electrons in the approximate range of 10 – 2000 degree Kelvin and the space potential in the range of 0 to 2V are measured. 4 digital data words (2 from each of the 2 ETP sensors) of 8 bits each sampled at 16 per second represent these parameters. The ETP experiment has an estimated approximate measuring accuracy of about 10 degrees in the electron temperature and about 50mV in the space potential.

Experiment Details

High Frequency Capacitance Probe

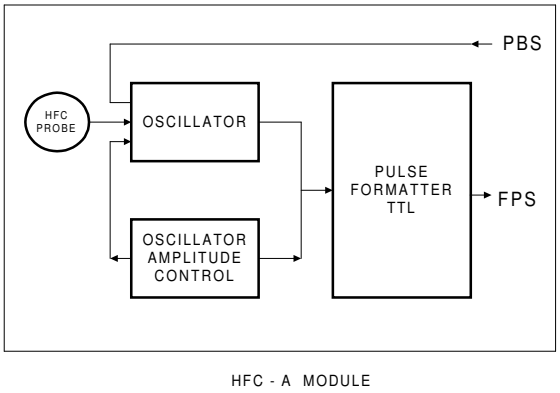

Figure 1.: The HFC MODULE-A, showing the oscillator, its amplitude control unit and the pulse formatter.

Figures 1 and 2 show the block diagrams of the HFC experiment. The oscillator signal appears at the HFC sensor and its amplitude is controlled to be always at a low level less than 100mV for not perturbing the ambient plasma surrounding the sensor. The counter circuit counts the number of the arriving pulses through a preset time gate of

approximately 60ms. This count information is sent to the on board experiment interface BPC by the formatter circuit. The pulse count is represented by 20 binary bits of three 8 bit words, HFC1, HFC2 and HFC3, only 4 low significant bits of the word HFC3 (HFC3 represents the highest significant bits of the pulse count) and 8 bits each of the words HFC2 and HFC1 being used for this purpose. The bias (-100V) status is monitored through one of the bits.

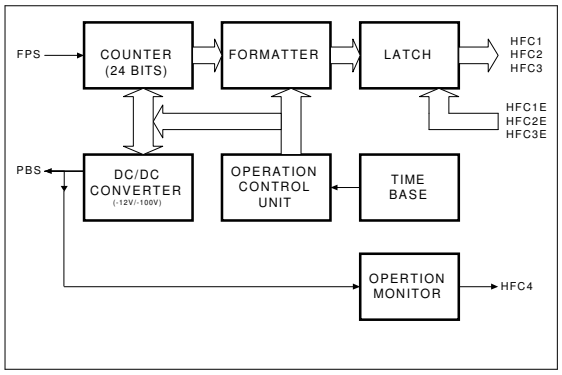

Figure 2. : HFC MODULE-B block diagram

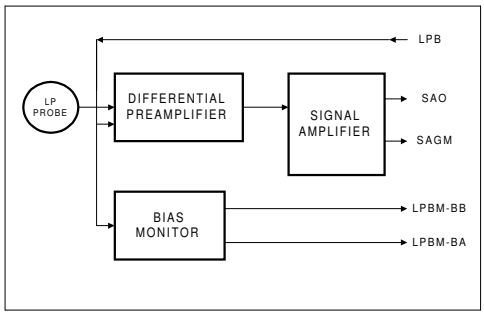

Figure 3.: Block Diagram of the LP MODULE-A

Langmuir Probe

The block diagrams of the Langmuir Probe electronics subsystem are shown in Figures 3 and 4. A negative, zero or positive potential is applied to the LP sensor (selected in a pre-programmed mode or through a telecommand) and the current collected by the sensor in the range of a few nano amperes to a few micro amperes is converted to a varying voltage using a high input impedance preamplifier(Figure 3).

The potential applied to the sensor, the preamplifier gain and the dc and ac amplifier gains as well as the status of the onboard FFT analysis performed on the ac signal are all monitored through an 8 bit digital word LP1.

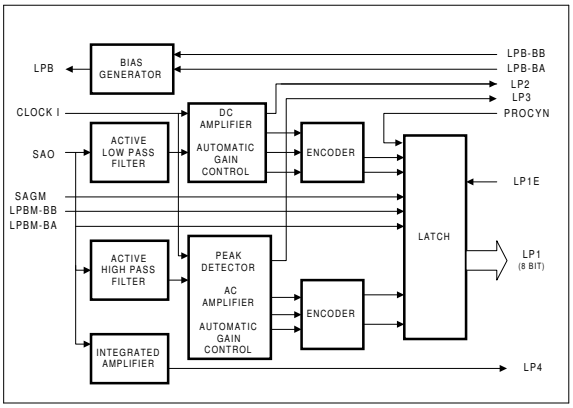

Figure 4.: Block Diagram of the LP MODULE-B

Electron Temperature Probe

Figures 5 and 6 show the block diagrams of the ETP electronics subsystem. It is proposed to use two ETP sensors mounted with an angle of about 20 degrees between them so as to increase the effective time of measurement for the experiment. Each ETP sensor is made out of a printed circuit board cut in the form of a disc of 100mm diameter (Figure 5). The metallic part of the disc along one diameter of the disc is removed and the disc is transformed into two semi-circular sensors. An rf signal of 30kHz is generated in an oscillator and modulated to amplitudes a and 2a alternately. This modulated signal is applied to one of the semi-circular sensors of the ETP. No potential is applied to the other semi-circular sensor and therefore provides the variations in the floating potential of the sensor. The difference in the potential between the two sensors is amplified in a differential amplifier. This potential difference can be related to the electron kinetic temperature.

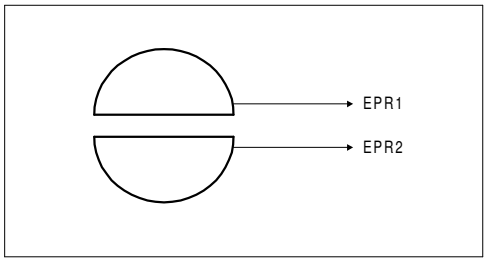

Figure 5.: ETP MODULE-A Showing one of the ETP Sensors

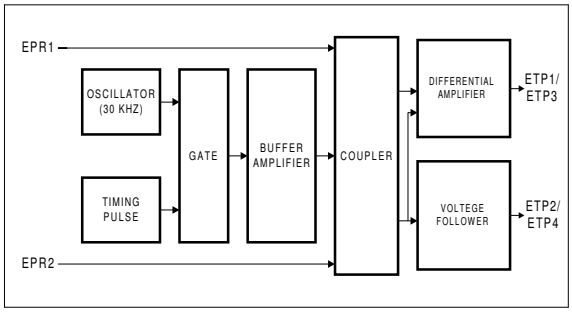

Figure 6.: ETP MODULE-B Block Diagram

Brazilian Payload Computer (BPC)

The operation of the PDP experiments will be controlled by the Brazilian Payload Computer (BPC) which will function as the interface between the Brazilian scientific experiments and the On Board Computer(OBC) and will take care of all the experiment operations and data transfer receiving commands from OBC whenever needed.

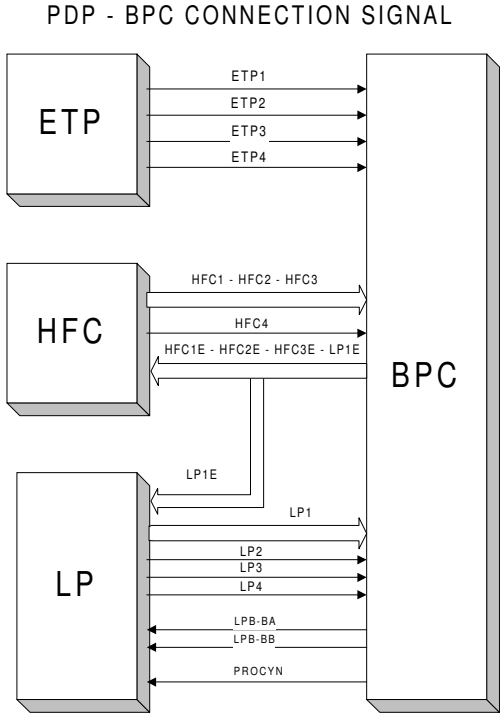

Figure 7: PDP-BPC Inter-Connection

On Board Processing of LP Data

In order to obtain the maximum possible information from the collected data on a global scale the analog ac data from the LP experiment that is sampled at a rate of 2048 samples per second is subjected to an on board processing, especially when the satellite is outside the visibility range of the ground TM station. This helps in adequating the data volume to a level acceptable for on board storage. Thus the LP ac data can be stored in the on board memory in two modes.

(1) Without On Board Processing (Mode R)
(2) After On Board Processing (Mode S)

The letter R in Mode R indicates that the data is **R**aw and the letter S in Mode S indicates that the data is of the **S**pectra of the density fluctuations.

When the satellite is in the telemetry visibility the LP ac signal (LP3) is transmitted without any onboard processing. But when the satellite is off the telemetry visibility, to reduce the amount of the data stored FFT analysis is made of the ac data and the average of a predetermined number of the FFT spectra thus obtained is stored in the place of raw data. Thus in the normal mode of operation the FFT processing can be programmed and it may not be necessary to send any telecommand to change this cycle. But, when one needs to collect the data over a certain gegraphic region this operation cycle may have to be interrupted by a telecommand and the onboard analysis command has to be generated.in the BPC following a different cycle. The bias level of the LP sensor also can follow a pre-programmed cyclic change in the normal mode of operation. The telecommand is needed only when one wants to interrupt this normal mode of operation.

REFERENCES

Abdu, M.A., I.S. Batista,and J.H. A. Sobral, A new aspect of magnetic declination control of equatorial spread F and F region dynamo, J. Geophys. Res., 97, 14897, 1992.

Sobral, J.H.A. and M.A.Abdu, Latitudinal gradient in the plasma bubble zonal velocities as observed by scanning 630nm airglow measurements, J. Geophys. Res., 95, 8253, 1990.

Muralikrishna, P., M. and A. Abdu, In situ measurements of ionospheric electron density by two techniques: a comparison, J. Atmos. Terr. Phys. 53, 787, 1991.

Abdu, M.A., P. Muralikrishna, I.S. Batista, and J.H. Sobral, Rocket observation of equatorial plasma bubbles over Brazil usinga High Frequency Capacitence Probe, J. Geophys. Res., 96, 7689, 1991.

Height-time diagrams of the July 25th (1999) halo coronal mass ejection obtained from LASCO observations

A. Dal Lago[1, 3], G. Stenborg[2, 3], R. Schwenn[3], W. D. Gonzalez[1], A. L. C. de Gonzalez[1], L. E. A. Vieira[1], N. J. Schuch[4]
[1]*Instituto Nacional de Pesquisas Espaciais, PO 515, 12201-970, São José dos Campos, SP, Brazil.*
[2]*Instituto de Astronomia y Fisica del Espacio, Buenos Aires, Argentina.*
[3]*Max Planck Institut für Aeronomie, Katlenburg-Lindau, Germany.*
[4]*Centro Regional Sul de Pesquisas Espaciais, Santa Maria, RS, Brazil.*
dallago@dge.inpe.br

Abstract

In this paper we present height-time diagrams of the halo coronal mass ejection observed in July 25th (1999) from the Large Angle and Spectroscopic Coronagraph (LASCO), which is an instrument on board of Solar and Heliopheric Observatory (SOHO) able to observe the solar corona from 2 to 32 solar radii. To obtain these diagrams we used a new technique in which we divide the LASCO images in angular slices and place side by side the same slice in different observation times, producing height-time diagrams. With this method we were able to identify a small deceleration of the July 25th halo CME in several directions around the sun. We propose that this technique is appropriated to identify whether there is acceleration or deceleration on halo CMEs near the sun which is an important parameter that can be used to predict the time of arrival and the velocity of these structures near the earth.

Introduction

Coronal mass ejections (CME) are expulsions of solar plasma from the gravitational field of the sun observed in the corona (Hundhausen et al., 1984; Schwenn, 1996; Hundhausen, 1997). These observations are made by instruments called coronagraphs that record the photospheric radiation (or white light) scattered by electrons in the ionized coronal plasma (Bruckner et al., 1995). Taking a temporal sequence of these observations it is possible to identify these coronal outflows. The most recent coronagraphs in operation are those from the Large Angle and Spectroscopic Coronagraph (LASCO) experiment on board of the Solar and Heliospheric Observatory (SOHO) satellite, which is a joint project from the National Aeronautics and Space Administration (NASA) and the European Space Agency (ESA). This satellite is located in the Lagrangian point L1 in the sun-earth line, distant 240 earth radii from the earth. LASCO provides plane of sky observations of the dynamics of the solar corona made by two coronagraphs named C2 and C3, which image the corona from 2 to 6 and 4 to 32 solar radii, respectively.

When the coronal mass ejections happens to occur in the line of sight of the satelite (sun-earth line), it appears as a halo structure expanding in all directions, the so called "halo CMEs" (Howard et al., 1982). When comming in the earth direction, these halo CMEs may produce geomagnetic storms (Gosling, 1990).

One of the difficulties experienced by the scientific community has been to quantify the observations provided by the LASCO images. In this sense we present a new technique applied in the July 25th (1999) halo CME images that helps to quantify these images.

The technique

The technique consists in dividing each LASCO image in angular sectors and performing an angular integration producing radial profiles in all directions. Since halo CMEs have circular symmetry, no information is lost in this integration. By placing side by side several profiles taken in different times for the same position we are able to produce a clear height-time figure for each angular position and then obtain a height-time scatter plot. The angular integration compensates the fading of the structures as they expand, making them visible at long distances in the corona. More details on the technique will come soon in a future detailed paper.

Height-time diagrams of the July 25th (1999) halo CME

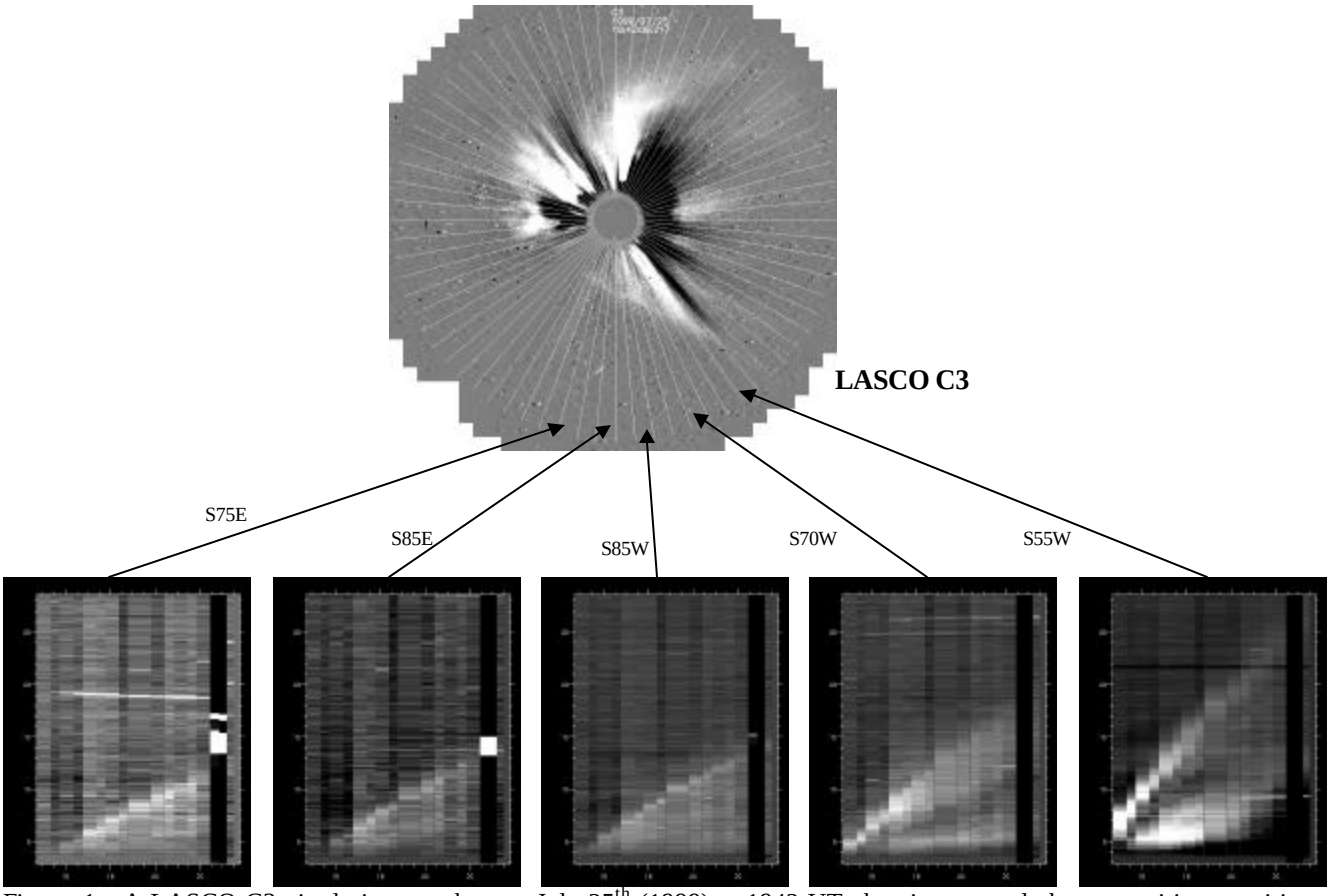

Figure 1 – A LASCO C3 single image taken on July 25th (1999) at 1942 UT showing several chosen positions positions The respective height-time images obtained from our technique are places in the bottom for the positions S75E, S85E, S85W, S70W and S55W.

The July 25th halo CME

The July 25th (1999) event was a full halo CME which was visible in all directions around the sun both in the C2 and C3 images. It was first seen at 1454 UT in the C2 and lasted beyond 2200 UT in the C3 field of view. We applied our technique for the positions S75E, S85E, S85W, S70W and S55W. Figure 1 shows a LASCO C3 single image taken on July 25th (1999) at 1942 UT. For all the positions mentioned above we applied our technique and the resulting height-time images are shown in the bottom of Figure 1. In each of these height-time images the "x" axis is time (hours) and the "y" axis is radial distance (solar radii).

Using the obtained height-time images of Figure 1 we could easily obtain their height-time scatter plots. Figure 2 shows the scatter plots for the positions of Figure 1. A second order polynomial fit was added to each of the diagrams, from which it is possible to observe a small deceleration in all the directions.

Table I shows the initial and final speeds and the accelerations for each of the directions shown in Figures 1 and 2. It is possible to see that there was a small deceleration in all the chosen directions. These results are in good accordance with another study made by Sheeley et al. (2000) using another technique.

Height-time diagrams of the July 25th (1999) halo CME

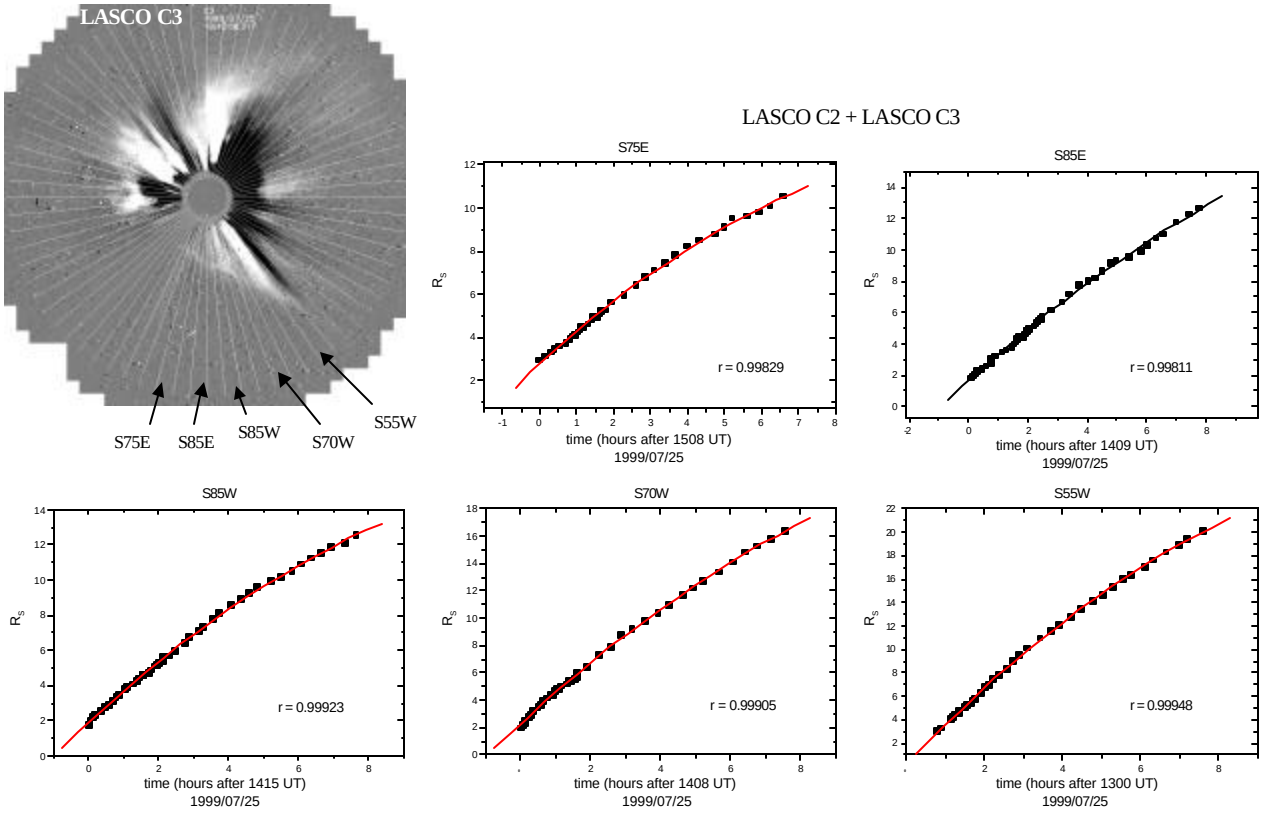

Figure 2 – Heiht-time scatter plots obtained from the bottom images of Figure 1 for the positions S75E, S85E, S85W, S70W and S55W. A second order polynomial fit was added to each of the diagrams.

Summary

Height-time diagrams for the July 25th halo coronal mass ejection were obtained from a new technique which permits easy visualization of radial outward movements in the solar corona.

Height-time images obtained with this technique have shown clearly the halo CME movement for all the chosen positions (S75E, S85E, S85W, S70W and S55W).

The technique, which performs an angular integration in the LASCO images, permitted the visualization of faint structures far in the corona.

Height-time scatter plots obtained from the images were very well fitted by a second order polynomial curve and have revealed a small deceleration in all the chosen directions.

We propose that this technique is appropriated to identify whether there is acceleration or deceleration on halo CMEs near the sun. These measurements can be of extreme importance for the space weather studies, providing a clue to predict the parameters of the CMEs near the earth as well as its travel time to earth.

Table I – Initial and final speeds and acceleration of the positions shown in Figures 1 and 2.

	V_0 (km/s)	V_f (km/s)	a (m/s^2)
S75E	310.49	145.59	-6.48
S85E	336.25	209.76	-4.24
S85W	368.18	175.10	-6.54
S70W	466.31	261.03	-7.06
S55W	649.87	325.69	-12.3

References

Brueckner, G. E.; Howard, R. A.; Koomen, M. J.; Korendyke, C. M.; Michels, D. J.; Moses, J. D.; Socker, D. G.; Dere, K. P.; Lamy, P. L.; Llebaria, A.; Bout, M. V.; Simnett, G. M.; Bedford, D. K.; Eyles, C. J. The large angle spectroscopic coronograph (LASCO). **Solar Phys.** v.162, p.357-402, 1995.

Gosling, J. T. Coronal mass ejections and magnetic flux ropes in interplanetary space. In: Russel, C. T. Priest, E. N. , e Lee, L. C. ed. **Physics os magnetic flux ropes**. Washington, DC: AGU, 1990. v.58, p.343-364.

Howard, R. A.; Michels, D. J.; Sheeley, N. R. Jr.; Koomen, M. J. The observation of a coronal transient directed at Earth, **Astrophys. J.** v.263, p.101-104, 1982.

Hunduhausen, A. J. An introduction. In: Crooker, N.; Joselyn J. A.; Feynman, J. ed. **Coronal mass ejections**, Washington, DC: AGU, 1997. v. 99, p.1-7.

Hundhausen, A. J., Sawyer, C. B., House, L. L., Illing, R. M. E., and Wagner, W. J. **J. Geophys. Res**., **89**, 2639, 1984.

Schwenn, R. An essay on terminology, myths, -and known facts: solar transients – flare – cme – driver gas – piston – BDE – magnetic cloud – shock wave – geomagnetic storm. **Astrophys. J.**, **243**, 187, 1996.

Sheeley, N. R., Hakala, W.N., Wang, Y.M. Detection of coronal mass ejection associated shock waves in the outer corona. **J. Geophys. Res.**, **105**, A3, 5081, 2000.

Acknowledgments

The authors would like to thank FAPESP for the support, under the projects 98/15959-0 and 98/04732-4.

In situ Observation of Electrostatic Waves Associated with Ionospheric Plasma Irregularities

P. . Muralikrishna, L. P. Vieira and M. A. Abdu, Instituto Nacional de Pesquisas Espaciais – INPE/MCT, C. P. 515, 12 201-970, São José dos Campos - SP, Brazil (e-mail: murali@dae.inpe.br)

Abstract

In-situ measurements of the height variation of the ionospheric electric field and electron density variations were made with a rocket-borne electric field double probe and two different types of electron density probes. A Brazilian made SONDA III rocket carrying these experiments in addition to other airglow experiments was launched on 18-th December, 1995 at 2117 hrs (LT) from the equatorial rocket launching station, Alcantara (2,31^{o}S;44,4^{o}W) in Brazil. The rocket reached an apogee altitude of 557km and covered a horizontal range of 589km. Several ground equipments were operated during the launch campaign with the specific objective of knowing the ionospheric conditions at the time of launch and thereby to launch the rocket into an F-region prone to the presence of plasma bubbles. The rocket in fact passed through several medium scale plasma bubbles and the electric field double probe and the electron density probes detected the presence of a wide spectrum of electric field and electron density irregularities. In the base of the F-region the electric field double probe measurements clearly indicated the presence of large amplitude fluctuations, closely associated with large amplitude electron density irregularities But in the height region close to the rocket apogee though the electron density profile showed the presence of large scale spatial structures, the electric field measurements did not show fluctuations of similar amplitude. In the nighttime F-region one would expect the electron density irregularities, if generated by the well-known cross-field instability mechanism, in height regions where the electron density gradient is downward, i.e in the same direction as the ambient Hall electric field. An FFT algorithm was then used to estimate the spectral distribution of the electric field and electron density fluctuations. Some new results on the association of these fluctuations with the plasma bubbles are presented here.

Introduction

In-situ measurements of the height variation of the ionospheric electric field and electron density variations were made with a rocket-borne electric field double probe and two different types of electron density probes. A Brazilian made SONDA III rocket carrying these experiments in addition to other airglow experiments was launched on 18-th December, 1995 at 2117 hrs (LT) from the equatorial rocket launching station, Alcantara (2,31^{o}S;44,4^{o}W) in Brazil. The rocket reached an apogee altitude of 557km and covered a horizontal range of 589km. Several ground equipments were operated during the launch campaign with the specific objective of knowing the ionospheric conditions at the time of launch and thereby to launch the rocket into an F-region prone to the presence of plasma bubbles.

Electron density irregularities present in the ionosphere manifest themselves in different forms at different heights and times. Sporadic-E, spread-F, radio star scintillations and VHF radar echoes are a few of such phenomena, familiar to ionospheric physicists. Basic knowledge of the plasma irregularities, responsible for these phenomena, has progressed considerably, both in theory and observations, since the discovery of the strong VHF radar echoes from the equatorial ionosphere (see Bowles et al 1963 and Balsley, 1969), from their spectral characteristics as observed by the VHF radar, classified the plasma irregularities into two groups, namely Type I and Type II. While the Type I irregularities are now identified to be consistent with the two-stream instability mechanism (Farley, 1963), the Type II irregularities are known to be produced by the nonlinear cross-field instability mechanism (see Rogister and d'Angelo, 1972; Balsley and Farley, 1973). Direct observations by Prakash et al (1970) using rocket-borne Langmuir probes flown from India, confirm the existence of the Type II irregularities in the equatorial E-region. Type II irregularities are characterized by scale sizes extending from a few meters upto tens of kilometers. The short wavelength irregularities apparently seem to be generated from larger scale sizes through nonlinear coupling or cascading processes (see Rogister and d'Angelo, 1972; Sato 1973; Sudan et al 1973). Neutral turbulance also seems to be another probable mechanism responsible for the generation of plasma irregularities (Prakash et al, 1970). The spectral characteristics of the different types of irregularities have been studied in detail (Prakash et al, 1970; Ott and Farley, 1974).

Experiment and Flight Details

The rocket payload designated IONEX-II had the principal objective of measuring the electric field, the electron density, the electron kinetic

temperature and the spectral distribution of plasma irregularities associated with what are known as ionospheric plasma bubbles. The payload consisted of the following experiments in addition to other airglow photometers.

- Electric Field Double Probe (EFP)
- Langmuir Probe (LP)
- High Frequency Capacitance probe (HFC)

The main objective of the EFP was to measure the dc electric field and the fluctuating component of it associated with the ionospheric plasma irregularities. Two spherical electric field sensors were mounted at the extremities of two booms that were deployed after the rocket nosecone was ejected at an altitude of about 65km. Though, in the fully deployed state the separation between the sensors was expected to be more than 3m, the booms did not open fully due to the unexpectedly low spin rate attained by the rocket and the separation between the sensors obtained was only about 1.3m.. This made the already difficult task of obtaining the dc component of the electric field practically impossible. However the ac component of the horizontal electric field were made in the altitude region of about 95 to 557km, the apogee altitude reached by the rocket and are being analysed.

The basic principle of operation, and the details of the electronic subsystem of the LP and HFC experiments are given in Muralikrishna and Abdu (1991). A spherical LP sensor of diameter about 60mm was mounted at the extremity of a short boom of about 50cm in length that remained inside the rocket nosecone. This boom was deployed along with the EFP booms soon after the ejection of the rocket nosecone. A sweep voltage varying from -1V to +2.5V in about 2.5sec. was applied to the LP sensor in order to measure both the electron density and the electron kinetic temperature. The main objective of the HFC probe was to measure the electron density height profile. The HFC sensor was identical to the LP sensor and was mounted also at the extremity of a short 50cm boom kept folded inside the rocket nosecone till the ejection of the nosecone like the LP sensor boom. The sensor formed part of the tank circuit of an electronic oscillator and any change in the sensor capacitance caused by changes in the ambient electron density, is measured through a counting circuit and this information is telemetered to the ground.

Results and Discussion

The electron density profiles estimated for the rocket upleg and downleg are shown in figure 1. The presence of a large number of plasma bubbles can be seen from the profiles. The bubbles seen in the downleg have higher amplitudes than thos seen during the upleg. In the present case the electron density and the electric field fluctuation data have a sampling rate of 1250 per second that decided the lower limit for the measurable scale size. The maximum observable fluctuation frequency is 625Hz. This corresponds to different scale sizes at different height regions beacuse of the continuously changing rocket speed. For example in a height region where the rocket velocity is about 2km per second the LP and EFP experiments could measure the ac fluctuations of wavelength down to about 3,2m. Close to the region of apogee where the vertical component of the rocket velocity is very small the lowest vertical scale size of irregularities that can be measured with the LP and EFP goes down to practically zero

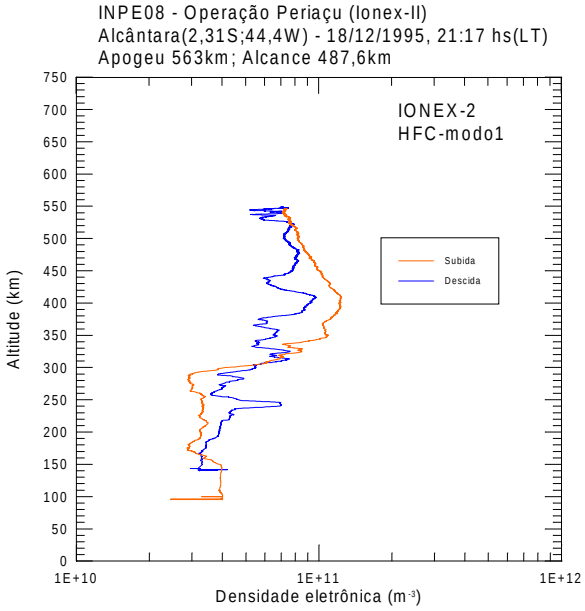

Figure 1: Upleg and downleg electron density profiles showing the presence of a large number of plasma bubbles especially in the downleg profile.

.

It should also be noted here that the E-Filed double probe measurements are modulated by the rocket spin and precession and there exists large base level noise in the fluctuation amplitude indicated. This base level noise can be removed by passing the E-field fluctuation data through appropriate band *pass* filters. However the existence of fluctuations with amplitudes higher than the base level noise can be clearly seen both in the electron density and the elctric field.

An FFT algorithm was then used to estimate the spectral distribution of the electric field and electron density fluctuations. Typical electron density and electric field spectra observed at different height regions during the rocket ascent are presented in figures 2 and 3.

A close look at the figures 2 and 3 which represent samples of the k spectra observed in the electron density variations and in the fluctuations in the elcteric field component perpendicular to the rocket axis, clearly shows the presence of corresponding peaks in the k spectra of electron density and electric field fluctuations. Similar features were observed in the downleg profile also. The presence of several plasma bubbles of varying amplitudes can be seen in both the upleg and downleg profiles.

Waves in general can be classified into two groups based on their fundamental properties:. electrostatic waves and electromagnetic waves

.

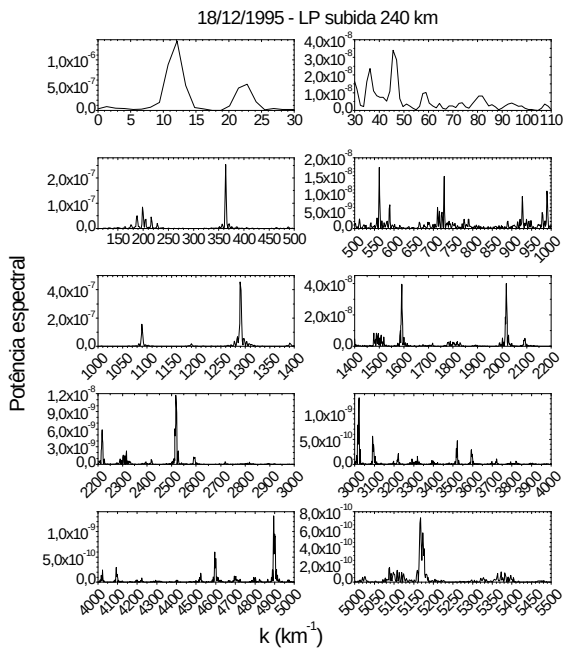

Figure 2: Spectral distribution of electron density irregularities in the height region around 240km.

Electrostatic waves are not associated with magnetic field fluctuations, and thereby may be derived from a scalar potential. Their amplitude $\delta\mathbf{E}$ is parallel to their wave vector **k**, (i.e., $\mathbf{k}\times\delta\mathbf{E} = 0$). These waves are associated with corresponding density oscillation component, δN. Electrostatic plasma waves and structures are important in space plasma because they transport and dissipate free energy, scatter electrons and ions, heat the thermal plasma population, transform ambient plasma gradients, and modulate current systems. Electromagnetic waves are associated with both electric and magnetic field variations. Electromagnetic plasma modes provide signatures of processes that often occur at larger distances from a spacecraft. Examples include *whistlers* created when lightning-induced electric field pulses penetrate the ionosphere and *auroral hiss* created when electrons are accelerated along magnetic field lines at high latitudes.

Electrostatic waves in the Earth's ionosphere exist over a large range of wavelengths, from centimetres to hundreds of kilometres, and over a large range of phase velocities, from quasi-static to speeds of hundreds of kilometres per second. Because of the motion of the spacecraft relative to ambient plasma, even quasi-static waves appear as temporal fluctuations in the spacecraft frame.

.

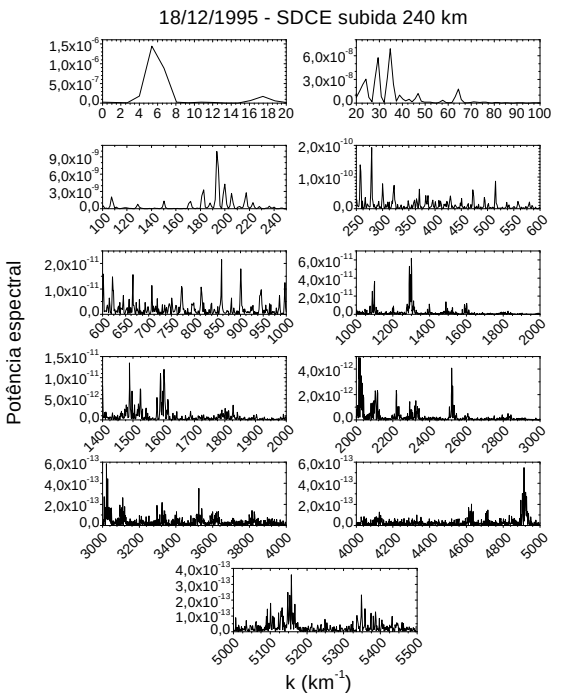

Figure 3: Spectral distribution of electric field fluctuations in the height region around 240km.

The present observation of electrostatic waves in the ionosphere clearly shows that electric field double probes can also be used to detect δ**E** fluctuations associated with electrostatic waves. Although both spherical and cylindrical sensors can be used to detect these waves, in general, double probes that employ spherical sensors are better suited for detecting electrostatic modes, particularly for low frequency, short scale waves. To determine the

instantaneous vector $\delta\mathbf{E}$ components from three orthogonally oriented double probes must be obtained simultaneously.

In the present case the rocket in fact passed through several medium scale plasma bubbles and the electric field double probe and the electron density probes detected the presence of a wide spectrum of electric field and electron density irregularities. In the base of the F-region the electric field double probe measurements clearly indicated the presence of large amplitude fluctuations, closely associated with large amplitude electron density irregularities But in the height region close to the rocket apogee though the electron density profile showed the presence of large scale spatial structures, the electric field measurements did not show fluctuations of similar amplitude. In the nighttime F-region one would expect the electron density irregularities, if generated by the well-known cross-field instability mechanism, in height regions where the electron density gradient is downward, i.e in the same direction as the ambient Hall electric field. Observation of bubble structures in the nighttime ionosphere is rather a familiar feature. The generation of large scale plasma irregularities by the mechanism of cross-field instability is now reasonably well understood (Reid, 1968; Tsuda et al., 1969). A necessary condition for the mechanism to operate is that there should exist an electron density gradient in the direction of the ambient electric field. In the nighttime ionosphere the Hall polarisation electric field is generally downwards and so the height regions favorable for the operation of the C-F instability mechanism are those where the ambient electron density gradients are downwards. Presence of large bubble structures in the bottom side F-region where the E-field is supposed to be downwards and the electron density gradient is upwards cannot be attributed to the operation of the cross-field instability mechanism. However, small scale plasma irregularities can be generated in the region of downward electron density gradients associated with the large scale bubbles..

CONCLUSIONS

- Bubble regions are associated with both electron density and electric field fluctuations.
- The electric field fluctuations are associated with electrostatic waves and thereby are associated with similar fluctuations in the ambient electron density.

Spectral analysis of the ac data is being under taken and slected height regions and their association with the various bubble regions is also being studied in detail. It is expected to give valuable information about the plasma instability mechanisms operating, among which the cross-field instability mechanism seems to be a definite one confirming the earlier observations. It should be noted here that the information that one gets from looking up at the phase relationship between fluctuating data is lost when one does the spectral analysis.

REFERENCES

Abdu, M. A.; P. Muralikrishna; I. S. Batista and J. H. A. Sobral, Rocket observation of equatorial plasma bubbles over Natal, Brazil using a High Frequency Capacitance probe, J. Geophys. Res., **96**, 7689-7695, 1991.

Balsley, B. B., Some characteristics of non-two-stream irregularities in the equatorial electrojet, J. Geophys. Res., **74**, 2333-2347, 1969.

Balsley, B. B. and D. T. Farley, Radar observation of two dimensional turbulence in the equatorial electrojet, J. Geophys. Res., **78**, 7471-7479, 1973.

Farley, D. T., Two stream instability as a source of irregularities in the ionospheres, Phys. Rev. Lett., **10**, 279-282, 1963.

Muralikrishna, P. and M. A. Abdu, In-situ measurement of ionospheric electron density by two different techniques - a comparison, J. Atmos. Terr. Phys., **53**, 787-793, 1991.

Ott, E. and D. T. Farley, The k spectrum of ionospheric irregularities, J. Geophys. Res., **79**, 2469-2472, 1974.

Prakash, S.; S. P. Gupta and B. H. Subbaraya, A study of irregularities in the nighttime equatorial E-region using a Langmuir probe and a plasma noise probe, Planet. Space Sci., **18**, 1307-1318, 1970.

Reid, G. C., Small scale irregularities in the ionosphere, J. Geophys. Res., **73**, 1627-1640, 1968.

Rogister, A., Nonlinear theory of cross-field instability with application to the equatorial electrojet, J. Geophys. Res., **77**, 2975-2981, 1972.

Rogister, A. and N. D'Angelo, On the origin of small scale Type II irregularities in the equatorial electrojet, J. Geophys. Res., **77**, 6298-6299, 1972.

Sato, T., A unified theory of Type I and II irregularities in the equatorial electrojet, J. Geophys. Res., **78**,2232-2243, 1973.

Tsuda, T.; T. Sato and S. Matsushita, Ionospheric irregularities and cross-field plasma instability, J. Geophys. Res., **74**, 2923-2932, 1969.

Influência de Marés Atmosféricas na Intensidade da Aeroluminecência Equatorial do OI557,7 nm e O_2(0,1)

R.A. Buriti (1); H. Takahashi (2); D. Gobbi (2)
(1) – Departamento de Física, UFPB, CEP 58109-970, Campina Grande, PB, Brasil
(2) *– INPE, CEP 12201-970, S. J. dos Campos, SP, Brasil*

Resumo

Os estudos da influencia de marés atmosféricas nas emissões de vários constituintes mesosféricos, tem revelado a presença de oscilações com períodos de 12 e 24 horas como predominantes. Estudos das variações noturnas de airglow OI557,7 nm e O_2(0,1) atmosférico têm mostrado que estas oscilações diurnas (24 h) e semi-diurnas (12 h) apresentam mudanças tanto na fase como na amplitude a cada período de estação do ano e que também depende da latitude goegráfica local. Nosso trabalho consistiu em analisar amplitudes e fases de ajustes matemáticos com períodos de 12 e 24 horas nas variações de intensidade médias mensais do I5577 e IO2. Trabalhamos com resultados cuja correlação entre o ajuste e a média mensal da intensidade relativa da emissão observada, ficou acima de 0,9. Nossos estudos, que envolveram observações na região equatorial ($7,4^0$S; $36,5^0$O) nos anos de 1998 e 1999, com um total de 300 noites de aquisição de dados, mostraram que nem sempre o comportamento destas emissões variam de modo semelhante durante todo ano, mas sim, dentro de 3 ou 4 períodos (meses) sequenciais. As componentes diurna e semi-diurna do IO2 corresponderam, em média, a cerca de 70% daquelas para o I5577. Isto significa que o I5577, cujo pico de emissão está a aproximadamente 6 km acima do pico do IO2, é mais influenciado pela dinâmica devido às marés.

Introdução

Vários estudos sobre a dinâmica da alta atmosfera têm revelado que as marés atmosféricas e as ondas de gravidade são os principais mecanismos que influenciam o comportamento temporal e sazonal das emissões de airglow do OI557,7 nm, O_2 (0,1), NaD e OH. Porém, apesar da origem destas emissões estarem concentradas em altitudes entre 80 e 100 km, o comportamento sazonal destas emissões tem apresentado respostas distintas aos processos que influenciam tais variações. É sabido que o mecanismo de emissão do OI557,7 nm e O_2(0,1), por exemplo, são semelhantes, mas, medidas de airglow têm mostrado que, em muitas situações, seus comportamentos são distintos. O pico de emissão do OI557,7 nm (OI5577) está em torno de 97 a 98 km de altitude, enquanto que, o pico de emissão do $O_2(b^1\Sigma_g)$ atmosférico banda (0,1), está em torno de 92 km. É provável que esta pequena diferença de altitude seja responsável por estes comportamentos, muitas vezes, distintos entre estas emissões. Além disso, esta região da atmosfera é rica em acontecimentos que influenciam os comportamentos destas emissões, tais como, quebra de ondas de gravidade, cisalhamento do vento e inflexão do perfil de temperatura. Estudos comparativos entre dados de região de baixa latitude e região equatorial têm revelando que variações diurnas são predominantes na região equatorial enquanto que, as variações semi-diurnas são predominantes nas regiões de baixa latitude (Takahashi et al., 1998, Buriti et al., 2000a).

Observações

Neste trabalho foram utilizados dados obtidos por um fotômetro multicanal instalado na região equatorial ($7,4^0$S; $36,5^0$O). Este fotômetro tem 5 filtros de interferência e mede a intensidade absoluta zenital da emissão do oxigênio atômico (OI557,7 nm e OI630 nm), O_2(0,1), OH(6,2) e NaD. Takahashi et al., 1989 descreve com detalhes este fotômetro cujos dados foram utilizados neste trabalho. O *back-ground* correspondente a cada emissão é obtido através da inclinação do respectivo filtro. Os dados de intensidade absoluta do airglow do OI557,7 nm mesosférico e O_2(0,1) são referentes aos anos de 1998 e 1999, correspondendo assim, um total de 300 noites de observação. Os dados foram tratados com a finalidade de retirar pontos considerados espúrios. Para cada período de observação, que equivale a 13 noites em torno da lua nova, foi obtida uma média da intensidade e, em seguida, o valor relativo da intensidade de emissão em função da hora local. Alguns períodos apresentaram, por um intervalo de tempo relativamente curto, comportamentos diferentes da tendência daquele período considerado. Tal fato deve-se a pequena quantidade de medidas durante vários dias, dentro de um período de observação, num determinado intervalo de hora local de aquisição de dados. Porém, este comportamento, de intervalo de tempo pequeno com relação comprimento da série completa, não tem influencia nos nossos resultados. O comportamento da intensidade do OI557,7 nm e do O_2(0,1) de 1998 e 1999 encontra-se mostrado na Figura 1. Podemos ver que os dados de IO2 de 1998 e 1999 apresentam

padrões de oscilações não esperado para uma média de 13 noites. Isto está claro principalmente, por exemplo, nos meses de janeiro, novembro e dezembro de 1998. A razão para isto é a pouca quantidade de dados nestes períodos observados. A forte dependência da intensidade com a hora local e a estação do ano, como podemos ver na Figura 1, pode ser devido à altura da camada de emissão e a ventos rico em oxigênio (Shepherd et al., 1995).

A Figura 1 mostra que existe um comportamento do OI557,7 nm e do $O_2(0,1)$ semelhante na maioria das vezes, entre períodos (13 noites de observação em torno da lua nova) iguais para os dois anos estudados. Isto é um forte indício da regularidade da sazonalidade do airglow. Alguns meses, porém, apresentam diferenças principalmente com relação à fase. Os meses de abril e julho é um bom exemplo deste comportamento para ambas as emissões.

A média mensal noturna das intensidades do OI557,7 nm e $O_2(0,1)$ durante o ano de 1998 e 1999 mostraram variação mensal semelhantes em vários períodos de observação. No ano de 1998, o OI5577 e o IO2 apresentaram variações mensais iguais, enquanto que o ano de 1999, o comportamento de ambas as emissões foram idênticos entre junho e dezembro. A intensidade média do IO2, por outro lado, sempre mostrou uma tendência de aumento durante o ano de 1999. A Figura 2 mostra a média mensal para ambas as emissões. Análises realizadas anteriormente (Buriti et al., 2000b) mostraram que a intensidade média mensal do OI5577 e do IO2 para o ano de 1998 apresentaram uma forte dependência sazonal com período de 6,6 e 7 meses, respectivamente. Este fato pode ser visto na Figura. 2, porém, o mesmo não aconteceu no ano seguinte.

Resultados e Discussão

A análise dos dados consistiu em determinar a amplitude e a fase da função de ajuste da média mensal do OI557,7 nm e do $O_2(0,1)$ além de realizar comparações entre estas emissões. As funções de ajustes são formadas por períodos de 12 e 24 horas, onde suas respectivas amplitudes e fases são determinadas matematicamente. A correlação entre cada curva de ajuste e a respectiva série de dados foi considerada neste trabalho porque ela fornece informações de quão próxima a curva de ajuste está da série observada. Ambas as emissões apresentaram correlação acima de 0,9 para os meses de fevereiro a outubro de 1998 e entre abril e novembro de 1999. A função que descreve o ajuste é:

$$A(t) = A_{12}\cos(2\pi t/12 - \Phi_{12}) + A_{24}\cos(2\pi t/24 - \Phi_{24})$$

onde A e Φ representam a amplitude e a fase relativa à cada período preestabelecido. Como trabalhamos com valores relativo, a média de cada série é muito próxima de zero.

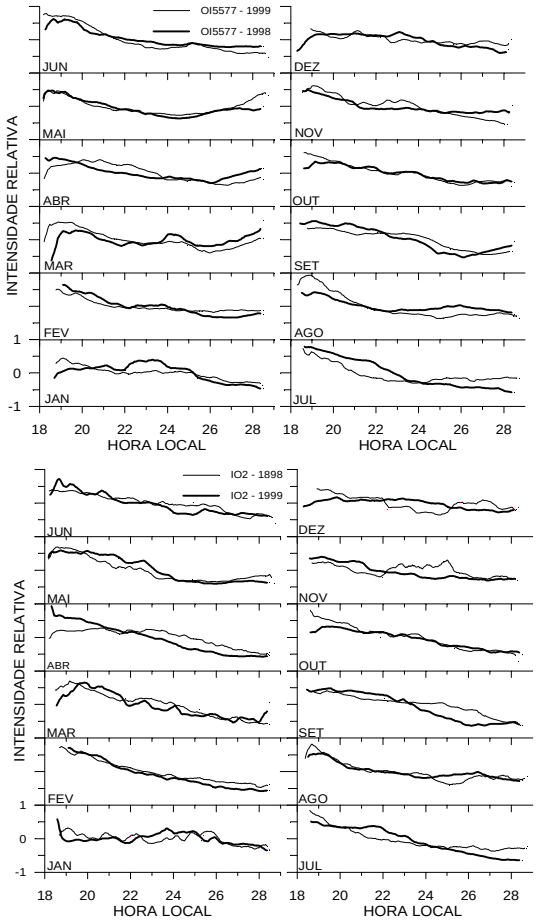

Fig. 1 – Média mensal noturna da intensidade do airglow do OI5577 (acima) e IO2 (abaixo) para os anos de 1998 (linha fina) e 1999 (linha grossa).

A Figura 3 mostra o comportamento das amplitudes de 12 e 24 horas para cada média noturna mensal observada. Estas amplitudes foram obtidas a partir dos resultados das curvas de ajustes com períodos de oscilação de 12 e 24 horas. Para o OI5577, de maneira geral, a amplitude de 12 horas teve um comportamento, durante estes dois anos, semelhante ao de 24 horas, porém, com cerca de 1/3, em média, do valor da amplitude de 24 horas. Em alguns meses, entretanto, enquanto a amplitude de 24 horas decresceu, a amplitude de 12 horas cresceu. Uma variação pronunciada da amplitude de 24 horas

ocorreu entre novembro de 1998 e abril de 1999. Não podemos associar este comportamento ao aumento da intensidade do OI5577 no final de 1998, pois, a intensidade volta a cair em dezembro de 1998 e permanece quase constante até agosto de 1999 (ver Figura 2). Devemos lembrar que estes meses apresentaram correlação menor que 0,9 e que o erro da amplitude de 24 horas, para este período, foi de 0,12, enquanto que nos outros meses, onde a correlação cruzada ficou acima de 0,9, o erro ficou em torno de 0,07.

As amplitudes de 12 e 24 horas para o IO2 também se comportaram de maneira semelhante. Exceções ocorreram para os meses de janeiro a junho de 1998, onde, enquanto a amplitude de 24 horas decresceu de valor, a de 12 cresceu e vice-versa. De

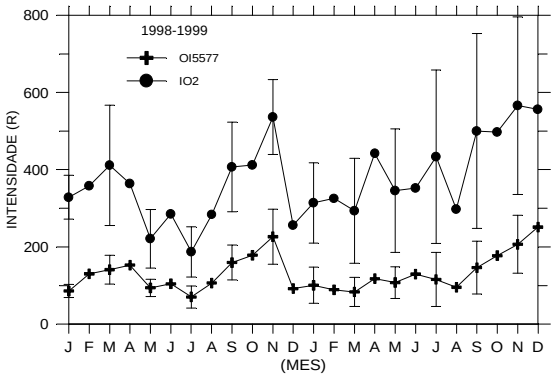

Fig. 2 – Média mensal das intensidade do OI5577 e IO2 para os anos de 1998-1999 no Cariri. As barras de erro foram colocadas em apenas em alguns pontos.

modo semelhante ao OI5577, a amplitude de 24 horas também apresentou valores superiores a de 12 horas. Isto pode ser uma evidencia do predomínio da maré diurna na região equatorial.

Em muitos períodos, as amplitudes apresentaram valores maiores do que 1. Isto não problema, pois, como procuramos os parâmetros que melhor se ajusta ao valor observado, pode, neste caso, resultar em amplitudes acima de 1 para qualquer um dos períodos. Caso tivéssemos escolhido um ajuste que levasse em conta apenas 1 período de oscilação, por exemplo, 24 horas, não poderíamos obter amplitude para este ajuste maior que 1.

A obtenção da fase de cada período é importante porque permite determinar onde as emissões apresentaram um valor máximo (ou mínimo) de intensidade relativa àquele período de oscilação. Para isto, é necessário conhecer a hora local quando começou a série de dados. Se a fase é zero significa que o máximo de intensidade ocorre exatamente no início da série.

As fases relativa à 12 horas de vários meses apresentaram valores positivo significando que o máximo ocorreu depois do início das observações. Entre os meses de outubro 1998 e abril de 1999, excluindo dezembro, por exemplo, a fase foi de ~150^0, ou seja, o máximo da componente semi-diurna

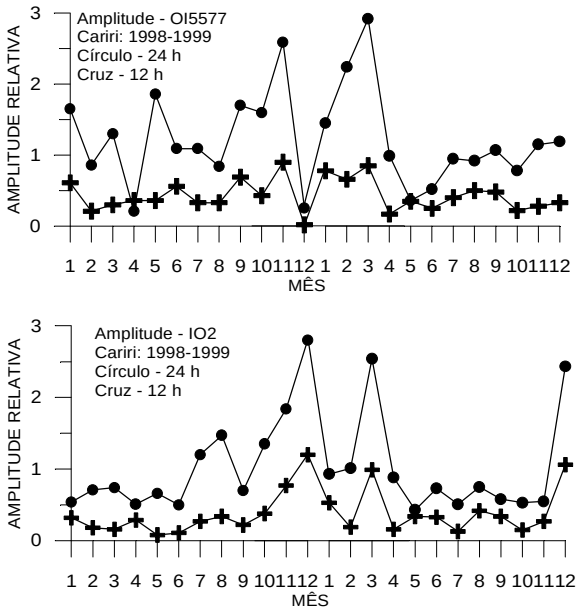

Fig. 3 – Comportamento da amplitude de 12 e 24 horas para o OI5577 (acima) e IO2. Os valores foram obtidos da curva de ajuste com períodos de 12 e 24 horas.

ficou próximo de 4:00 horas da manhã. No caso da componente diurna (24 horas) os máximos ocorreram próximo do meio-dia local. Para o IO2, as fases de 12 e 24 horas oscilaram entre os meses dos anos de 1998 e 1999. Isto dificulta estabelecer um padrão de variação sazonal. Porém, é fácil notar que no ano de 1998, o máximo do período diurno ocorreu antes das 18:00 horas, fato que não ocorreu com frequência no ano de 1999. Os máximos da componente semi-diurna prevaleceram antes do início das observações até setembro de 1998 e em seguida, ficou mais frequente após o início das observações.

Conclusão

A obtenção de parâmetros das funções de ajuste com períodos fixados em 12 e 24 horas, referentes a marés semi-diurna e diurna, na média mensal noturna do OI557,7 nm e $O_2(0,1)$ atmosférico, mostrou que não

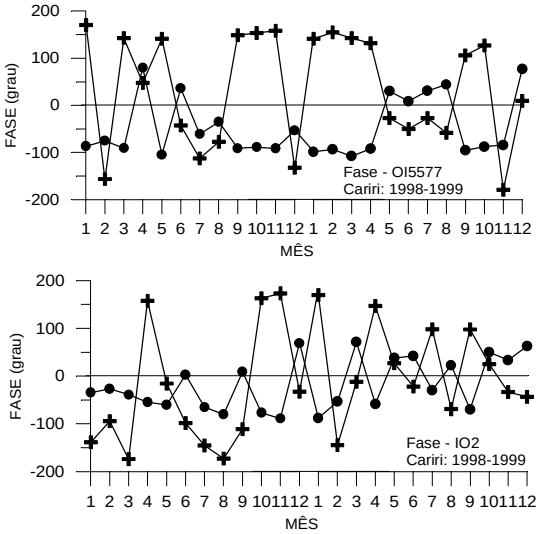

Fig. 4 – Comportamento da fase de 12 e 24 horas para o OI5577(acima) e IO2. Os valores foram obtidos do ajuste com períodos de 12 e 24 horas. Os círculos cheios e as cruzes representam a fase de 24 e 12 horas, respectivamente.

existe um padrão de variação sazonal destas emissões. As amplitudes de 12 e 24 horas, mostraram comportamentos semelhantes paras ambas as emissões. Isto é esperado pois o mecanismo de excitação são parecidos. A amplitudes de 24 horas mostrou-se predominante o que pode indicar uma participação maior de maré diurna como responsável pela variação noturna. Tanto a fase relativa ao período semi-diurno como diurno, não apresentou comportamento sazonal, principalmente para o IO2. Com relação as fases do OI557,7 nm, verificou-se que, entre setembro de 1998 e abril de 1999 não houve variação significativa, contrário do que aconteceu com o $O_2(0,1)$.

Referência

Buriti, T. A., H. Takahashi, D. Gobbi. Temporal variation of the volume emission rates between OI5577 and $O_2(0,1)$. *Adv. Space Sci.* Submetido em 2000a.

Buriti, T. A., H. Takahashi, D. Gobbi. First mesospheric airglow observation results from 7.5 S. *Brazilian Journal of Geophysics* – Submetido em 2000b.

Shepherd, G. G., C. McLandress and B. H. Solheim. Tidal influence on $O(^1S)$ airglow emission rate distributions at the geographic equator as observed by WINDII. *Geophy. Res. Letter*, 22, 3, pp. 275-278, 1995.

Takahashi, H., Y. Sahai, B.R. Clemesha, D.M. Sinomich, N.R. Teixeira, R.M. Lobo, and A. Eras. Equatorial mesosphereric and F-region airglow emissions observed from latitude 4 South. *Planet. Space Sci.*, *37*(6), 649-655, 1989.

Takahashi, H., D. Gobbi, P. P. Batista, S. M. L. Melo, N. R. Teixeira, R. A. Buriti. Dynamical influence on the equatorial airglow observed from the south american sector. *Adv. Space Res.*, 21, 6, pp. 817-825, 1998.

Agradecimentos

Somos gratos a Prefeitura de S. J. do Cariri pelo apoio ao nosso trabalho e ao operador Sr. J. A. Souza. O Observatório é apoiado financeiramente pela Universidade Federal da Paraíba (UFPB), Instituto Nacional de Pesquisas Espaciais (INPE) e FINEP Pronex No. 76.97.1079.00.

Investigating the Dynamics of the Earth's Middle Atmosphere Using the CEDAR Mesospheric Temperature Mapper

by

M.J. Taylor, W.R. Pendleton Jr., and L.C. Gardner
Space Dynamics Laboratory and Physics Department
Utah State University, Logan, Utah, USA

C.Y. She,
Department of Physics, Colorado State University,
Ft. Collins, Colorado, USA.

and

H.L. Liu, and R. G. Roble, NCAR, Boulder, Colorado, USA

The CEDAR Mesospheric Temperature Mapper (MTM) is a versatile CCD imager that was designed to investigate the properties of short period (<1hour) atmospheric gravity waves as they propagate through the earth's upper mesosphere. The imager samples two selected emission lines in the hydroxyl OH M (6,2) band emission (peak altitude ~87 km) to determine nocturnal temperature and wave-induced intensity and temperature perturbations with high precision. In addition the MTM has also proven to be exceptionally capable of studying much larger scale wave perturbations of tidal and planetary wave origin. To date, observations have been made at mid-latitudes alongside two powerful Na lidar systems: at Ft. Collins, CO (June 1997-May-1998) and at the Starfire Optical Range, NM (November 1998 – January 2000). However, an enhanced MTM system will shortly be deployed at Haleakala Crater, Maui, HI for low-latitude studies as part of the MAUI-MALT program. The potential of this imaging system for investigating short-term, wave-induced, and seasonal dynamics within the Mesosphere and Lower Thermosphere (MLT) region (~80-100 km) will be discussed with reference to recent measurements of terdiurnal (8-hr) tidal oscillations in OH intensity and rotational temperature and the unexpected detection of a large-scale, recurrent perturbation in mesospheric temperature around the autumnal equinox period associated with the penetration of planetary wave energy from the troposphere into the mesosphere. Plans for coordinated ground-based measurements using the MTM (and other instrumentation) during the forthcoming NASA TIMED satellite mission will also be discussed.

IONOSPHERIC SCINTILLATIONS AT EQUATORIAL AND LOW LATITUDES IN INDIA

K.N.IYER[1], M.A.ABDU[1], J.R de SOUZA[1], M. N.JIVANI,[2] and B.M.PATHAN[3]

1 Instituto Nacional de Pesquisas Espaciais,Sao Jose dos Campos,SP, Brazil

2 Department of Electronics,Saurashtra University, Rajkot,India

3 Indian Institute of Geomagnetism, Mumbai, India

Abstract:

Ionospheric scintillations are one of the manifestations of plasma irregularities generated in the post-sunset equatorial ionosphere by various instability mechanisms. Scintillations at VHF(250 MHz) from FLEETSAT satellite at 73° E were recorded at a number of stations extending from the geomagnetic equator to the crest of the equatorial anomaly and beyond in India during 1987 to 1993 covering solar minimum to maximum and beyond. The paper describes the results of nocturnal variation, seasonal , solar and magnetic activity dependence of the scintillation occurrence and the latitudinal width of the scintillation belt. Their association with spread F and the irregularity parameters derived by spectral analysis will be reported. The zonal plasma drift velocity derived from spaced receiver scintillation measurement is discussed. An attempt to model the occurrence and intensity of scintillation will be described.

Introduction:

Fluctuations in electron density, with spatial scale sizes ranging from 10s of cm to 100s of km, known as ionospheric irregularities are usually present in the post-sunset equatorial ionospheric F region. These are responsible for spreading of the echo trace in ionograms and hence the name Equatorial Spread-F (ESF). ESF is often associated with plasma depleted flux tubes,called plasma bubbles, produced by the generalised Rayleigh –Taylor gravitational fluid instability mechanism followed by cascading process through secondary instability mechanisms,giving rise to the broad spectrum of their scale sizes.

The wide variety of techniques utilized for observing the different scale size domains include: ground based ionosondes (Chandra and Rastogi,1972, Abdu et.al,1998), satelliteborne topside sounders (Calvertand Schmid,1964,Pulinets,1989), scintillation of trans-ionospheric VHF/UHF/GHz signals(Aarons,1977,Das Gupta et.al,1982, Pathak et. al 1995), VHF backscatter radar plumes(Woodman and La Hoz,1976, Tsunoda,1980, Kelley et.al, 1985, Patra et.al 1995), and in-situ measurements(Hanson and Sanatani,1973,Young et.al 1984,Prakash et.al,1991). Scintillation technique has been extensively used in the Indian equatorial zone(Rastogi et.al,1977,Chandra et al,1979, Krishnamoorthy et.al,1979) and near the anomaly crest(Rastogi et.al, 1990,Pathan et.al,1992, Mathew et.al,1992). In this paper,results of long term VHF scintillation measurements of Fleetsat (73° E) signals at a chain of stations in India are reported.

Data Base used :

For the present investigation, data of ionospheric scintillation of signals at 250 MHz, from the FLEETSAT satellite positioned at 73° E longitude recorded at the magnetic equatorial station, Trivandrum (subionospheric point:7.8° N, 75.8° E geogr. ,0.6° S mag. Lat.) and the equatorial anomaly crest station (sub ionospheric point:22.1° N,72.3° E geogr.,16.8° N mag.lat.) during the period 1987-1993 are used. Data from other stations in thechain are also used for specific periods. For comparison with spread –F occurrence, ionosonde data of Kodaikanal(10.2°N,77.5°E geogr.,1.7° N mag.lat.) and Ahmedabad (23.1°N,72.6° E geogr.,18.6° N mag.lat.) are also used. From the analogue recording of the satellite signal, mean occurrence percentage of scintillations >0.5 dB for each hour of each month is computed and the monthly mean percentage occurrence of spread-F is obtained from published ionospheric data.

Results and Discussion:

The contour plots of scintillation occurrence on a local time of night vs month grid are shown in fig.1 for the equatorial and anomaly crest stations for the years 1987 through 1989 with annual mean Zurich sunspot number 30,100 and 160 respectively. Scintillation occurrence is found to have mainly pre-midnight peak during equinoxes and a secondary peak during midnight to post-midnight period in summer at equatorial latitudes. The occurrence in all seasons increases with solar activity.At anomaly crest location, in the low solar activity year1987, the occurrence peaks during midnight in summer, the magnitude of which decreases with increasing solar activity. As the solar activity increases,the equinoxial peaks during premidnight period befin to appear and its magnitude increases with solar activity.

During equinox of high sunspot years the conditions favourable for Rayleigh-Taylor instability generation exist in the post sunset equatorial F region. This suggests that the premidnight scintillations are caused by plasma irregularities produced at the magnetic equator, by this mechanism,which rise under the ExB drift to sufficient altitudes and diffuse along the field lines to anomaly crest latitudese only during high solar activity conditions. The plasma instability mechanism responsible for irregularity generation during summer may be different at equator and low latitudes. The effect of magnetic activity is to suppress

scintillation in all seasons except during summer post- mid-night period of low solar activity period.

The width of the equatorial scintillation belt, as estimated from multistation measurements, varies during the course of the night.(Chandra et.al,1993) Pre-midnight scintillations are found to be associated with range type of spread F on ionograms while post-midnight scintillations are associated with frequency type spread F. The irregularity parameters are derived from the spectral analysis of high time resolution digital data.

The power spectrum (Fig.2) typically shows an upper roll of frequency,which can be related to the Fresnel size of the irregularity spatial scale, and a power law index(slope) ranging from –2 to –4. The fade rate, upper roll off frequency, S_4 index(intensity of scintillation), and spectral slope ,all vary with time of the night ,as shown in Fig.3, the physical interpretation of which will be discussed.Employing spaced receiver scintillation measurements and using cross correlation analysis the zonal plasma drift velocity is estimated and compared with values obtained by other techniques. The zonal drift velocity is found to decrease with the time of night and also with magnetic activity thereby revealing its electric field control.

An empirical model based on cubic spline method is developed to describe the scintillation occurrence. The intensity of scintillation expressed in SI(dB) is compared with the empirical model of Aarons (1985) and the S_4 index is compared with WBMOD model (Secan et.al.1995)based on an irregularity environment and propagation definition.

.

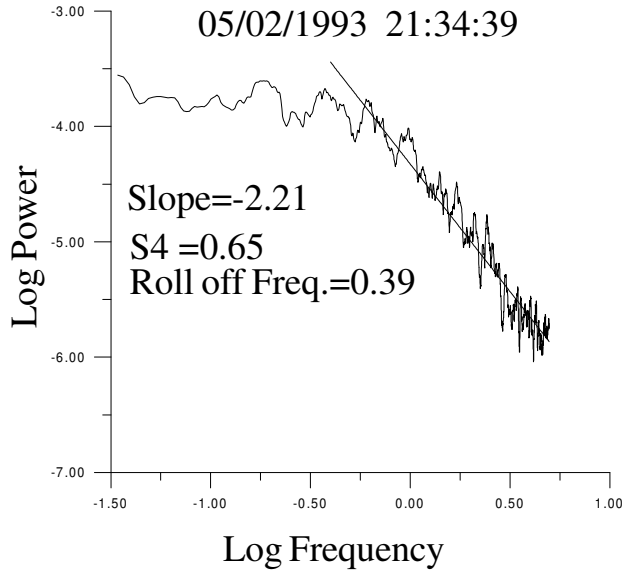

Fig.2: Typical Power Spectrum

Conclusions:

1.Scintillation characteristics differ at equator and anomaly crest locations in the Indian region.

2.The spectral parameters vary with time of the night.

3.The zonal plasma drift velocity derived from spaced receiver scintillation measurement at Rajkot varies from ~150 m/s at 21 hrs to ~80 m/s at 02 hrs,consistent with measurements by other techniques.

4.An empirical model for scintillation occurrence is developed

Acknowledgements:

One of the authors,KNI ,is thankful to CNPq for providing a visiting scientistship at INPE under processo 301213/00-3 and to Saurashtra University for providing sabbatical leave.

References:

Aarons J, IEEE Trans.,Antenna Prop.,**25**,429,1977

AbduM.A.,J.H.A.Sobral,I.S.Batista,V.H.Rios,C.Medina,Adv. Space Res.,**22**,851,1998

Calvert W.and Schmid C.H.,J Geophys.Res.,**69**,1839,1964

Chandra H. and Rastogi R.G.,Ann. Geophys.**28**,37,1972

Chandra H.,Vats H.O.,Sethia G.,Deshpande M.R.,Rastogi R.G., Sastri J.H. and Murthy B.S., Ann. Geophys., **35,** 145, 1979

Chandra H et.al., Indian J Radio Space Phys. **22**,69,1993

Das Gupta A, J. Aarons, J.A.Klobuchar, Su Basu, A. Bushby, Geophys. Res. Lett.**9**,147,1982

Hanson W.B.and SanataniS.,J.Geophys.Res.**78**,1167,1973

Kelley M.C., J Atmos.Terr.Phys., **47**, 745, 1985

Krishnamoorthy K, Raghava Reddy C and Krishnamurthy B.V., J Atmos. Terr. Phys.**41**,123,1979

Mathew Boby, Iyer K.N., and Pathan B.M.,Indian J. Radio space Phys.,**21**, 237 1992

Pathak K.N.,R.D.Jivrajani,Boby Mathew,H.P.Joshi and K.N.Iyer,Indian J.Radio Space Phys.,**24**,138, 1995

Pathan B.M., Rastogi R.G., and Rao D.R.K., J Geomagn Geoelectr., **44**,129, et.al, 1992

Patra A.K.,V.K. Anandan, P.B.Rao and A.R.Jain, Radio Sci., **30**, 1159, 1995

Prakash S.,Pal S. and Chandra H, J Atmos. Terr. Phys., **53**, 977, 1991

Pulinets S.A.,WITS Handbook, No2, Chapter 3, SCOSTEP Publ, Urbana, Illinois, p99,1989

Rastogi R.G.,Deshpande,M.R.,Vats H.O.,Davies K,and Grubb R.N., Pramana, **8**, 1, 1977

Rastogi R.G.,P.V.Koparkar,and B.M.Pathan,J.Geomagn. Geoelectr.,**42**,1,1990

Tsunoda R.T., J . Atmos.Terr.Phys., **42**, 743, 1980

Woodman R.F.and LaHoz C,J.Geophys. Res., **81**, 5447,1976,

Young E.R.,W.J.Burke,F.J.Rich and R.C.Sagalyn, J Geophys. Res.,**89**,5565, 1984,

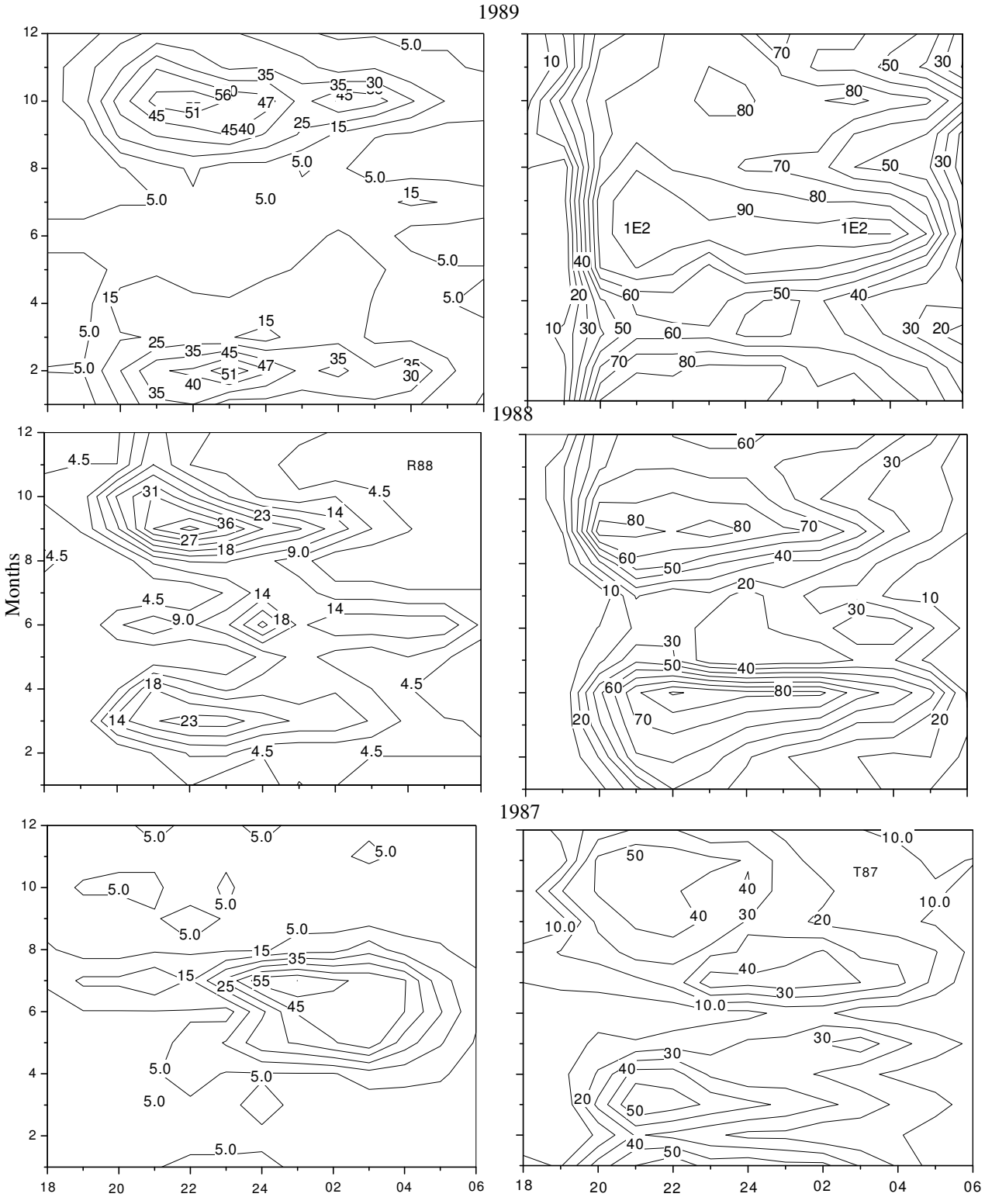

Fig.1 Contours of Scintillation occurrence

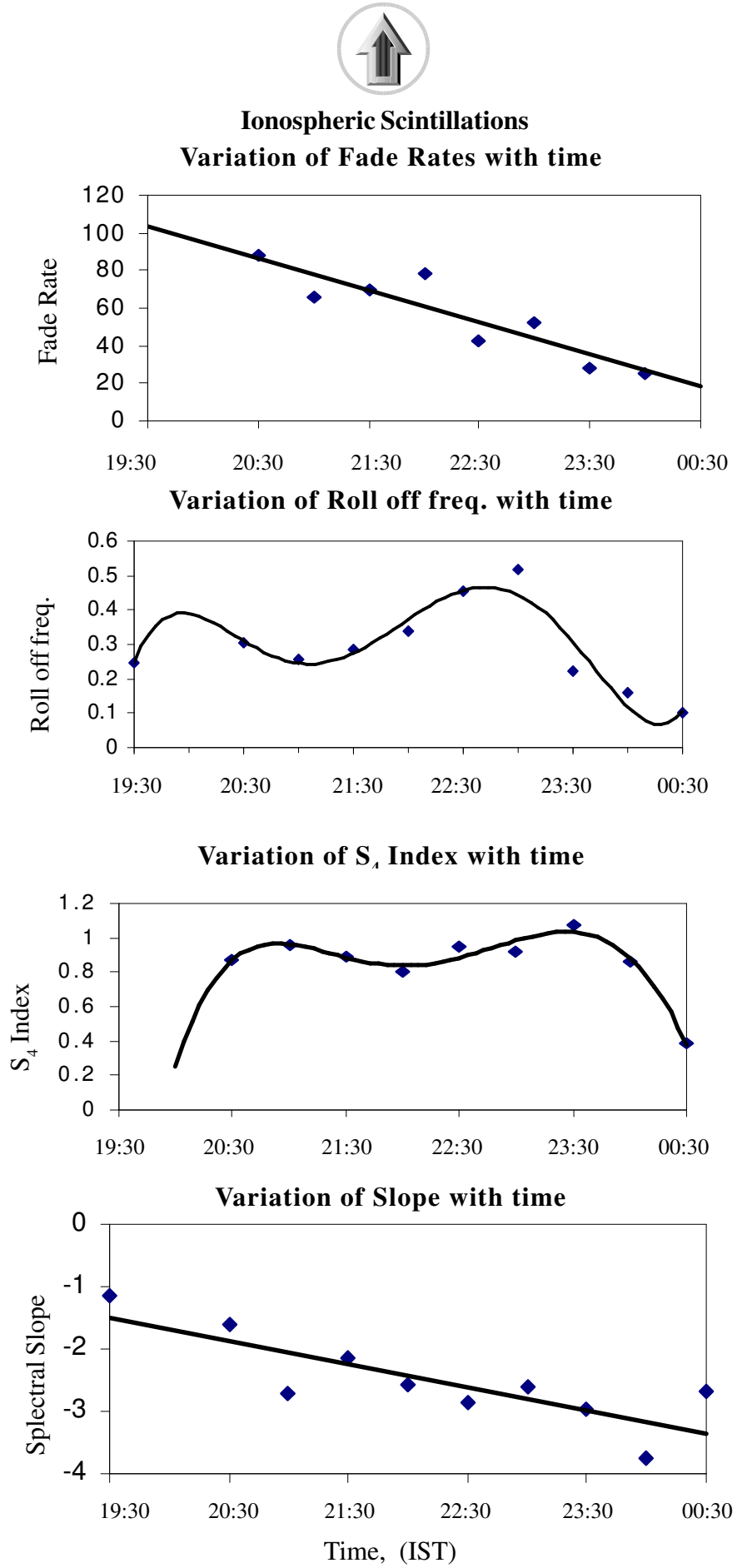

Fig. 3 Variation of scintillation parameters with the time of the night for the pre-midnight period for the year 1991-93.

Long Period Geomagnetic Pulsations Associated with the March 31, 2001 Magnetic Storm

José M. da Costa[1] , University of Taubaté, SP, Brazil; Severino L. G. Dutra and Nalin B. Trivedi, National Space Research Institute, São José dos Campos, SP, Brazil; Luiz M. Barreto, National Observatory, Rio de Janeiro, RJ, Brazil and Rodrigo P. Sampaio, UNITAU/INPE/CNPq-PIBIC, Brazil

Abstract

The measurement of geomagnetic pulsations is very important for understanding the behavior of the earth's magnetic field and its relation with sun´s activity. The present study shows preliminary results on the detection geomagnetic pulsations, in the Pc5 and Pc6 frequency range, associated with March 31, 2001 magnetic storm at Vassouras. This geomagnetic observatory is situated in the South Atlantic Magnetic Anomaly region and has 22.24° South and 316.21° East as its geographic coordinates. The pulsations were measured using a high sensitivity ring core three-axis (H,D,Z) fluxgate magnetometer. The data analysis included the identification of the dominant frequencies, Pc5 and Pc6, using Fast Fourier Transform (FFT). The occurrences of both Pc5 and Pc6 pulsations were intensified during the storm. The main results are discussed taking account the interaction between the solar wind and the earth's magnetic cavity. *1. Also at National Space Research Institute-INPE.*

Introduction

A storm sudden commencement (SSC) is known to trigger or stimulate a complex ULF phenomena and these pulsations are referred in the literature as (Psc). It seems that a pulse of solar wind pressure may induce in the magnetosphere standing waves along the geomagnetic field lines (e.g. Pilipenko et al. 1997, Trivedi et al. 1997, and Yumoto et al. 1997). The present study shows some preliminary results on the detection of Psc geomagnetic pulsations at Vassouras, in the Pc5 and Pc6 frequency range, associated with the large magnetic storm occurred on March 31, 2001 ($\Sigma Kp = 61^{o}$). The geomagnetic observatory of Vassouras is situated in the South Atlantic Magnetic Anomaly and has 22.24° South and 316.21° East as its geographic coordinates.

Long period geomagnetic pulsations like Pc5 (45-150 s) and Pc6 (150-600 s) are explained by Kelvin Helmholtz type instability at the magnetopause.

Instrumentation

The geomagnetic observatory of Vassouras carries continuous measurements of H, D and Z components using a high sensitivity INTERMAGNET fluxgate magnetometer, which shows the following technical characteristics:

Resolution: 0.1 nT;
Dynamic range: 2000 nT for mid latitude and 6000 nT for Auroral and Equatorial regions;
Band pass: DC to 0.1 Hz,
Sampling rate: .2 Hz (5 s),
Thermal stability: .25 nT/°C
Long term stability: 5 nT/year
Accuracy: ±5 nT for definitive data.

Data Analysis and Results

The data analysis included the study of the geomagnetic field daily variation and the identification of the dominant frequencies using Fast Fourier Transform (FFT) for the period of March 30-April 1, 2001. The plots of the daily variations on H, D and Z components are shown in Figure 1. The storm sudden commencement occurred on March 31, at 00:52 UT, and the H-component showed a variation higher than 400 nT which revealed the detection of a large geomagnetic event.

Figure 2 and Figure 3 show, respectively, the plots of the filtered data for Pc5 and Pc6 pulsations, occurred during the period of March 30-April 1, 2001. Large enhancements in the occurrences of Pc5 and Pc6 pulsations associated with the storm time period are evident from the analysis of Figure 2 and Figure 3, as well as from the dynamic spectra shown in Figure 4a,b. The intensification of Pc6 pulsations started on the evening of March 30, a few hours before the occurrence of the SSC on March 31. The intensification in the Pc5 pulsation range coincides with the start time of the initial phase of the storm.

Discussion and Conclusion

The analysis of the geomagnetic data measured at Vassouras during the period of March 30-April 1, 2001 revealed the occurrence of Psc long period geomagnetic pulsations (Pc5 and Pc6) associated with the March 31, 2001 large magnetic storm. It shows a clear intensification on the occurrences of both Pc5 and Pc6 pulsations, which last during all phases of the storm period. The beginning of the intensification of Pc5 pulsations coincides with the initial phase of the magnetic storm. The intensification of Pc6 pulsations a few hours before the SSC could give some indication on the enhancement of the interaction between the high-speed solar wind plasma and the boundaries of the dusk side of the magnetosphere. Long period geomagnetic pulsations as Pc5 and Pc6 could be explained by Kelvin Helmholtz type instability at the magnetopause.

References

Pilipenko V., N. Kleimenova, O. Kozyreva, M. Engebretson and O Rasmussen, Long-Period Magnetic Activity During the May 15, 1997 Storm.

Trivedi, N. B., B. R. Arora, A. L. Padilha, J. M. Da Costa, S. L. G. Dutra, F. H. Chamalaun, and A. Rigoti, Global Pc5 geomagnetic pulsation of March 24, 1991, as observed along the American sector, Geophysical Research Letters, 24 (13):1683-1686, 1997.

Yumoto, K., V. Pilipenko, E. Federov, N. Kurneva, M. DE Lauretis, and K. Kitamura, Magnetospheric ULF Wave Phenomena Stimulated by SSC, J. Geomag. Geoelectr., 49, 1179-1195, 1997.

Acknowledgments

This research was possible due to UNITAU/INPE/ON-CNPq collaboration. Rodrigo P. Sampaio, undergraduate student at the University of Taubaté-UNITAU, has an INPE/CNPq-PIBIC fellowship.

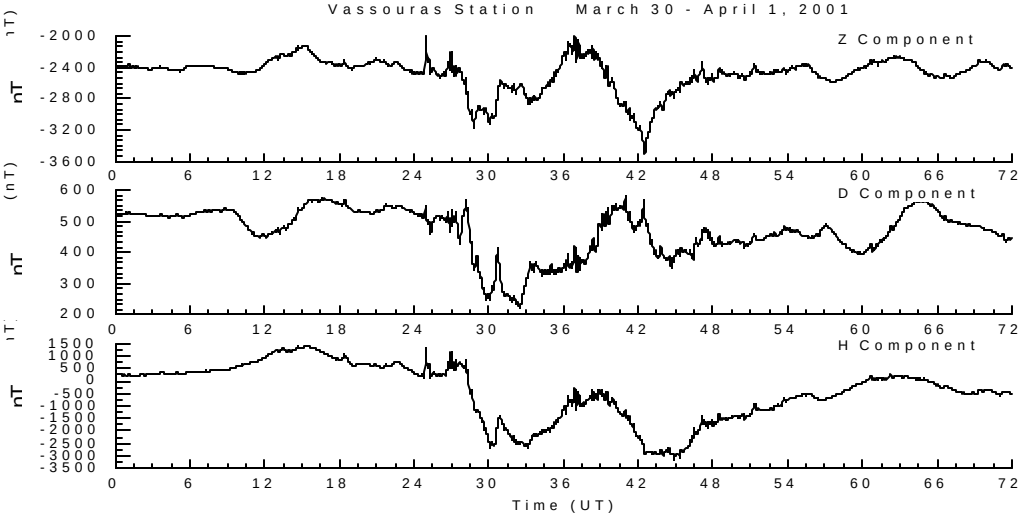

Figure 1 – H, D and Z Variations on March 30 – April 1, 2001

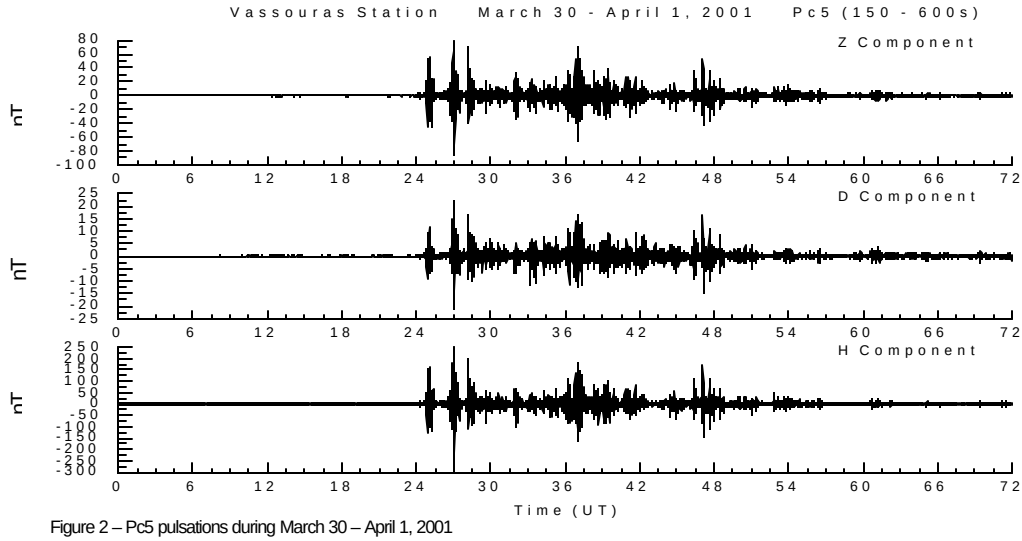

Figure 2 – Pc5 pulsations during March 30 – April 1, 2001

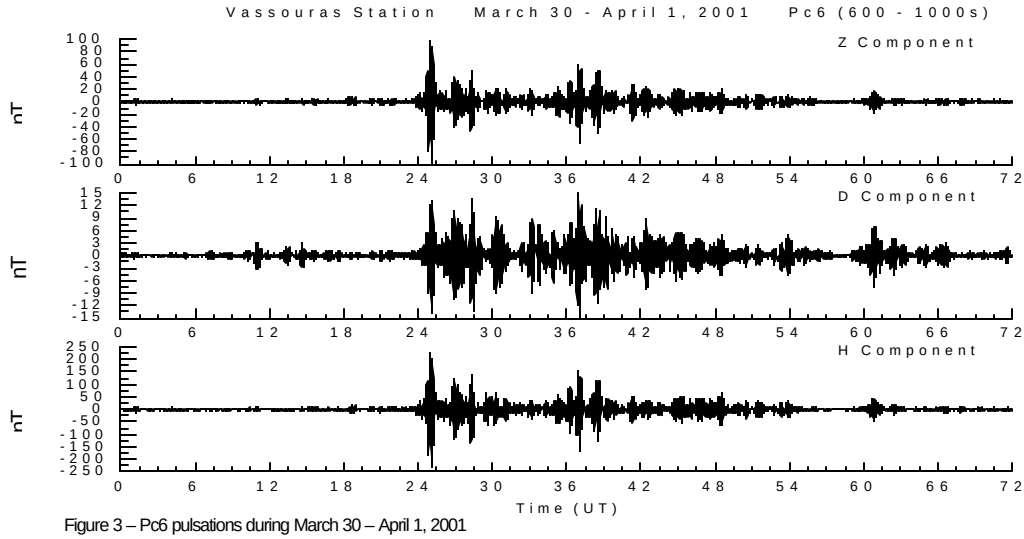

Figure 3 – Pc6 pulsations during March 30 – April 1, 2001

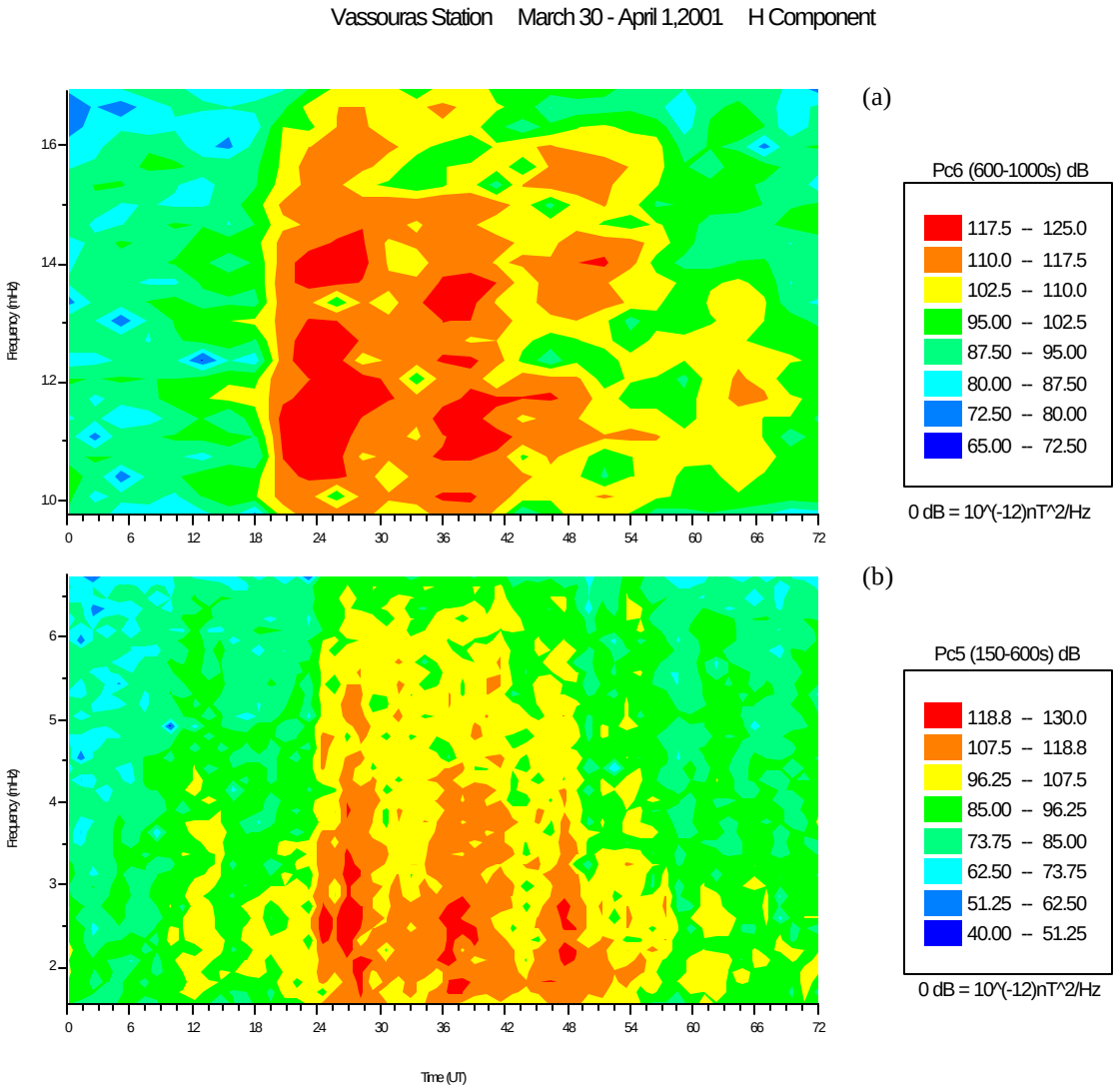

Figura 4a,b – March 30-April 1, 2001 Pc5 and Pc6 pulsations, respectively.

Long term trends in F_3 layer over Fortaleza, Brazil

I. S. Batista, M. A. Abdu, A. M. Silva and J. R. Souza, Instituto Nacional de Pesquisas Espaciais, inez@dae.inpe.br

Abstract

Recent studies using model calculation and ionospheric observations have revealed the existence of an additional layer in the topside equatorial ionosphere that was called the F_3 layer. The observations using bottomside ionograms from locations close to the magnetic equator in Brazilian region have shown that the occurrence of the layer is very high in the December solstice (local summer), less frequent in the June solstice (local winter) and very low in the equinoxes. In this work we use 25 years of data to investigate how the layer occurrence varies with the magnetic dip angle and solar activity.

Introduction

Recent modeling studies showed the occurrence of an additional layer above the F_2 peak, called F_3 layer (Balan and Bailey, 1995; Balan et al., 1997; Jenkins et al., 1997). The model predicts that the layer will be formed during the morning-noon period at the equatorial region, where the combined effect of the upward **ExB** drift at the geomagnetic equator and the magnetic meridional neutral wind provides vertically upward plasma velocity at altitudes near and above the F_2 peak. According to the mechanism discussed by Balan et al. (1998), this upward plasma movement causes the F_2 peak to drift upward and form the F_3 layer while the normal F_2 layer develops at lower altitudes through the usual photochemical and dynamical processes of the equatorial region. Ionospheric data from Fortaleza (4^o S, 38^o W, dip angle -11^o), Brazil, and theoretical simulation using SUPIM (Sheffield University Plasmasphere Ionosphere Model) were used to study the physical mechanism and frequency of occurrence of the layer (Balan et al., 1998, 1999; Batista et al., 2000) and its variability over the Brazilian region (Balan et al., 2000). They observed the layer to occur very frequently on December and June solstices, and less frequently in the equinoxes. The present paper reports a detailed statistics of occurrence of the layer recorded at Fortaleza from 1975 to 2000, that comprises two and a half solar cycles, in which period the magnetic dip angle of the location has varied from 1.7^o S to 11^o S (see also Abdu et al., 1996).

Observations

Ionospheric data have been recorded over the Brazilian location Fortaleza since 1975. From 1975 to 1993 a C4 ionosonde was recording ionograms at 15 min. intervals and from 1994 to 2000 the data were recorded by a digital ionosonde (CADI - Canadian Advanced Digital Ionosonde) at 5 min. intervals. Over the Brazilian region the geomagnetic equator is drifting northward at a very high rate. Due to this drift the geomagnetic dip angle over Fortaleza varied from 1.7^o S in 1975 to 11^o S in 2000 (a rate of approximately –22 min/year). The long time series of ionospheric data registered at that location gives us the opportunity to study the dependence of ionospheric parameters with the geomagnetic position of the station and with solar activity.

In this study we have used the months of January and August as representative of December solstice (local summer) and June solstice (local winter), respectively, based on the statistics made for all months of the year 1995 (Balan et al., 1998). Figure 1 shows sample ionograms for those two months to illustrate the appearance of the F_3 layer. The F_3 layer can appears in the ionogram as a cusp near the high frequency end, here called as type 1 (Figure 1a), or as an inflexion in the middle part of the main F trace, called type 2 (Figure 1b). The type 1 layers are formed at very high heights, but generally their critical frequencies (foF_3) are very close to that of the F_2 layer (foF_2). The difference between the virtual heights of F_3 and F_2 layers ($h'F_3$ - $h'F_2$) is of the order of 150-200 km and the difference between critical frequencies (foF_3 – foF_2) is between 0.5 and 1.0 MHz for type 1 layers. On the other hand, the type 2 layers are formed at lower heights, with $h'F_3$ exceeding $h'F_2$ by 80-120 km and with foF_3 exceeding foF_2 by values between 1.0 and 1.5 MHz. Most of the F_3 layers formed during December solstices are of type 1, and most of the layers formed during June solstices and equinoxes are of type 2, as can be seen from the frequency and height values in Batista et al. (2000) and in Balan et al. (1998).

The occurrence of the F_3 layer as a function of the year is shown in Figure 2. The two upper panels show the number of days with F_3 layer present on the ionograms, for the months included in this work and the third panel shows the variation of the magnetic dip angle over Fortaleza during the studied period. The vertical dashed lines indicate lack of data. Also

shown in the same figure (lower panel) is the solar flux variation at 10.7 cm (F10.7). Data presented in Figure 2 are summarized in Table 1, in which we have denoted the three low solar activity periods by L1 (1975-1978), L2 (1984-1988) and L3 (1995-1998), and the high solar activity periods by H1 (1979-1983), H2 (1989-1993) and H3 (1999-2000).

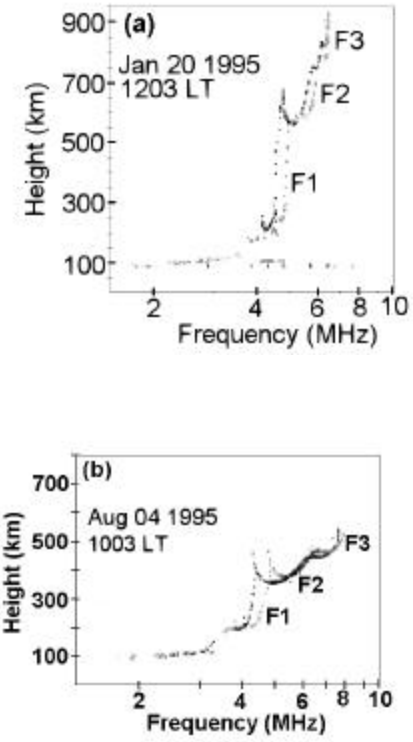

Figure 1 – Sample ionograms showing F_3 layer

For the month of January no F_3 layer is observed for dip angles between 1.7° S and 5° S. The occurrence then increases with increasing dip angle, but it is modulated by the solar activity. In fact the occurrence of the layer is continuously increasing with the dip angle during the low solar activity periods. It increases from 0 occurrence in period L1, to a mean value of 18 days/month in period L3, while the dip angle changed from 1.7° S to 10.4° S in the same period. During the high solar activity periods H1 and H2 the occurrence remains very low (less than 1 day/month) despite the increase in dip angle from 3.2° S to 8.4° S. In 1999-2000 (period H3) the solar activity is high again, and the occurrence of the layer decreases in relation to the previous (L3) period. Considering the three high solar activity periods the occurrence is increasing from 0 (period H1) to 8 days/month (period H3) while the dip angle increases from 3.2 to 11.2 in the same period. The mean values of the solar flux during occurrence and no occurrence of F_3 layers in January, shown in Figure 2, are 108.3 and 150.6, respectively, which confirms the tendency of the layer to be present predominantly during low solar activity periods.

The variation of the F_3 layer occurrence with solar cycle and dip angle for August is similar to that observed for January. During the three low solar activity periods the occurrence of F_3 layer increased from 1 to 18 days/month, with increasing dip angle. The occurrence during the high solar activity periods H1 and H2 is very low, but it increases to 8 days/month in period H3. The mean values of the solar flux during occurrence and no occurrence of F_3 layers in August, shown in Figure 2 are 129.4 and 139.4, respectively. Despite the similar behavior on both months, the solar cycle and dip angle dependencies are more evident in January than in August.

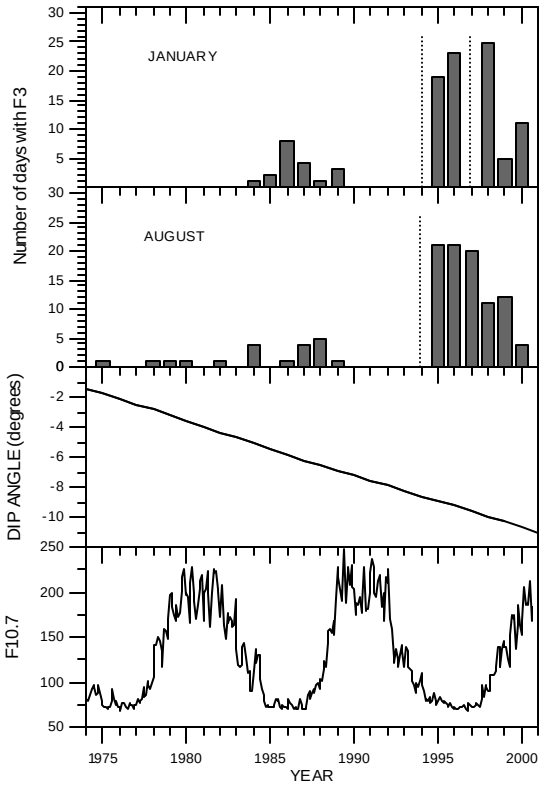

Figure 2 - Occurrence of F_3 layer over Fortaleza and magnetic dip angle of the location during the two and a half most recent solar cycles

Trends in F_3 layer

Table 1 – Occurrence of F_3 layer as a function of dip angle and time period

Period	Years	Dip Angle (degree S)	January		August	
			Mean Flux	Mean occurrence (days)	Mean Flux	Mean occurrence (days)
L1	**1975-1978**	**1.7 < I < 3.1**	**82.1**	**0**	**93.2**	**1.0**
H1	1979-1983	3.2 < I < 5	175.2	0	174.6	0.6
L2	**1984-1988**	**5.1 < I < 6.8**	**86.0**	**4.0**	**95.9**	**2.5**
H2	1989-1993	6.9 < I < 8.4	196.2	0.6	177.4	0.2
L3	**1995-1998**	**8.9 < I < 10.4**	**78.5**	**18.0**	**92.6**	**18.2**
H3	1999-2000	10.5 < I < 11.2	145.6	8.0	171.1	8.0

Discussion

Many of the features observed in our data are in agreement with the model calculations of Balan et al. (1998) that explain the F_3 layer formation as a consequence of the combined effects of the upward **ExB** drift and the magnetic meridional wind at equatorial regions, plus the usual daytime photochemical and dynamical processes. Our data show that the occurrence of the layer is higher during the low solar activity periods. This is in accordance to what should be expected by simulation because the morning-noon ionosphere becomes broad and intense with increasing solar activity, while the corresponding driving mechanism for the F_3 layer formation (drift and wind) remains more or less constant (Balan et al., 1998). Thus the upward force arising from drift and wind becomes less efficient to rise the morning F_2 peak to the topside altitude to form an F_3 layer during solar maximum.

Our data also indicates that the F_3 layer occurrence during the months of January and August increases with increasing magnetic dip angle (away from magnetic equator), during the low and high solar activity periods. According to model calculations performed for low solar activity period using SUPIM, considering **ExB** drift velocities measured at Jicamarca and the neutral wind velocities calculated from HWM90for the longitude of Fortaleza (Balan et al., 1998) the F_3 layer will be centered at around 4^o S (mag. lat.) in December solstice, and 6^o N at June solstice, with latitude extension of about 10^o and 14^o, respectively. According to that simulation the layer can extend up to 9^o S (mag. lat.) at the longitude of Fortaleza, during December solstices. Our results show that the layer can be observed at ~12^o S dip angle (6^o S mag. lat.), during both December and June solstices. This shows that the model calculations are consistent with observations for December solstice but they disagree for the June solstice.

Recently some discussion has arisen concerning a possible lunar control on F_3 layer formation, based on some earlier works on lunar control of the F layer (see Rishbeth, 2000 and references on that paper). Although some preliminary calculations using Fortaleza data do not show any strong lunar control on F_3 layer occurrence, it seems that the layers here classified as type 2 could have more influence of the moon than those classified as type 1.

As already mentioned our results show a similar behavior with dip angle and solar activity during both solstices. The occurrence of the layer increases away from magnetic equator, and it is modulated by the solar activity, but both the solar cycle and the dip angle dependences are more evident in January than in August. One of the possible reasons for the disagreement between simulation and observation during June solstices could be attributed to the great difference that exist between HWM90 and real winds, as already pointed out by Batista et al. (1996) and Souza et al. (2000). Another possibility could be a greater lunar influence on the layer formation on June solstices. Most of the layers observed during the June solstices are of the type 2. It seems that the F_3 layers classified here as type 2 could have more influence of the moon while those classified as type 1 are

produced by the mechanism proposed by Balan et al. (1998).

In conclusion, the F_3 layer is a very common feature of the daytime equatorial ionosphere during low solar activity periods at the Brazilian longitude of Fortaleza (38° W) at locations having dip angle between 9° S and 11° S, during both December and June solstices. The occurrence decreases with decreasing dip angle, and it is very low close to the magnetic dip equator (dip angle < 5°). The occurrence is higher during low solar activity periods than under high solar activity conditions. The morphology of the F_3 layer trace and comparison with model results indicate that the events occurring in June solstice could possibly be more influenced by lunar effects, while those in December solstices are found to be produced by the mechanism explained by the combined effects of the upward **ExB** drift and the magnetic meridional wind at equatorial regions.

References

Abdu, M. A., Batista, I. S., Muralikrishna, P., Sobral, J. H. 1996, A. Long term trends in sporadic E layer and electric fields over Fortaleza, Brazil, Geophys. Res. Lett., 23, 757-760.

Balan, N., Bailey, G. J., 1995, Equatorial plasma fountain and its effects: Possibility of an additional layer, J. Geophys. Res., 100, 21421-21432.

Balan, N., Bailey, G. J., Abdu, M. A., Oyama, K. I., Richards, P. G., MacDougall, J., Batista, I. S., 1997, Equatorial plasma fountain and its effects over three locations: Evidence for an additional layer, the F_3 layer, J. Geophys. Res., 102, 2047-2056.

Balan, N., Batista, I. S., Abdu, M. A., MacDougall, J., Bailey, G. J., 1998, Physical mechanism and statistics of occurrence of an additional layer in the equatorial ionosphere, J. Geophys. Res., 103, 29169-29181.

Balan, N., Batista, I. S., Abdu, M. A., Sobral, J. H. A., MacDougall, J., Bailey, G. J., 1999, Occurrence of an additional layer in the ionosphere over Fortaleza, Adv. Space Res., 11, 1481-1484.

Balan, N., Batista, I. S., Abdu, M. A., Bailey, G. J., MacDougall, J., Sobral, J. H. A., 2000, Variability of an additional layer in the equatorial ionosphere over Fortaleza, J. Geophys. Res., 105, 10603-10613.

Batista, I. S., Medeiros, R. T., Abdu, M. A., Souza, J. R., Bailey, G. J., de Paula, E. R., 1996, Equatorial ionospheric vertical plasma drift model over the Brazilian region, J. Geophys. Res., 101, 10887-10892.

Batista, I. S., Balan, N., Abdu, M. A., MacDougall, J., Barbosa Neto, P. F., 2000, F_3 layer observations at low and equatorial latitudes in Brazil, Geofisica International, 39, 57-64.

Jenkins, B., G. J. Bailey, M. A. Abdu, I. S. Batista, and N. Balan, 1997, Observations and model calculations of an additional layer in the topside ionosphere above Fortaleza, Brazil, Ann. Geophys., 15, 753-759.

Rishbeth, H. et al., 2000. Lunar control of the F_3 layer, submitted.

Souza, J. R., Abdu, M. A., Batista, I. S., Bailey, G. J., 2000, Determination of vertical plasma drift and meridional wind using SUPIM and ionospheric data at equatorial and low latitudes in Brazil: Summer solar minimum and maximum conditions. J. Geophys. Res., 105, 12813-12821.

Acknowledgements

This work was partially funded by FAPESP (99/00437-0) and by CNPq (5000003/91-2).

Low Latitude Mesospheric Gravity Wave and F-Region Plasma Depletion Studies from Cachoeira-Paulista, Brasil

by

M.J. Taylor
Space Dynamics Laboratory and Physics Department
Utah State University, Logan, Utah, USA

and

A. Fragoso de Medeiros and H. Takahashi,
INPE, CP-515, 12201-970 Sao Jose dos Campos, SP, Brasil.

An all-sky, monochromatic CCD imaging system has been used to investigate the occurrence and properties of short-period (<1 hour) gravity waves in the mesosphere and lower thermosphere (MLT) region at low latitudes. Novel measurements of several visible and near infrared nightglow emissions (spanning the altitude range ~80-100 km) were made from the INPE site at Cachoeira-Paulista, Brasil (23°S) during 1998-2000 and have revealed a wealth of wave structure. Measurements of gravity waves at low latitudes, particularly in the Southern Hemisphere, are rare and these data provide new information on their characteristics and occurrence frequency important for quantifying their seasonal signatures and variability. In addition to the MLT studies measurements of the thermospheric (~250 km) OI (557.7 nm and 630 nm) emission signatures of F-Region depletions were conducted during this period. A number of events were measured exhibiting unusually complex and detailed features. A summary of these results together with a statistical and case study of the mesospheric wave data will be presented.

Low-latitude Electron Density Data versus the International Reference Ionosphere Model

J. H. A. Sobral (1), M. A. Abdu (1), P. Muralikrishna (1), LaBelle, J. W. (2)
Sobral@dae.inpe.br Fax: 55-12-345 6990

(1)Instituto Nacional de Pesquisas Espaciais, São José dos Campos, Brazil
(2) Dartmouth College, Hanover, U. S. A

Abstract

The *F*-region cut-off frequency foF2 and the hpF2 parameter obtained at 15-minute intervals at the equatorial station Fortaleza (3^o 53' S, 38^o 25' W , dip 3.5^o S) and the low latitude station Cachoeira Paulista (22^o 41' S, 45^o 00' W dip 24^o S) in the months of February, May, August and November, 1978, are analyzed here in the light of the International Reference Ionosphere prediction. Similarly, the electron density profiles obtained by three rocket flights in the Brazilian equatorial region are analyzed here. The three launchings were carried out on July 7, 1984, December 11, 1985 and October 14, 1994. The first and the second launchings were performed at the subequatorial station Natal (35°14'W, 5°55'S, dip -9.6°S) and the third one at the magnetic equator station Alcântara (2°19'S, 44°22W, dip -0.5°S).

Introduction

Ionospheric research has been conducted by the Aeronomy Division of INPE by means of rocket experiments during the last three decades (Mendonça et al., 1969). Starting in July 1984, a series of about 10 rocket experiments were carried out from the two Brazilian rocket equatorial launching sites Natal (5^o 51S, 35^o14W) and Alcântara (2^o 19′ S, 44° 22′ W) by Brazilian made rockets (Abdu et al. 1979, 1984,1991; Takahashi et al., 1987, 1996; Muralikrishna and Abdu, 1991; Sobral et al. 1992, 1993, 1994, 1997, Jahn et al., 1997; LaBelle et al., 1997; Pfaff and Sobral, 1994; Pfaff et al. 1997). From August to October 1994 about 33 rocket experiments of the Guará/NASA campaign were carried out from Alcântara. The name of the Campaign, "Guará", was suggested by Rob Pfaff to remind the beautiful reddish bird guará, very similar to the "Flamingo", that live around Alcântara and is in danger of extinction. This work concerns the results from three rocket experiments carried out on 26/07/1984 1505LT from Natal, on 11/12/1985 21:30LT from Natal and on (Guará) 14/10/1994 19:55 LT Alcântara.

The Rocket Experiments

The three launchings presented here were carried out on the days, times and sites as indicated in the abstract of this text. The rocket experiments of 1984 and 1985 were performed with Brazilian Sonda III rockets and the experiment of 1994 was performed by a NASA Black Brant X rocket (LaBellle et al., 1997). In the three cases the electron density profiles were obtained by plasma probes developed in INPE. The Black Brant X rocket carried another plasma probe from Dartmouth College, but the results are not shown here (LaBelle et al., 1997).

Experimental Results

The basic rocket data consisted of electron density (Ne) profiles from the ascending (upleg) and descending (downleg) parts of the rocket trajectories of the three experiments. In order to organize and facilitate this analysis the electron density data were interpolated every 5 km both for the ascending and descending parts of the trajectory.

The altitude ranges for the 1984, 1985 and 1994 experiments were 95-565 km, 60-565 km, 180-840 km, respectively. Consequently, the latter experiment provided data for a more thorough analysis of the electron density altitude variations.

There is no electron density data in the 1985 experiment in the altitude range of 270-450 km due to technical problems in the plasma probe.

Discussion

Notice that in the six figures here presented, the horizontal scales for the profiles in the center of the panels are shown on the top of the panels and the scales of the other two profiles are in the bottom side. Figure 1 shows the experimental and model electron density profiles. Figures 2 and 3 show comparisons between model and experimental values. Figures 4, 5 and 6 present electron density differences in the horizontal plane.

Figure 1 shows the electron density profiles of the three rocket experiments with the respective International Reference Atmosphere - IRI model profiles. In the 1994 profiles the IRI peak height hmF and maximum electron density Ne are 280 km and 7.33×10^{-5} cm^{-3}. The electron density bite-out in the experimental upleg profile in the altitude range of about 350-820 km, caused by the presence of a bubble, introduced a difficulty in the estimation of Nemax and hmax which can roughly estimated to be around 400 km. The model and experimental Ne

values are close to each but the peak height presents a difference of the order of 120km.

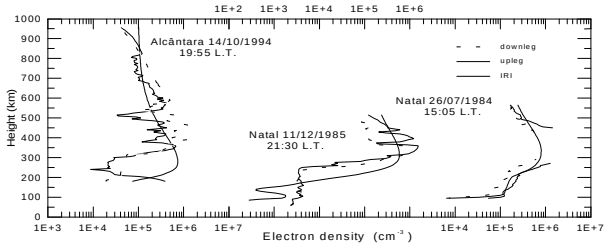

Figure 1 – Experimental rocket and IRI electron density profiles.

Figures 2 and 3 show profiles of the ratio [NeIRI]/[Ne experimental] where NeIRI and Ne experimental stand for the IRI and the rocket electron density profiles. For the experiment of 1994 between 340 km and 375 km the ratio in the upleg ranged from 0.86 to 1.6 which is reasonable agreement. Below 300 km it shows a large discrepancy with a maximum of ratio equal to 69.07 at 240 km.

Both of the nocturnal profiles of Figures 2 and 3 show the largest discrepancies below the altitude of approximately 350 km reaching a maximum discrepancy around 250 km where the NeIRI exceeded the experimental Ne over one order of magnitude.

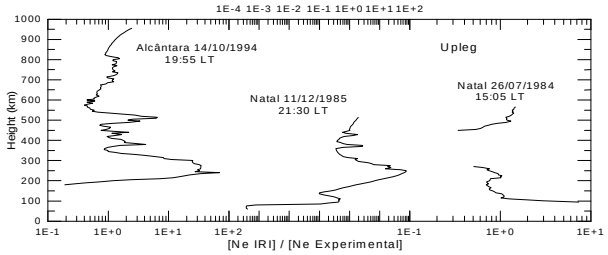

Figure 2 – Comparison between the IRI and the experimental electron density profiles for the ascending parts (upleg) of the rockets trajectories.

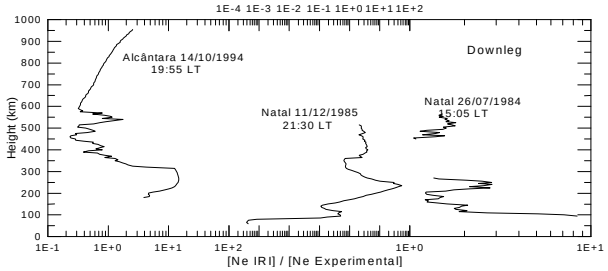

Figure 3 – Same as Figure 2, for the descending parts of the rockets trajectories.

Figure 4 shows profiles of upleg electron density Neu minus downleg electron density Ned. The 1994 profile shows small differences below 300 km and above about 550 km and large discrepancies in between those two altitudes. These discrepancies are caused by the presence of strong plasma bubbles. The case of the December 11 experiment showed very little electron density values differences (Neu minus Ned).

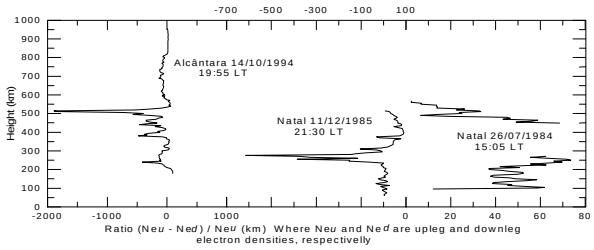

Figure 4 – Height profiles of the diferences between the rockets ascending and descending electron density profiles.

Figure 5 shows profiles of the ratio (Neu-Ned)/Neu where Neu and Ned are electron densities of the upleg and downleg parts of the trajectory, respectively, for a relative comparison of the difference Neu-Ned with respect to the upleg electron density. This parameter showed a clear peak for the nocturnal experiments of 1994 and 1984 at the heights of 515km (ratio equal to- 1893) and 275 km (ratio equal to-615).

Figure 5 – Height profiles of the relative differences between the rockets ascending and descending electron density profiles.

Figure 6 shows the profile of the electron density horizontal gradient ($cm^{-3}km^{-1}$) expressed by the ratio (Neu-Ned)/r where r is the horizontal distance between the ascending and descending parts of the trajectory. The results of 1994 show very small horizontal electron the gradients, namely, ranging from -.0013 to 11.1 electrons $cm^{-3}km^{-1}$ from 210 km to 305 km of altitude, and from -343 to 111 electrons $cm^{-3}km^{-1}$ in the altitude range of 575km to 840 km. In the altitude range of 305 km to 575 km the gradient presented greater values due to the presence of the ionospheric plasma bubble, and the gradients varied up to a maximum -1316 electrons $cm^{-3}km^{-1}$ at the

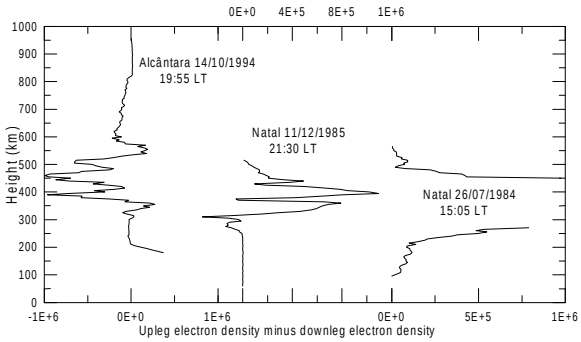

altitude of 460 km. Therefore the gradients inside the bubble region were, in aboslute value, at least 1316/343=3.84 bigger that outside the bubble zone.

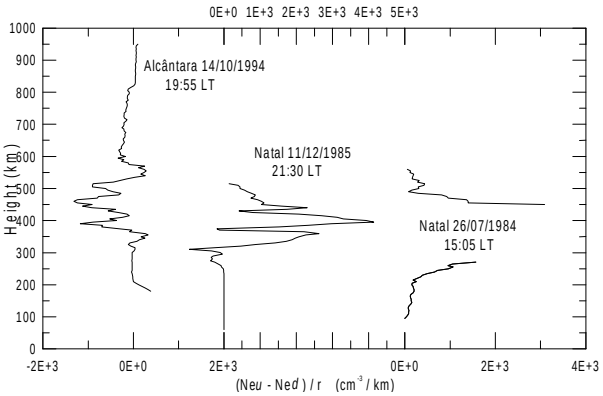

Figure 6 – Profiles of the electron density gradient given by the expression (Neu – Ned)/r, where Neu and Ned are the rockets upleg and downleg electron densities and r is horizontal distance between the ascending and descending parts of the rocket trajectory.

Conclusions

This work presented the experimental results of three rocket experiments carried out at Brazilian equatorial rocket launching sites (see the abstract here for the dates, times and launching sites). The results consisted of electron density profiles corresponding to the the altitude ranges of 95-565 km, 0-565 km, 180-840 km for the 1984, 1985 and 1994 experiments, respectively. The electron densities are compared with the IRI in Figures 1, 2 and 3 and their horizontal variation plotted in three different ways in Figures 4, 5 and 6.

The main conclusions are:

The IRI model results for the electron density were in fair agreement with the rocket results. The best overall agreement occurred on the day-time (15:05) experiment of 1984.

Large discrepancies appear, however, in the nocturnal experiments of 1984 and 1994, below the altitude of approximately 350 km (Figures 2 and 3) in which a maximum discrepancy occurred around 250 km where the NeIRI exceeded the experimental Ne by around one order of magnitude, both in the upleg and in the downleg parts of the trajectory. The fact that the ionospheric plasma is moving upward rapidly around that time, might explain the differences between the model and experimental results.

The Guará experiment in 1994 had the largest altitude span and so it permitted a more thorough height analysis of the electron concentration

The horizontal electron density gradient Neu-Ned/r, inside the bubbles of the 1994 experiments were found to be more than 3.84 times that outside such altitude range.

The discrepancies between the model and experimental electron density values shown here tended to be larger for the 1984 and 1994 experiments because of the rapid post-sunset rise of the ionosphere.

The parameter (Neu-Ned)/Neu showed clear negative peaks for the nocturnal experiments of 1994 and 1984 at the heights of 515km (ratio equal to -1893) and 275 km (ratio equal to -615), respectively.

References

Abdu, M. A., I. S. Batista, J. H. A. Sobral, Particle Ionization in the Lower Ionosphere over the South Atlantic Geomagnetic Anomaly from Rocket Results During the Total Eclipse of 1966, J. Geophys. Res., **84**(A8), 4328-4334, 1979.

Abdu, M. A., J. H. A. Sobral, I. S. Batista Comment on "Modelling the Ion Chemistry of the D-Region: A Case Study Based Upon the 1966 Total Eclipse" by Sears et al. J. Geophys. Res., **89**(A4), 2406-2408, 1984.

Abdu, M. A. , P. Muralikrishna, , I. S. Batista, J. H. A. Sobral, Rocket Observations of Equatorial Plasma Bubbles over Natal, Brazil, using a High Frequency Capacitance Probe, J. Geophys. Res., **96**(A5), 7689-7696, 1991.

Jahn J. -M., J. W. LaBelle, J. H. A. Sobral, T. L. Aggson,; W. B. Hanson, Detection of an Equatorial Spread-F Bubble by Ground-Based Photometers and the San Marco 5 Satellite. J. Atoms. Terr. Phys., **59**(13), 1601-1609, 1997.

LaBelle, J., J. -M. Jahn,; R. F. Pfaff, R. F., W. E. Swartz, J. H. A. Sobral, M. A. Abdu, P. Muralikrishna, and E. R. de Paula The Brazil/Guará Equatorial Spread F Campaign: Results if the Large-Scale Measurements. Geophys. Res. Lett., **24**(13), 1691-1694, 1997.

Mendonça, F., J. H. A. Sobral, D. B. Rai, Equatorial Atmosphere Measurements Obtained with the Sounding Rocket Grenade Experiment Radio Science, **4**(9), 741-750, 1969.

Muralikrishna, P. and Abdu, M. A., In-situ Measurement of Ionospheric Plasma Densityby two Different techniques – A comparison, J. Atoms. Terr. Phys., **53**(8), 787-793, 1991.

Pfaff, R., J. H. A. Sobral, The GUARÁ Rocket/Radar Equatorial Campaign. Int. STEP Newsletter, **4**(1), 1-7, 1994.

Pfaff, R. F. , J. H. A. Sobral, M. A. Abdu, W. E. Swartz, J. W. LaBelle, M. F. Larsen, R. A. Goldberg, and F. J. Schmidlin, The Guará Campaign: A

series of Rocket-Radar Investigations of the Earth's upper Atmosphere at the Magnetic Equator. Geophys. Res. Lett., **24**(13), 1663-1666, 1997.

Sobral, J. H. A., H. Takahashi, M. A. Abdu, P. Muralikrishna, Y. Sahai, C. J. Zamlutti, C. J. O(^{1}S) and O(^{1}D) Quantum Yields from Rocket Measurements fo Electron Densities and 557.7 nm and 630 nm Emissions in the Nocturnal F-Region. Planet. Space Sci. **40**(5), 607-619, 1992.

Sobral, J. H. A, H. Takahashi, M. A. Abdu, P. Muralikrishna, Y. Sahai, C. J. Zamlutti, E. R. de Paula Determination of the Quenching Rate of the O(1D) by O(3P) from Rocket-Borne Optical (630 nm) and Electron Density Data. J. Geophys. Res., **98**(A5), 7791-7798, 1993.

Sobral, J. H. A, H. Takahashi, M. A. Abdu, P. Muralikrishna, Y. Sahai, C. J. Zamlutti, E. R. de Paula,. Contribution of the Cascading Process $0(^1S)\rightarrow 0(^1D)$ to the Production of the Atomic Oxygen O(^{1}D) and OI 630 nm Airglow in the Nocturnal Ionosphere, J. Geom. Geoel., **46**, 747-754, 1994.

Sobral, J. H. A. , M. A. Abdu, M. A. , P. Muralikrishna, H. Takahashi, H. S. Sawant, C. J. Zamlutti, M. G. S. Aquino, Horizontal Gradients of the Nocturnal OI 557.7 nm and OI 630 nm Photoemission Rates in the Equatorial Ionosphere based on Rocket Electron Density Data. Adv. Space Res., **20**(6), 1317-1320, 1997.

Takahashi, H., B. R. Clemesha, Y. Sahai, P. P. Batista, A. Eras, H. P. Chaves, B. Rossire, J. R. Daniel, Rocket Observations of the Atomic and Molecular Oxygen Emissions in the Equatorial Region, Adv. Space Res., **7**(10), 47-50, 1987.

Takahashi, H., B. R. Clemesha, D. M. Simonich, S. M. L. Melo, N. R. Teixeira, A. Eras, Rocket Measurements of the Equatorial Airglow:MULTIFOT92 Database, J. Atmos.Terr.Phys., **58**(16), 1953-1961, 1996.

Acknowledgments

This work was partially supported by the Conselho Nacional de Desenvolvimento Científico e Tecnológico – CNPq (Grants 522919/96-0 and 520185/95-1) and Fundação de Amparo à Pesquisa do Estado de São Paulo – FAPESP (Grant number 1999/00437-0). Vivian Moreira Castilho who held CNPq junior research grants helped the data processing of his work with.

Magnetic Activity and Equatorial Anomaly Effects over GPS Scintillations

Eurico R. de Paula, Fabiano S. Rodrigues, Ivan J. Kantor, Mangalathayil A. Abdu, José H. A. Sobral
INPE, CP 515, 12.201-970 São José dos Campos SP - Brazil

Abstract

Amplitude signal scintillations during ionospheric irregularities, measured by an array of modified GPS (Global Positioning System) receivers, over the brazilian sector, was used to study the effects of magnetic activity and equatorial anomaly over their percentage of occurrence and intensity. It was observed that there is a decrease of percentage of scintillation occurrence during high magnetic activity in the premidnight sector mainly during moderate and high solar flux, but not during low solar flux. Some strong storms triggered ionospheric irregularities during periods out of spread-F season. The effect of equatorial anomaly is to increase the magnitude of scintillations due to the higher ambient plasma density.

Introduction

When a radio signal transmitted by a satellite pass trough an irregular density medium the amplitude and phase of this signal becomes unstable and oscillates around a mean value. It is caused by the interference of the signals that are refracted by the irregular medium they propagates. This amplitude or phase fluctuation is called scintillation and its occurrence have been used as an indicator of the presence of ionospheric plasma irregularities (Hysell and Burcham, 1998; Kil et al., 2000; Kintner et al., 2001) in the satellite sight line. The effect of the irregularities were first observed by ionosondes measurements that sometimes observed a spreading in ionograms for ionospheric F layer heights. The equatorial irregularities can develop to large plasma depleted regions, called bubbles, that can be mapped along magnetic field lines. Data from an array of modified GPS receivers distribuited over the Brazilian territory were analyzed to study the effects of the magnetic activity and equatorial ionospheric anomaly.

Methodology

In order to study the irregularity caused scintillations the scientists from the Cornell University, USA, have modified GPS receivers to acquire amplitude values of the L1 (1.575 GHz) signal at a high sample rate (50 Hz). In cooperation with Cornell, INPE has used this system to study the irregularities over the brazilian territory. The modified receiver is based in the GEC – Plessey GPS development kit which has 12 channels able to track the satellite in view and digitally process the received signal (Beach, 1998). The observations are made during the nighttime from 18:00 to 06:00 LT, which is the period of the irregularities occurrence. Figure 1 shows an example of the scintillation observed at São Luís, MA (2.33°S, -56.46°W; dip latitude: 1.3° S) for November, 11 of 1999. Initially the amplitude of the L1 signal is stable and about 22.50 UT (19:30 LT) the signal becomes unstable due irregularities in the satellite line of sight.

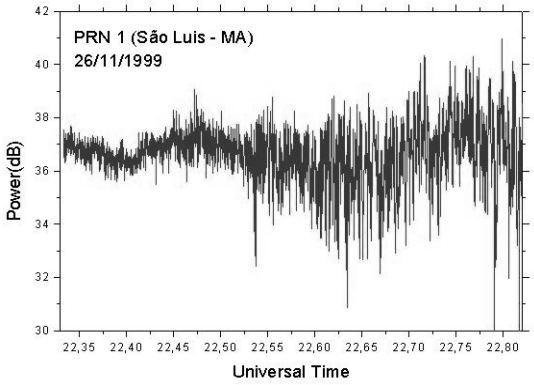

Figure 1 – Example of scintillation occurrence observed in the GPS L1 signal transmitted by the PRN 1 satellite and received at São Luís – MA.

Nowadays INPE/Cornell have six observation sites over the Brazilian territory and new observations sites are been planned to be settled. Figure 2 shows the locations of the installed GPS receivers.

Figure 2 – Location of the of the scintillation observation sites in operation by INPE/Cornell.

Results

For the study of the magnetic activity effects we have used data obtained at São José dos Campos (23.21° S, 45.86° W, dip latitude:17.43° S) for three consecutive years under different solar activity levels. The data used are from January, February and March, for 1998 ($\overline{\Phi}_{10.7}$ = 98.9), 1999 ($\overline{\Phi}_{10.7}$ = 136.1) and 2000 ($\overline{\Phi}_{10.7}$ = 180.2). The Figure 3 shows the results for the magnetic activity analysis. The criteria to distinguish magnetically quiet and disturbed used was the five international quietest and most disturbed days of each month.

For the study of the Equatorial Anomaly effects over the scintillation occurrence were used data from three different observations sites: São Luís located at the magnetic equator; São José dos Campos under the crest of the equatorial anomaly and Cuiabá located in a intermediate point between the magnetic equator and the equatorial anomaly. The results are shown in the Figure 4. The geographic coordinates, magnetic declination and inclination of these observation sites are shown in the Table 1. Figure 5 shows the scintillation percentage occurrences for two different S4 index levels for São Luís, Cuiabá and Cachoeira Paulista (22.41°S, 45.00°W, dip latitude: 17.8°S). The data are for November, 23 to December, 26, 1999.

Table 1 – Geographic coordinates and magnetic declination and inclinations values for the observation sites.

	São Luís	Cuiabá	SJ dos Campos
Geographic Coordinates	23.21°S 45.86°W	15.33°S 56.46°W	2.33°S 44.00°W
Declination	-20° 42´	-14° 27´	-19° 48´
Inclination	-02° 42´	-12°12´	-32° 59´

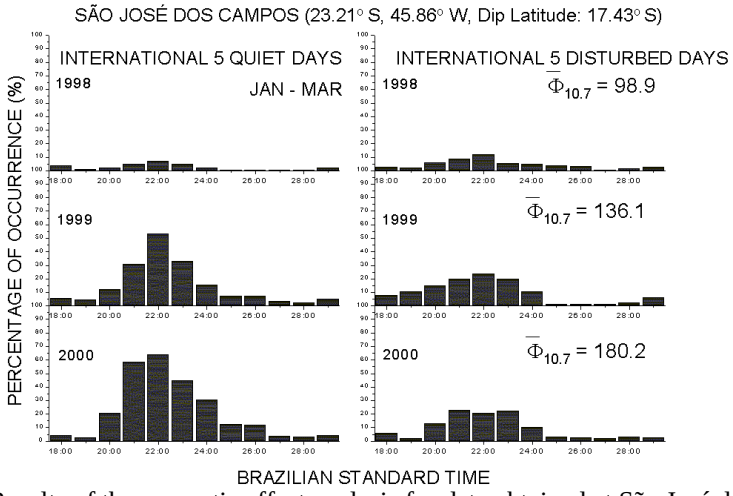

Figura 3 - Results of the magnetic effect analysis for data obtained at São José dos Campos.

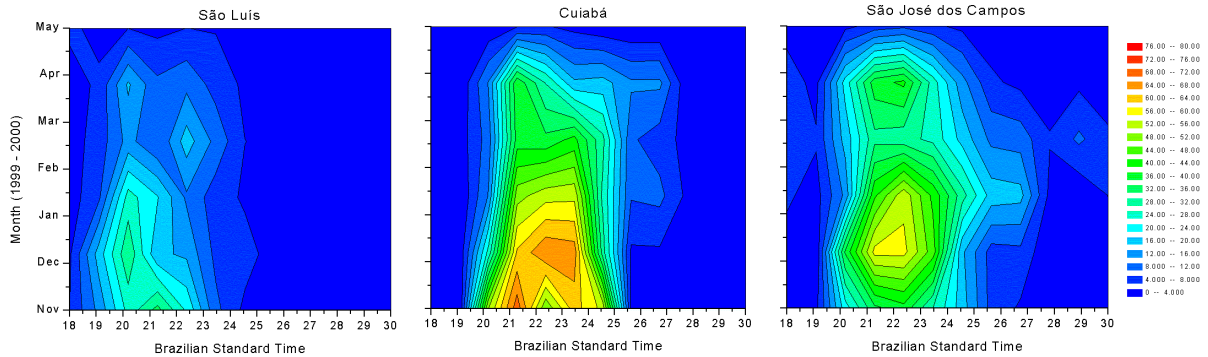

Figura 4 –.Results of the percentage of occurrence of scintillations (S4 > 0.1) observed at magnetic equator (São Luís), under the crest of the equatorial ionospheric anomaly (São José dos Campos) and at an intermediate point between the magnetic equator and the equatorial ionospheric anomaly (Cuiabá).

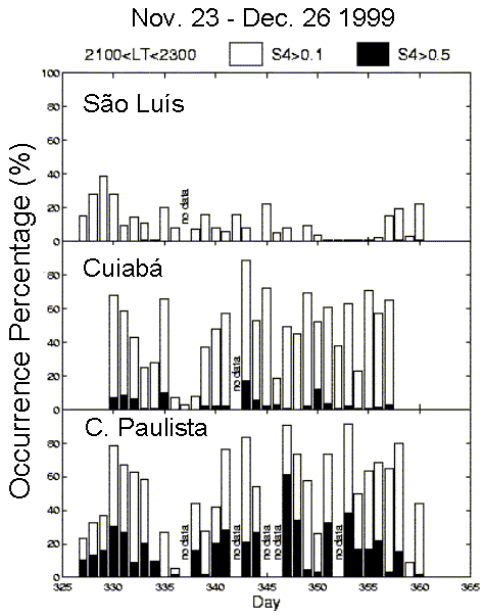

Figure 5 – Scintillation ocurrence percentage for two S4 index level and for three sites.

Discussion and Conclusions

The results in the figure 3 show that occurrence percentage of scintillations (scintillation index S4 > 0.1) is smaller during magnetically disturbed days than during quiet days for medium and high solar activity, however, this is not observed during low solar activity. It is observed that Figure 4 and 5 show that the scintillation percentage of occurrence is larger at Cuiabá than at São Luís and São José dos Campos, however, scintillation of greater index values are more observable at Cachoeira Paulista (close to São José dos Campos) under the Equatorial Anomaly crest. The larger occurrence observed at Cuiabá compared to São José dos Campos can be related to bubbles that are generated at the equator and reach an equatorial altitude enough to map over Cuiabá, but don´t reach São José dos Campos or Cachoeira Paulista. The smaller scintillation percentage of occurrence observed at São Luís is due to the low ambient plasma density at the equator. It is also observed that the higher plasma density of the Equatorial Anomaly causes a larger incidence of scintillations with S4 index higher than 0.5 at Cachoeira Paulista.

Data from different periods and sites are been analyzed and will be useful for the understanding of the irregularities behavior during magnetically quiet and disturbed periods for low and high solar activity.

References

Beach, T.L., 1998, Global Positioning System studies of equatorial scintillations, Ph.D. dissertation, Cornell University, Ithaca, N.Y.

Hysell, D.L., Burcham, J.D., 1998, JULIA radar studies of equatorial spread F, Journal of Geophysical Research 103 (A12), 29155-29167.

Kil, H., Kintner, P.M., de Paula, E.R., Kantor, I.J., 2000, Global Positioning System measurements of the ionospheric apparent velocity at Cachoeira Paulista in Brazil, Journal of Geophysical Research 105 (A3), 5317-5327.

Kintner, P.M., Kil, H., Beach, T.L., de Paula E.R., Fading timescales associated with GPS signals and potential consequences, accepted to Radio Science, 2001.

Acknowledgments

E. R. de Paula is grateful to FAPESP under Process 1997/3342-5 and to CNPq under process 502223/91-0 and F. S. Rodrigues was suportted by FAPESP under process 00/13325-5.

Magnetospheric Disturbance Effects on Equatorial Spread F and Thermospheric Winds

M. A. ABDU(1), J. R. Souza(1), I. S. Batista(1), J. H. A. Sobral(1), H. Takahashi(1), J. MacDougall(2) and E. R de Paula, (1)Instituto Nacional de Pesquisas Espaciais- INPE, Sao Jose dos Campos, Brazil, (2)Dept. of Electrical Engineering, The University of Western Ontario, London, Canada

Abstract

Magnetospheric disturbances are known to modify the equatorial thermospheric dynamics and chemistry. The disturbance winds and electric fields in turn could modify equatorial spread F /plasma bubble irregularity development conditions in ways to enhance or inhibit its occurrences. Digital ionosonde/digisonde and optical data from Brazilian equatorial/low latitudes are analyzed during some recent magnetospheric disturbances to examine the control of disturbance electric fields and winds (especially the disturbance meridional winds) on the generation and/or inhibition of the spread F. The SUPIM (Sheffield University Plasmasphere-Ionosphere Model) has been used (based on a new methodology, Souza et al., 2000 JGR in press) to model the maridional wind and equatorial zonal electric field for quiet conditions to be used as reference for determining the disturbance components of these parameters and to identify their possible effects on the spread F developments. Preliminary analysis of some storm event that occurred in 1998 already show disturbance associated post sunset spread F development and associated perturbations (in zonal and meridional) winds as observed over Cachorira Paulista, Fortalez and Sao Luiz. The paper will present results based on analysis for a few quiet days and storm conditions.

Measurements of GPS L1 Scintillations at the Equatorial Anomaly

A Paul M. Kintner, Jr. and Brent Ledvina, School of Electrical and Computer Engineering, Cornell University, Ithaca, NY; Eurico R. de Paula, INPE-DAE, São José dos Campos, São Paulo, Brazil; Hyosub Kil, Johns Hopkins Applied Physics Laboratory, Laurel, MD

I

Abstract

Nighttime equatorial ionospheric irregularities, sometimes called spread-F, are known to produce amplitude and phase scintillations at L-band frequencies including GPS signals. The GPS signal scintillations, on one hand, are useful for remote sensing of the ionosphere and, on the other hand, are a cause for concern when GPS is used in situations requiring high reliability. We have developed a GPS scintillation monitor (Scintmon) that permits us to explore both viewpoints of GPS and ionospheric scintillations. Using Scintmon data acquired in Brazil we will first demonstrate the relation of GPS scintillations to TEC holes in the ionosphere. Next we will show how GPS scintillations can be used to determine ionospheric drift velocities and that, when ionospheric drift velocities match the GPS ionospheric signal puncture point velocity, and fading time scale increases. Finally we shall show how scintillations can cause loss of GPS receiver tracking and comment on the situations that are most susceptible to this disturbance..

Introduction

Ionospheric storms, sometimes called equatorial spread-F, are a well-known and long studied property of the equatorial and near-equatorial ionosphere. After sunset a shelf forms in the ionospheric density profile that is supported by the horizontal magnetic field. This shelf is unstable to the electromagnetic analog of the Raleigh-Taylor instability and regions of lower plasma density bubble upward into the higher altitude and higher density volumes of the F-region ionosphere. Associated with the upwelling bubbles are turbulent plasmas and plasma density irregularities over scale sizes from 100 km to less than a meter. As the equatorial spread-F evolves upward, it also typically drifts eastward at roughly 100 m/s. The development phase is during the first one to two hours after sunset after which the irregularities slowly decay over the course of the night. Global geomagnetic storms can change the overall morphology of the development and drifts of the irregularities but the process of upwelling bubbles and development of irregularities is essentially the same. Also the extent to which the plasma bubbles develop vertically at the equator determines the extent to which the bubbles extend north and south by mapping along geomagnetic field lines. If the bubbles develop at least modestly in altitude, they map to the equatorial anomalies and regions of larger ionospheric plasma density.

The plasma irregularities produce scintillations of trans-ionospheric radio signals primarily from satellites and this phenomena has also been studied for decades. For frequencies above the maximum plasma frequency (roughly 10-30 MHz), the plasma density irregularities correspond to small changes in the index of refraction for the propagating radio signal. These small changes in the index of refraction scatter radio waves by small angles. Each radio wave frequency is sensitive to a particular scale size of irregularities call the Fresnel length. The Fresnel length can be calculated by estimating the horizontal separation in the ionosphere between a direct path from the ionosphere to the receiver on the ground and a scattered path whose distance between the ionosphere and the ground is equal to the direct path plus one wave length. For the Global Positioning System L1 frequency (1.6 GHz) the Fresnel length is about 400 m.

The behavior of the scintillation pattern on the ground is a function of the properties of the ionospheric irregularities. Larger absolute density irregularity amplitudes produce larger amplitude fades on the ground and the fading time scale depends on the motion of the ionosphere with which the irregularities are convecting. Next we will give some examples of scintillations and fading of GPS signals. We will also show how the translating spatial pattern of fade can be used to measure the drift speed of the scintillation pattern and infer the ionospheric drift velocity. Finally we will show an example where the scintillation amplitude is so large that GPS receivers lose lock and discuss in general when GPS receivers should be vulnerable to fading signals.

Figure 1 shows an example of a typical GPS satellite pass during a period of equatorial spread-F and GPS signal scintillations. This is a rather complicated plot but it serves to illustrate most of the effects of the disturbed equatorial ionosphere on GPS signals. Starting from the bottom of Figure 1, a polar plot (elevation-azimuth) shows the path of a GPS satellite in the sky from the viewpoint of the receiver. The satellite rises in the southwest at about 1730 local time (LT) and turns northward, eventually setting in the north at about 2430 LT. The dashed line represents the geomagnetic meridian.

Above the elevation-azimuth panel is a plot of total electron content (TEC) between the receiver and the GPS satellite (panel e). The value of TEC at the

start of the record is large, about 80 TEC units (one TEC unit is 10^{16} electrons/m^2), because of the low elevation of the satellite and the large slant path through the ionosphere. As the satellite rises the value of TEC drops rapidly as expected. Then between 2000 LT and 2100 LT the TEC value begins to behave more erratically as regions of disturbed ionosphere pass between the receiver and the satellite; this behavior continues until the satellite sets at roughly 2430 LT.

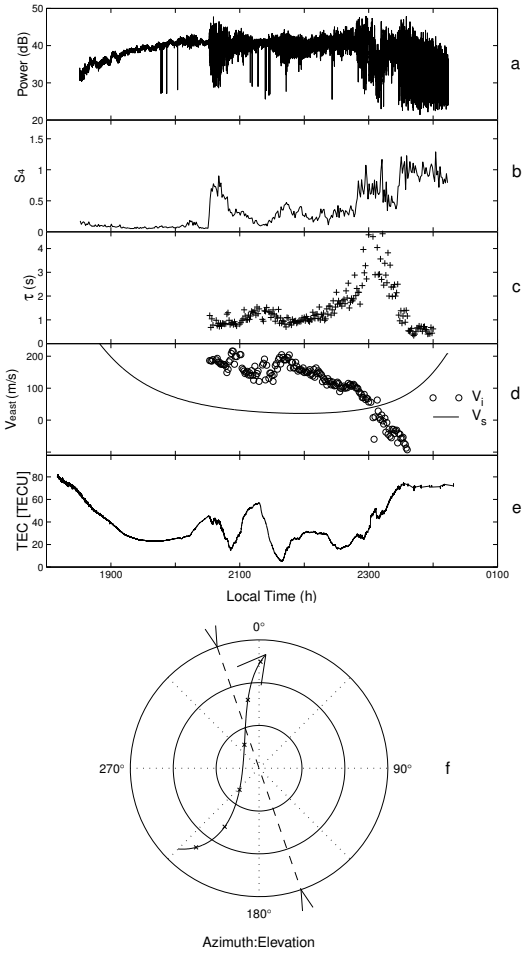

Figure 1 - An example of scintillations measured at Cachoeira Paulista, Brazil (22.7º S 45.0º W) on Nov. 8, 1998.

The top panel of Figure 1 shows the amplitude of the received GPS signal (panel a). The signal begins at a relatively low amplitude and increases in amplitude as the satellite rises in elevation and the distance to the receiver decreases. Then at 2030 LT the signal amplitude begins to fluctuate rapidly as scintillations begin to produce signals amplitude increases and decreases, called fades, and this behavior continues until the satellite sets in the north. The second panel (panel b) from the top shows the S4 index, which closely mirrors the behavior of the signal fades, reaching a value in excess of one and indicating an intense event. The middle panel (c) shows the width of the signal autocorrelation function at a value of 0.5, compared to the normalized peak at 1.0, and for S4 value greater than 0.2. This value is a measure of the fading time scale. For most of the event the derived fading time scale is about 1 sec but for a brief period it exceeds 4 sec. We will return to the reason and consequences of the increased fading time scale in a moment.

Panel d shows two different velocities. The velocity of the scintillation pattern across the ground can be estimated using two receivers that sample the pattern at a high rate. The two receivers are aligned about 50 m apart in the east-west direction. By creating the cross correlation function between the signal amplitudes recorded at each receiver the time of optimal lag can be determined. The separation distance between the receivers and the lag time yield the velocity of the scintillation pattern. If the GPS satellites were in geosynchronous orbits (they are not), then the velocity of the scintillation pattern would be the same as the ionospheric velocity. The velocity of the GPS signal ionospheric puncture point must be removed from the scintillation pattern velocity to yield the ionospheric velocity. In panel d the circles represent the corrected ionospheric velocity and the line represents the signal ionospheric puncture point velocity. When these two cross then the scintillation pattern speed seen by the receiver should slow down greatly. This can be seen in the autocorrelation time shown in panel c. Just after 2300 LT the ionospheric puncture point velocity and ionospheric velocity cross implying velocity matching between the ionospheric velocity and the GPS signal velocity. On the ground the scintillation pattern should slow down, which it does, as shown in panel c.

GPS Vulnerability to Scintillations

GPS receiver operate using a tracking loop to synchronize codes embedded in the GPS signal with replicas in the receiver. When the signal amplitude fades below about 26 dB they can no longer track. However, if the fade is short, the tracking loop can maintain synchronization. When the fade is long, the tracking loop is expected to fail during fades. Figure 2 shows an example of tracking failure or loss of lock. This example occurred when the fading time scale was a maximum (see panel c) and when the fade amplitude was large. These examples of loss of lock

are modest in part because the fading time scale never exceeded 5 sec. Other examples of loss of lock show longer times of tracking failure, sometime exceeding 15 seconds.

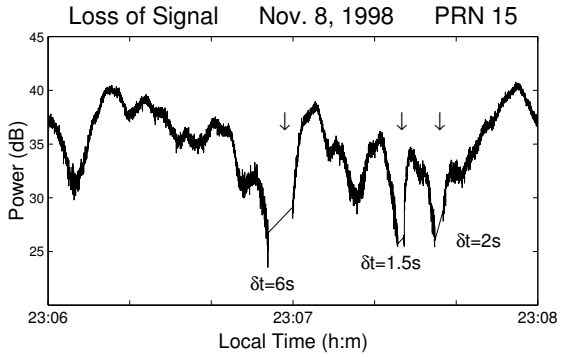

Figure 2 - Example of tracking loss of lock when the fading time scale is a maximum.

The times when the satellite velocity and the ionospheric drift velocity match or resonate are relatively infrequent for this stationary receiver. Resonance requires a special set of conditions since the east-west velocity of the puncture point only matches the east-west velocity of the ionosphere when the satellite elevation is typically small. However, for a moving receiver, resonance may occur much more frequently. The typical scintillation pattern drift speed is about 100 m/s corresponding to the landing speed of a commercial airplane. One would expect that GPS receivers on airplanes may be more vulnerable to scintillation induced tracking loss.

Summary and Conclusions

Equatorial spread-F and the density irregularities produced during this phenomena cause amplitude scintillations in GPS L-band signals. Density irregularities with scale lengths of about 400 m at altitudes of about 350 km refract GPS signals so that they add out of phase on the ground producing signal fades. The result scintillation pattern on the ground produces a time varying signal at a stationary receiver primarily by translating in a east-west direction with a speed of roughly 100 m/s. The ground speed is determined by the difference of the ionospheric drift velocity and the puncture point velocity.

When the receiver velocity and the scintillation pattern velocity match, the probability of receiver loss of lock increases because the tracking loop cannot track through the long time-scale fades. Of course, this assumes that the fading level is below the tracking threshold as well. For a stationary ground based receiver the combination of large amplitude fades and long time-scale fades is relatively infrequent. However, for moving receivers, such as those on commercial airplanes, the likelihood of velocity matching is more probable.

Does this mean that one should exchange their airline ticket for a cruise on an ocean liner? No. For the time being GPS receivers are not the primary source of navigation for airplanes. Furthermore, as the solar cycle declines the maximum level of fading will also decline. The real danger is in the next solar cycle maximum about 10 years from now. By then GPS will be woven into our technical infrastructure more thoroughly. For high reliability applications, such as air travel, the possibility of scintillations causing receiver degradation or failure is real. To protect against this eventuality it is imperative that users be aware of this possibility and have alternatives to GPS available.

Medidas da velocidade zonal das bolhas de plasma na região equatorial e em baixas latitudes usando imageadores all-sky na emissão OI 630 nm

Alexandre Alvares Pimenta[1], José Augusto Bittencourt[1], Paulo Roberto Fagundes [2], , Ricardo Arlen Buriti da Costa[3], Hisao Takahashi[1]
1.Instituto Nacional de Pesquisas Espaciais (INPE) – Brasil
2. Universidade do Vale do Paraíba
3. Universidade Federal da Paraíba

Abstract
Medidas da velocidade zonal das bolhas de plasma na região equatorial e em baixas latitudes utilizando imageadores all-sky na emissão OI 630,0 nm são apresentados. A análise dos dados durante esse período mostram que a velocidade zonal das bolhas de plasma está fortemente correlacionada com a hora local e com a latitude no qual são efetuadas as medidas. Na noite de 10 de janeiro de 2000, as imagens mostram a fase de formação das bolhas de plasma após o por do sol. Medidas simultâneas durante essa noite na região equatorial e em baixas latitudes mostram que a velocidade zonal das bolhas de plasma sobre São João do Cariri (7.4° S, 36.5° W) foi de 30-70% maior que Cachoeira Paulista (22.7° S, 45° W), indicando a presença de um forte vento zonal na direção leste ou um campo elétrico vertical bastante intenso sobre o equador. Foi observado também que as bolhas de plasma tinham extensão leste-oeste cerca de 350-450 km e que os níveis de depleção dessas bolhas foi bastante elevado. O comportamento da velocidade zonal dessas irregularidades no plasma da região F na região equatorial e em baixas latitudes são apresentados e discutidos nesse trabalho.

Models of Quasi-Periodic Turbulence in the E-Region Driven by Neutral Wind Shears

P A Bernhardt, Beam Physics Branch, Plasma Physics Division, Naval Research Laboratory, Washington, DC 20375, Ph. 202-767-0196, Fax 202-767-0631, e-mail: bern@ppdu.nrl.navy.mil

Modulation of electron densities in ion layers between 90 and 150 km altitude has been observed using a number of ionospheric diagnostic measurements including scatter of VHF radar waves, artificially pumped optical emissions, scintillations of satellite beacon transmissions. Kelvin-Helmholtz (K-H) turbulence driven by a sheared wind profile is a strong candidate for the source of these modulaions. A two-dimensional numerical model is used to calculate the nonlinear evolution of ion layers in ionosphere near 100 and 120 km altitude in response to neutral turbulence driven by a wind shear. The amplitude of a K-H billow is allowed to grow as a linear perturbation on the neutral atmosphere to a level that is 10% of the wind shear. The time dependent model of the ionosphere responds to neutral wind perturbation initially by imposing a quasi-sinusoidal modulation near the altitude of the ion layer. This is followed by compression of the initially stratified layer into structures with the period of the K-H instability. These structures are uniform strips in the meridian perpendicular to the direction of the zonal wind. Near 120 km, where the ion gyro frequency ($\tilde{\cdot}$ i) is about equal to the ion collision frequency ($\tilde{\cdot}$ i), the equilibrium solutions are clumps at the altitude of the shear. Near 100 km, two stable, rippled layers are produced with a separation of about 1 km. The amplitudes of the density modulations in the ion layers vary by as much as 500% throughout the simulation. This simulation illustrates the complex evolution of the ion layer structures from small-amplitude, K-H wind turbulence. This paper provides a numerical simulation of quasi-periodic irregularities generated by sheared neutral winds acting on the ion-layer (or E-region) plasma near 100 and 120 km. These two altitudes are chosen so that the effective differences in ion-neutral collision frequencies can be highlighted. A computer model is used to simultaneously form Kelvin-Helmholtz billows in the neutrals and sporadic-E layers in the plasma. The coupled neutral-plasma model shows that only small amplitude perturbations in the neutral wind are needed to produce large-amplitude modulations of the sporadic-E layer densities. The formation of a structured E-layer is modeled using a system of coupled equations for continuity and momentum that describes both the neutrals and plasma. In the model, an externally imposed neutral wind shear drives the neutral atmosphere unstable and produces Kelvin-Helmholtz billows. This same wind shear compresses the ions into a layer with a well-defined vertical profile. The Kelvin-Helmholtz turbulence introduces quasi-periodic (Q-P) structures on the layer in the horizontal direction. Small-scale plasma irregularities can grow on the surfaces of the Q-P structures.

The computations are limited to a two-dimensional geometry. The theory has focused on the effects of Kelvin-Helmholtz instabilities in the neutral atmosphere that produce irregularities in the ion-layer that have k-vectors aligned with the neutral wind and have transverse symmetry with respect to the neutral wind direction and the direction of the gradient in the wind shear. If the full three-dimensional nature of the problem is considered, it is possible to generate secondary instabilities that produce irregularities with wave numbers at an oblique angle to the neutral wind vector. The two sources for these instabilities are (a) secondary turbulence in the neutral atmosphere the yields longitudinal symmetry and (b) gradient drift instabilities that produces irregularities aligned with the magnetic field.

The results are consistent with many features of the observations mentioned in the Introduction. The computed ion layers are relatively flat. The quasi-equilibrium solution in has a 1 km by 5 km aspect ratio. Since the solution is uniform in the y-direction perpendicular to the simulation space, the modulated layers can be viewed as horizontal strips. This result matches the observations reported using satellite radio transmissions, VHF backscatter and optical images excited by high power radio waves. The 8 to 10 km separation between horizontal strips is close to the separation of 10 to 11 km deduced from satellite observations by Bowman [1989] and Maruyama, Fukao, and Matsumoto [2000]. This dimension also matches that obtained for periodic variations in VHF radar echoes [Larsen, 2000]. The bands of enhanced 557.7 nm optical emissions reported by Kagan et al. [2000] that have a similar separation of 7 km. These excited optical emissions come from overdense strips that reflect high power radio waves.

References

Bowman, G.G., Quasi-periodic scintillations at mid-latitudes and the possible association with ionospheric sporadic-E structures, Annales Geophysicae, 7, 259-268, 1989.

Maruyama, T., S. Fukao, and M. Yamamoto, A possible mechanism for echo striation generation of radar backscatter from midlatitude sporadic E, Radio Sci., 35, 1155-1164, 2000.

Larsen M.F., A shear instability seeding mechanism for quasiperiodic radar echoes, J. Geophys. Res., 105, 24931-24940, 2000.

Kagan, L.M., MC Kelley, F. Garcia, PA Bernhardt, FT Djuth, MP Sulzer, CA Tepley, The structure of electromagnetic wave-induced 557.7-nm emission associated with a sporadic-E event over Arecibo, Physical Review Letters, 85, 218-221, 2000.

Monitoramento de cintilações em comunicações por satélite na faixa de 4GHz

***Alexandre Pinhel Soares**, Furnas Centrais Elétricas S/A, Brasil*

Resumo

Esse artigo apresenta alguns resultados obtidos a partir da monitoração de um enlace do satélite Brasilsat B2 (Banda C). Os dados foram aquisitados por um sistema automatizado que registrou, o espectro de frequência do transponder 2A (3.74GHz a 3.78GHz), de 10 de outubro de 2000 a 15 de abril de 2001. Neste período registraram-se 37 cintilações noturnas no sinal, sendo 21 de forte intensidade e, dentre essas, 16 com mais de uma hora de duração. Por comparação com dados geofísicos confirmou-se que as anomalias no sinal foram causadas por depleções no plasma ionosférico, eventos mais conhecidos como Bolhas Ionosféricas. Para interpretação dos resultados contou-se com o apoio do Instituto Nacional de Pesquisas Espaciais (INPE).

Introdução

Resumidamente pode-se dizer que existem dois mecanismos atmosféricos que conseguem modificar a potência recebidade de um sinal de satélite : absorção e cancelamento de harmônicos. Na faixa de 4GHz praticamente não há absorção de sinal em nenhuma camada da atmosfera porém há cancelamento de harmônicos na Ionosfera.

O cancelamento de harmônicos ocorre porque uma onda eletromagnética ao passar por um plasma com presença de campo magnético sofre alterações que são proporcionais à intensidade do campo magnético, à densidade eletrônica do plasma e à frequência da onda (ITU-R, 1998). Esse cenário é observado nas comunicações por satélite, pois o enlace (onda eletromagnética) atravessa a Ionosfera (plasma) na presença de um campo magnético (o da Terra).

Tendo em vista essa realidade, decidiu-se implementar um sistema de monitoramento que fornecesse os dados necessários ao diagnóstico de alguns problemas noturnos que têm sido verificados nos enlaces do satélite Brasilsat B2 contratados pela Empresa. Esse trabalho apresenta os resultados de 6 meses de monitoramento.

Monitoramento das cintilações

O monitoramento é realizado sobre o sinal do satélite Brasilsat B2 (ver tabela 1 e figura 1) recebido no Rio de Janeiro. O sinal derivado do receptor entra em um analisador de espectro que fica conectado a um PC via interface GPIB (General Purpose Interface Bus).

O PC executa um aplicativo que controla o analisador e registra os valores de potência (em dBm) do sinal a cada 10 segundos. O sistema foi ligado em 10/10/2000 e os dados aqui utilizados correspondem ao período de 10/10/2000 à 15/04/2001, num total de, aproximadamente, 1.600.000 registros.

Tabela 1 : Características do enlace monitorado.

Tipo	Banda C
Localização	22º57'S, 43º11'W
Azimute	314.26º
Elevação	53.60º
Transponder	2A - 3740MHz a 3780MHz
Frequência central	3760 MHz
Largura de banda	36 MHz
Faixa	3742 to 3778 MHz
Polarização	Horizontal
FI	70MHz

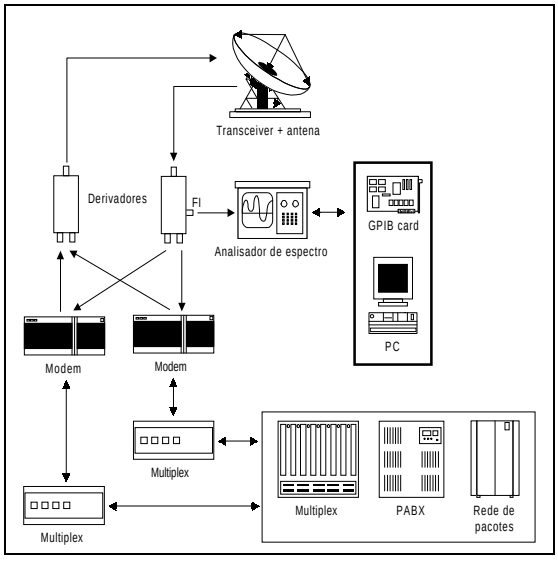

Figura 1. Esquema de interligação do Sistema de Monitoramento.

Resultados

Considerou-se que um sinal estaria com cintilação se possuísse determinada diferença com o sinal registrado às 18:00, i.e., pouco antes do anoitecer. Definiu-se como cintilação Tipo 2 aquela que fizesse pelo menos 50% das frequências do espectro variarem de ±2dB e cintilação Tipo 3 aquela que fizesse pelo menos 50% das frequências do espectro variarem de ±3dB.

No período aqui utilizado registraram-se 37 cintilações noturnas no sinal, sendo 21 de forte intensidade e, dentre essas, 16 com mais de uma hora de duração. Através de comparações com experimentos do INPE constatou-se serem Bolhas Ionosféricas as principais responsáveis pelas cintilações.

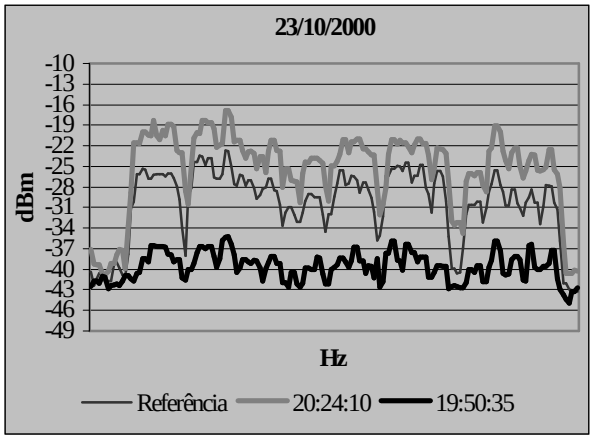

Figura 2. Exemplo de cintilação no espectro.

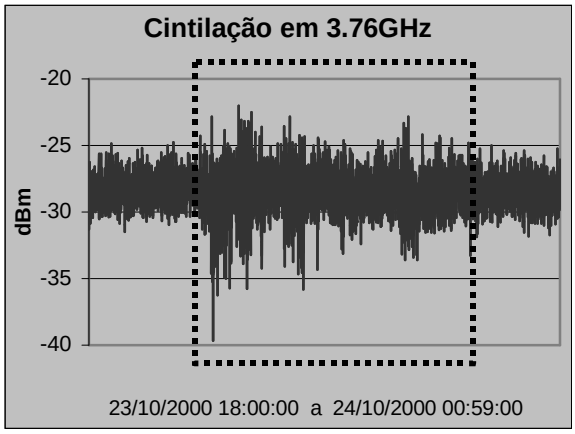

Figura 3. Exemplo de cintilação no tempo.
(sinal dentro da área pontilhada – ver tabela 4)

A tabela 4 mostra os dados das cintilações noturnas no sinal e as datas de ocorrência de Bolhas Ionosféricas registradas pelo imageador do INPE em São João do Cariri (PB - 7°S 37°W). O raio de abrangência desse instrumento é de 15.8 graus, conseguindo alcançar o local do enlace monitorado.

Pesquisou-se também quais os valores de alguns índices geomagnéticos e solares visando correlacionar a ocorrência de tempestades magnéticas com as cintilações (ver tabelas 2, 3 e 4 e figura 4).

Tabela 2 : Valores do índice Kp

Valores iniciais	Valores finais	Tipo do dia
0	24o	Calmo
24+	indeterminado	Perturbado

Fonte : INPE

Tabela 3 : Valores do índice Dst

Valores iniciais	Valores finais	Tipo da Tempestade Magnética
>0	-30	Ausência
-31	-50	Fraca
-51	-100	Moderada
-101	indeterminado	Intensa

Fonte : INPE

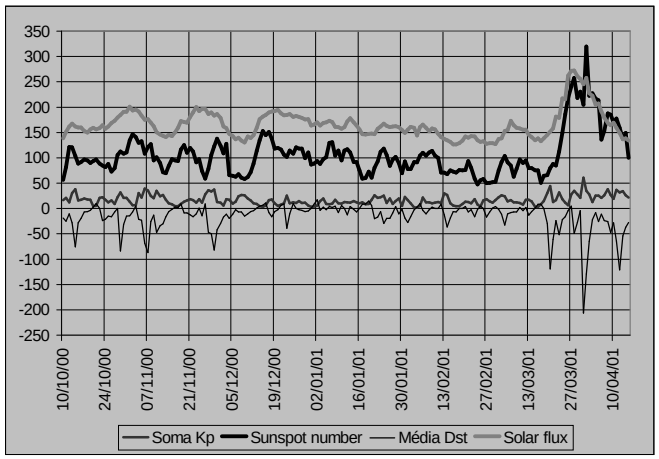

Fontes :
ftp.gfz-potsdam.de/pub/home/obs/kp-ap/tab/ para Kp de abril
swdcdb.kugi.kyoto-u.ac.jp/dstdir/index.html para Dst de abril
www.dxlc.com/solar para os sunspot numbers e solar flux de abril
ftp.ngdc.noaa.gov para demais Kp, Dst, sunspot numbers e solar flux

Figura 4. Índices solares e geomagnéticos no período (ver tabela 4)

Cintilações em 4GHz

Tabela 4 : Cintilações noturnas no enlace Brasilsat B2 e índices solares e geomagnéticos (10/10/2000 a 15/04/2001).

Data	Início	Fim	Duração	Tipo[1]	ΣKp[2]	Dst[3]	Sunspot[4]	Solar flux[5]
10/10/2000	20:59:35	23:24:35	2:25:00	3	16+	-18	57	139.1
12/10/2000	20:13:45	22:34:05	2:20:20	3	12+	-10	122	161.9
13/10/2000	20:04:25	21:26:45	1:22:20	3	31-	-28	121	167.2
14/10/2000	21:06:25	21:14:20	0:07:55	3	39-	-76	104	162.3
15/10/2000	20:10:50	21:59:20	1:48:30	3	16o	-28	89	160.1
16/10/2000	19:31:20	21:28:05	1:56:45	3	17+	-19	92	159.8
18/10/2000	20:26:50	22:16:30	1:49:40	3	18-	-6	95	149.9
19/10/2000	20:28:00	22:14:25	1:46:25	3	17+	-3	90	156.5
20/10/2000	20:25:20	22:21:25	1:56:05	3	5o	3	94	159.3
21/10/2000	19:58:40	23:42:45	3:44:05	3	6-	10	97	156.5
23/10/2000	19:43:10	23:46:55	4:03:45	3	23o	-24	85	164.8
24/10/2000	19:45:30	23:17:05	3:31:35	3	17o	-21	82	157.5
25/10/2000	20:01:40	1:12:30	5:10:50	3	12+	-15	88	162
26/10/2000	20:47:00	20:47:00	0:00:00	3	16o	-16	73	168.9
28/10/2000	23:56:10	23:56:10	0:00:00	2	23o	0	106	179.7
31/10/2000	20:55:50	21:19:20	0:23:30	3	21+	-15	111	190.5
08/11/2000	21:19:00	22:28:50	1:09:50	3	25-	-26	127	169.5
09/11/2000	21:21:20	23:47:10	2:25:50	3	21-	-13	95	163
11/11/2000	21:51:30	21:51:30	0:00:00	2	24o	-34	90	146.6
13/11/2000	21:09:10	21:38:20	0:29:10	2	17+	-16	70	140.6
14/11/2000	20:33:50	20:33:50	0:00:00	3	10+	-6	84	145.4
15/11/2000	19:40:50	20:53:20	1:12:30	3	8o	-1	98	143.2
16/11/2000	19:35:50	19:35:50	0:00:00	3	5o	3	95	150.7
19/11/2000	20:02:40	20:03:10	0:00:30	2	14o	-9	125	170.7
23/12/2000	21:09:40	21:09:40	0:00:00	2	25+	-39	102	184.7
24/12/2000	21:23:30	21:23:30	0:00:00	2	10+	-10	115	186.7
12/01/2001	21:44:30	21:44:30	0:00:00	2	12+	-12	117	172.5
03/02/2001	22:08:00	22:08:00	0:00:00	2	2o	-2	92	159
06/02/2001	22:01:30	22:17:40	0:16:10	2	22o	-3	110	165.3
20/02/2001	20:48:50	20:48:50	0:00:00	2	14-	4	76	142.3
02/03/2001	20:26:40	20:26:40	0:00:00	2	16+	4	53	127.4
07/03/2001	21:32:10	21:32:10	0:00:00	2	17-	-8	85	174
11/03/2001	21:19:20	21:19:20	0:00:00	2	7+	-4	90	155.8
14/03/2001	20:56:40	21:01:30	0:04:50	2	14+	-6	80	140.7
15/03/2001	20:26:40	20:42:10	0:15:30	2	4-	1	75	134.7
05/04/2001	19:51:40	20:00:00	0:08:20	2	26-	-26	214	207.5
11/04/2001	20:06:00	22:21:10	2:15:10	3	37o	-64	178	159.6

Obs1. : Ausência de dados nos dias 29/11/2000, 17 a 18/12/2000, 15 a 18/02/2001 e 22 a 26/03/2000
Obs2 : Aquisição de 10 em 10 segundos, de 10/10/2000 a 15/04/2001, num total de, aproximadamente, 1.600.000 registros.
Obs3 : Data em negrito = Ocorrência de Bolhas Ionosféricas; Data em itálico = Dias em que o imageador não funcionou.
[1]Tipo : 3 = 50% das frequências com variações de +- 3dB em relação ao sinal de referência;
2 = 50% das frequências com variações de +- 2dB em relação ao sinal de referência;
Sinal de referência = espectro às 18:00 do dia em questão.
[2] ΣKp = Número proporcional ao grau de perturbação do campo geomagnético global, porém mais representatido do hemisfério norte.
[3] Dst = Disturbance Storm Time. Número, em nT, proporcional ao grau de perturbação do campo geomagnético equatorial.
[4] Sunspot = Número de manchas solares.
[5] Solar flux = Fluxo do disco solar em J/s/m^2/Hz, na frequência de 2800MHz.

Conclusões

A concordância entre as observações do INPE e as cintilações no sinal monitorado mostram que as comunicações por satélite na faixa de 4GHz, pelo menos até latitudes próximas a 22^{o}S, podem ser severamente afetadas pela presença de Bolhas Ionosféricas, especialmente entre 19:30 e 00:00, hora local.

A ocorrência de Bolhas Ionosféricas em dias em que não foram registradas cintilações no sinal monitorado explica-se pelo fato de que nem todas as bolhas têm tamanho suficiente para alcançar baixas latitudes (Rio de Janeiro, por exemplo), enquanto que o instrumento do INPE está localizado muito próximo ao Equador Magnético, detectando também as bolhas menores.

As cintilações ocorreram com maior intensidade em outubro de 2000 e abril de 2001, com boa correlação com os índices Dst e Kp, porém sem muita correlação com o número de manchas solares e com o fluxo solar em 2800MHz.

As cintilações intensas em baixas latitudes parecem estar mais relacionadas a Tempestades Magnéticas moderadas (ver tabelas 3 e 4 e figura 4) pois o período de Tempestades Magnéticas intensas de março e abril só produziu um evento (14/04) enquanto os períodos de Tempestades Magnéticas moderadas de outubro e novembro produziram 20. Em outras palavras, parece que as Bolhas Ionosféricas com tamanho suficiente para ultrapassar as latitudes equatoriais (até $\cong 10^{o}$) estão mais associadas a Tempestades Magnéticas moderadas.

Para estudar o efeito da latitude pretende-se instalar um sistema de aquisição na localidade de Barro Alto (15º07'S, 48º55'W), em Goiás, que terá os seus dados comparados com os do Rio de Janeiro.

Apesar de alguns dos equipamentos envolvidos nesse experimento possuírem registro de erro, por motivos diversos não foi possível utilizá-los convenientemente de forma que não se obteve uma correlação temporal precisa entre os eventos ionosféricos e os erros nos enlaces. Esse problema será resolvido por um sistema que ficará enviando e recebendo uma mensagem pré-definida. A comparação dos dados enviados com os recebidos indicará ocorrência de erro que será registrado para posterior análise.

O acompanhamento do desempenho e da qualidade dos serviços de telecomunicações por satélite é muito importante sendo recomendável que os usuários tenham a maior clareza possível sobre a confiabilidade dos serviços contratados. No caso de sistemas satélite os únicos problemas amplamente divulgados são os causados pela Interferência Solar (alinhamento antena-satélite-Sol). Essa deficiência na divulgação de outras causas de problemas deve ser alvo de atenção por parte da comunidade.

O monitoramento contínuo com análise diária da qualidade de um enlace satélite pode ser muito útil na logística das telecomunicações de uma empresa uma vez que o início de um período de cintilação pode ser percebido antecipadamente às possíveis falhas, proporcionando mais tempo para o acionamento das medidas cabíveis.

Por fim pode-se concluir que a utilização de dados geomagnéticos e solares proporcionam um contexto geofísico mais completo facilitando a estimativa da confiabilidade dos enlaces e proporcionando mais tempo para tomadas de decisão.

Referências

ITU-R, 1998, The Ionosphere and its effects on radiowave propagation - A guide with background to ITU-R procedures for radioplanners and users.

Santana, D. C, 2000, Estudos da evolução temporal/espacial das derivas das depleções do plasma ionosférico por imagens digitais da aeroluminescência OI 630nm noturna, Dissertação de mestrado, INPE, São José dos Campos.

Agradecimentos

O autor agradece a C. B. Menezes, do Departamento de Equipamentos Eletroeletrônicos, pelo apoio com a instrumentação e a J. H. A. Sobral e D. C. Santana, do Instituto Nacional de Pesquisas Espaciais (INPE), pelas informações fornecidas e esclarecimentos sobre Geofísica Espacial.

Observação de Bolhas de Plasma por Fotômetro e Imageador

R. A. Buriti (1); A. F. de Medeiros (2); J. H. A. Sobral (2); H. Takahashi (2); D. Gobbi (2); A. A. Nepomuceno (1); M. F. Costa (1).– Departamento de Física, CCT/UFPB, CEP 58109-970, Campina Grande, PB, Brasil (2) – CEA/INPE, CEP 12201-970, S. J. dos Campos, SP, Brasil

Resumo

Medidas simultâneas da luminescência atmosférica (ou *airglow*, na língua inglesa) proveniente do oxigênio atômico da região F noturna, no comprimento de onda de 630nm (OI630 nm), através de fotômetro e imageador *all-sky*, permitiram registrar a passagem de bolhas de plasmas na região do nordeste brasileiro (7^0S, 35^0O). As observações simultâneas têm sido realizadas desde outubro de 2000. Dezenas de trabalhos já foram publicados desde as primeiras detecções das bolhas ionosférias sobre o território nacional por Sobral et al. (1980a,b). Neste trabalho foram utilizadas quatro noites em que a passagem das bolhas foram detectadas por ambos os equipamentos. Uma grande variação de intensidade absoluta do OI630 nm caracterizou a presença destas perturbações ionosféricas. A bolha, quando observada por fotômetros, provoca uma queda brusca da intensidade da emissão do OI630 nm. Algumas bolhas tiveram uma queda acentuada da intensidade do OI630 nm e, em torno de 0,5 a 1 hora depois, retornou a valores de intensidade anterior à passagem da bolha. Por outro lado, a imagem de bolhas registradas pelo imageador *all-sky*, é facilmente reconhecida porque deixam estrias claras e escuras, principalmente no sentido norte-sul da imagem. As noites estudadas neste trabalho foram 18 e 29/11, 02 e 24/12/2000. Registramos, dentro de um intervalo de 1 hora de observação, a diminuição do sinal em até 67% do valor máximo antes da passagem da bolha pelo campo de visão do fotômetro (2^0 x 2^0) e aumento de até 225% após a passagem da bolha. A noite de 24/12, por outro lado, apresentou queda de 82% em aproximadamente 20 minutos de observação. A observação da bolha através de imageador, permite estudar a sua morfologia, direção e velocidade zonal de propagação, fato que não é possível apenas com dados de fotômetro. As características das bolhas observadas serão apresentadas e discutidas neste trabalho.

Introdução

A bolha de plasma é uma diminuição da concentração do plasma na ionosfera, que resulta de uma instabilidade do plasma inosférico equatorial (magnética) noturna. Ela é o resultado do acoplamento entre o campo geomagnético e o movimento dinâmico das partículas ionizadas. Seu deslocamento é sempre de oeste para leste, mas, o sentido contrário de observação já foi reportada na literatura (Taylor, et al., 1997).

As bolhas podem ser detectadas por instrumentos óticos do chão ou à bordo de foguetes ou satélites quando estes registram uma forte queda da intensidade do *airglow* do OI630 nm. A intensidade de luz desta emissão deve-se a uma recombinação dissociativa entre os íons O_2^+ e elétrons presentes na camada F noturna da ionosfera produzindo assim, átomos de oxigênio em dois estados excitados, ou seja:

$$O_2^+ + e^- \rightarrow O(^1S) + O(^1D).$$

A fração de cada espécie excitada na reação acima representa a eficiência quântica para aquele estado excitado (Sobral et al., 1994). No caso do $O(^1S_0)$, quando relaxado para o estado excitado $^1D_2$, emite luz no comprimento de 557,7 nm, enquanto que o $O(^1D_2)$ emite no comprimento de 630 nm quando relaxa para o estado $^3P_1$. A inexistência da emissão do 630 nm próximo da mesopausa, ao contrário do 557,7 nm, deve-se ao fato que, nestas altitudes, o oxigênio atômico no estado $O(^1D)$ tem um tempo de vida (~110 s) maior que o tempo de colisão com outras moléculas nestas altitudes. Quando ocorre a diminuição da concentração de elétrons na camada F é de se esperar uma diminuição da intensidade do 630 nm.

Desde outubro de 2000, está em operação um imageador de varredura *all-sky* na região equatorial (7^0S, 35^0O). Este equipamento, juntamente com um fotômetro e um magnetômetro, é capaz de realizar um estudo mais detalhado dos fenômenos geofísicos da região equatorial. Este trabalho utiliza quatro noites de observação simultâneas da variação da intensidade absoluta do OI630 nm medida com o fotômetro zenital Multi-3 e a imagem *all-sky* desta emissão com imageador.

Instrumentação

A observação ótica simultânea de bolhas de plasma através de um fotômetro zenital e de um imageador de varredura do céu todo (*all-sky*), permite obter um conjunto de dados com mais informações sobre este fenômeno. O fotômetro Multi-3 tem operado desde novembro de 1997 no Observatório de Luminescência

Atmosférica da Paraíba (OLAP). Este equipamento foi desenvolvido pelo Grupo LUME do INPE O equipamento realiza medidas rotineiras durante 13 noites em torno da lua nova. O gerenciamento do fotômetro é feito por um micro PC que também é responsável pela aquisição de dados e cálculo de intensidade absoluta e temperatura em tempo real. Detalhes deste equipamento pode ser encontrado em Takahashi et al., 1989.

O imageador *all-sky* só começou a operar no OLAP a partir de outubro de 2000. Ele fotografa a emissão do oxigênio atômico 630 nm durante o tempo de exposição de 90 segundos. A resolução temporal para a emissão do OI630 nm é ~7,5 min.

Resultados

A comparação entre o que foi observado por fotômetro (Figura 1) e por imageador (Figura 2) mostra o quanto é importante o estudo destas bolhas com imageador, pois, o fotômetro, observando apenas a região zenital, fornece muito pouco sobre o perfil da bolha de plasma. A Figura 2 representa a seqüência de imagens obtidas pelo imageador, a cada 27 minutos, para o dia 18/11/2000, entre 19h53'15" e 22h09'31". Percebe-se a formação e o deslocamento de oeste para leste de várias regiões escuras dentro deste intervalo de tempo. Figura 1, por outro lado, mostra a variação local do OI630 nm obtida pelo fotômetro. É fácil perceber a o que acontece com a intensidade quando uma bolha entra e sai do campo de visão do fotômetro. Em torno das 20h10min, o valor da intensidade medido pelo fotômetro foi de ~ 30 R quando começa a subir para valores ~ 310 R, isto corresponde a um aumento de quase 1000 % dentro de um intervalo de 35 minutos. Em seguida, a intensidade começou a cair até um valor de ~ 100 R, ou seja, sua intensidade caiu em torno de 67%. A intensidade do OI630 nm voltou a subir até atingir um valor de 460 R às 22h12min, quando novamente começou a descer. Pela Figura 1 é possível notar que a intensidade voltou a cair, porém, pelas duas últimas imagens, mostradas na Figura 2, a bolha começou a entrar no campo de visão do fotômetro. O fato de a linha OI630 nm apresentar um sinal muito fraco no início da noite deve-se a altura elevada da camada F; a camada tende a descer e, em torno da meia-noite, a intensidade atinge valor máximo. Isto só é válido para os meses de setembro a abril do ano seguinte, segundo observações desta emissão nos de 1998 e 1999 (Buriti et al., 2000). Nos meses de maio a agosto, o máximo desta emissão, quando observado a noite, encontra-se em torno das 18h00min (hora local).

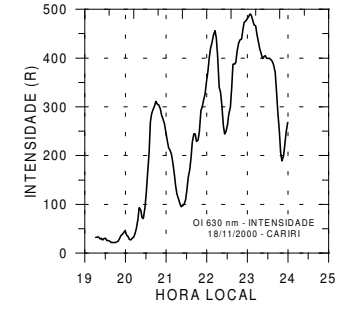

Fig. 1 – Variação do OI630 nm para 18/11/2001.

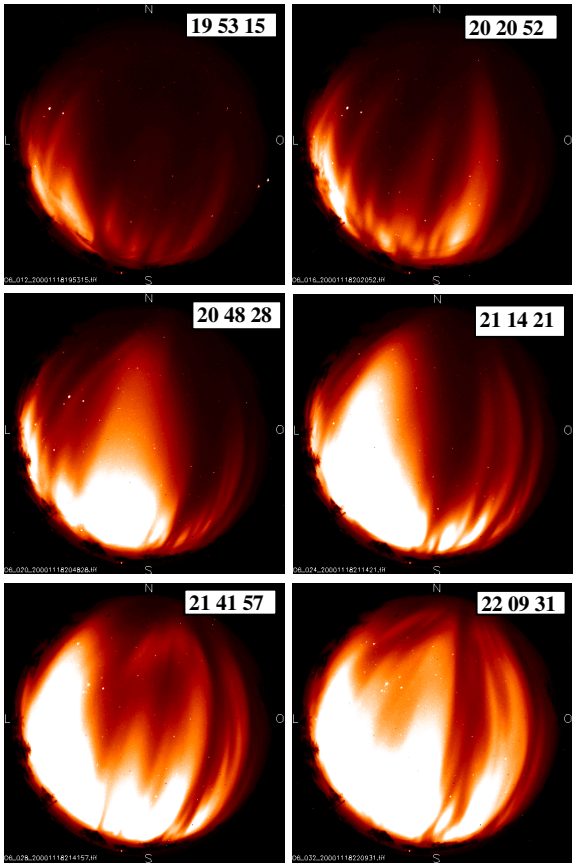

Fig. 2 – Seqüência temporal (hhmmss) de imagens de OI630 nm obtida em 18/11/2000 em S. J. do Cariri (7,4^{0}S, 36,5^{0}O). O número no canto superior direito é a hora local em que cada imagem foi obtida. A parte superior da imagem é o norte e a direita é o oeste.

A Figura 3 mostra o comportamento da intensidade do OI630 nm, medida pelo fotômetro, para os dias 29/11, 02 e 24/12. Para o dia 29/11, o fotômetro registrou a presença de bolhas de plasma, porém, a variação não foi tão acentuada quanto aquela observada para o dia 18/11. Entre 21h55min e 22h20min o sinal a intensidade caiu 50%. Às 23h00min o sinal atinge um valor de 328 R, o que corresponde um aumento de ~ 200 R ou 228 %, em apenas 40 minutos. À meia-noite o fotômetro apresentou um pequeno decréscimo no sinal por um curto intervalo de tempo,

isto, segundo os dados de imageador, que também apresentou uma diminuição da intensidade da imagem neste horário, corresponde a parte mais escura de uma bolha de plasma que continha várias ramificações. A última bolha observada neste dia (mais especificamente o dia 30/11/2000) ocorreu à 1h40min.

O tempo de aquisição de dados de imageador referente ao dia 02/12, ao contrário dos dados de fotômetro, é bem menor, a aquisição de imagem começou às 22h25min e foi até 3h00min (03/12). A primeira imagem disponível já mostra a presença de várias bolhas no céu. O aumento do sinal do OI630 nm a partir das 22h, é observado também no imageador. Podemos ver que, juntamente com este aumento, existe duas depressões em torno das 23h. A linha acompanhando o sinal do OI630 nm para este dia (ver Figura 3) representa um ajuste polinomial e mostra como seria o sinal desta emissão sem a presença de bolhas. Este comportamento, como já descrito no texto, é uma característica do OI630 nm para este mês de dezembro. O comportamento da intensidade do OI630 nm do dia 24/12, medido pelo fotômetro, registrou um pico de intensidade às 21h45min. Segundo as imagens de OI630 nm, este pico deve-se a um período de tempo em que não existia bolhas no campo de visão do fotômetro, porém, a presença de bolhas antes e depois do pico de intensidade é marcante. Isto equivale a dizer que, as bolhas reduziram o sinal em aproximadamente 3 vezes o valor em torno de 23 h. A linha acompanhando o sinal do OI630 nm para este dia (ver Figura 3) representa um ajuste polinomial.

O comportamento da intensidade do OI630 nm do dia 24/12, medido pelo fotômetro, registrou um pico de intensidade às 21h45min (ver Figura 4). Segundo as imagens de OI630 nm, este pico deve-se a um período de tempo em que não existia bolhas no campo de visão do fotômetro, porém, a presença de bolhas antes e depois do pico de intensidade é marcante. Isto equivale a dizer que, as bolhas reduziram o sinal em quase 3 vezes o valor em torno de 23h.

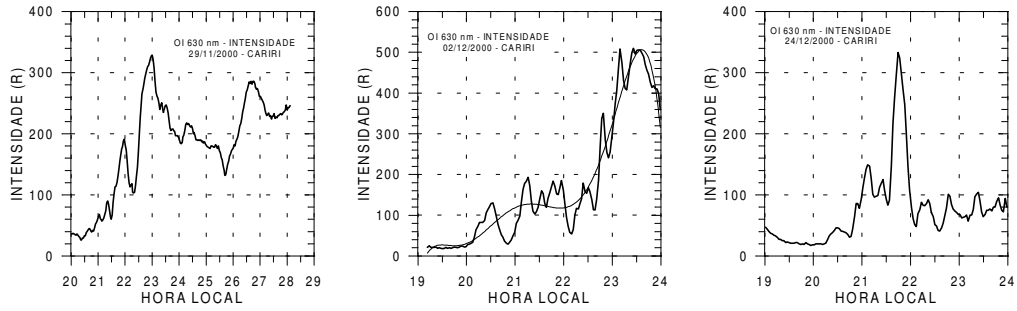

Fig. 3 – Variação temporal da intensidade do OI630 nm para os dias 29/11, 02 e 24/12/2000. Fortes variações do sinal indicam a presença de bolhas de plasmas dentro do campo de visão do fotômetro. As imagens das bolhas de plasma nos respectivos dias (não mostradas neste trabalho), confirmam a sua presença. A linha que acompanha o OI630 nm do dia 02/12/2000 representa um ajuste polinomial.

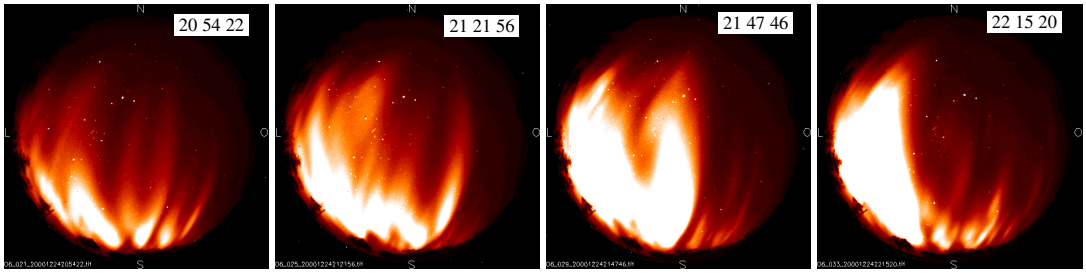

Fig. 4 – Seqüência temporal (hhmmss) de 4 imagens de bolhas de plasma para o dia 24/12/2000. A parte superior de cada imagem é o norte enquanto que o lado esquerda é o leste.

A velocidade de deslocamento das bolhas foi determinada por métodos computacionais. A calibração do imageador é fundamental para este cálculo, pois, relaciona o deslocamento da bolha nas imagens com a sua velocidade real. O cálculo da velocidade consistiu basicamente em fazer a correlação cruzada entre todas as linhas de pixels da CCD de duas ima-

gens, espaçadas de ~7 minutos, contendo bolha. Esta correlação é uma matriz de 512x512 elementos cujo *lag* permite calcular a velocidade média de deslocamento zonal da bolha dentro de uma área do céu de 256x256 km^2. O resultado encontra-se na Tabela 1 que mostra hora de cada imagem utilizada para determinar a velocidade zonal do deslocamento da bolha. Em algumas situações o desvio padrão apresentou-se alto. Isto deve-se ao fato de o cálculo ter envolvido vários pés de bolha. Naturalmente, todas as partes de uma bolha de plasma não se move com a mesma velocidade e isto acarreta um alargamento no desvio da velocidade determinada, além disto, a mudança de formato da bolha ao longo do tempo, também ocasiona erro na determinação deste parâmetro. A última coluna mostra o valor da correlação máxima entre duas linhas de duas imagens utilizadas par determinar a velocidade.

Conclusões TABELA 1 – Velocidade média zonal de deslocamento de bolha de plasma.

DATA	IMAGEM INICIAL (hhmmss)	IMAGEM FINAL (hhmmss)	VELOCIDADE (m/s)	DESVIO (m/s)	CORRELAÇÃO
18/11/2000	21 41 57	21 48 25	87,3	19,5	0,74
	22 09 31	22 15 59	73,9	2,8	0,94
29/11/2000	22 17 34	22 24 02	64,8	7,2	0,7
	23 38 33	23 45 01	36,7	15,1	0,85
02/12/2000	22 25 38	22 32 07	124,0	16,2	0,9
	23 46 40	23 53 08	95,8	26,3	0,75
24/12/2000	21 00 49	21 07 17	84,4	8,6	0,79

O estudo de bolhas a partir de dados de fotômetro de observação zenital permite determinar a presença de bolhas quando esta entra no campo de visão do fotômetro, porém, como estas ocupam grandes dimensões na atmosfera, fica impossível para este equipamento informar sobre a forma destas bolhas. A utilização de imageador permite acompanhar o desenvolvimento das bolhas ao longo da noite, e ainda observar sua forma na região de emissão do OI630 nm que está próximo dos 250 km de altitude. Reduções de até 3 vezes na intensidade do *airglow* pode acontecer quando uma bolha está presente na região de emissão. Fortes variações de até 1000% de aumento dentro de 35 minutos foi observado. A velocidade média zonal de deslocamento das bolhas ficou, para os dias observados, entre 37 e 124 m/s (130 e 446 km/h) e mostrou uma tendência de queda durante a noite.

Referências

Buriti, R. A., H. Takahashi e D. Gobbi. First OI6300 and OI5577 airglow observation results from 7.5^0 S. 6^0 International Congress of Brazilian Geophysical Society, Rio de Janeiro, 1999.

Sobral, J. H. A., Abdu, M. A., Batista, I. S. Airglow studies on the ionosphere dynamics over low latitude in Brazil. *Ann. Geophysicae* 36(2), 199-204, 1980a.

Sobral, J. H. A., Abdu, M. A., Batista, I. S., Zamlutti, C. J. Association between plasma bubble and airglow disturbances over Brazilian low latitudes. *Geophys.l Res. Letters*, 11(7), 980-982, 1980b.

Sobral, J. H. A., H. Takahashi, M. A. Abdu, P. Muralikrisna, G. L. Borba, Y. Sahai, C. J. Zamlutti, E. R. de Paula e P. P. Batista. Contribution of the cascading process O(^{1}S) → O(^{1}D) to the production of the atomic oxygen O(^{1}D) and OI5577 630 nm airglow in the nocturnal thermosphere. *J. Geomag. Geoelectr.*, 46, 747-754, 1994.

Taylor, M. J., J. V. Eccles, J. LaBelle and J. H. A Sobral. High resolution OI (630 nm) image measurements of F-region depletion drifts during the Guará campaign. *Geophys. Res. Letters.*, 24, 13, 1699-1702, 1997.

Takahashi, H., B. R. Clemesha, D. M. Simonich, N. R. Teixeira, R. M. Lobo e A. Eras. Equatorial mesospheric and F-region airglow emission observed from latitude 4 S. *Planet. Space Sci.,* 37(6), 649-655, 1989.

Agradecimentos

Estes autores agradecem à Prefeitura de S. J. do Cariri pelo apoio ao nosso trabalho incluindo um auxílio técnico cedido ao operador Sr. J. A. Souza. O Observatório é apoiado financeiramente pela Universidade Federal da Paraíba (UFPB), Instituto Nacional de Pesquisas Espaciais (INPE) e FINEP Pronex No. 76.97.1079.00.

Observed Auroral Electric Field Modulation In The Equatorial Electrojet

Clezio M. Denardini, Mangalathayil A. Abdu, José H. A. Sobral, INPE, Brazil

Abstract

We will present Range Time Intensity (RTI) maps and H component of the Earth magnetic field from magnetometer data to show an observed auroral electric field modulation in the equatorial electrojet during specific disturbed period of December 1999. The RTI maps were obtained from data of the RESCO radar placed in São Luís (2.3° S; 44.2° W; dip: -0.5°), locate at the dip equator. The magnetometer data are from in Vassouras (22.4° S, 43.7° W, dip: -34°) and Jicamarca (12° S, 76.9° W, dip: 1°). We use also the auroral geomagnetic indexes AU and AL to characterize auroral activity and the Dst index as an equivalent equatorial magnetic disturbance index. We start summarizing some important features of the equatorial electrojet. In this paper, we present the technique applied to process our data, to be followed by a discussion of some interesting events observed, and our conclusions.

Introduction

The equatorial electrojet current (EEJ) is an eastward current sheet that flows at the E layer heights between about 90 and 120 km centered at the magnetic equator. The current sheet extends in a zone of ~ 600 km in the North-South direction. It is driven by the global dynamo electric field and is produced as a consequence of the high Cowling conductivity, which occurs at the dip equator. In the E region over dip equator the plasma density gradient, zonal electric field, and geomagnetic filed are mutually perpendicular (Forbes, 1981; Reddy, 1989).

The EEJ can drive plasma instabilities and produce field-aligned irregularities. They are present day and night, except for short periods during sunset and sunrise (Farley and Balsley, 1973; Fejer, 1996). It is well known that the horizontal component of Earth magnetic filed (H component) gets enhanced during the day due to the eastward EEJ current. Nevertheless, during disturbed time when the EEJ get weak or is totally inhibited the H component goes through a corresponding reduction in intensity.

Techniques

The coherent backscatter radar detects energy back scattered by plasma irregularities of scale size half the probing wavelength. The radar technique has been applied to study the ionospheric irregularities characteristics in a wide range of latitudes and through all ionospheric altitudes (Bowles et al., 1960; Bowles e Cohen, 1962; Fejer, 1979; Fejer e Kelley, 1980; Hanuise, 1983; Fejer, 1985; Fejer e Providakes, 1987; Krishna Murthy e Sudha Ravindran, 1994; Krishna Murthy et al., 1998). The RESCO (Radar de Espalhamento Coerente) radar is a coherent backscatter radar operating at 50 MHz, which is sensitive to field aligned irregularities of 3m-size. The radar uses a coaxial-collinear array antenna consisting of 768 dipoles arranged in 16 antenna each of 48 dipoles.

During December 1999, we have carried out an EEJ observational campaign, and a few days of E region coherent scatter observation were made during daytime. In addition, observations of EEJ effect over the H component of earth magnetic field were monitored by a flux gate magnetometer in both Jicamarca and Vassouras sites. On some days the EEJ was observed between 07:30 and 18:00 LT. The RESCO radar was operated with narrow antenna beam tilted 30° westward in the magnetic equatorial plane. By comparing the RTI maps with the H-component variations we have tried to study some characteristics of disturbance electric fields that propagate from high latitude to equatorial regions during magnetically disturbed conditions.

RTI maps were constructed for each day of observation. These maps are generated through integrating the Doppler power spectral distribution obtained from FFT analysis for all range gates at each set of 512 echoes received. One-minute average of the spectra at each range bin was used to obtain the RTI values. The H components at both sites were subtracted from their local midnight values to eliminate the calibration effects, which then yielded the values of the ΔH component. The effect of the EEJ over the H component is computed by taking the difference between the ΔH values of Jicamarca and that of Vassouras.

All the RTI maps obtained for the period of study are shown in the figure 1. In the lower half of each panel is shown the RTI pattern superimposed on the ΔH variations over Jicamarca and Vassouras. Also shown, in the upper half of each panel in figure 1, are the auroral indices AU and AL.

Discussion

Here we will not make distinction between type 1 and type 2 irregularities because we are interested in the total power backscattered from them. We only need to remember that these irregularities are driven basically by electric fields, which influence their movement through the EEJ.

We have noted in figure 1 the RTI maps during disturbed time in comparison with those from quiet

time. Figure 2 shows the variations of the AU, AL and Dst indices during the campaign period. From this figure it may noted that after December 13 the auroral activity reduced drastically. The RTI maps from disturbed time compose the left column while RTI maps from quiet time compose the right column of figure 1.

We can observe from the disturbed time that some days have a strong correlation between the ΔH component and the total power backscattered from the EEJ in determined periods of daytime. On December 12 it is evident the relations between the second maximum in the RTI map with de ΔH component as well as the other subsequent maximum. Another good correlation is around midday on December 13, when the maximum in the RTI map agrees perfectly with the peak in the ΔH component. On these days, during the periods of very good agreement, the AL

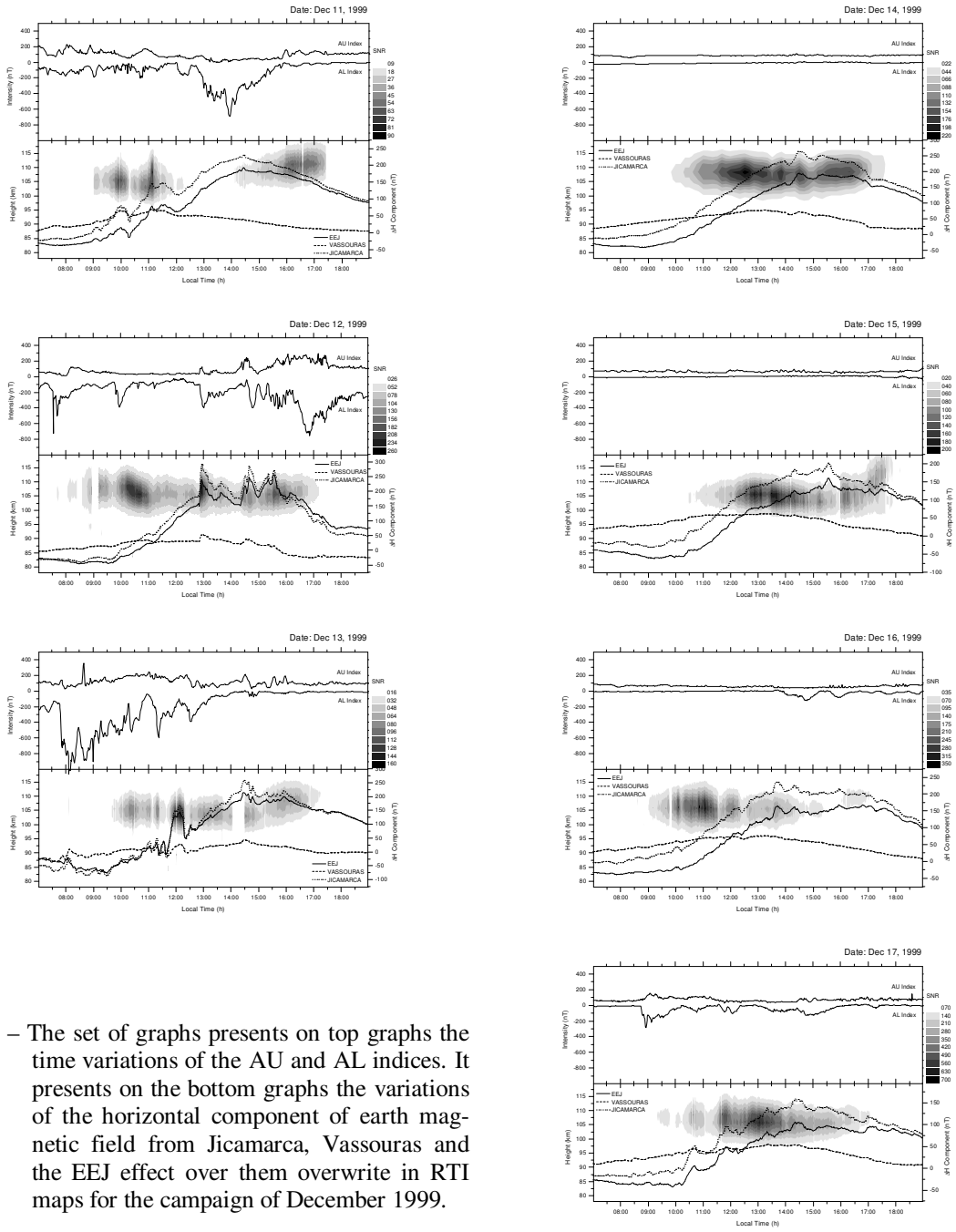

Fig. 1 – The set of graphs presents on top graphs the time variations of the AU and AL indices. It presents on the bottom graphs the variations of the horizontal component of earth magnetic field from Jicamarca, Vassouras and the EEJ effect over them overwrite in RTI maps for the campaign of December 1999.

index was always under -400 nT, indicating auroral activity.

With respect to December 11, it is hard to say we have a very good correlation between the RTI map and the ΔH component, although the magnetic disturbances start on this day and the two firsts peaks on the map seems to agree with the ΔH component variation. Furthermore, during these periods of agreement the AL index were almost always under about -200 nT and we used data from Jicamarca (two hours lag). So, it is possible that if we had used data from São Luís we could see better agreements. Besides, on December 11 the Dst index was varying around -30 and -15 nT when irregularities were observed by the RESCO radar. Then, it fell down quickly to –90 nT and the EEJ was completely inhibited between 12:00 and 14:00 LT though the ΔH

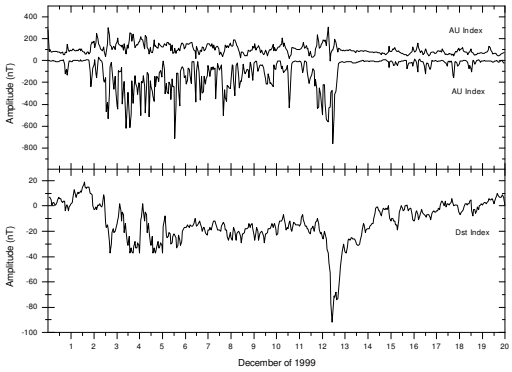

Fig. 2 – Variation of the AU, AL and Dst indices from 1 to 20 December 1999.

component continued to increase its value.

We attribute the observed modulation during the disturbed periods to prompt penetration (PP) of electric field of magnetospheric/auroral origin, which occurs at almost the same time in low and high latitudes. This PP is driven by Pedersen currents that generates DP2 fluctuation (Sastri et al., 1993) and it is amplified on the equator by the Cowling effect. Gonzales et al. (1979) presented a study concluding that a probable source of equatorial disturbances can be prompt penetration of magnetospheric/auroral electric fields into the equatorial zone through the plasmasphere. Abdu et al. (1997) pointed out that during magnetospheric disturbances short period electric fields associated with development and recovery phase of a magnetic sub storms can take place in the low latitude ionosphere. Abdu et al. (1998) concluded that the coherent occurrence of magnetic fluctuation in both high and equatorial latitudes indicates that magnetospheric/auroral electric fields penetrate to the equatorial ionosphere from the polar ionosphere.

During the quiet days, on the right column, we observe low correlation between the ΔH component and the total power backscattered from the EEJ. On these days the poor agreement between the ΔH component and the backscattered power from the irregularities seem to be caused by the EEJ itself. If we look carefully to these graphs, we can see a weak correlation between some maximums in the RTI maps and the ΔH component. But the AL index does not show any disturbance in the auroral zone, meaning that there are no external electric fields propagating to the equatorial zone. Therefore, these observed variations can be generated by internal sources acting over the dynamo system yielding variation in the EEJ, and consequently inducing currents which increases/decreases the H component amplitude. It is usual not to be easy to identify source of internal perturbation, but just to give an example; these internal sources can be gravity waves, which rearrange the plasma distribution and affect the EEJ behavior.

Conclusions

We have noted that during moderate disturbed period we can have a clear modulation of the EEJ observed through backscatter radars. It becomes more evident when the auroral index AU reach values under -400 nT. But it must be taken account the Dst index, which determines the degree of disturbance in the equatorial region as it was done on December 11. In this case the EEJ was totally inhibited and the Dst index showed a great decreasing on its value. The modulations were attributed to PP from magnetospheric/auroral region.

During quiet days there were vary poor correlation between the ΔH component and the EEJ backscattered power, except for some specifics periods of time. In this case, the agreements are believed to be due to the EEJ itself, and it was probably caused by internal sources such as gravity waves.

References

Abdu, M. A.; Sastri, J. H.; Luhr, H.; Tachihara, H.; Kitamura, T.; Trivedi, N. B.; Sobral, J. H. A. *DP 2 electric field fluctuations in the dusk-time dip equatorial ionosphere*. **Geophysical Research Letters**, n. 25, n. 9, p. 1511-1514, May 1998.

Abdu, M. A.; Sastri, J. H.; MacDougall, J.; Batista, I. S., Sobral; J. H. A. *Equatorial disturbance dynamo electric field longitudinal structure and spread F: a case study from GUARA/EITS campaigns.* **Geophysical Research Letters**, v. 24, n. 13, p. 1707-1710, July 1997.

Bowles, K. L.; Cohen, R. *A study of radio wave scattering from sporadic E near the magnetic equator*. In: Smith, E. K. e Matsushita, S. ed., **Ionospheric sporadic E**, London: Pergamon Press, 1962.

Bowles, K. L.; Cohen, R.; Ochs, G. R.; Balsley, B. B. *Radio echoes from field–aligned ionization above the magnetic equator and their resemblance to auroral echoes.* **Journal of Geophysical Research**, v. 65, n. A6, p. 1853-1855, June 1960.

Farley, D. T., Balsley, B. B. *Instabilities in the equatorial electrojet*. **Journal of Geophysical Research**, v. 78, n. A01, p. 227-239, Jan. 1973.

Fejer, B. G. *Natural ionospheric plasma waves*. In: Kohl, H., Rüster, R., Schleger, K. eds. ***Modern ionospheric Science***, Max–Plank Institute for Aeronomy, Katlenburg-Lindau: Germany, 1996. Cap. 8, p. 216-273.

Fejer, B. G. *Small scale plasma irregularities in the auroral ionosphere*. **Proceedings of the 1982-1984 MIT symposia**, v. 5, p. 73-97, 1985.

Fejer B. G; Kelley, M. C. *Ionospheric Irregularities*. **Reviews of Geophysics and Space Physics**, v. 18, n. 2, p. 401-454, May 1980.

Fejer, B. G., Providakes, J. F. *High latitude E region irregularities: new results*. **Physica Scripta**, t. 18, p. 167-178, 1987.

Fejer, J. A. *Ionospheric instabilities and fine structure*. **Journal of Atmospheric and Terrestrial Physics**, v. 41, p. 895-915, 1979.

Forbes, J. M. *The equatorial electrojet.* **Reviews of Geophysics and Space Physics**, v. 19, n. 3, p. 469-504, Aug. 1981.

Gonzales, S. A.; Kelley, M. C.; Fejer, B. G.; Vickrey, J. F.; Woodman, R. F. *Equatorial electric fields during magnetically disturbed conditions 2. Implications of simultaneous auroral and equatorial measurements.* **Journal of Geophysics Research**, v. 84, n. A10, p. 5803-5812, Out. 1979.

Hanuise, C. *High latitude ionospheric irregularities. A review of recent results.* **Radio Science**, v. 18, p. 1093-1121, 1983.

Krishna Murthy, B. V., Sudha Ravindran *Effects of small–scale plasma turbulence on altitude profiles of electron drift velocity in the equatorial electrojet: An experimental study*. **Journal of Geophysical Research**, v. 99, n. A10, p. 19549-19554, Oct. 1994.

Krishna Murthy, B. V., Sudha Ravindran, Viswanathan, K. S., Subbarao, K. V. *Small–scale (~3 m) E region irregularities at and off the magnetic equator*. **Journal of Geophysical Research**, v. 103, n. A9, p. 20761-20772, Sep. 1998.

Reddy, C. A. *The equatorial electrojet.* **Pure and Applied Geophysics**, v. 131, n. 3, p. 486, 1989.

Sastri, J. H.; Rao, J. V. S. V.; Ramesh, K. B. *Penetration of polar electric field to the nightside dip equator at times of geomagnetic sudden commencements*. **Journal of Geophysics Research**, v. 98, n. A10, p. 17517-17523, Out. 1993.

Acknowledgments

C. M. D. wishes to thank FAPESP for financial support to his doctoral degree program through the project n° 98/16156-8, and to Dr. Toyo Kamei from University of Kyoto for the support in provide the auroral data index. M. A. A. wishes to acknowledge the support received from FAPESP through the process 96/05234-2 for the development of the radar project.

On the Deviations of Measured Electron Density Profiles from IRI Predictions for Low Latitudes

P. . Muralikrishna, L. P. Vieira and M. A. Abdu, and E. R. de Paula Instituto Nacional de Pesquisas Espaciais – INPE/MCT, C. P. 515, 12 201-970, São José dos Campos - SP, Brazil (e-mail: murali@dae.inpe.br)

Abstract

In situ electron density profiles obtained from the equatorial stations in Brazil using conventional Langmuir probes and High Frequency Capacitance probes are compared with the IRI predictions in the light of the spectral distribution of the plasma density irregularities observed. Plasma instability mechanisms, especially the Rayleigh-Taylor and the Cross-Field instability mechanisms responsible for the generation of the observed plasma irregularities are used to estimate the growth time and the minimum scale size of irregularities that can be observed at different height regions along the electron density profile. For this purpose simple polynomial approximations are used to represent the observed electron density profiles. A comparative study of the observed characteristics of the plasma irregularities with those expected from the theories can give us information on the reliability of the observed profiles. This reliability estimate is all the more important because of the fact that the techniques used for the measurement of electron density are known to be associated with some inherent problems. Thus one can see whether the deviations of the observed electron density profiles from the IRI predictions are genuine or not. From this comparative study one can also obtain information as to what are the physical parameters responsible for the observed deviations in the profiles and thereby suggest some possible improvements in the methods used for IRI predictions for low latitudes.

Introduction

The International Reference Ionosphere, since its first publication in 1978 by Rawer et al (1978) has undergone periodic modifications in attempts to improve its accuracy in representing the quiet time ionospheric parameters as functions of height, geographic location, local time and sunspot number. To provide a larger data base for these modifications a series of in-situ measurements of electron density and electron temperature were undertaken from the equatorial region in Brazil, where the models proposed so far seem to be less accurate probably due to the diverse electrodynamic and dynamic effects produced by the large magnetic declination angle existing in this region (Abdu et al, 1981). Abdu et al (1990) reported in-situ measurements of electron density and for the first time compared them with the IRI (International Reference Ionosphere, see Rawer et al, 1978) predictions from this region. They found that there existed a reasonably good agreement between the IRI predictions and the rocket measurements, especially for daytime. However the electron temperature estimates made from Langmuir Probe measurements, reported by Kantor et al (1990) deviated considerably from the IRI predictions.

Brazilian SONDA III rockets and a Black Brant X rocket carrying plasma and optical diagnostic experiments were launched from the Brazilian rocket launching stations in Natal (5.9^{o}S, 35.2^{o}W Geog. Lat.) and Alcantara (2.31^{o}S, 44.4^{o}W Geog. Lat.). Langmuir Probes (LP) were used to measure the height profiles of the electron density and electron temperature and High Frequency Capacitance probes (HFC) were used to measure the electron density. The height profiles of electron density obtained on various occasions are compared with the IRI predictions appropriate for the location and time and an attempt is made to understand the differences between them.

The main objectives of the present study are the following

- To compare the observed electron density profiles with the IRI Model predictions.
- To study the spectral characteristics of the plasma irregularities observed at different height regions in the light of their generation mechanisms, especially the Cross-Field instability
- To have a critical view on the reliability of the observed electron density profiles by comparing the expected and observed characteristics of the plasma irregularities.
- Having concluded that the deviations in the observed electron density profiles from the IRI predictions are genuine, to look into the possible reasons for these deviations.
- To look into the possibility of obtaining improvements in the IRI predictions for the equatorial and low latitude regions.

RESULTS AND DISCUSSION

Given in Table 1 is a summary of the rocket flights for which the electron density and temperature height profiles were obtained. Some of these results

especially those related with the deviations of the electron density profiles from the IRI predictions are presented and discussed in here. Also given in the Table are the location, date and time of launch, the experiments flown on board to measure ionospheric parameters, the parameters measured and the apogee height reached by the rocket.

Table 1

Date	Time	Location	Experiments	Parameters	Apogee
26-07-84	1505	Natal	HFC	Ne	565km
11-12-85	2130	Natal	HFC, LP	Ne, Te	516km
31-10-86	2359	Natal	HFC, LP	Ne, Te	444km
29-04-91	1437	Alcantara	HFC, LP	Ne, Te	443km
31-05-92	2351	Alcantara	LP, ETP	Ne, Te	282km
17-11-93	1934	Alcantara	EF,LP,HFC	E, Ne, Te	555km
14-10-94	1915	Alcantara	HFC	Ne	957km
18-12-95	2117	Alcantara	HFC, LP	Ne, Te	564km
11-11-96	2000	Alcantara	LP, ETP	Ne, Te	326km

The electron density profiles and the power spectra of plasma irregularities observed in selected height regions are shown in the following figures. Also shown in the figures are the electron density profiles calculated from the IRI90 model appropriate for the location, local time and the solar activity index.

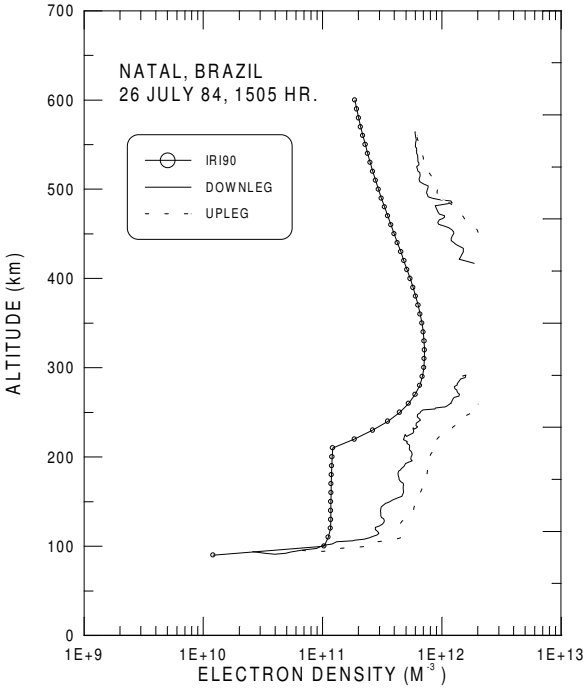

Figure 1 - Daytime electron number density measurements made with an HFC probe on 26-th July, 1984 compared with the IRI90 profile.

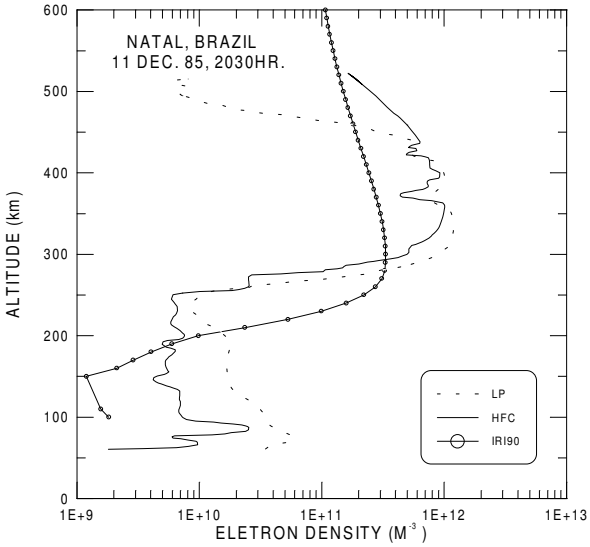

Figure 2 - Nighttime electron number density measurements made with an HFC probe and a Langmuir Probe on 11-th December, 1985 compared with the IRI90 profile.

2130LT, 11-th December, 1985, NATAL

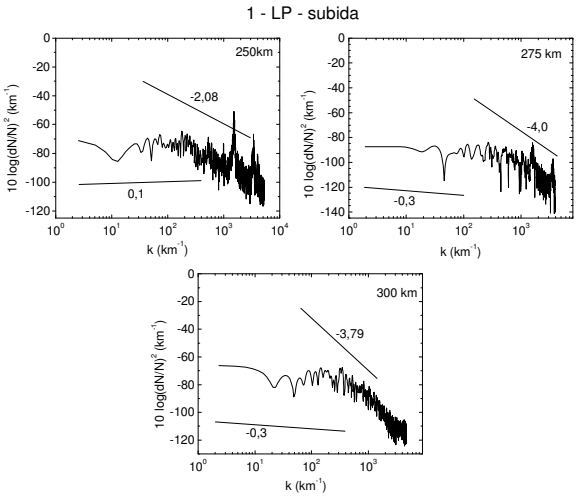

Figure 3 – Plasma irregularity spectra corresponding to selected height regions

From the figures it can be seen that the electron density profiles estimated deviate considerably from the IRI90 model profiles. The main cause of this deviation seems to be the inadequacy of the model to incorporate into it the large day to day variability of the electron density distribution in the equatorial ionosphere over the American sector. However, errors in the LP estimates of the electron density, introduced through the use of relations based on unrealistic approximations also

seem to be partly responsible for the large deviation of the model from the observations. For example, one can easily see that the saturation electron current is not strictly proportional to the electron number density, but depends also on the mean thermal velocity of electrons and thereby also on the electron temperature and the so called "constant" of proportionality increases with increasing Te. At lower

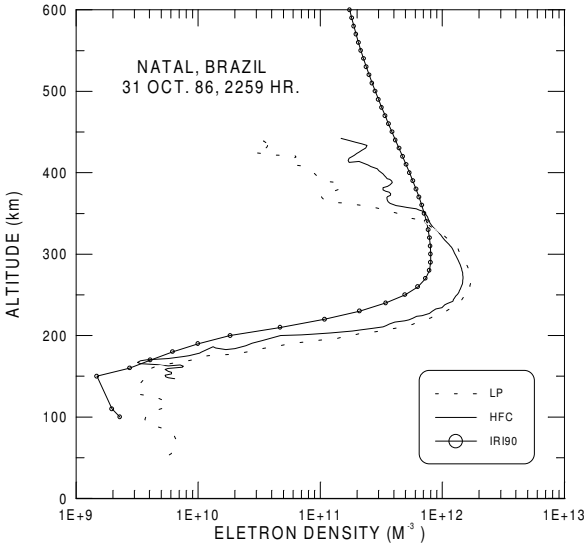

Figure 4 - Nighttime electron number density measurements made with an HFC probe and a Langmuir Probe on 31-st October, 1986 compared with the IRI90 profile.

altitudes, where Te is lower, the constant of proportionality is also lower when compared with its value at higher altitudes where Te is higher and consequently the constant of proportionality is also higher. In other words the use of an altitude independent constant of proportionality overestimates the electron density values at lower altitudes where Te is lower. This seems to be one of the reasons why the electron density values estimated from the LP measurements are higher than the model predictions at lower altitudes. Muralikrishna and Abdu (1991) report that the formation of plasma sheath surrounding the LP sensor can increase the effective surface area of the sensor and thereby result in an overestimation of the electron density as originally suggested by Baker et al. (1985). They also report on the possible effect of the changing floating potential of the rocket on the LP electron density values especially at higher altitudes resulting in an underestimation of the electron density in this height region. Of course, this is a very simplified and qualitative picture of what really occurs; a detailed analysis will be much more complicated and is beyond the scope of this paper.

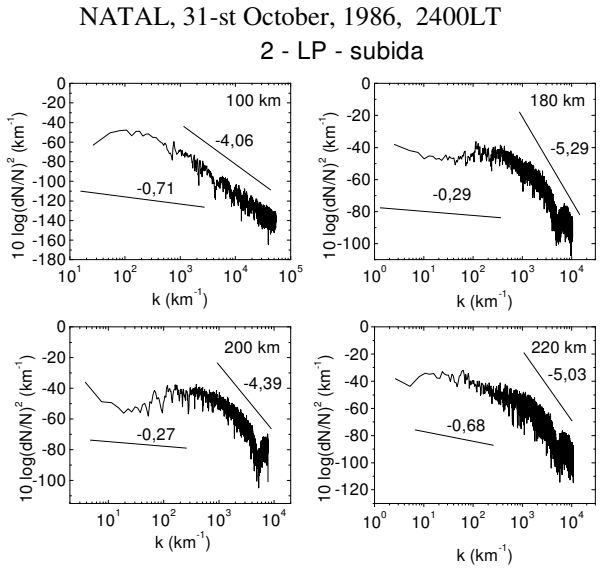

Figure 5 – Plasma irregularity spectra corresponding to selected height regions

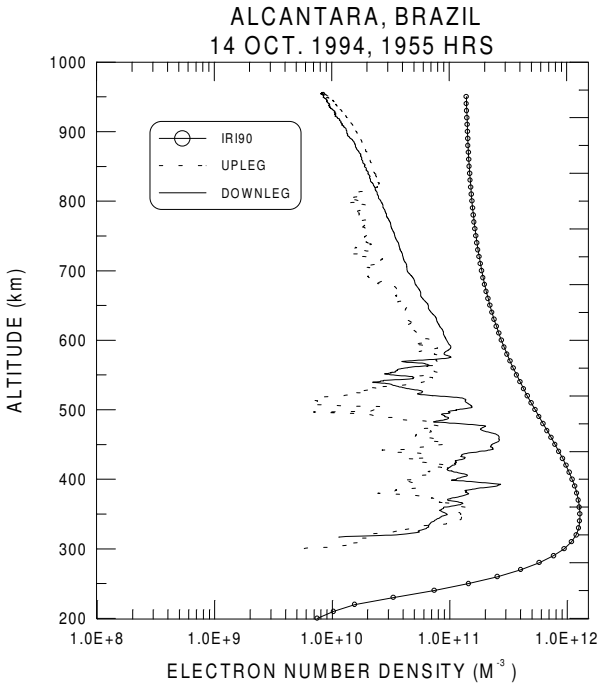

Figure 6 - Nighttime electron number density measurements made with an HFC probe on 14-th October, 1994 compared with the IRI90 profile.

Electron Density Profiles – Deviations from IRI

Alcântara, 1955LT, 14-th October, 1994

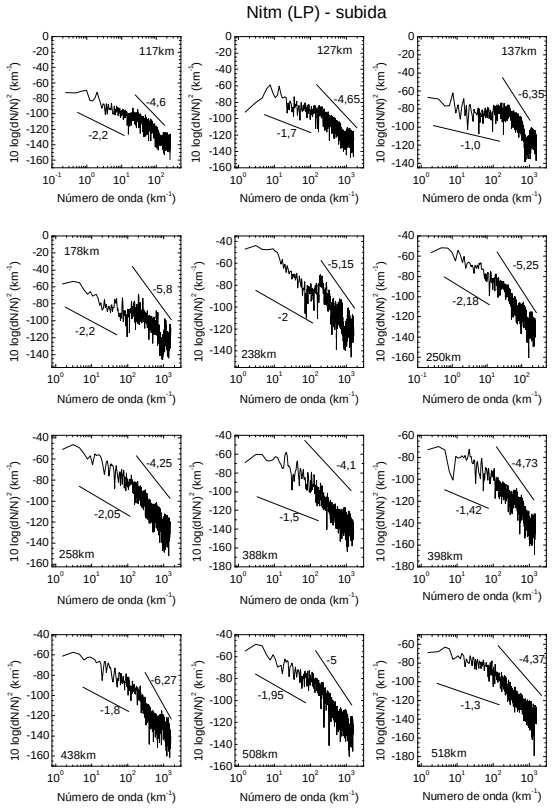

Figure 7 – Plasma irregularity spectra corresponding to selected height regions

CONCLUSIONS

The main conclusions of the present study are the following:

- The observed electron density profiles in the equatorial ionosphere over Brazil deviates considerably from the IRI predictions.
- A comparative study of the spectral features of the plasma and electricfield fluctuations shows that the observed profiles are reliable.
- Electrodynamic processes and meridional winds (by vertically drifting the ionospheric layers) are probably responsible for the large deviations of the observed electron density profiles from the IRI predictions.
- IRI model has to be improved considerably to represent the equatorial ionosphere, especially during the post sunset period when the electrodynamic processes seem to dominate in the equatorial F-region.

References

ABDU, M.A., BITTENCOURT, J.A and BATISTA, I.S., Magnetic declination control of the equatorial F-region dynamo field development and spread-F, J. Geophys. Res., 86, 11443, 1981.

ABDU, M.A., MURALIKRISHNA, P., DE PAULA, E.R. and KANTOR, I.J., Rocket-borne measurements of equatorial ionospheric electron densities and their comparison with IRI-10 predictions, Adv. Space Res., 10, (8) 41-44, 1990.

ABDU, M. A.; P. MURALIKRISHNA; I. S. BATISTA and J. H. A. SOBRAL, Rocket observation of equatorial plasma bubbles over Natal, Brazil using a High Frequency Capacitance probe, J. Geophys. Res., **96**, 7689-7695, 1991.

BAKER, K.D., LA BELLE, J., PFAFF, R.F., HOWLETT, L.C., RAO, N.B., ULWICK, J.C., and KELLY, M.C., Absolute electron density measurement in the equatorial ionosphere, J. Atmos. Terr. Phys. 47, 781, 1985.

KANTOR, I.J., MURALIKRISHNA, P. and ABDU, M.A., Comparison of ionospheric electron temperature rocket measurements over Natal, Brazil with IRI-10 predictions, Adv. Space Res. 10, (8) 91.

MURALIKRISHNA, P. and M. A. ABDU, In-situ measurement of ionospheric electron density by two different techniques - a comparison, J. Atmos. Terr. Phys., **53**, 787-793, 1991.

RAWER, K., RAMAKRISHNAN, S and BILITZA, D.,International Reference Ionosphere B, International Union of Radio Science, 1180, Brussels, 1978.

OYAMA, K.-I, A systematic investigation of several phenomena associated with contaminated Langmuir probes, Planet. and Space Sci., 24, 183-190, 1976.

SPENCER, N.W., BRACE, L.H., and CARIGNAN, G.R., Electron temperature evidence for non-thermal equilibrium in the ionosphere, J. Geophys. Res., 67, 157-175, 1962.

SZUSZCZEWICZ, E.P. and HOLMES, J.C., Surface contamination of active electrodes in plasmas: distortion of conventional Langmuir probe measurements, J. App. Phys. 46, 5134-5139, 1975.

OPTICAL STUDIES OF THE IONOSPHERIC IRREGULARITIES OVER THE BRAZILIAN REGION BY NOCTURNAL IMAGES OF THE OI 630 nm EMISSION

Daniela C. Santana[1], J. H. A. Sobral[1], H. Takahashi[1], M. J. Taylor[2]

[1]*Instituto Nacional de Pesquisas Espaciais, São José dos Campos, Sãp Paulo, Brazil*
[2] *Utah State University, Logan, Utah, USA*

Abstract

This study is an extension of previous statistical studies (Sobral et al., 1990,1991,1999) of the latitude variations of the ionospheric plasma depletions zonal drift velocities over the Brazilian low latitude station Cachoeira Paulista – CP (22.54ºS, 45.00ºW). The experimental ionospheric plasma bubble zonal drift velocities reported here are inferred from the *F*-region OI 630 nm nocturnal airglow whose data were gathered between October 1998 and October 1999 at CP by an all-sky imager system. The present results show that, in general, the velocities magnitudes clearly tended to decrease with local time and during Equinox, the velocities magnitudes clearly tended to decrease at lower rates as compared with Spring and Summer. The highest and lowest zonal drift velocities, from all three seasons considered here, were observed to be in the Summer 180 ms^{-1} at 21:45 LT, and 25 ms^{-1} in the Spring at 03:15 LT, respectively.

Introduction

Aeronomic studies through rockets, satellites, incoherent back scatter radar, UHF/VHF scintillation systems, GPS systems, and optical (airglow) instrumentation have been used to study the spread-F/ionopheric plasma depletions, or plasma bubbles, in the equatorial region (Woodman and LaHoz, 1976; Anderson and Mendillo, 1983; Sahai et al., 1988; Sobral et al. 1980a,b, 1985, 1990, 1997; Abdu et al. 1985, 1991; Jahn et al., 1997; Kelley, 1985). The OI 630 nm airglow technique offers a convenient way of monitoring the large-scale ionospheric plasma bubbles. Those studies are of particular interest for practical applications in South America because of the drastic interference of the ionospheric plasma bubbles in telecommunications over that region, that is, causing strong telecommunication signal degradation and blackouts.

The OI 630 nm airglow observations discussed here were obtained by a all-sky imager system which viewed the sky through a circular area with diameters in the NS and EW directions of 6.8ºS to 38.4ºS and 29.2ºW to 60.8ºW, respectively, considering a reference altitude of 250 km.

The present study is the first statistical study of such drift velocities, based on digital OI 630 nm airglow images obtained by an all-sky (180^o view angle) imager system located at Cachoeira Paulista – CP.

Observations

The set of OI 630 nm digital images of this work was originally geometrically nonlinear, that is, a given view angle (solid angle) corresponded to different areas of the ~40 km thick airglow emitting layer at 250 km of altitude, depending on the zenith position of the view angle. In order to facilitate the present analysis, the original digital images were linearized, according to the method described by Garcia et al. (1997) and the resulting linearized images correspond to square shaped areas, centered at CP, of 1100 km x 1100 km, considering the reference altitude of 250 km and to the latitude (longitude) ranges of about 17.61^{o}S to 27.44^{o}S (40.10^{o}W to 49.90^{o}W). Figure 1 were constructed from those linearized images. The velocity error bars are here estimated to be of the order of 3% based on geometrical considerations and instrumental resolution.

During the period of study, from October 1998 to October 1999, 72 nights of OI 630 nm airglow experiments were carried out at CP, of which 18 nights detected the plasma bubbles. These 18 nights correspond to magnetically quiet days and were grouped according approximately to their season, as follows (underlined are the dates common to two groups): Equinox: 7 nights (23/10/98, 15/3/99, 18/3/99, 7/9/99, 6/10/99, 7/10/99 and 13/10/99); Summer: 8 nights (18/1/99, 19/1/99, 21/1/99, 12/2/99, 16/2/99, 20/2/99, 15/3/99 and 18/3/99) and Spring: 9 nights (23/10/98, 16/11/98, 17/11/98, 24/11/98, 20/12/98, 21/12/98, 6/10/99, 7/10/99 and 13/10/99).

Results And Discussion

The zonal drift of the ionospheric plasma is caused by *F*-region vertical electric fields, which, in turn, are generated by the action of zonal neutral winds. It should be reminded that the plasma reaction to such a wind action is not a local effect, but an integrated flux-tube effect. So that the net zonal plasma drift velocity at a given geographic location is not a consequence of a local mechanism but a result of the interaction of the zonal winds with the plasma along the flux tube. The net flux-tube plasma eastward velocity V_z is given by (see Anderson and Mendillo, 1983) $V_z = \int\sigma_p UBds / B\int\sigma_p ds$ where σ_p is the Pedersen conductivity, U is the zonal component of the neutral wind, B is the magnitude of the geomagnetic filed and ds is the differential linear element along the flux-

tube. In the presence of the ionospheric plasma bubbles the drift velocity V_z becomes a function of the disturbed electron densities and polarization electric fields introduced by the complex bubbles' electron density spatial structures.

The experimental ionospheric plasma bubble zonal drift velocities reported here are inferred from the *F*-region OI 630 nm nocturnal airglow in the following way. Such airglow emission stems from the dissociative recombination reaction $O_2^+ + e \rightarrow O + O + h\nu$ from which one or two of the resulting oxygen atoms may be able to emit a 630nm photon through the de-excitation process $O(^3P) \rightarrow O(^1D) + h\nu$(630nm). The intensity of the OI 630 nm emission is proportional to the product of the concentrations of the molecular oxygen and electrons (see Sobral et al., 1992, 1993). In this way, the drastic depletions of the electron concentration occurring inside the plasma bubble cause equivalent drastic reductions of the OI 630 nm emission. The zonal drift velocities here reported were derived from the zonal velocities of the OI 630 nm intensity minima, as inferred from the digital optical images.

Figure 1 shows the ionospheric plasma bubble zonal drift velocities versus 11 geographical latitudes around CP, namely, 17.61°S, 18.59°S, 19.58°S, 20.56°S, 21.54°S, 22.54°S, 23.51°S, 24.49°S, 25.48°S, 26.46°S and 27.44°S for the set of 18 nights of the occurrence of ionospheric plasma bubbles events that presented, in general, mild geomagnetic activity (Most intense magnetic storm: 23/10/98, D_{st} = -45 nT, $\sum$Kp = 23o; Least intense one: 21/12/98, D_{st} = 2 nT, $\sum$Kp = 7 ¯). The velocity magnitudes clearly tend to decrease with local time both in Spring, Summer and Equinox, as consequence of the decrease in the component of the ambient electric field, since the zonal drifts are cold plasma **ExB** drifts where **E** and **B** are the ambient (*F*-region*)* electric field and geomagnetic field intensities respectively. The electric field strength decrease results from the nocturnal *F*-region recombination process.

Figure 1(a), shows the average Equinox zonal velocity profiles of 7 nights for the time interval of 20:15 LT to 01:15 LT. After 03:15 LT the velocity is of just one night (September 7, 1999) since this was the only night in which the bubbles have occurred after 03:15 LT. The velocity magnitudes of Figure 1(a) varied from ~43 ms^{-1} at 04:15 LT to ~140 ms^{-1} at 20:15 LT. They clearly tended to decrease with local time at lower rates as compared with Spring and Summer possibly caused by the more symmetric latitudinal distribution around the magnetic equator of the zonal neutral wind magnitudes during Equinox.

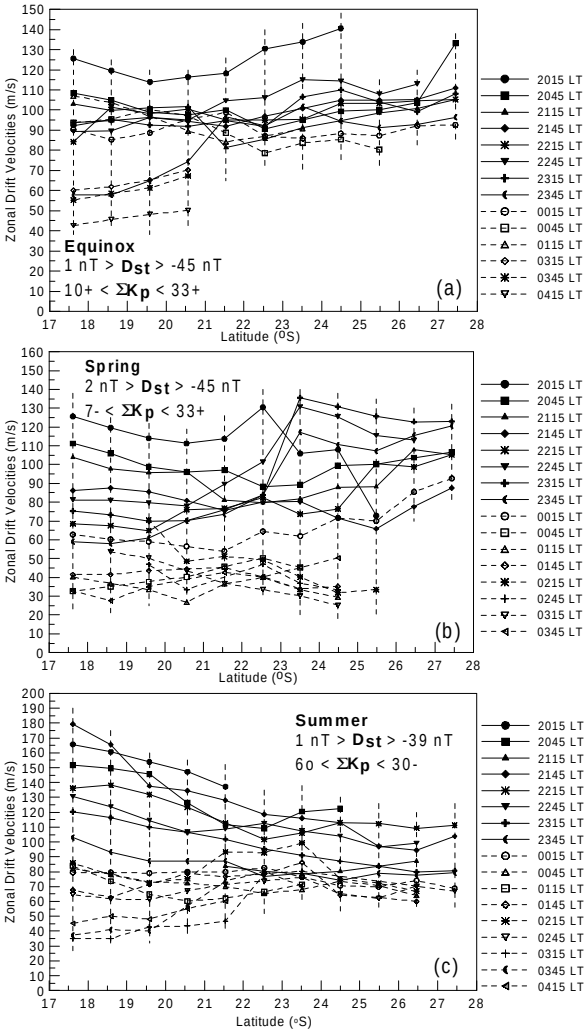

Fig. 1 - Latitudinal distribution ionospheric plasma bubble zonal drift velocities over Cachoeira Paulista during Equinox (a), Spring (b) and Summer (c) from October 1998 to October 1999.

Figure 1(b) shows the average Spring zonal velocity profiles of 9 nights, from 20:15 LT to 03:45 LT. The velocities varied from ~135 ms^{-1} at 23:15 LT to ~25 ms^{-1} at 03:15 LT. The velocities presented less latitude variation than during Equinox and Summer, except for 22:45 LT, 23:15 LT and 23:45 LT in whose times a sharp decrease of magnitude occurred at the latitude of about 23°S. Figure 1(c) shows the average Summer velocities of 8 nights from 20:15 LT to 04:15 LT. The velocity magnitudes presented smaller dispersion (~60 ms^{-1} to ~125 ms^{-1}) at higher latitudes than at lower latitudes (~35 ms^{-1} to ~180 ms^{-1}). It is interesting to note that below the latitude of approximately 22.5 °S the zonal velocity magnitudes decrease with latitude before the midnight, and

increase with latitude, after the midnight. The highest (lowest) values were ~180 ms^{-1} at 21:45 LT (~35 ms^{-1}, at 03:15 LT). In general, the plasma bubble zonal drift velocities were larger during Summer, especially in the pre-midnight period.

Conclusions

In the present study, about 18 nights were considered focusing the variations of the ionospheric plasma bubble zonal drift velocities with geographical latitudes. All the velocities mentioned below refer to the zonal drift velocities of the ionospheric plasma bubbles except otherwise specified. The general conclusions of this study were:

1) The digital OI 630 nm images were seen to be useful in the study of the zonal drift velocities of the ionospheric plasma depletions, or bubbles, in particular because of the improved space and time resolutions.

2) In general, the velocities magnitudes clearly tended to decrease with local time and such decrease associated to decreasing intensity of the vertical component of the ambient electric field which, in turn can be accounted by the recombination.

3) All zonal drifts obtained for all the 18 nights considered were eastwards.

4) During Equinox, the velocities magnitudes clearly tended to decrease with local time at lower rates as compared with Spring and Summer.

5) The highest and lowest zonal drift velocities, from all three seasons considered here, were observed to be in the Summer ~180 ms^{-1} at 21:45 LT, and ~25 ms^{-1} in the Spring at 03:15 LT, respectively.

6) All the present ionospheric plasma bubble zonal drift velocities are consistent with those obtained through scanning photometers that operated at Cachoeira Paulista in the last maximum solar cycle (Sobral et al., 1991).

7) Ionospheric plasma bubbles were detected the until the maximum extra-tropical geographical latitude of ~28^o S, that was the largest latitude position analyzed in this study.

8) During Summer, below the latitude of approximately 22.5^o S, the zonal velocity magnitudes decrease (increase) with latitude, before (after) the midnight.

References

Abdu, M. A., J. H. A. Sobral, O. R. Nelson and I. S. Batista, Solar Cycle Related Range Type Spread-F Occurrence Characteristics over Equatorial and Low Latitude Stations in Brazil, *J. Atmos. Terr. Phys.*, **47**, 901 (1985).

Abdu, M. A., P. Muralikrishna, I. S. Batista, J. H. A. Sobral, Rocket Observations of Equatorial Plasma Bubbles over Natal, Brazil, using High Frequency Capacitance Probe, *J. Geophys. Res.*, **96**, 7689 (1991).

Anderson, D. N., M. Mendillo, Ionospheric Conditions Affecting the Evolution of Equatorial Plasma Depletions, *Geophys. Res. Lett.*, **10**, 541 (1983).

Garcia, F. J.; Taylor, M. J.; Kelley, M. C. Two-Dimensional Spectral Analysis of Mesospheric Airglow Image Data. *Appl. Optics*, **36**, 7374 (1997).

Jahn, J. M., J. LaBelle, J. H. A. Sobral, T. L. Aggson, W. B. Hanson, Detection of an Equatorial Spread-F Bubble by Ground-Based Photometers and the San Marco Satellite, *J. Atmos. Terr. Phys.*, **59**, 1601 (1997).

Kelley, M. C. Equatorial Spread F: Recent Results and Outstanding Problems, *J. Geophys. Res.*, **47**, 745 (1985).

Mendillo, M. and J. Baumgardner, Airglow Characteristics of Equatorial Plasma Depletions, *J. Geophys. Res.*, **87**, 7641 (1982).

Sahai, Y., J. A. Bittencourt, H. Takahashi, N. R. Teixeira, J. H. A. Sobral., B. A. Tinsley and R. P. Rohrbaugh, Multispectral Optical Observations of Ionospheric *F*-Region Storm Effects at Low Latitude, *Planet. Space Sci.*, **36**, 371 (1988).

Sobral, J. H. A., M. A. Abdu and I.S. Batista, Airglow Studies on the Ionosphere Dynamics over Low Latitude in Brazil. *Ann. Geophys.*, **36**, 199 (1980a).

Sobral, J. H. A., M. A. Abdu, I. S. Batista, and C. J. Zamlutti, Association Between Plasma Bubble Irregularities and Airglow Disturbances over Brazilian Low Latitudes. *Geophys. Res. Lett.*, 11, 980 (1980b).

Sobral, J. H. A., M. A. Abdu, M. A. and Y. Sahai, Equatorial Plasma Bubbles Eastward Velocity Characteristics from Scanning Photometer Measurements over Cachoeira Paulista *J. Atmos. Terr. Phys.*, **47**, 895 (1985).

Sobral, J. H. A. and M.A. Abdu, Latitudinal Gradient in the Plasma Bubble Zonal Velocities as Observed by Scanning 630 nm Emission Measurements, *J. Geophys. Res.*, **95**, 8253 (1990).

Sobral, J. H. A. and M. A. Abdu, Solar Activity Effects on Equatorial Plasma Bubble Zonal Velocity and its Latitude Gradient as Measured by Airglow Scanning Photometers, *J. Atmos. Terr. Phys.*, **53**, 729 (1991).

Sobral, J. H. A., H. Takahashi, M. A. Abdu, P. Muralikrishna, Y. Sahai and C. J. Zamlutti, O(1S) and O(1D) Quantum Yields from Rocket Measure-

ments of Electron Densities and 557.7 and 630.0 nm Emissions in the Nocturnal F-Region, *Planet. Space Sci.*, **40**, 607 (1992).

Sobral, J. H. A., H. Takahashi, M. A. Abdu, P. Muralikrishna, Y. Sahai, C. J. Zamlutti, E. R. De Paula and P. P. Batista, Determination of the Quenching Rate of the O(1D) by O(3P) from Rocket-Borne Optical (630 nm) and Electron Density Data, *J. Geophys. Res.*, **98**, 7791 (1993).

Sobral, J. H. A., M. A. Abdu, P. Muralikrishna, H. Takahashi, H. S. Sawant, C. J. Zamlutti and M. G. de Aquino, Horizontal Gradients of the Nocturnal OI 557.7 nm and OI 630 nm Photoemission Rates in the Equatorial Ionosphere Based on Rocket Electron Density Data, *Adv. Space Res.*, **20**, 1317 (1997).

Sobral, J. H. A, M. A. Abdu, H. Takahashi, H. Sawant, C. J. Zamlutti, C. J.; Borba, G. L., Solar and Geomagnetic Activity Effects on Nocturnal Zonal Drifts of Ionospheric Plasma Depletions, *Adv. Space Res.*, **24**, 1507 (1999).

Woodman, R. F. and C. LaHoz, Radar Observations of Equatorial Irregularities, *J. Geophys. Res.*, **81**, 5447 (1976).

Acknowledgments

This study was partially supported by the Fundação de Amparo à Pesquisa do Estado de São Paulo – FAPESP (proc. nº 1998/00828-7, 1999/00437-2 and 1999/00437-0) and Conselho Nacional de Desenvolvimento Científico e Tecnológico – CNPq through grant no. 522919/96-0. The authors wish to thank both referees for their comments.

Signatures of Traveling Convection Vortices (TCV) in Ground Magnetograms under the Equatorial Electrojet (EEJ)

N. B. Trivedi, Centro Regional Sul de Pesquisas Espaciais, Santa Maria, Brazil, e Instituto Nacional de Pesquisas Espaciais, S. J. Campos, SP, Brazil; D. G. Sibeck, Johns Hopkins University Applied Physics Laboratory, Laurel, MD 20723-6099,USA; E. Zesta, Dept. of Atmospheric Sciences, Univ. of California Los Angeles, USA; J. C. Santos, Centro Regional Sul de Pesquisas Espaciais, Santa Maria, Brazil; K. Yumoto, and T. Kitamura, Dept. of Earth and Planetary Sciences, Kyushu University, Fukuoka, Japan; and S. L. G. Dutra, Instituto Nacional de Pesquisas Espaciais-INPE, S. J. Campos, SP, Brazil

Abstract

Traveling Convection Vortices (TCVs) are transient events in high-latitude ground magnetograms that can be interpreted as evidence for localized vortical flows in the high-latitude ionosphere. Their centers travel eastward or westward at geomagnetic latitudes near 72° to 74°. TCVs have been attributed to various types of transient interaction at the magnetopause, but also to processes occurring deeper within the magnetosphere. Each interaction mechanism should launch shear Alfvén waves that produce high-latitude ground signatures, but also compressional waves that should produce signatures at lower latitudes. In this paper, we present evidence for corresponding signatures at Belém, São Luis, and Teresina and other stations under or nearby the equatorial electrojet (EEJ). The equatorial signatures are most pronounced when the high-latitude signatures are (a) longitudinally extended, (b) isolated, and (c) attain greatest amplitudes.

Introduction

The magnetopause hosts a wide range of transient disturbances. The Kelvin-Helmholtz instability may drive quasi-periodic waves on the boundary during periods of enhanced solar wind velocities. Bursty merging may generate flux ropes of interconnected magnetospheric and magnetic field lines, known as flux transfer events (FTEs), on the equatorial magnetopause during periods of southward interplanetary magnetic field (IMF) orientation. Pressure pulses, whether of intrinsic solar wind origin or generated within the foreshock, may drive riplets on the magnetopause [Sibeck et al., 1989]. Each disturbance should launch fast mode waves across magnetospheric magnetic field lines and parallel-propagating Alfvén mode waves along outer magnetospheric magnetic field lines.

The effects of the Alfvén mode waves (and corresponding field-aligned currents) should be observable at the ionospheric footprints of outer magnetospheric magnetic field lines. Magnetic impulse events (MIEs) with durations from 5 to 20 min and amplitudes greater than 40 nT are indeed common in the high-latitude dayside ionosphere. On average one occurs each day [Sibeck and Korotova, 1996], but repetitive sequences are not uncommon. Efforts to identify the origin of the events have not met with great success. They show no tendency to occur for high solar wind velocities as predicted by the Kelvin-Helmholtz mechanism, for highly variable solar wind pressures as predicted for the pressure-pulse mechanism, or for southward IMF orientations as predicted by the bursty merging mechanism. They may not even be associated with transient processes at the magnetopause [Yahnin and Moretto, 1996]. Efforts to identify corresponding signatures of the fast mode waves at geosynchronous orbit or at low-latitudes on the ground have met with mixed success. While some case and statistical surveys report evidence for corresponding equatorial and geosynchronous signatures at the times of MIEs [Sibeck, 1993], others do not.

With the help of observations from ground magnetometer arrays, the TCVs can be identified on the basis of eastward or westward propagating ionospheric convection flows (magnetic field signatures) that reverse from westward (southward) to eastward (northward), or vice-versa, with latitude. The purpose of this paper is to examine high amplitude and time resolution low-latitude ground magnetograms for several well documented TCVs recently reported by Moretto et al. [1997], Ridley et al. [1998], and Zesta et al. [1999] and determine the conditions under which corresponding signatures can be seen under the equatorial electrojet.

Events with clear equatorial signatures

All of the TCVs studied in this paper were first identified by previous authors in high latitude North American and Greenland ground magnetograms. We present the observations at 5s time resolution for events identified in the MACCs array, and 60s time resolution for events identified in the Greenland ground magnetogram. For comparison, we will present observations from low-latitude stations at similar local times in Brazil. See Figure 1. Some TCVs are isolated, some repetitive, and the repetition times can vary. The signatures of some TCVs can be observed over a wide longitudinal range of high latitude locations, while others cannot. Finally,

amplitudes vary from less than 40 nT to greater than 200 nT.

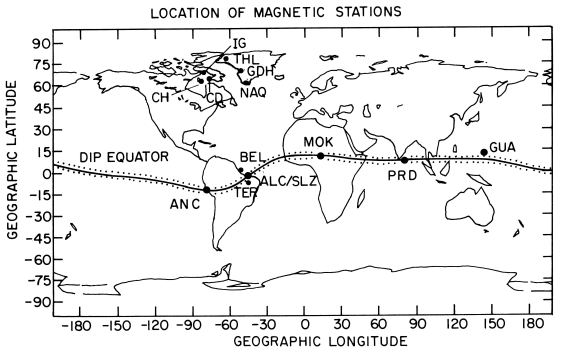

Figure 1. Locations of ground stations and the magnetic dip equator in geographic coordinates.

1715 UT on November 9, 1993. Figure 2 presents magnetic field observations during the period from 1600 to 1800 UT on November 9, 1993. As indicated by the vertical lines in the lower panel, Zesta et al. [1999] identified four TCVs in the MACCS observations immediately after 1710 UT. Their amplitudes reached ~300 nT at some of the MACCs stations (not shown). As required for identification as TCVs, the sense of each *H* component perturbation reversed from low to high latitudes, so that positive (negative) perturbations in the *H* component at higher latitude (79.4°) IGC corresponded to negative (positive) perturbations in the *H* component at lower latitude CDC (74.6°) and CHC (74.8°). Corresponding events, with amplitudes reaching ~100 nT can also be seen in the Greenland ground magnetograms. However, the events cannot be classified as TCVs over Greenland because there is no clear reversal in the *H* component with latitude.

Zesta et al. [1999] noted that a transient event in the MACCS array observations at 1615 UT exhibited equally strong amplitude perturbations, but less clear TCV signatures. As indicated by the vertical lines, there was no reversal in the *H* component with latitude at either the Greenland or the MACCs stations for this event.

For comparison, Figure 3 shows the high pass (30 min) filtered *H* components recorded at eight equatorial stations. The variations corresponding to the 1715 UT TCV event reached peak amplitudes (10~12 nT) at Ancon (LT=12:00) and São Luis (LT=14:25), both nearly directly under the dayside equatorial electrojet. The amplitudes were somewhat less (5 nT) at Teresina, Belem, and Santa Maria, all at local times similar that of São Luis, but well outside the equatorial electrojet. The perturbations reached still lower amplitudes (~3 nT) at Mokolo (LT= 18:30), Peredenia (23:00), and Guam (LT=03:00), all on the nightside.Taken together, the observations indicate coherent variations whose amplitudes diminish with increasing local time from noon.

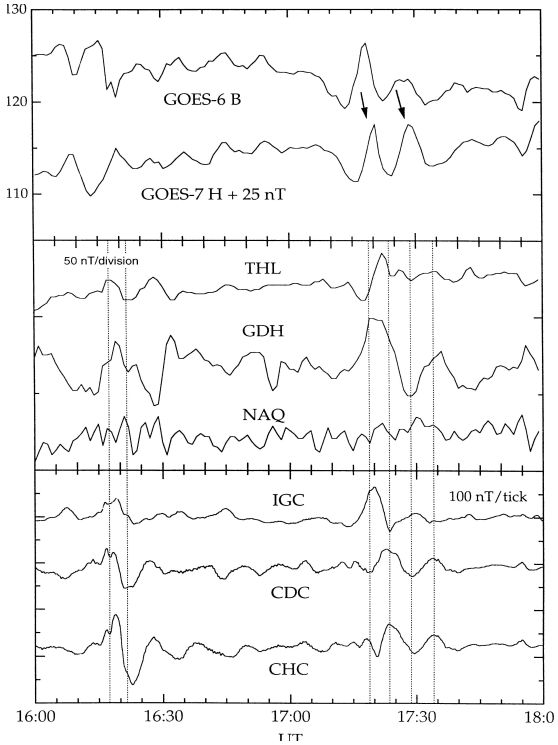

Figure 2. From top to bottom: GOES-6 and -7 geosynchronous magnetic field observations, the *H* component of Greenland ground magnetograms at THL, GDH, and NAQ, and the X component of MACCS array stations IGC, CDC, and CHC from 1600 to 1800 UT on November 9, 1993.

Finally, note that both Ancon and São Luis recorded weaker and less prominent (i.e. less isolated) perturbations from 16:10 to 16:20 UT and 1645 to 1700 UT. The examples below will provide further evidence that clear events under the equatorial electrojet correspond to strong and isolated TCV's at higher latitudes. *1350 UT on December 18, 1993.*

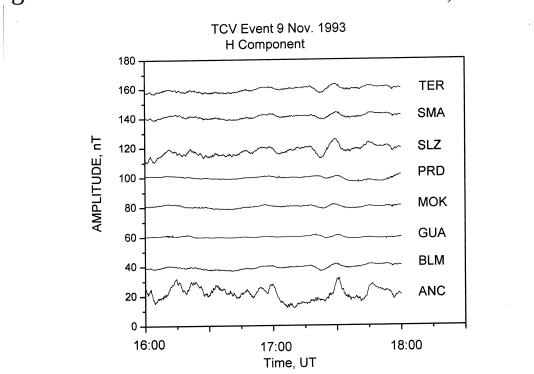

Figure 3. The *H* component of ANC, GUA, MOK, PRD, BLM, SLZ, SMA, and TER ground magnetograms from 1600 to 1800 UT on November 9, 1993.

The lower panel of Figure 4 presents the *H* components of Greenland ground magnetograms from 1300 to 1500 UT on December 18, 1993. As indicated by a vertical dashed line, Moretto et al. [1997] identified several TCVs near 1350 UT. The *H* component perturbations reversed from positive/negative at NAR (where the amplitude approaches 200 nT) to negative/positive at GDH. THL observed a transient negative bay rather than a bipolar signature. This event could be interpreted as an isolated set of two or possibly three convection vortices moving eastward over the western coast of Greenland. The middle panel provides X-component from the three stations in the MACCS array whose longitudes are closest to those in the Greenland chain. CDC and CHC observed positive/negative signatures, and IGC recorded only a weak positive perturbation at 1350 UT.

The MACCS and Greenland observations provide evidence for a second impulsive event at 1427 UT on the same day. At CDC and CHC, this event represents a significant (~200 nT) intensification of an ongoing pulsation with a period of about 4 min. At IGC it can be identified as a slight increase in the X component. Positive perturbations mark the event at GDH and NAR, but a transient negative bay marks the event at THL.

The top panel of Figure 4 presents GOES-6 and -7 geosynchronous magnetic field observations for the same time interval. Both GOES-6 and -7 observed only modest compressions at 1347 UT just prior to the 1350 UT event in Greenland, but the GOES spacecraft observed a particularly striking compression at 1425 UT followed by an equally transient rarefaction at 1429 UT, presumably corresponding to the 1427 UT ground event.

Figure 5 presents equatorial magnetograms for the same time interval. *H* component observations by the two stations located nearest local noon, ANC and ALC, indicate two pulsed increases at 1352 and 1428 UT, corresponding to both transient events at high latitudes on the ground. Dusk station MOK and nightside station PRD recorded similar signatures with greatly depressed amplitudes. Guam, located on the nightside and at higher latitudes, observed virtually no signatures corresponding to either event.

Discussion and Conclusions

We obtained mixed results from our search for signatures in equatorial ground magnetograms corresponding to previously reported TCVs at higher latitudes. In part, this is due to the differing characteristics of the high-latitude events. As noted by Trivedi et al. [1997] and Abdu et al. [1998], the electric fields corresponding to long period geomagnetic pulsations travel equatorward through the ionosphere. Whatever their origin, such variations pose a difficulty in establishing a one-to-one correspondence between event signatures in high- and low-latitude ground magnetograms.

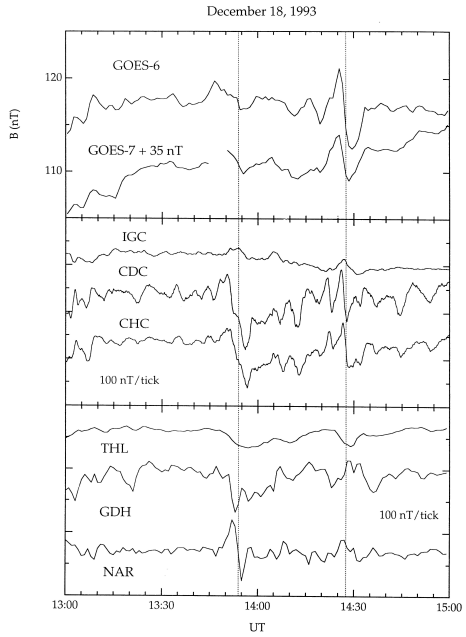

Figure 4. From top to bottom: GOES-6 and -7 geosynchronous magnetic field observations, the X component of MACCS array stations IGC, CDC, and CHC, and the *H* component of Greenland ground magnetograms at THL, GDH, and NAQ from 1600 to 1800 UT on December 18, 1993.

The relationships between the high- and low-latitude signatures on November 9 and December 18, 1993 were simpler to understand. The *H*-component signature seen during the 1350 UT event on December 18 exceeded 200 nT, was bipolar, reversed with latitude over Greenland, and was seen in the MACCS array. A second event at 1425 UT exhibited an equally clear signature in the MACCS array observations, but a poor signature over Greenland. Both events were isolated and corresponded to clear compression/rarefactions at geosynchronous orbit and transient compressions in all the dayside equatorial ground magnetograms.

The high-latitude events on November 9 were equally clear. Isolated impulsive *H* component signatures with amplitudes greater than 100 nT reversed with latitude over the MACCS array and were also detected by the Greenland ground magnetograms. The GOES spacecraft recorded transient disturbances that were particularly clear for the second set of events near 1730 UT. The same was true for stations within the Brazilian network of

ground magnetograms (BLM, SLZ, SMA, and TER). The signatures observed in the equatorial ground magnetograms varied, as did those at high latitudes. One contrast throughout the observations is that the signatures always reached greater amplitudes at stations under the dayside equatorial ionosphere than at stations at higher latitudes or on the nightside. This is to be expected, for this is where the strength of the equatorial electrojet and ionospheric densities reach greatest amplitudes [Trivedi and Rastogi, 1968].

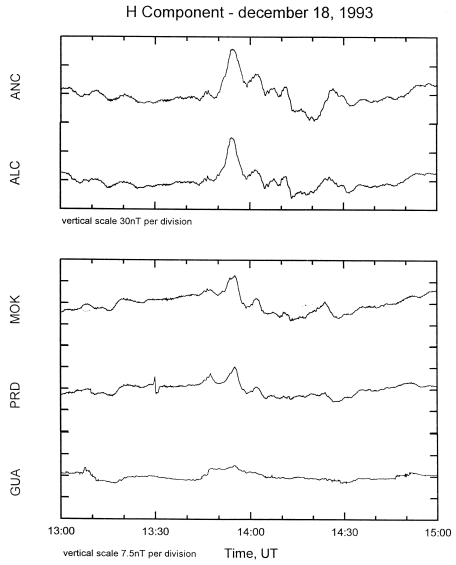

Figure 5. The *H* component of ANC, ALC, MOK, PRD, and GUA ground magnetograms from 1600 to 1800 UT on December 18, 1993.

To summarize, we have inspected geosynchronous and equatorial ground magnetograms at the times of previously reported high-latitude transient events. When the high-latitude transient events exhibited clear, strong, isolated signatures corresponding to TCVs, we generally detected isolated bipolar compressional signatures at geosynchronous orbit and transient impulses in equatorial ground magnetograms. We had difficulty identifying corresponding equatorial signatures for high-latitude events that were quasi-periodic, weaker, spatially limited, or did not exhibit clear TCV signatures.

Acknowledgements. We thank H. J. Singer, NOAA, and NASA/GSFC SPDF for supplying the GOES geosynchronous magnetic field observations, The Danish Meteorological Institute for supplying the Greenland ground magnetograms, and M. Engebretson for supplying the MACCS ground magnetograms. Research at JHU/APL was supported by NSF Grant ATM-9803800 with a supplement for joint work with Brazilian scientists. The Research in Brazil was supported by the Instituto Nacional de Pesquisas Espaciais – INPE/MCT and FAPESP 1998/15197-2.

References

Abdu, M. A., J. H. Sastri, H. Lühr, H. Tachihara, N. B. Trivedi, and J. H. A. Sobral, DP2 electric field fluctuations in the dusk-time dip equatorial ionosphere, Geophys. Res. Lett., 25, 1511-1514, 1998.

Moretto, T., E. Friis-Christensen, H. Lühr, and E. Zesta, Global perspective of ionospheric traveling convection vortices: Case studies of two Geospace Environmental Modeling events, J. Geophys. Res., 102, 11597-11610, 1997.

Ridley, A. J., T. Moretto, P. Ernström, and C. R. Clauer, Global analysis of three traveling vortex events during the November 1993 storm using the assimilative mapping of ionospheric electrodynamics technique, J. Geophys. Res., 103, 26349-26358, 1998.

Sibeck, D. G., et al., The magnetospheric response to 8 min. period strong amplitude upstream pressure variations, J. Geophys. Res., 94, 2505-2519, 1989.

Sibeck, D. G., Transient magnetic field signatures at high latitudes, J. Geophys. Res., 98, 43-256, 1993.

Sibeck, D. G., and G. I. Korotova, Occurrence patterns for transient magnetic field signatures at high latitudes, J. Geophys. Res., 101, 13413-13428, 1996.

Trivedi, N. B. and R. G. Rastogi, Studies of sudden changes in H and Z at equatorial stations in the Indian Zone, Ann. Geophys., 24, 1037-1046, 1968.

Trivedi, N. B., B. R. Arora, A. L. Padilha, J. M. da Costa, S. L. G. Dutra, F. H. Chamalaun, and A. Rigoti, Global Pc5 geomagnetic pulsations of March 24, 1991 as observed along the American sector, Geophy. Res. Lett., 24, 1683-1686, 1997.

Yahnin, A. and T. Moretto, Travelling convection vortices in the ionosphere map to the central plasma sheet, Ann. Geophys., 14, 1025-1031, 1996.

Zesta, E., W. J. Hughes, M. J. Engebretson, T. J. Hughes, A. J. Lazarus, and K. I. Paularena, The November 9, 1993, traveling convection vortex event: A case study, J. Geophys. Res., 104, 28041-28058, 1999.

Structure of the mean winds and Tides at the meteor region over Cachoeira Paulista

Paulo P. Batista, Barclay R. Clemesha and Aparecido S. Tokumoto, INPE, Brazil

Abstract

Zonal and meridional winds in the region of the upper mesosphere and lower thermosphere (MLT) have been measured with a meteor radar in Cachoeira Paulista, Brazil (22.7°S, 45°W) during two years, from March 1999 to February 2001. Winds were calculated with temporal resolution of 1 h and vertical resolution of 2 km from 80 to 100 km height. Monthly means were calculated and the wind structure was decomposed into the mean, diurnal, semidiurnal and terdiurnal components. The mean wind showed the zonal component to dominate with westward wind above 90 km from May to September, a dominance of an Eastward wind from September to April between 80 and 100 km and a small interannual variation. The dominant mode in the diurnal tide is the $S_{1,1}$ with wavelength from 25- to 30 km, in good agreement with the GWSM model. Large interannual variations and different phases were noted during November and December. The diurnal amplitudes are in general smaller than those predicted by the model, mainly during October. The semidiurnal amplitudes are in general greater than that for the model and the phases show some vertical propagation or are almost evanescent. The terdiurnal component although weak shows good height and interannual coherence.

Introduction

The knowledge of the climatology of the winds in the MLT region is of great importance. The motions in this region of the atmosphere are dominated by atmospheric tides, planetary waves and gravity waves, in addition to large scale motions (annual and semiannual). Tides and gravity waves have their origin in the troposphere and stratosphere and propagate upward transferring energy via dissipation to higher regions, modifying the basic circulation in these regions. This climatology is sufficiently well known in middle and high latitudes, mainly in northern hemisphere (Manson et al., 1985, 1989, 1991) but there is a big gap mainly in equatorial and subtropical regions of the southern hemisphere. Theoretical models (Forbes and Vial, 1989, Hagan et al., 1995, 1998) predict that the maximum amplitude for the horizontal winds diurnal tide occurs from 18-24 degrees of latitude. Few measurements have been reported in these latitudes. Vincent and Ball, 1981, based on a few measurements in Townsville, (19° S) found that the $S_{1,1}$ mode was dominant in November, but presented large variability and evanescent modes in July. More recently, measurements with a MF radar were carried out in Hawaii (22^0 N) by Fritts and Isler, 1992, 1994. This work, based on two years of measurements, showed that at 22^0 N the zonal wind had a semiannual motion (MSAM), characteristic of equatorial regions and an annual motion, characteristic of middle latitudes. Strong oscillations on a planetary wave scale, mainly the quasi two day wave was also observed. Strong seasonal and interannual oscillations in the amplitudes and phases of the tides, modulated by the planetary waves were noted .

Since March, 1999 a meteor radar was installed in Cachoeira Paulista, SP with support of the CNPq program PRONEX (Programa de apoio a núcleos de excelência). This radar has been operated continuously since the installation providing the zonal and meridional winds with a 3-km height resolution and 1-h time resolution. Data obtained during these two first years will be here discussed.

Equipment and data analysis

The SkiYmet is an all sky interferometric radar. It uses an antenna that transmits pulses at the frequency of 35.24 MHz and five receiver antennae. The signals from each antenna (amplitudes and phases) are registered. For each meteor echo the radial velocity of the wind is determined and the height and azimuth are located by correlation between the signals from the various antennae. The echoes are binned in height and time and the zonal and meridional winds are calculated. The radar provides typically around 3000 useful echoes per day, giving a time resolution of one hour and a height resolution of 2-3 km. This data reduction can be made for individual days , a group or a sequence of days. In this work the winds will be evaluated for each month using a group superposition.

For each height the zonal and meridional winds are divided in their prevailing, diurnal, semidiurnal and terdiurnal components by the least mean square method, according to the formula:

$$u, v = u_0, v_0 + \sum_{i=1}^{3} (u_i, v_i \cos(\frac{2\pi it}{24} - \phi_i)$$

Where u,v are the zonal (positive to east) and meridional (positive to north) wind amplitudes and ϕ is the phase (hour of the occurrence of maximum).

Mean winds

Figure 1 shows the structure of the prevailing wind for each month from March 1999 to February 2000 and from March 2000 to February 2001. Dashed lines refer to the period 1999/2000 and solid lines to the 2000/2001 period. The zonal prevailing winds are more important than the meridional. This is in accordance with models (Hedin et al, 1993) and other observations. Interannual variability is small for the majority of the months (except for July in the meridional wind).

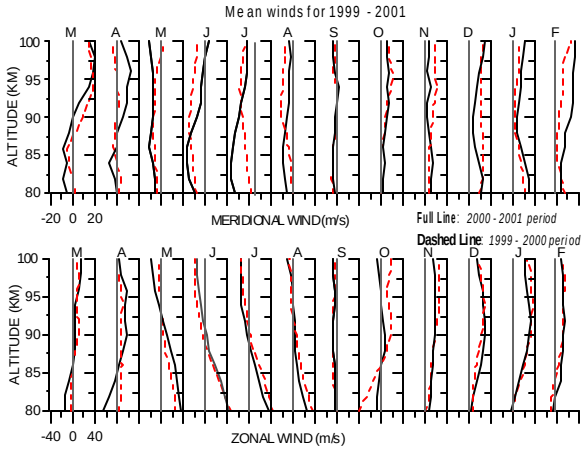

Figure 1. Monthly variation of the mean wind. Upper panel is for Meridional wind and bottom panel is for Zonal wind. Dashed lines are for March 1999 to February 2000 and full lines for March 2000 to February 2001.

The diurnal tide

Plots for the amplitudes and phases of the diurnal component of the tide are shown in Figure 2. Also shown, for the months of January, April, October and December which are representative of summer, fall, winter and spring, are the results of the model GSWM98 (Hagan et al, 1995, 1999). For the amplitudes a small interannual variation is noted. In general, the GSWM model predicts higher amplitudes, mainly for the equinoxes.

The phases show the dominance of the $S_{1,1}$ mode, with vertical wavelength of 25-30 km. During November and December there is a large interannual variation and a deviation from the general behavior, mainly in 1999/2000. There is a tendency for modes with larger vertical wavelengths or even evanescent

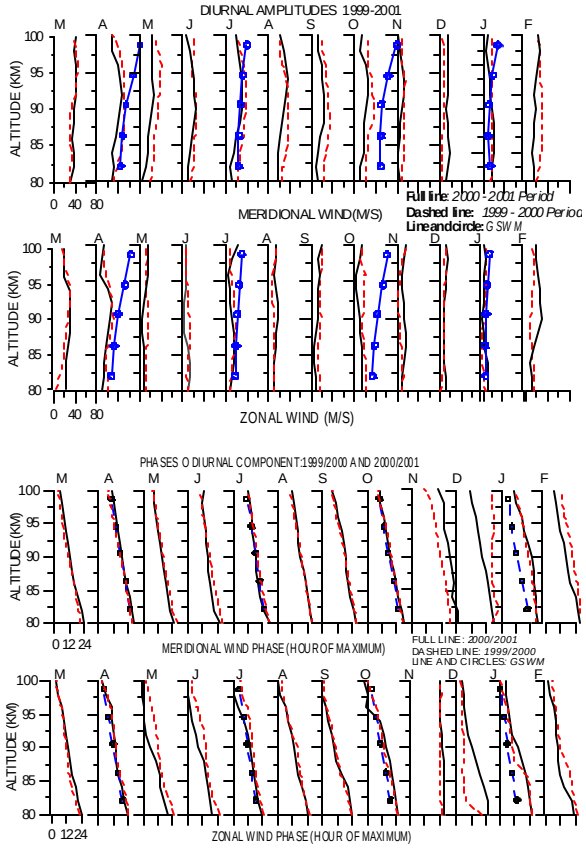

Figure 2. Amplitudes (upper panel) and phases (lower panel) for the diurnal tide as a function of months and height. In both panels upper plot is for meridional wind and lower plot is for zonal wind.

modes. This can be seen mainly in the zonal wind during November.

The semidiurnal tide

The semidiurnal component shown in Figure 3 presents a behavior more complex than that of the diurnal one. The model predicts low amplitudes increasing with the height between 80 and 100 km. In general, the experimental data present higher amplitudes and not always increasing with height. For the zonal wind the model gives very low amplitudes, but the data show larger amplitudes.

The phases show a large interannual variation. Generally, the model gives large wavelengths (> 40 km), but for some months (February, March and November) there are short vertical wavelengths (~20 km). There are large differences in the phases for the month of October. For July there is an outstanding agreement in the phase jump between 85 and 90 km.

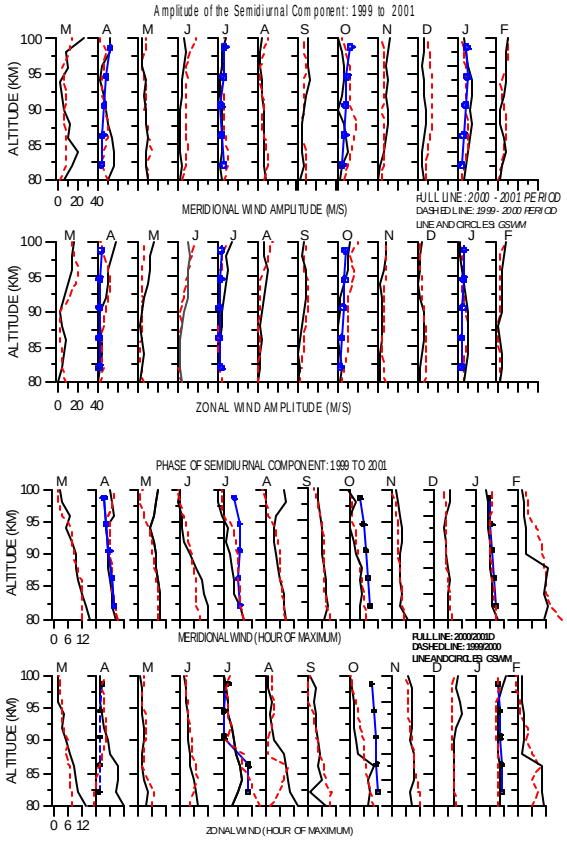

Figure 3. Amplitudes (upper panel) and phases (lower panel) for the semidiurnal tide as a function of months and height. In both panels upper plot is for meridional wind and lower plot is for zonal.

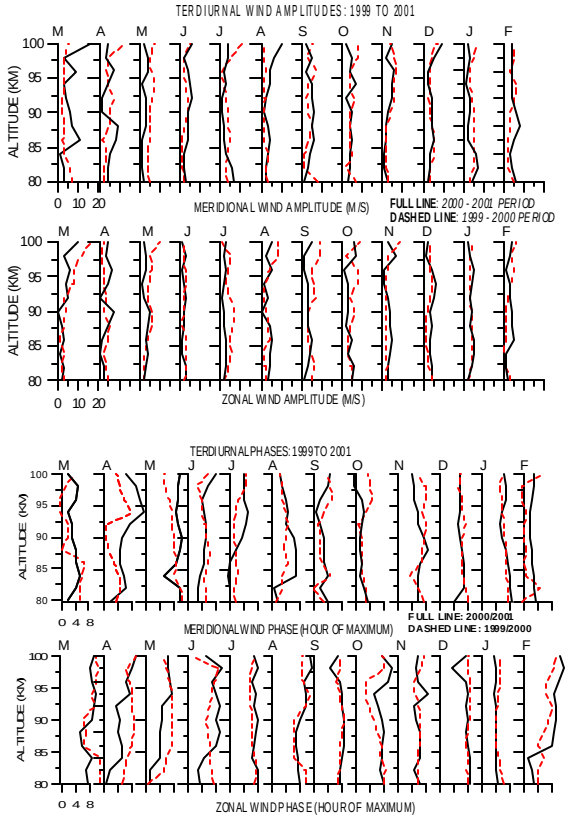

Figure 4. Amplitudes (upper panel) and phases (lower panel) for the terdiurnal tide as a function of months and height. In both panels upper plot is for meridional wind and lower plot is for zonal

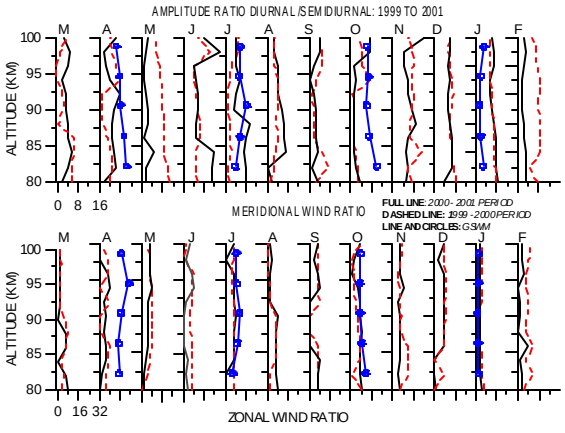

Figure 5. Ratio between diurnal and semidiurnal amplitudes. Upper panel is for meridional wind and lower panel is for zonal wind.

The terdiurnal tide

The amplitudes of the terdiurnal component shown in Figure 4 is about half of the semidiurnal and the inter-annual variation is large. No remarkable characteristics for the amplitudes or phases are noted, except for the long vertical wavelengths from November to January.

Diurnal to semidiurnal ratios

One relevant characteristic for the tides is the relative importance of the diurnal and semidiurnal components. In Figure 5 is shown the amplitude ratio A_d/A_s (Diurnal amplitude/ Semidiurnal amplitude) for each month of the year. The same ratio is shown for the model for January, March, July and October. It is noted that except for summer the ratios are smaller for the experimental data than for the model. For a more complete view of the ratio along the all year we show in Figure 6 the yearly average for the two periods. Note that for the zonal wind the model gives a diurnal amplitude 7-8 times the semidiurnal, but the experimental data show ratios below 3, decreasing with height and approaching unity in the 95 to 100 km region. For the meridional wind the theoretical ratios are also larger, varying between 5 and 7 and the experimental data show ratios between 2 and 4, also decreasing at heights above 95 km.

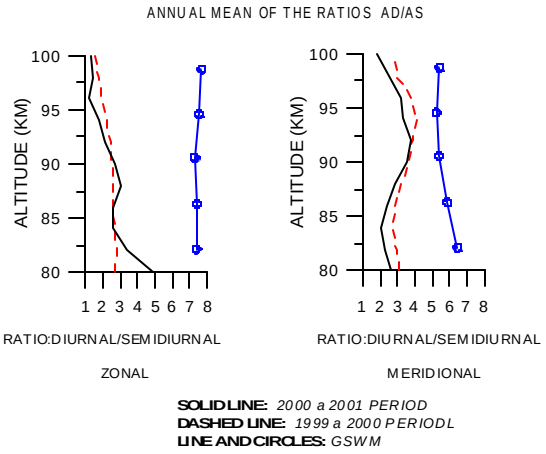

Figure 6. Annual average of the ratios between the diurnal and semidiurnal components.

Conclusion

Measurements of meteor winds at a low latitude southern hemisphere station show results which are generally in agreement with models, although there are some discrepancies. These results can be used to improve future versions of the models.

References

Forbes, J. M., and Vial, F., 1989, Montly simulations of the solar tide in the thermosphere and lower atmosphere, Journal of Atmospheric and Terrestrial Physics, 51(7/8), 649-661.

Fritts, D. C., and Isler, J. R., 1992, First observations of mesospheric dynamics with a partial reflections radar in Hawaii (22^0 N, 160^0 W), Geophysical Research Letters, 19, 409-412.

Fritts, D. C., and Isler, J. R., 1994, Mean motions and tidal and two-day wave structure and variability in the mesosphere and lower thermosphere over Hawaii, Journal of Atmospheric Sciences, 51, 2145-2164.

Hagan, M. E., Forbes, J. M., and Vial, F., 1994, On modeling migrating solar tides, Geophysical Research Letters, 22, 893-896.

Hagan, M. E., Burrage, M. D., Forbes, J. M., Hackney, J., Randel, W. J., and Zhang, X., 1999,GSWM-98: Results for migrating solar tides, Journal of Geophysical Research,104(A4), 6813-6827.

Hedin, A. E., Fleming, E. L., Manson, A.H., Schmidlin, F. J., Avery, S. K., Clark, R. R., Franke, S. J., Fraser, G. J., 1996, Empirical wind models for the upper, middle and lower atmosphere, Journal of Atmospheric and TerrestrialPhysics,58, 1421-1477.

Manson, A. H., Meek, C., Massebeuf, M., Fellous, J. L., Elford, W. G., Vincent, R. A., Craig, R. L., Roper, R.G., Avery, S., Balsley, B. B., Fraser, G. J., Smith, M.J., Clark, R. R., Kato, S, Tsuda, T., and Ebel, E., 1985, Mean winds of the upper middle atmosphere (60-110 km): A global distribution from radar systems (M. F., Meteor, VHF) , Handbook for MAP, 16, Eds. K. Labitzke, J. J. Barnett, and B. Edwards, Urbana IL, 239-268.

Manson, A. H., Meek, C.C., Teitelbaun, H., Vial, F., Schminder, D., Kurchner, D., Smith, Fraser, G. J, and Clark, R. R.,1989, Climatologies of the semidiurnal and diurnal tides in the middle atmosphere (70-110 km) at middle latitudes (40-55), Journal of Atmospheric and Terrestrial Physics, 51, 579-593.

Manson, A. H., Meek, C. E., Fleming, E. L, Chandra, S., Vincent, A. R., Phillips, A., Avery, S. K., Fraser, G. J., Smith, M. J., Fellous, J. L., and Massebeuf, M., 1991, Comparisons between satellite-derived gradioent winds and radar-derived winds from the CIRA-86, Journal of Atmospheric Sciences, 48, 411-428.

Vincent, R. A., and Ball, S. M., 1981, Mesospheric winds at low- and Mid-latitudes in the Southern Hemisphere, Journal of Geophysical Research, 86(A11), 9159-9169.

Acknowledgments

I would like to thank Eng. Synval Domingos and Tec. Cristiano de Castilho for technical support concerning to radar maintenance. We also than to CNPq , through PRONEX program in Aeronomy for making possible the acquisition of the equipment for this work.

THE BGK COLLISION MODEL REVISED

Carlos J. Zamlutti, INPE, C.P. 515 - 12201-970 - São José dos Campos, SP, Brazil

Abstract

Since its initial proposal the BGK (Bhatnagar, Gross, Krook) collision model suffered many criticisms due to the lack of a theoretical support for it. Among the weaknesses attributed to it were the use of a constant collision frequency and the presentation of a linear behavior. Despite its deficiencies it has proven to be quite useful in the study of many aspects of the terrestrial upper atmosphere physics, as well as in conjunction of the kinetic Boltzmann equation to study plasma instabilities. Besides its regular applications for elastic collision problems it can be as useful as in problems involving reactive interactions. A renewed interest in appropriate collision models like the BGK and Fokker Planck appeared recently to handle the transition between collision dominated to collisionless regions of the solar and polar winds. Here an investigation of its reliability is carried out to the light of recent advances in the collision theory. The purpose was to extend the validity to allow for large departure from thermal equilibrium applicability regardless the form of the distribution function, the magnitude of the flow velocity and the value of the effective cross section. In particular it is shown that the Boltzmann equation with Boltzmann collision integral can be cast to a collisional Vlasov equation with a revised BGK collision term.

Model development

The BGK collision model (Bhatnagar et al., 1954) was proposed to circumvent the difficulties to handle the complicated integrals of the collision term (Liboff, 1969; Chapman and Cowling, 1970; Bird, 1994; Zamlutti, 1994). It was required to obey the conservation laws and to express the relaxational aspect. The original version accounts for self-relaxation of a single gas it was extended by Sirovich (1962) to account for gas mixtures and by Burgers (1969) to include reactive interactions.

The basic form of the BGK collision model is:

$$\delta f = -\sum_j \upsilon_j \left(f - n n_{oj}^{-1} f_{oj} \right) \qquad (1)$$

where f denotes particle distribution function, n the number density and υ the collision frequencies (see Burgers, 1969). Unsubscripted symbols refer to the incident particle, subscript j to the target species and subscript o to the equilibrium state. The fundamental works use:

a) A constant collision frequency.

b) Maxwellian equilibrium states.

Both constraints and the fact that it was not theoretically derived suffered criticisms in the literature (Lair and Marsch, 1986; Stubbe, 1987, 1990).

Notwithstanding its limitation it provides quite valuable in the computation of the stress tensor and heat flow vector of the Navier-Stokes approximation of the transport equations (see Schunk, 1977) and constitutes the solely form of assessing collisional effects in inhomogeneous media. Besides it may account also for dynamical equilibrium states like the case of reactive interactions when f stands for production of a considered species and f_{oj} for its loss through a chemical reaction with species j.

Liu and Marsch (1986) showed that constraint *a* above could be released with the introduction of a velocity-dependent relaxation rate. Constraint *b* as commented above is not so severe since dynamic equilibrium can also be treated with the same model. Hence the only remaining query concerns the possibility of making it equivalent to the Boltzmann collision integral by properly defining convenient coefficients for f and f_{oj} of (1). This is done in the present work.

One starts from the Boltzmann collision integral:

$$C\left(f, f_j\right) = \int \left(f' f_j' - f f_j \right) w \sigma \sin\beta \, d\psi \, d\beta \, d\underline{v}_j \qquad (2)$$

where f is the velocity distribution function, $\underline{v}$ the incident particle velocity, $\underline{w} = \underline{v}_j - \underline{v}$ the relative velocity in the encounter, σ the differential scattering cross section, β the scattering angle and ψ the angular variation orthogonal to the plane of incident. Underlined symbol denotes a vector and the same symbol not underlined its magnitude. The integral sign with non specified limits indicates integration over the entire space.

We call

$$\upsilon_j = n_j < w_j >_j \text{ - collision frequency} \qquad (3)$$

$$S_j = \int_{\pi}^{o} \int_{o}^{2\pi} \sigma \sin\beta \, d\psi \, d\beta \text{ - cross section} \qquad (4)$$

$$< w >= \left(n n_j\right)^{-1} \int w f f_j \, d\underline{v} \, d\underline{v}_j \text{ average relative velocity} \qquad (5)$$

and develop $\left(f' f_j' - f f_j \right)$ in a Taylor series as in Zamlutti (1999) which yields upon substitution in (2):

$$C(f,f_j)=\upsilon_j\int\sum_j\left[\underline{A}_j^*\cdot G_j(ff_j)+0.5\underline{\underline{D}}_j^*:G_jG_j(ff_j)+\ldots\right] \quad (6)$$

Eq. (6) establishes the equivalence between the Boltzmann collision integral and the Fokker-Planck form with:

$$A_j^*=(\mu_j/m)\underline{w}_jS_{1j}$$

$$\underline{\underline{D}}_j^*=0.5(\mu_j/m)^2\left(w_j^2S_{2j}\underline{\underline{I}}+4S_{1j}\underline{w}_j\underline{w}_j-3S_{2j}\underline{ww}_j\right)$$

$$G_j=\nabla_v-(m/m_j)\nabla_v$$

$$S_{ij}=2\pi\int_o^\pi\sigma_j\left(1-\cos^i\beta\right)\sin\beta d\beta \qquad \text{i = 1, 2, …}$$

where μ_j is the reduced mass and ∇_v the velocity gradient.

Using a mathematical development and recalling that

$$\int\nabla_{vj}\cdot\left[Q_r(\underline{v}_1)f_j\right]d\underline{v}_j=0$$

when $Q_r(\underline{v}_j)$ is a polynomial of degree *r*, the operator *G* transforms into ∇_v and each component of (6) becomes:

$$C_j(f,f_j)\cong\upsilon_j\left[-\underline{B}_j\cdot\nabla_vf+0.5\nabla_v\cdot\left(\underline{\underline{D}}_j\cdot\nabla_vf\right)\right](n_jS_j)^{-1} \quad (7)$$

where

$$B_j=-(\mu_j/m)(5S_{1j}-2{,}5S_{2j})\int\underline{w}_jf_jd\underline{v}_j$$

$$\underline{\underline{D}}_j=0.5(\mu_j/m)^2\int\left(S_{2j}w_j^2\underline{\underline{I}}+4S_{1j}\underline{w}_j\underline{w}_j-3S_{2j}\underline{w}_j\underline{w}_j\right)f_jjd\underline{v}_j$$

Recalling that $\nabla_vf=\nabla_cf$, with $\underline{c}$ as the thermal velocity (Burgers, 1969), and using.

$$f=f_o(1+\phi)$$

where f_o is the local equilibrium distribution and ϕ is a polynomial correction factor (Schunk, 1977; Barakat and Schunk, 1982) one can further advance in the development of (7) and finally get:

$$C_j(f,f_j)=v_j^*;f+v_{jo}^*f_o \quad (8)$$

with

$$v_j^*=0.5v_j(n_jS_j)^{-1}\left[b_1^2\left(\underline{\underline{D}}_j:C_oC_o\right)+b_1\nabla_c\cdot\left(\underline{\underline{D}}_j\cdot\underline{c}_o\right)\right]$$

$$v_{jo}^*=0.5v_j(n_jS_j)^{-1}\left[2b_1\left(\underline{\underline{D}}_j\cdot\underline{c}_o\cdot\nabla_c\phi\right)+\nabla_c\cdot\left(\underline{\underline{D}}_j\cdot\nabla_o\phi\right)\right]$$

when establishes the theoretically equivalent BGK form with b_1 a constant and $\underline{C}_o$ the thermal velocity for equilibrium conditions.

Conclusions

The BGK model was shown to be equivalent to the Fokker Planck approximation for the Boltzmann collision integral and thus is a very satisfactory model for most of the usual needs in aeronomy and solar terrestrial physics.

REFERENCES

Barakat, A. R. and Schunk, R. W. Transport equations for multicomponent anisotropic space plasmas: a review. Plasma Phys. 24, 389-418, 1982.

Bhatnagar, P. L.; Gross, E. P. and Krook, M. A model for collision processes in gases I. Small amplitude processes in charged and neutral one-component systems. Phys. Rev. 94, 511-525, 1954.

Bird, G. A. Molecular gas dynamics and the direct simulation of gas flows. Clarendon. Press Oxford, 1994.

Burgers, J. M. Flow equations for composite gases. Academic Press, New York, 1969.

Chapman, S. and Cowling, T. G. The mathematical theory of non-uniform gases. Cambridge University Press, Cambridge, 1970.

Liboff, R. L. Introduction to the theory of kinetic equations. Wiley, New York, 1969.

Livi, S. and Marsch, E. Comparison of the Bhatnagar-Gross-Krook approximation with the exact Coulomb collision operator. Phys. Rev. A 34, 533-540, 1986.

Schunk, R. W. Mathematical structure of transport equations for multispecies flow. Rev. Geophys. Space Phys. 15, 429-445, 1977.

Sirovich, L. Kinetic modeling of gas mixtures. Phys. Fluids 5, 908-918, 1962.

Stubbe, P. A new collisional relaxation model for small deviations from equilibrium. J. Plasma Phys. 38, 95-116, 1987.

Stubbe, P. The concept of a kinetic transport theory. Phys. Fluids 82, 22-23, 1990.

Zamlutti, C. J. Transport equations for multicomponent isotropic and anisotropic high speed space plasma. *Planet. Space Sci.* 42, 557-568, 1994.

Zamlutti, C. J. Long range collision effects for drifting velocity distributions. Planet Space Sci. 47, 57-66, 1999.

Typical phenomena observed in Brazilian geomagnetic anomaly region.

Kazuo M akita*, Masonori Nishino** N. J.Schuch***, Hisao Takahashi***, Abdu Mangalathayil ***
*Takushoku University, Japan, **STE Lab.Nagoya University, ***INPE, Brazil

Abstract

Upper atmosphere observation under a weak geomagnetic field region began in cooperative study between Brazil and Japan. Magnetometer, Imaging Riometer, UVB meter, CCD Imager, Photometer and Cosmic Ray detector and others were installed at newly constructed Southern Space Observatory (SSO) in 1998. Several typical phenomena were detected in these few years. For example, cosmic noise absorption was seen in association with a Sudden Commencement (SC) followed by a big magnetic storm. The absorption appeared at the western part of the imaging riometer and drifted azimuthally to eastward direction about 200m/s. For optical observation, several typical emissions ? Multiple band structure ? Cloud structure ? Faint band structure were observed. These emissions seem to be related to atmospheric gravity wave observed at mid latitude.

(1) Introduction

According to the recent geomagnetic field study, the earth magnetic field has been monotonically decreasing for past one thousands years. If the present decreasing rate of geomagnetic field is continued, its intensity will become half after one thousand year later. As well known, the magnetic field intensity is especially weak in the southern part of Brazil. Since the decreasing rate of geomagnetic field is also large around South Atlantic Sea, South America and Caribbean Sea, thus the geomagnetic field in this region will become very weak within a few hundreds years later[1)].

Recent satellite observations indicate that a large number of high energetic particles (a few tens keV ~ a few tens MeV) are precipitating into Brazilian geomagnetic anomaly region due to the weak geomagnetic field. These particles are radiating X-rays at altitude of a few tens km. If the decreasing of geomagnetic filed continues, the number flux of precipitating particle will become increase and its precipitating region will expand. The objective of our study is to make clear the effect of upper atmosphere environment due to this high energetic particle precipitation.

(2) Observations

In order to investigate the upper atmosphere environment due to these particle precipitation, Brazil-Japan joint study started in 1996 and INPE Southern Space Observatory (**SSO** ; 29.70S, 306.18E) was newly constructed at San Martinho da Serra, RS, Brazil in 1998[2)] .The belonging organizations of participating scientists are INPE, Federal University of Santa Maria in Brazil and Takushoku University, Nagoya University, Kyushu University, National Institute of Polar Research (NIPR), Communication Research Laboratory (CRL), National Institute of Radiological Sciences (NIRS), Rikkyo University,

Shinshu University in Japan. At presents, two magnetometer (Kyushu University and CRL), Imaging Riometer, normal Riometer and Natural VLF emission detector (Nagoya University, STE Lab.), UVB detector, two pan-chromatic CCD imagers, one night viewer TV Camera and Two colors (557.7nm and 630nm) zenith photometer (Takushoku University and NIPR), Mesosphere Temperature (OH band) detector (Rikkyo University) and Cosmic Ray detector (NIRS and Shinshu University). In order to compare upper atmosphere phenomena at the geomagnetic conjugate point of SSO in Brazil, magnetometer (Kyushu University) and Riometer (Takushoku University) are installed at Trinidad Island (9.57N, 297.82E) in cooperative with University of West Indies. The SSO and Trinidad must be connecting with nearly same geomagnetic field line but the total geomagnetic intensity in both observatories is quite different. The geomagnetic intensity at SSO is about 22000nT and Trinidad is about 32000nT (about 30% difference). Since the mirror height are quite different in both hemispheres, so the number fluxes of precipitating particles are also different. We expect that typical different phenomena will be detected in these conjugate points. From our observations at SSO, Brazil, several typical cosmic noise absorption [3]and optical emission phenomena[4)] were obtained by Imaging Riometer and CCD camera are described.

(A) Imaging Riometer

Riometer antenna is composed of a two-dimensional array of 4 x 4 half wavelength dipoles in 38.2MHz.The resolution of obtained image data is about 50km when the image is projected at 100km altitude. Typical absorption phenomena was observed at SSO in associated with geomagnetic storm on September 22,1999. Figure 1 shows H-component magnetograms obtained at mid- and low- latitude. Sudden Commencement (SC) began at about 12h UT on September 22. The intensity increased continuously until 20h UT (Initial Phase) and then sharply decreased (Main Phase). The minimum value (-170nT at Hermunus) is seen at 23h30m UT and then it gradually increased (Recovery Phase). Figure 2 shows the image data obtained from 23h31m39s to 00h10m36s UT. Each image is averaged by 128 seconds. Topside is the equatorward (Magnetic North) and left side is eastward. The typical absorption event was observed in the north and west regions at 23h38m03s UT. The western absorption region moved to the east and became weak after 23h46m35s and northern absorption region was continuously seen till 23h52m59s. After 23h55m07s. The absorption region became weak with moving to the equator ward and disappeared at 00h10m36s UT. The maximum absorption value is about 1.5dB in this event.

The absorption region drifted to the east side by about 200m/s velocity. If this drift relates to the electric field (E× B) and the magnitude of this electric field is assumed to be 3mV/m, the precipitating electron energy is calculated to be 17keV. It means that these electrons are precipitating to E- or D-Layer ionosphere and induced cosmic noise absorption during storm time.

(B) Optical emission

Pan-chromatic CCD imager and photometer started to operate in August, 1999. Since then several typical phenomena were observed and these events were summarized as follows.

H-component Magnetogram 1999

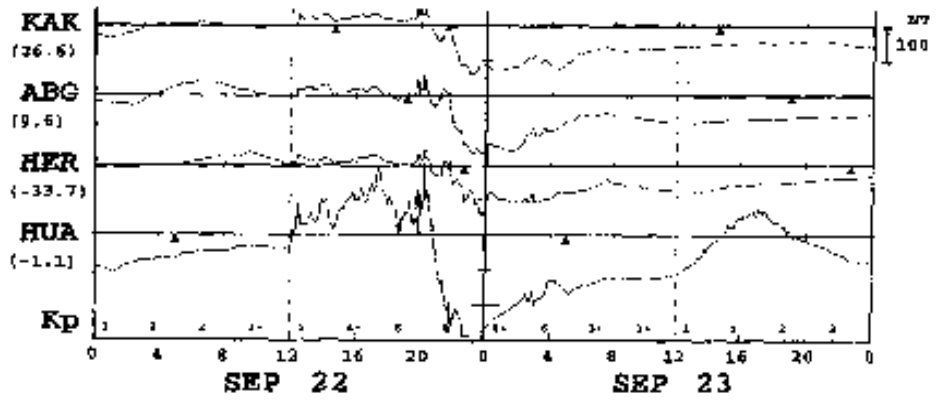

Figure 1

Imaging Riometer Sep 23/24, 1999

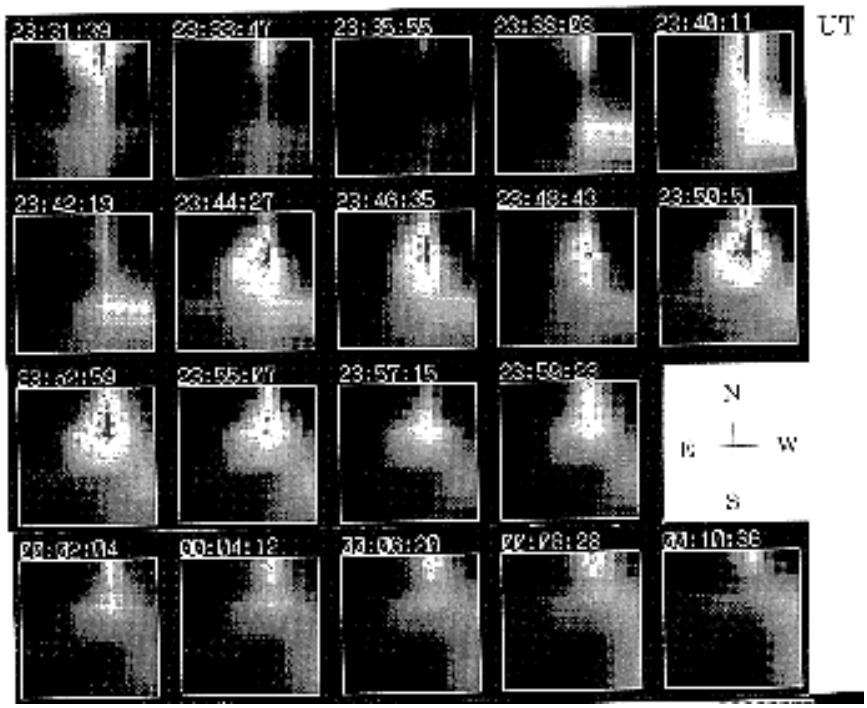

Figure 2

Figure 3a is multiple band phenomena recognized at south-west region. Milky Way is seen in the center of this figure. These bands move from the west to east direction with 500m/s velocity. The

luminosity is about a few hundreds Reyleigh (R). In this period, Kp= 4- , IMF Bz = –2 nT, solar wind velocity is 420km/s. Figure 3b is cloud structure phenomena. Isolated Bright region (a few hundreds R) appears in the southward and extends to the northward with moving to the east side. In this period, Kp= 2+ , IMF Bz is +6nT and solar wind velocity is 250km/s. Figure 3c is faint band structure. The faint bands extending from the south - north direction are seen in this figure. The luminosity of this event is extremely weak as compared with multiple bands and Cloud structure phenomena. In this period, Kp= 1 , IMF Bz is near 0nT and solar wind velocity is 350km/s.

Multiple Band (Aug.9,1999) **Cloud Structure(Aug.10,1999)** **Faint Band (Aug.14,1999)**

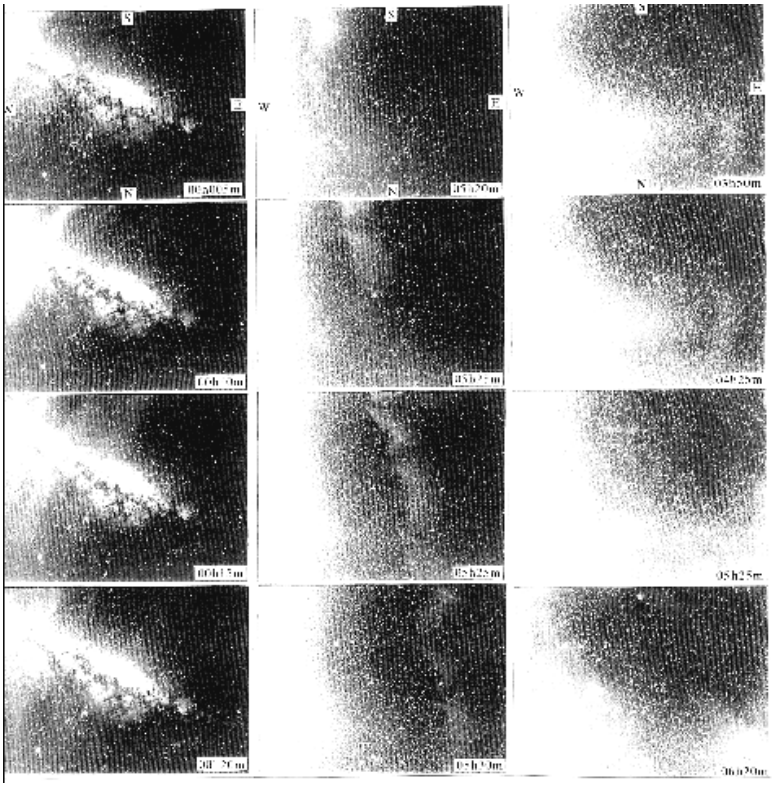

Figure 3a **Figure3b** **Figure 3c**

References

1) Makita K., and N.J.Schuch,Geomagnetic hole, Bulletin of science and engineering, Takushoku Univ. 7(2), 59-66,1999

2) Makita K. et.al. Upper atmosphere observations in the Brazilian geomagnetic Anomaly Region, Bulletin of science and engineering, Takushoku Univ. 6(2), 69-72,1997

3) Mendillo M., et.al. Investigation of thermospheric-ionospheric dynamics with 6300A images from the Arecibo Observatory,J.Geophys.Res.102,7331-7343,1997

ULF Pulsations in the Pc5 Range Near the Magnetospheric Equatorial Plane and Their Ground Signatures

José M. da Costa[1], University of Taubaté, Taubaté, São Paulo, Brazil; Gordon Rostoker[2],Solar-Terrestrial Environment Laboratory, Nagoya University, Toyokawa, Aichi 442-8507, Japan; Frances R. Fenrich and John C. Samson, Department of Physics, University of Alberta, Edmonton, Alberta, Canada

Abstract

Geotail satellite and CANOPUS network magnetometer data and SuperDARN flow measurements are used to show that, when activity levels are low, it is possible to detect the ground signatures of ULF magnetosphere wave trains. The space and the respective ground signatures of one near monochromatic Pc5 wave train were successfully observed on November 21, 1997 event. Dominant spectral field line resonance peaks near 2.5 and 3.2 mHz were found in the data observed by Geotail, SuperDARN and CANOPUS. The analysis of Geotail data also reveals that the spacecraft may have crossed an oscillating magnetospheric structure near the magnetopause boundary. *1 Also at National Space Research Institute, Sao José dos Campos, Sao Paulo, Brazil; 2 Also at Department of Physics, University of Alberta, Edmonton, Alberta, Canada*

Introduction

Patel and Cahill (1964) gave the first reports on experimental evidences about the propagation of magnetospheric ULF wave trains to earth's surface**.** Several other examples have been reported since then (*i.e. Ohtani et al.* 1999; *Korotova et al.* 2000; *Kokubun et al.* 2000). The present work reports on one near monochromatic ULF pulsations event occurred on November 21, 1997, in the Pc5 wave range. The pulsations were observed close to the magnetosphere equatorial plane by Geotail and their respective ground signatures were detected by CANOPUS magnetometers. Dominant spectral field line resonance peaks near 2.5 and 3.2 mHz were found in the data observed by all three instruments (Geotail, CANOPUS and SuperDARN)

Instrumentation

The CANOPUS magnetometer array (*Samson et al.* 1991; and *Rostoker et al.* 1995) consists of 13 stations distributed in the northern part of Canada from about 50ºN to 70ºN geographic latitudes and longitudes from 220ºE to 270ºE. Each station is equipped with a three component ring core fluxgate magnetometer designed to measure the geographic north-south (X), east-west(Y), and vertical (Z) component of the geomagnetic variation field with a resolution of 0.025 nT at a sampling rate of 8 Hz.The SuperDARN network (*Greenwald et al.* 1985) consists of numerous radars, three of which are installed in Saskatoon, Kapuskasing and Goose Bay. Each one has two linear phased-arrays of log periodic antennas, operating in the 8-20 mHz band. By means of a phasing matrix, the radar scans from east to west or vice versa through 16 different beams. The integration time at each beam is 6.25 s, resulting in a sampling rate of about 100 s for a complete 16-beam scan. See *Kokubun et al.* (1994) for a detailed description of Geotail magnetic field experiment.

Data Analysis and Results

The November 21, 1997 event had quiet solar and interplanetary magnetic field activity conditions**.** During the event Geotail was crossing the dusk side of the geomagnetic cavity. Both magnetic data observed by Geotail and CANOPUS magnetometers were analyzed using bandpass and FFT. Cross-spectral and analytic signal tecniques developed by *Fenrich et al.* (1995) were used to identify field line resonances in SuperDARN radar data and also to determine their spectral characteristics and spatial variations.

The analysis of Bx, By and Bz magnetic variations observed by Geotail reveals the occurence of ULF waves. The magnetic field data measured by CANOPUS stations also indicate the detection of ULF waves in that interval of time. Figure 1a,b,c,d show, respectively, plots of spectral power for the Geotail Bx, By, and Bz data, during the time interval 00:30-02:30 UT, SuperDARN beam1 gate22 line-of-sight velocity component, and CANOPUS (CONT, GILL, RABB and FSMI) Bx and By components for 00:00-01:00 UT. A common dominant spectral peak near 2.5-3.0 mHz could be seen on all three instruments.

Figure 2a,b show plots of normalized spectral power and phase versus latitude for the 2.5 mHz spectral component observed in the line-of-sight velocity on beam 1(gate 22) of SuperDARN and the Bx and By components of the CANOPUS meridian line of stations for the time interval 00:00-01:00 UT, November 21, 1997. A narrow peak in power observed by SuperDARN at ~70.7 degrees has a

phase decrease of ~100. This characteristic indicates standing shear Alfven field line resonance (FLR). The evidence of FLR is not so apparent in the Bx component (Figure 2a) of the CANOPUS stations. A similar FLR characteristic is apparent in the By component of the CANOPUS stations (Figure 2b), but it is shifted in latitude to 69.7 degrees and much broader with a smaller phase decrease.

A more detailed power spectrum analysis of Geotail magnetic data reveals dominant peaks near 3.2 mHz and 2.5 mHz for the time intervals of 00:30-01:00 UT and 01:30-02:00 UT, respectively. For interval of time before 00:30 UT and after 02:00 UT the analysis does not show any dominant peak, which may indicate that Geotail could have crossed na oscillating magnetospheric structure from 00:30-02:00 UT. Taking in account Geotail data orbit in the magnetosphere for the time interval from 00:30 UT to 02:00 UT, it seems that this structure could measure 2.6 Re, approximately, as one of its dimensions.

Discussion and Conclusions

We used Geotail satellite magnetic data, ground magnetic variations detected by CANOPUS magnetometer network and SuperDARN flow measurements to demonstrate that, when activity levels are low, it is possible to detect the ground signatures of Pc5 magnetospheric ULF wave trains.

The space and the respective ground signatures of one near monochromatic ULF Pc5 waves event were successfully observed on November 21, 1997. This event occurred close to the magnetospheric equatorial plane and also had quiet solar and interplanetary magnetic field (IMF) activity conditions. During the event the satellite was in the dusk side of the geomagnetic cavity.

Dominant spectral field line resonance peaks near 2.5 and 3.2 mHz were found in the data observed by all three instruments (Geotail, CANOPUS and SuperDARN). The 3.2 mHz peak is dominant from 0030 to 0100 UT and the peak near 2.5 mHz is dominant from 0100 to 0200 UT. The CANOPUS and SuperDARN data show a difference of about 01º PACE latitude for both 2.5 and 3.2 mHz peaks. This lag could, perhaps, be due to the geographical positions of the CANOPUS stations in respect to the region where the resonance peaks.

The change in the dominant frequency from near 3.2 mHz to 2.5 mHz is, perhaps, due to an inward evanescently decay of the compressional wave. The calculated azimuthal m wave number for the peak near 2.5 mHz from SuperDARN data is ~14 (apparent phase speed ~2.4 km/s) with propagation anti-sunward. For CANOPUS data the azimuthal m wave number is m~3-5 (apparent phase speed ~6.8 km/s). These results are consistent with Pc5 waves generated by Kelvin_Helmholtz instability near the magnetopause. The higher value for CANOPUS is in agreement with one of the events studied by *Ziesolleck et al.* (1998), which has 5.2 km/s for SuperDARN and 9.3 km/s for CANOPUS apparent phase velocity.

It seems that the analysis of Geotail magnetic data also reveals that the spacecraft may have crossed an oscillating magnetospheric structure near the magnetopause boundary, from 00:00 UT to 02:00 UT on November 21, 1997. The length of one of the dimensions of this structure was estimated from Geotail orbit data as measuring approximately 2.6 Re.

References

Fenrich, F. R., J. C. Samson, G. Sofko, and R. A. Greenwald, ULF high-and low-m field line resonances observed with Super Dual Auroral Radar Network, J. Geophys. Res., 100, 21,535-21,547, 1995.

Greenwald, R. A., K. B. Baker, R. A. Hutchins, and C. Hanuise, An HF phase_array radar for studying small-scale structure in the high-latitude ionosphere, Radio Sci., 20, 63, 1985.

Kokubun, S., T. Yamamoto, M. H. Acuna, K. Hayashi, K. Shiokawa, and H. Kawano, The GEOTAIL magnetic experiment, J. Geomag. Geoelectr., 46, 7-22, 1994.

Kokubun, S., H. Kawano, T. Mukai, Y. Saito, K. Tsuruda, T. Yamamoto, and G. Rostoker, Surface waves on the dawn magnetopuse: connection with ground Pc5 pulsations, Adv. Space Res., 25, No. 7/8,1493-1502, 2000.

Korotova, G. I., M. G. Kivelson, D. G. Sibeck, T. A. Potemra, and P. Stauning, Multipoint observations of global magnetospheric compressions, J. Geophys. Res., 105, 23,293-23,302, 2000.

Patel, V. L. and L. J. Cahill, Jr., Evidence of hydromagnetic waves in the earth's magnetosphere and of their propagation to the earth's surface, Phys. Rev. Lett., 12, 213-215, 1964.

Ohtani, S., G. Rostoker, K. Takahashi, V. Angelopoulos, M. Nakamura, C. Waters, H. Singer, S. Kokubun, K. Tsuruda, W. J. Hughes, T. A. Potemra, L. J. Zanetti, J. B. Gary, A. T. Y. Lui,

and D. J. Williams, Coordinated ISTP satellite and ground observations of morningside Pc5 waves, J. Geophys. Res., 104, 2381-2397, 1999.

Rostoker, G., J. C. Samson, F. Creutzberg, T. J. Hughes, D. R. McDiarmid, A. G. McNamara, A. Vallance Jones, D. D. Wallis, and L. L. Cogger, CANOPUS-A ground-based instrument array for remote sensing the high-latitude ionosphere during the ISTP/GGS program, Space Sci. Rev., 71, 743, 1995.

Samson, J. C., R. A. Greenwald, J. M. Ruohoniemi, T. J. Hughes, and D. D. Wallis, Magnetometer and radar observations of magnetohydrodynamics cavity modes in the earth's magnetosphere, Can. J. Phys., 69,929, 1991.

Ziesolleck, C. W. S., F. R. Fenrich, J. C. Samson, and D. R. McDiarmid, Pc5 field line resonance frequencies and structure observed by SuperDARN and CANOPUS, J. Geophys. Res. 103, 11,771-11,785, 1998.

Acknowledgements.

The CANOPUS array was constructed, and is maintained and operated by the Canadian Space Agency. The SuperDARN Saskatoon radar is supported by the Canadian National Science and Engineering Research Council; the Kapuskasing and Goose Bay radars are supported in part by the U. S. National Science Foundation. José. M. da Costa received financial support from UNITAU and FAPESP, both from Brazil.

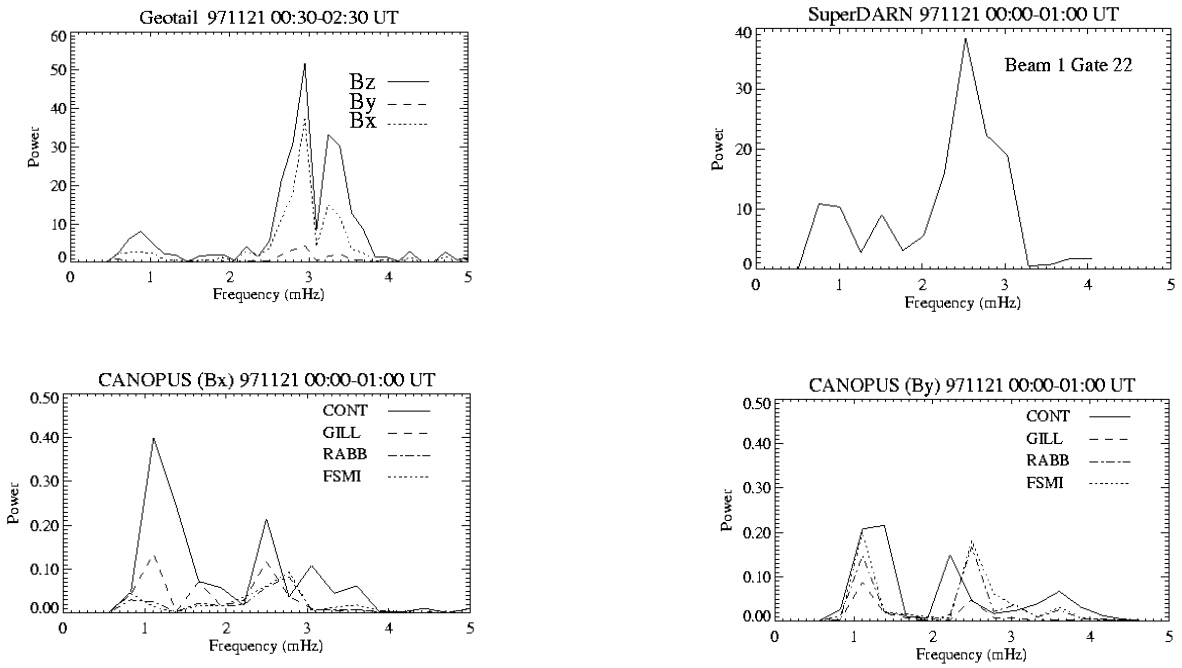

Figure 1a,b,c,d – Spectral power for Geotail Bx, By and Bz, SuperDARN beam1 gate 22line-of-sight velocity component, and selected CANOPUS stations Bx and By components.

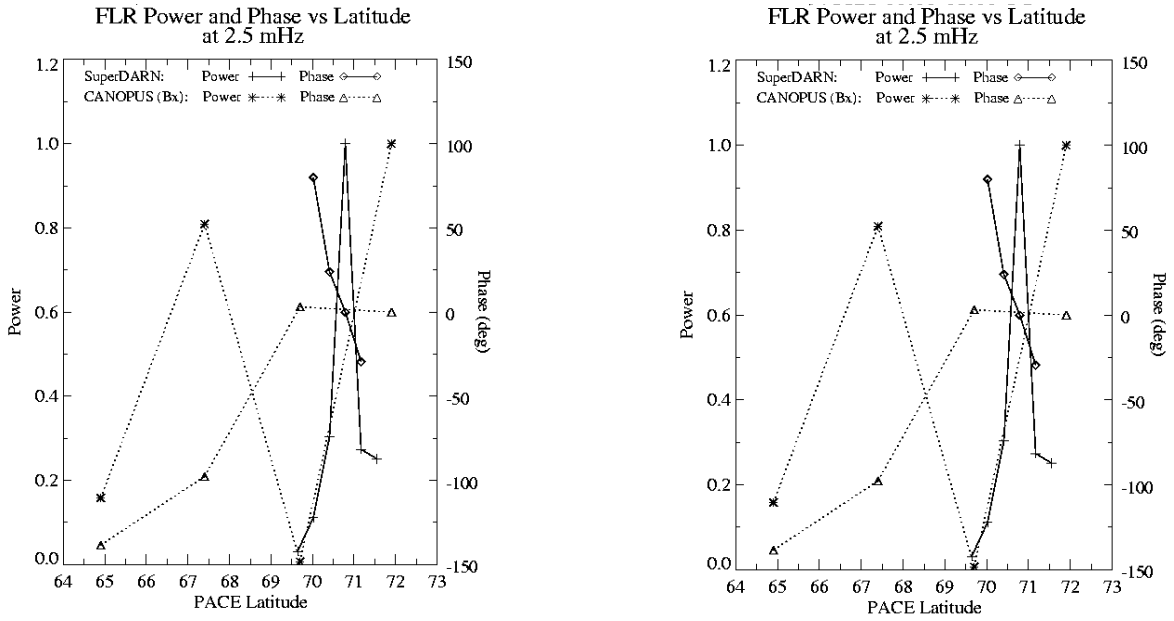

Figure 2a,b – Normalized spectral power and phase versus PACE latitude for 2.5 mHZ observed in the line-of-sight velocity on beam 1 gate 22 of SuperDARN and CANOPUS Bx and By components for 00:00 01:00 UT, Novvember 21, 1997.

Validation of GPS Data-Driven Ionospheric Specification Models

Brian Wilson, George Hajj, Anthony Mannucci, Xiaoqing Pi, Thomas Runge, and Lawrence Sparks, Jet Propulsion Laboratory, Chunming Wang, University of Southern California

Abstract

Dual-frequency transmissions from the Global Positioning System satellites have been used for many years to measure and map ionospheric total electron content (TEC) on global scales. JPL's Global Ionospheric Mapping (GIM) software uses observations from ~100 GPS sites, an extended "shell" model, and Kalman filtering to compute global maps of vertical TEC with 15-minute time resolution and ~5-degree spatial resolution. Recently, the GIM algorithms have been enhanced to solve for multiple parameters on a shell grid, instead of just the single value of vertical TEC. Such multi-parameter models are designed to improve the accuracy of slant TEC retrievals and the ability to calibrate slant TEC delays for arbitrary raypaths. The extra parameters allow GIM to better model horizontal gradients and variations in peak height, while still retaining a simple, constrained fitting model as compared to a full tomographic density solution which is vastly underdetermined. A fully 3-dimensional Global Assimilative Ionosphere Model (GAIM) is currently being developed by a joint University of Southern California and JPL team. GAIM uses a first-principles ionospheric physics model ("forward" model) and Kalman filtering and 3DVAR techniques to solve for densities on a 3D grid. Although GAIM will ultimately use multiple datatypes and many data sources, one can perform a first test of quantitative accuracy by ingesting GPS-derived TEC observations and then comparing the accuracy of the retrieval to a corresponding run of the enhanced GIM model. A series of such GAIM versus GIM comparisons will be presented and the accuracy of both retrievals will be validated by comparisons to several kinds of independent ionospheric observations: vertical TEC data from the TOPEX altimeter, slant TEC data from GPS sites that were not included in the assimilation runs, and global ionosonde data (F0F2, HMF2, and bottom-side profiles where available). By presenting animated movies of the GAIM densities and TEC maps, and their errors computed as differences from the independent observations, we will characterize the reasonableness and physicality of the climatology derived from the GAIM forward model and the quantitative accuracy of the ionospheric "weather" specification provided by the assimilation retrievals.

Variation of the zonal plasma bubble drift velocities with solar cycle at low latitude

Pedrina M. T. Santos, INPE, Brazil; J. H. A.Sobral, INPE, Brazil; M. A. Abdu, INPE, Brazil; J. R. Souza, INPE, Brazil..

Abstract

A detailed study of the zonal drift velocities of the ionospheric bubbles is carried out using experimental airglow data registered at Cachoeira Paulista (22.5 S, 45 W, dip 30 S) during the period of October to March, between 1980-1994. This study is based upon 172 nights of zonal scanning photometer measurements of OI 630 nm airglow. The zonal velocity magnitudes of the ionospheric bubbles are investigated taking into account the solar effects. In general, it is verified that the zonal velocities of the bubbles increase with solar flux F10.7 cm. Analysis of the monthly variations shows that the velocities tend to decrease faster with local time during solar minimum than during solar maximum.

Introduction

The *Instituto Nacional de Pesquisas Espaciais* detects in 1976, for the first time, ionospheric bubbles over Cachoeira Paulista (22.6^0S, 45^0W) through the monitoring of airglow 6300 nm by fotometers of the meridional (north to south) and zonal (east to west) scanning (Sobral et al., 1980a, 1980b and 1981). Analysis of these data showed that the meridional and zonal motions of the airglow profile are associated with ionospheric bubbles. These motions occur due to a combination between the action of vertical electric ionospheric and the geomagnetic fields. These motions resulted in displacements which are usually called drifts **E x B** or zonal drift.

The study of the zonal drift of the ionospheric bubbles is very important to understand the low latitude ionospheric dynamics, since these bubbles are a consequence of the action of the total ionospheric dinamo system on these regions (Heelis et al., 1974; Richmond et al., 1976; Fejer et al., 1985). Another application for this study is providing input data to the model and theorical simulation developments of the ionospheric dynamics (Anderson e Mendillo, 1983; Nakamura et al., 1984).

The purpose of this work is a detailed study of the zonal drift velocities of the ionospheric bubbles which occurs over Cachoeira Paulista region. It was-made used a photometric observational database of the airglow 6300 nm, which was registered over that region in the period between 1980 and 1994.

The large photometric data registration period at Cachoeira Paulista show relevant importance to this work, since the observations exceed a 11 year complete solar cycle. This fact allows the comparative analyses between the obtained velocities during the maximum and minimum solar activity.

Analyses method of the zonal drift velocities of ionospheric bubbles.

To the analyses of the zonal drift velocities of the ionospheric bubbles related to the solar activity the period was chosen according to the maximum and minimum sunspot number index. The solar minimum and maximum activity period division was made with annual means of the sunspot number (NMS) presented on Table 1.

Table 1 – Mean annual sunspot number values between 1980 and 1994

	Média Anual		Média Anual		Média Anual
1980	154,6	**1985**	17,9	**1990**	142,6
1981	140,4	**1986**	13,4	**1991**	145,7
1982	115,9	**1987**	29,4	**1992**	94,3
1983	66,6	**1988**	100,2	**1993**	54,6
1984	45,9	**1989**	157,6	**1994**	29,9

It was determined that the maximum solar activity period corresponds to NMS > 94.3 (1980 – 1982 and 1988 – 1992) and the minimum to NMS < 67 (1983 – 1987 and 1993 – 1994). See Table 1.

It is important to emphasize that the magnetic activity and sazonal parameters were fixed. We selected ten nights with lower relative ΣKp values to each month of the minimum and maximum solar activity period (Table 2). The ΣKp values are related to the first night bubble occurrence.

Tabela 2 – Nights with the smallest ΣKp during the period of October to March, between 1980-1994, of maximum and minimum solar activity.

PERÍODO DE ATIVIDADE SOLAR MÁXIMA (1980-1982/1988-1992)											
Janeiro	ΣKp	Fevereiro	ΣKp	Março	ΣKp	Outubro	ΣKp	Novembro	ΣKp	Dezembro	ΣKp
27-28/1/90	7o	13-14/2/80	4+	12-13/3/80	2+	1-2/10/80	5-	14-15/11/90	2+	6-7/12/80	7-
23-24/1/80	10-	10-11/2/80	7o	22-23/3/88	6o	24-25/10/92	5+	25-26/11/89	3+	5-6/12/88	7+
13-14/1/88	13+	11-12/2/80	8+	9-10/3/81	8-	31/101/11/81	9+	13-14/11/90	6o	18-19/12/90	10-
28-29/1/90	13+	17-18/2/80	12o	20-21/3/80	9+	2-3/10/80	10-	15-16/11/90	6o	8-9/12/88	10o
17-18/1/88	14o	16-17/2/82	13+	13-14/3/88	10-	15-16/10/88	11+	29-30/11/92	11-	7-8/12/80	12+
5-6/1/81	18o	9-10/2/80	20+	23-24/3/88	10+	25-26/10/92	14o	3-4/11/80	11o	17-18/12/90	12+
17-18/1/82	18o	3-4/2/81	22o	16-17/3/91	13-	13-14/10/91	15o	8-9/11/80	13-	20-21/12/81	13+
18-19/1/88	18o	14-15/2/80	24o	18-19/3/91	14-	23-24/10/90	16o	6-7/11/80	13o	22-23/12/92	16-
19-20/1/88	19-	21-22/2/90	25-	10-11/3/81	15+	2-3/10/89	17-	20-21/11/90	13+	4-5/12/80	16-
1-2/1/92	21-	15-16/2/80	27+	19-20/3/80	16o	3-4/10/89	19-	26-27/11/89	17+	19-20/12/81	18-
PERÍODO DE ATIVIDADE SOLAR MÍNIMA (1983-1987/1993-1994)											
Janeiro	ΣKp	Fevereiro	ΣKp	Março	ΣKp	Outubro	ΣKp	Novembro	ΣKp	Dezembro	ΣKp
4-5/1/87	5+	16-17/2/85	13+	22-23/3/85	8o	30-31/10/84	12+	17-18/11/87	12+	14-15/12/93	8-
5-6/1/87	5+	6-7/2/86	16o	30-31/3/87	8+	31/101/11/86	13+	18-19/11/87	11-	15-16/12/87	15o
13-14/1/86	6+	28/2-1/3/87	21+	24-25/3/87	9o	28-29/10/86	14+	28-29/11/84	11+	11-12/12/93	14+
7-8/1/83	8o	23-24/2/87	23o	20-21/3/85	10-	14-15/10/85	16o	2-3/11/86	12o		
7-8/1/87	9o	22-23/2/87	25-	25-26/3/87	11-	27-28/10/84	16+	19-20/11/87	21-		
4-5/1/86	10o	21-22/2/87	26-	23-24/3/87	12o	28-29/10/84	17o	20-21/11/87	19+		
8-9/1/83	17-	11-12/2/83	26-	8-9/3/83	13-	26-27/10/87	19o	1-2/11/86	18o		
3-4/1/86	17o	16-17/2/94	29+	10-11/3/83	13o	30-31/10/86	23o				
26-27/1/93	28o	15-16/2/83	30+	9-10/3/83	15-	29-30/10/86	23o				
		16-17/2/83	33-	28-29/3/87	18-	15-16/10/85	23+				

To complete this analyses is used the Solar Flux F10.7 cm. This flux is emitted by Sun with a daily variability, as response to Sunspot numbers over the Solar disk. The flux density at 2800 MHz is registered by telescopes. The F10.7 cm values used in this work were obtained in the site: ftp://ftp.ngdc.noaa.gov/STP/SOLAR_DATA/SOLAR_RADIO/FLUX/.

Results and Discussions

The mean zonal drift velocities of the ionospheric bubbles calculated to the nights related in Table 1 were plotted as local time function, to each month in the studied period. Thus were obtained the accelerations and the mean initial and final velocities for each period (Table 3).

Table3 – Accelerations and velocities.

Period	Aceleration (ms-1h-1)	Vi (ms-1)	Vf(ms-1)
January/maximum	-16,08	138,25	41,79
January/minimum	-10,26	97,29	35,71
February/maximum	-11,62	178,15	108,41
February/minimum	-17,44	134,12	46,9
March/maximum	0,02	128,43	128,53
March/minimum	-3,2	104,46	78,84
October/maximum	-5,67	148,72	114,68
October/minimum	-14,5	122,25	6,26
November/maximum	-12,97	159,56	81,76
November/minimum	-9,9	133,69	64,4
December/maximum	-13,12	139,81	61,06
December/minimum	-28,24	162,36	21,12

Trough Table 3 it is observed that the largest negative accelerations occur on December/minimum and on February/minimum. However, it is important mention that on December/minimum the representative of data was small. The only period which presented positive acceleration was on March/maximum. Except December, the velocities were larger in the maximum solar activity period, as expected. The largest (smallest) values of the zonal velocities of the ionospheric bubbles were registered on February/maximum (October/minimum).

Figure 1 presents the dispersion diagrams at local time to the 172 studied nights.

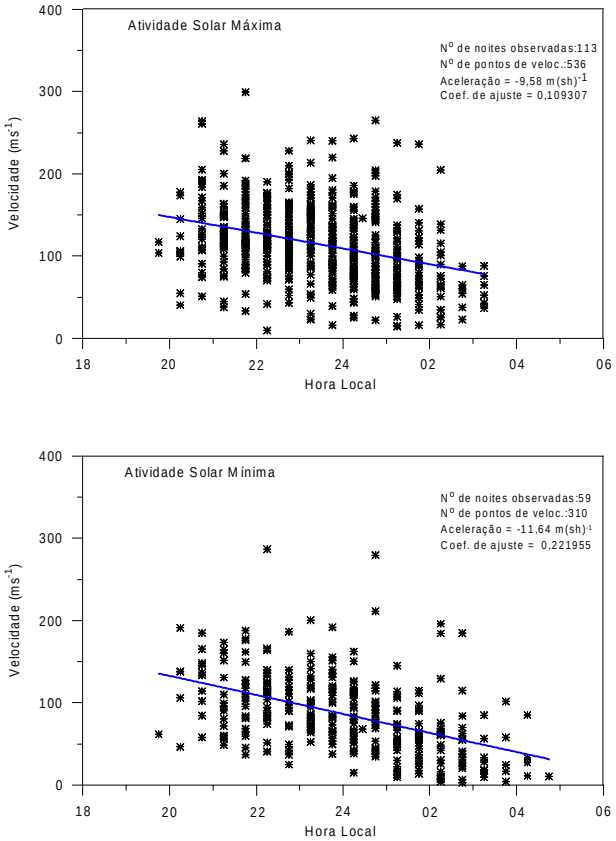

Figure 1 – Velocity dispersion diagrams of the zonal drift of the ionospheric bubbles registered over Cachoeira Paulista of October to March, between 1980-1994, to the maximum and minimum solar activity period.

As observed in the Figure 1, it is noticed that, in both cases, the bubble drift velocities decrease with local time. Though the linear adjustment between the two periods, we obtained the accelerations and the mean values of zonal velocities at 20LT and 03LT, which were presented in Table 4.

Table 4 – Accelerations and Zonal mean velocities at 20 and 03 LT obtained in Figure 1.

Period	V20LT(ms-1)	V03LT(ms-1)	Aceleration (ms-1h-1)
Solar Minimum	147,43	99,52	-9,58
Solar Maximum	132,69	40,04	-11,64

The Table 4 shows clearly that the larger zonal drift velocities of the ionospheric bubble occur during the maximum solar activity period. It is also observed that the minimum solar activity periods decrease in a steep way.

The analyses about the solar activity were finished observing the variation behavior of zonal drift velocities with the Solar Flux F10.7 cm, in the interval between 18LT and 22:45LT. The obtained result is showed in the Figure 2.

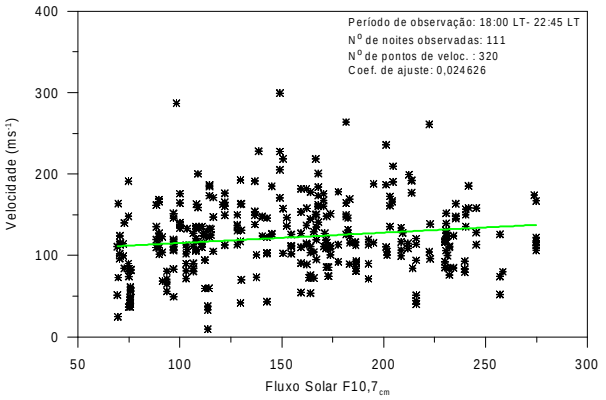

Figure 2 – Dispersion diagram of the drift zonal velocities of the ionospheric bubbles registered at Cachoeira Paulista in the interval 18LT- 22:45LT as function of the flux F10.7 cm.

From the linear adjustment (Figure 3) were calculated the mean initial and final velocity variations on each curve. To the F10,7cm values of 75 and 275 ($x10^{22}Wm^2Hz^{-1}$) were obtained 112,11 ms^{-1} and 137,55 ms^{-1} as mean velocities, respectively. It demonstrates that the velocities are proportional to the Solar Flux F10.7 cm between 18LT and 22:45LT.

Conclusions

In this work was made a detailed study of the behavior of the zonal drift velocities of the ionospheric bubbles detected at Cachoeira Paulista during the period of October to March, between 1980-1994. The zonal velocity magnitudes of the ionospheric bubbles are investigated taking into account the solar effects. It was made a detailed study about the behavior of the zonal velocities monthly.

The principal conclusions of this study are:

- To the periods of maximum and minimum solar activity the results show that the mean velocities of the zonal drifts decrease with local time, except on March.
- It was observed that the mean velocity values are larger during the solar maximum activity period, except on December.
- Generally, the zonal velocity behavior is proportional to the Solar Flux F10.7cm increase. To the F10,7cm values of 75 and 275 ($x10^{22}Wm^2Hz^{-1}$) were obtained 112,11 ms^{-1} and 137,55 ms^{-1} as mean velocities, respectively (see Figure 3).

References

Anderson, D. N.; Mendillo, M. *Ionospheric conditions affecting the evolution of equatorial plasma depletions*. Geophysical Research Letters, v. 10, n. 7, p. 541-544, Julho, 1983.

Fejer, B. G; Kudeki, B. G.; Farley, D. T. *Equatorial F region zonal plasma drifts*. Journal of Geophysical Research**,** v.90, n. A12, p. 12.249-12.255, Dezembro, 1985

Heelis, R. A.; Kendall, P. C.; Moffett R. J.; Windle D. W.; Rishbeth, H. *Electrical coupling of the E- and F- regions and its effect on F-region drifts and winds*. Planet Space Science, v. 22, p. 743-756, 1974.

Nakamura, Y.; Sobral, J.H.A.; Abdu, M.A. *A simulation of equatorial plasma bubble signatures on the 01 630 nm nightglow meridional profile over brazilian low latitude*. Revista Brasileira de Geofísica, v.2, p.65-77, 1984.

Richmond, A. D.; Matsushita, S.; Tarpley, J. D. *On the production mechanism of electric currents and fields in the ionosphere*. Journal of Geophysical Research, v.81, n.4, p.546-555, Fevereiro, 1976.

Sobral, J.H.A.; Abdu, M.A.; Batista, I.S. *Airglow studies on the ionosphere dynamics over low latitude in Brazil*. Ann. Géophys**.**, v.2, p. 199-204, 1980a.

Sobral, J.H.A.; Abdu, M.A.; Zamlutti, C.J.;Batista, I.S. *Association between plasma irregularities and airglow brazilian low latitudes*. Geophysical

Sobral, J.H.A.; Abdu, M.A.;Batista, I.S.; Zamlutti, C.J. *Wave disturbances in the low latitude ionosphere and equatorial ionospheric plasma depletions***.** Journal of Geophysical Research, v.86, n.A3, p.1374-1378, Março, 1981.

Variation of the ionospheric equatorial anomaly with solar cycle in the Brazilian region during autumn equinox condition

Jonas R. Souza[1], Mangalathayil A Abdu[1] and Graham J. Bailey[2], 1-Instituto Nacional de Pesquisas Espaciais, Brazil, 2-University of Sheffield, England

Abstract

An investigation of the equatorial anomaly dependence on solar activity is carried out using a sophisticated theoretical model, the Sheffield University Plasmasphere Ionosphere Model (SUPIM). Measurements of the ionospheric electron content (TEC) over Cachoeira Paulista (22.5° S, 45° W and dip lat.= 15°), which is near the southern anomaly crest, have shown a decrease for F10.7 solar flux greater than 180. SUPIM results have revealed that this behaviour of TEC is a consequence of an increased equatorial **E**×**B** drift. An increase in the upward equatorial **E**×**B** drift causes the equatorial anomaly to expand, i.e, the position of the anomaly crests move poleward, so that Cachoeira Paulista is in the anomaly trough rather than at the southern crest.

Introduction

The equatorial anomaly is caused by the combined effects of **E**×**B** drift and ambipolar diffusion, where **E** is the electric field generated by the E region dynamo and **B** is the geomagnetic field (Anderson, 1973a,b). At equatorial latitude, an upward **E**×**B** drift moves the plasma from low to high altitudes. At the same time, gravitational and pressure gradients move the ionisation downward along the magnetic field lines thus transporting plasma away from the equatorial sector towards higher latitudes. In this way ionisation maxima are formed north and south of the dip equator. As an illustration of this phenomenon, see Figure 1.

The Sheffield University Plasmasphere Ionosphere Model (SUPIM - Bailey *et al.*, 1993; Bailey *et al.,* 1996) is a first principles model in which coupled time-dependent equations of continuity, momentum and energy balance are solved along closed magnetic field lines between base altitudes of about 130 km in conjugate hemispheres to give values for the densities, field-aligned fluxes and temperatures of the electrons and of the O^+, H^+, He^+, N_2^+, O_2^+ and NO^+ ions. The model requires several input parameters, which include empirical models for the neutral atmosphere densities and temperatures, neutral wind and plasma **E**×**B** drift. For the present work, the respective models used are MSIS86 (Hedin, 1987),

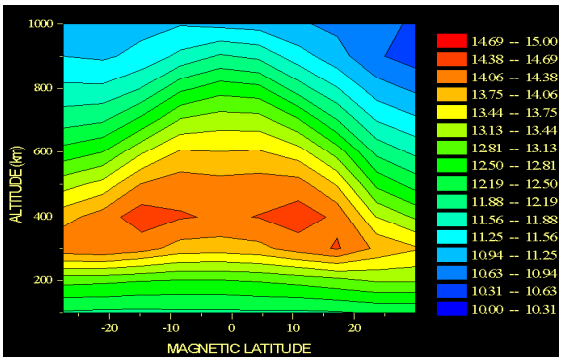

Figure 1 – Equatorial anomaly cross-section at 16 LT. Values of isolines are $\log_{10}$ Ne

HWM90 (Hedin *et al.*, 1991) and a model due to Scherliess and Fejer (1999).

In this work, we present a theoretical investigation of the contraction and expansion of the equatorial anomaly crests along the magnetic meridian. Also, we provide evidence of this behaviour in TEC data obtained at Cachoeira Paulista.

Experimental Data

Values of TEC for quiet conditions obtained from Faraday rotation technique are used in this study. The data were recorded over Cachoeira Paulista during the years 1982, 1984, 1986, 1988 and 1989. The satellites from which the data were received are given in Table 1. The data were recorded on February, March and April and have been grouped to represent autumn equinox conditions. Averages for 20 overlapping solar flux bins, spaced by 10 units were carried out to study the TEC solar flux dependence.

Results and Discussion

Figure 2 shows mean TEC variations with solar flux at 16 LT for autumn equinox conditions. As we can see, the TEC values decrease when the solar flux is greater than ~190. In order to investigate this unexpected feature we have carried out model calculations using SUPIM for autumn equinox conditions and for six values of F10.7.

Table 1 – Satellite and the years with data

Satellite	Year
	1986
GOES I	1988
	1989
GOES II/II	1982
	1984

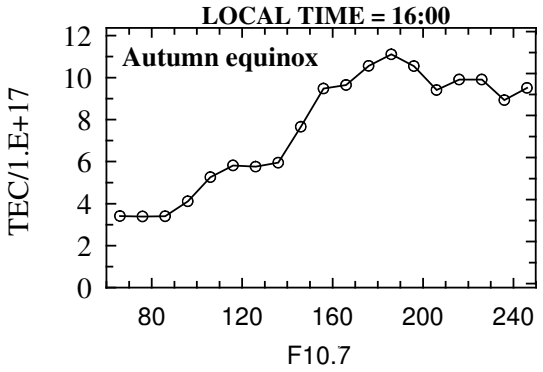

Figure 2 – Ionospheric total electron content variation with the solar flux 10.7 cm.

Figure 3 presents latitudinal variations of foF2 at 16 LT calculated by SUPIM for solar flux values equal to 66 (yellow curve), 146 (black), 186 (blue), 226 (green) 256 (pink) and 276 (red). During low solar flux condition there are no anomaly crests. In contrast, with increasing solar activity the anomaly crests increase in magnitude and expand in a poleward direction. Batista et al. (1994) have suggested that the saturation or decrease in TEC over Cachoeira Paulista is attributed to the southward movement of the equatorial anomaly. The results of this study support this suggestion.

Conclusions

Calculations carried out by SUPIM have revealed that for high solar flux (F10.7 > 190) the equatorial anomaly crests expand in a poleward direction. Consequentially, TEC present an unexpected behaviour, i.e., TEC decreases when F10.7 increases. This is a consequence of an increased equatorial **E×B** drift. An increase in the upward equatorial **E×B** drift has caused the equatorial anomaly expansion, i.e, the position of the anomaly crest move in the poleward direction so that Cachoeira Paulista is in the anomaly trough instead of at the crest.

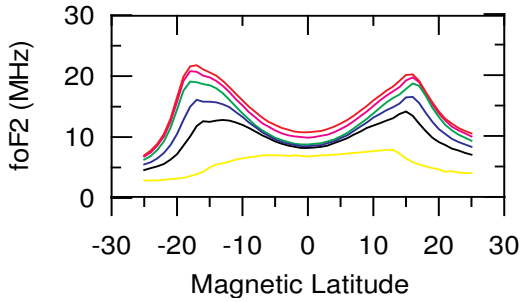

Figure 3 – Latitudinal variation of foF2 calculated by SUPIM for solar flux equals to 66 (yellow curve), 146 (black), 186 (blue), 226 (green) 256 (pink) and 276 (red) respectively.

Reference

Anderson, D.N. Theoretical study of the ionospheric F region equatorial anomaly-I. *Planet. and Space Sci.*, 21(3):409-419, Mar. 1973a.

Anderson, D.N. Theoretical study of the ionospheric F region equatorial anomaly-II. Results in the America and Asian sectors. *Planet. and Space Sci.*, 21 (3):421-442, Mar. 1973b.

Bailey, G. J., and N. Balan, A low latitude ionosphere-plasmasphere model, in *STEP Hand Book of Ionospheric models*, edited by R. W. Schunk, pp. 173-206, Utah State University, 1996.

Batista, I. S. ,J. R. Souza, M. A. Abdu, E. R. de Paula, Total electron content at low latitudes and its comparison with the IRI90. *Adv. Space Res.* 14 (12), 87-90, 1994.

Hedin, A. E. MSIS-86 thermospheric model. *J. Geophys. Res.*, *92*, 4649-4662, 1987.

Hedin, A. E. et al., Revised global model of thermosphere winds using satellite and ground-based observations. *J. Geophys. Res*., *96*, 7657-7688, 1991.

Scherliess, L., and B. G. Fejer, Radar and satellite global equatorial F region vertical drift model, *J. Geophys. Res*., *104*, 6829-6842, 1999.

Acknowledgements

This work was supported by the Fundação e Amparo à Pesquisa do Estado de São Paulo (FAPESP) under the contracts 99/00437-0 and 00/12735-5